THESIS

Optomechanical Torsion Pendulum for Measurement of Quantum Radiation Pressure Fluctuation

Kentaro Komori

Department of Physics
University of Tokyo

January 2019

Abstract

Quantum radiation pressure fluctuation is caused by a vacuum field coupling with laser light. The amplitude of the laser light changes randomly, resulting in the fluctuation of intra-cavity power in an optical cavity and shaking of the mirror. It is important to measure it around 10-100 Hz using a massive oscillator heavier than mg from two view points of gravitational wave detectors and optomechanics. A torsion pendulum is used as a common mirror of two triangle cavities constructed on both edges in order to observe this phenomenon. The rotational mode is measured by subtracting signals from the two cavities. The optomechanical torsion pendulum has three advantages. First, it has low suspension thermal noise due to the low resonant frequency of the rotational mode. Second, common noises at both cavities are reduced by the common mode rejection. Third, the rotational mode is more sensitive because its effective mass is lighter than that of the pendulum mode. Due to these benefits, we succeed in observing quantum radiation pressure fluctuation around 60-100 Hz with a signal to noise ratio of 0.14 ± 0.03. This is the highest signal to noise ratio to date around the frequency band of gravitational-wave detectors using a mechanical oscillator above a milligram scale. Our work is important from the aspect of the frequency band, around which the detector sensitivity will be limited by the radiation pressure noise. The mass scale is also meaningful in terms of optomechanical research on the various scales.

Thesis Supervisor: Masaki Ando (Associate Professor)
Thesis Title: Optomechanical Torsion Pendulum for Measurement of Quantum Radiation Pressure Fluctuation

Contents

List of Figures

Glossary

i	imaginary unit $i = \sqrt{-1}$
c	speed of light $c = 299792458$ m/s
h	Planck constant $h = 6.626070040(81) \times 10^{-34}$ J·s
$\hbar$	Dirac constant $\hbar = h/2\pi$
k_B	Boltzmann constant $k_\mathrm{B} = 1.38064852(79) \times 10^{-23}$ J/K
G	Gravity constant $G = 6.67408(31) \times 10^{-11}$ $\mathrm{m}^3/\mathrm{kg}/\mathrm{s}^2$
e	elementary charge $e = 1.6021766208(98) \times 10^{-19}$ C
ω_L	angular frequency of laser light [Hz]
ω_c	angular resonant frequency of a cavity [Hz]
ω_m	angular resonant frequency of a mechanical mode [Hz]
γ_m	dissipation of a mechanical mode [Hz]
Q_m	Q-value of a mechanical mode
g	optomechanical coupling constant [Hz/m]
$\mathcal{F}$	cavity finesse
κ	cavity line width [Hz]
L_r	cavity roundtrip length [m]
m	mass of a mechanical oscillator [kg]
T_th	temperature of thermal bath [K]
P	laser power [W]
χ_c	cavity susceptibility [/Hz]
χ_m	mechanical susceptibility [m/N]
n_pn	phonon number
S_x	displacement power spectrum $[\mathrm{m}^2/\mathrm{Hz}]$
S_f	force power spectrum $[\mathrm{N}^2/\mathrm{Hz}]$
$\mathrm{M}_\odot$	solar mass $\mathrm{M}_\odot = 1.998 \times 10^{30}$ kg

AOM	Acousto Optic Modulator
BS	Beam Splitter
EOM	Electro Optic Modulator
FI	Faraday Isolator
FSR	Free Spectral Range
HWP	Half Wave Plate
QWP	Quarter Wave Plate
PBS	Polarizing Beam Splitter
PD	Photo Detector
QPD	Quadruple Photo Detector
UGF	Unity Gain Frequency
SQL	Standard Quantum Limit

Chapter 1

Introduction

Laser light couples with a vacuum field and propagates without lossing the vacuum fluctuation. It is because the energy scale of a photon from a laser $\hbar\omega_{\mathrm{L}}$ is much higher than that of room temperature $k_{\mathrm{B}}T_{\mathrm{th}}$. The laser photon is not excited thermally even at room temperature. The vacuum fluctuation has two degrees of freedom, amplitude and phase quadratures. These amplitude and phase degrees of freedom correspond to radiation pressure fluctuation and shot noise, respectively, in the displacement measurement of oscillators with laser light. In particular, it is important in terms of two perspective to observe the amplitude fluctuation, *i.e.*, the quantum radiation pressure fluctuation. One is related to gravitational-wave detectors, and the other is associated with optomechanics.

Gravitational wave detectors

Graviational waves (GWs) are ripples of space time predicted by Einstein almost one hundred years ago [1,2]. We can get a wave equation by linearizing the Einstein equation after splitting the metric of space time to Minkowski plus a tiny fluctuation. The solution shows the GW. It is generally difficult to observe the GWs compared with electromagnetic waves because of the tiny amplitude. Emission of large GWs is expected from drastic astronomical phenomena, such as coalescence of binary compact stars, explosion of supernova, and the big-bang at the start of the universe. GWs bring us information which cannot be

obtained with electromagnetic waves thanks to its great transparency.

Even if these phenomena happen, the amplitude of the GW reaching the earth is too small to catch easily, so it had never been observed directly until 2015. On September 14th in 2015, Laser Interferometer Gravitational-wave Observatory (LIGO) directly observed GWs at last. These came from a binary black hole merger [3]. This event is not only the first detection of GWs, but also revealed the existence of binary black holes. Moreover, Virgo, which is the third GW detector in Italy, started operating and contributed to the joint observation of GWs with LIGO in 2017 [4]. That event was followed by, at last, GWs from a binary neutron star merger [5]. At the same time electro-magnetic waves were observed by dozens of telescopes at various wave lengths [6, 7]. In 2018, all of the binary black hole mergers in their two observation phases were reported and the total number of GW events grew up to 11 [8]. The era of GW astronomy and multi-messenger astronomy thus opened.

LIGO and Virgo are currently improving their sensitivities, and the Japanese GW detector KAGRA [9,10] will join the detector network in late 2019. Moreover, the next-generation GW detectors such as Einstein Telescope (ET) [11] and Cosmic Explorer (CE) [12] are expected to constructed in the 2030s. These detectors in the future will observe much more GWs from binary stellar-mass compact stars with their improved sensitivities. In particular, CE will catch almost all binary black hole mergers in the universe and can test for the existence of primordial black holes [13].

For observation of GWs from binary stellar-mass compact stars, the frequency range between 10 Hz and 100 Hz is the most important to obtain the signal to noise ratio during their inspiral phase towards merger. The future sensitivities of the detectors around that frequency region will be limited by radiation pressure noise, which is one of fundamental noises [14,15]. Radiation pressure noise, however, has not been observed yet around the detector band, especially at the radiation pressure noise regime. The sensitivities of the previous works [16–21] are worse than the radiation pressure noise by one order of magnitude or more. It is important to measure it and demonstrate how to reduce the quantum noise on a table-top scale experiment ahead of real GW detectors.

Optomechanics

Can we prepare quantum entangled states of massive oscillators? Such states have never been observed yet. Is this because of only technical issues in isolating the massive objects from the environment, or due to something fundamental preventing them from existing in a quantum state?

Optomechanics is about the interaction between eigen modes of mechanical oscillators and radiation pressure of laser light [22]. Radiation pressure can suppress mechanical motion. This means that it can reduce the effective temperature of the mechanical modes. The cooling effect can be used even for cooling the mechanical oscillator to its quantum ground state and observing the zero-point oscillation [23]. Moreover, the method was proposed to realize entangled states of the massive oscillators using the quantum coherence of laser light if the mechanical mode is cooled enough [24].

In order to do these experiments, we have to cool the mechanical oscillator to the ground state or reach its standard quantum limit (SQL). Observation of quantum radiation pressure fluctuation acting on the oscillator is the first necessary condition for that. The quantum radiation pressure fluctuation on mechanical oscillators was first observed with a nano-scale silicon beam in 2012 [25], followed by an experiment with membranes [26, 27]. These oscillators were also cooled to ground state [28–30]. In addition, it was reported that entangled states between distinct two mechanical modes were finally realized [31–33].

On the other hand, although the progress is great in the field of optomechanics whose mass scale is lighter than the μg-scale, it has not been developed much in the heavier mass scale [16–21]. It is important to develop optomechanics in various mass scales including above the μg-scale because some theories predict the mass dependence on the time scale of quantum coherence. In order to test the quantumness of the massive object, it is necessary to improve the displacement sensitivity of the mechanical motion up to near the standard quantum limit, and one of the necessary conditions is to observe the radiation pressure fluctuation. Therefore, we try to measure the quantum radiation pressure fluctuation acting on a massive objects. Our experiment is the first step to realize macroscopic (in terms of the mass) quantum superposition states.

We aim at observation of quantum radiation pressure fluctuation with a mg-scale mechanical oscillator around 10-100 Hz. In previous works on this regime, classical noises such as suspension thermal noise hid the quantum fluctuation. Thus, we design the setup using a rotational mode of a torsion pendulum which has low suspension thermal noise due to the low mechanical resonant frequency. A 10-mg bar-shaped tiny mirror is used as a torsion pendulum. Two optical cavities are constructed on both edges of the bar mirror. We can get the quantum fluctuation signal by subtracting displacement of the two cavities and measuring the rotational mode of the torsion pendulum. The quantum fluctuation causes the differential force and almost all classical noises contribute to the displacement identically across both cavities. This common mode rejection is one of advantages in our setup. Moreover, the rotational mode is more sensitive to tiny force than the usual pendulum mode owing to the lighter effective mass, which is also a main benefit.

This thesis consists of 7 chapters including this introduction. In Chapter 2, we introduce GW detectors and its noise sources including radiation pressure noise with previous works for measuring it. Chapter 3 shows theories of optical cavities and radiation pressure fluctuation from a viewpoint of optomechanics. In Chapter 4, our experimental design and setup are written, followed by the results of our experiments and data analysis in Chapter 5. In Chapter 6, various noise sources are discussed and finally future prospects for our research and conclusion of this thesis are described in Chapter 7. Additional contents for this thesis are given in the appendix, such as the suspension thermal noise with a temperature gradient in the cryogenic detector (Appendix A), and the sensitivity design of the current and future KAGRA (Appendix B).

Chapter 2

Quantum noises in a gravitational wave detector

The amplitude of the GW is so small that we have to reduce all noises in order to catch the GW with the detectors. Radiation pressure noise is one of the most fundamental noises in GW detectors. In this chapter, we discuss quantum noises from a viewpoint of the GW detectors.

First, theories on the GW and the detector are given in Section 2.1. After that Section 2.2 describes noises in the detectors, followed by reduction of the quantum noises and its necessity in Section 2.3. Finally, previous works on the quantum noises are introduced in Section 2.4.

2.1 Theories on the GW and the detector

Einstein predicted the GW as a wave solution in his general relativity in 1916 [1, 2]. The amplitude of the GW is so small because the interaction of gravity is tiny. The GW brings us unique information which is not accessible by usual electromagnetic wave observation. On the other hand, its smallness get the direct detection of the GW too difficult. Even though it was considered to be impossible to detect the GW for a while, experimental works for detection were developed step by step.

The development started from a resonant-bar type in the 1960s [34], and it was followed by an interferometric type in the 1960s [35] and the 1970s [36]

used mainly these days. Besides, indirect detection of the GW was realized by measuring the orbital period of a binary neutron star getting short with radio waves in 1982 [37] after the discovery of that in 1975 [38]. In 2000s, km-scale interferometric GW detectors were constructed and have been upgraded to current LIGO [14], Virgo [15], and KAGRA [9]. Finally two LIGOs directly detected GWs from a binary black hole merger in 2015 [3].

Here we show theories on the GW including the derivation and sources [39, 40]. The method and system of detectors are described after that.

2.1.1 Derivation of the GW

According to the general relativity, the strain of time-space is related to the distribution of the energy as follows:

$$R_{\mu\nu} - \frac{1}{2}g_{\mu\nu}R = \frac{8\pi G}{c^4}T_{\mu\nu}, \tag{2.1}$$

which is called the Einstein equation. The Ricci scalar R, the Ricci tensor $R_{\mu\nu}$, the Rieman tensor $R^{\alpha}_{\beta\mu\nu}$, the Christoffel symbol $\Gamma^{\alpha}_{\mu\nu}$, and the metric tensor $g_{\mu\nu}$ are defined as below:

$$R = R^{\mu}_{\mu}, \tag{2.2}$$

$$R_{\mu\nu} = R^{\alpha}_{\mu\alpha\nu}, \tag{2.3}$$

$$R^{\alpha}_{\beta\gamma\delta} = \Gamma^{\alpha}_{\beta\delta,\gamma} - \Gamma^{\alpha}_{\gamma\delta,\beta} + \Gamma^{\alpha}_{\gamma\mu}\Gamma^{\mu}_{\beta\delta} - \Gamma^{\alpha}_{\beta\mu}\Gamma^{\mu}_{\gamma\delta}, \tag{2.4}$$

$$\Gamma^{\alpha}_{\beta\gamma} = \frac{1}{2}g^{\alpha\mu}\left(g_{\gamma\mu,\beta} + g_{\mu\beta,\gamma} - g_{\beta\gamma,\mu}\right), \tag{2.5}$$

$$ds^2 = g_{\mu\nu}dx^{\mu}dx^{\nu}, \tag{2.6}$$

where ds is the interval between two points.

Assuming that the metric can be divided by Minkowski space-time $\eta_{\mu\nu}$ and small perturbation $h_{\mu\nu}$ which satisfies $|h_{\mu\nu}| \ll 1$, Eq. (2.1) can be written as

$$\Box\bar{h}_{\mu\nu} = -\frac{16\pi G}{c^4}T_{\mu\nu}, \tag{2.7}$$

where

$$\bar{h}_{\mu\nu} = h_{\mu\nu} - \frac{1}{2}\eta_{\mu\nu}h^{\alpha}_{\alpha} \tag{2.8}$$

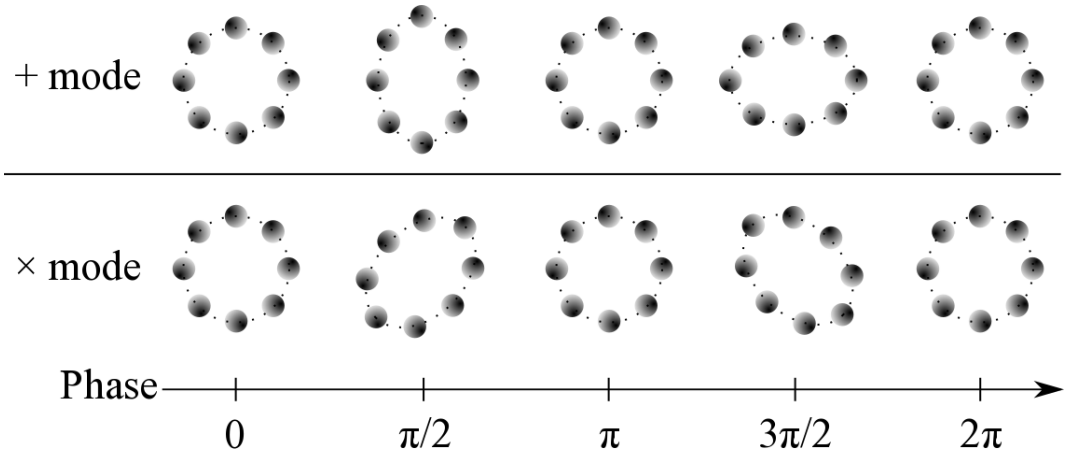

Figure 2.1: A drawing of the two polarizations of GWs. The shapes of the strain due to the GWs are described at each phase. Free particles move as shown when the GWs propagate perpendicularly to the page space.

is satisfied and the Lorenz gauge is chosen. This means that there is a wave solution of the Einstein equation and the wave propagates at the speed of light even in vacuum $T_{\mu\nu} = 0$.

In the transverse traceless (TT) gauge, we can set

$$h^{0\mu} = 0,\ h^i_i = 0,\ \partial^j h_{ij} = 0. \tag{2.9}$$

Considering that the wave direction is along z axis, the solution shows

$$h^{TT}_{ij}(t,z) = \begin{pmatrix} h_+ & h_\times & 0 \\ h_\times & -h_+ & 0 \\ 0 & 0 & 0 \end{pmatrix} \cos\left[\omega(t - z/c)\right], \tag{2.10}$$

and at this time the interval can be described as

$$\begin{aligned} ds^2 =& -c^2dt^2 + dz^2 + \{1 + h_+ \cos\left[\omega(t - z/c)\right]\}dx^2 \\ &+ \{1 - h_+ \cos\left[\omega(t - z/c)\right]\}dy^2 + 2h_\times \cos\left[\omega(t - z/c)\right] dxdy. \end{aligned} \tag{2.11}$$

The GW in general relativity has two polarizations, h_+ and $h_\times$. According to Eq. (2.11), The GW stretches the surface perpendicular to the propagating direction to one direction and shrinks to another at the same time with ratio

of h. The number of degrees of freedom is two. They are different by 45°. Fig. 2.1 shows the effect of the GW on the free particles in the plane perpendicular to the propagation at each phase. The GW has two polarizations of the plus and cross mode.

2.1.2 GW sources

In this section, we describe various sources of GWs after deriving the radiation formula. Here we adopt the far-zone approximation. Distance between observer and the GW sources r is much greater than the GW wave length λ, which is greater than size of the source R,

$$R \ll \lambda \ll r. \tag{2.12}$$

Under this situation Eq. (2.7) can be solved with Green's function as

$$h_{ij}^{TT}(r, \mathbf{x}) \simeq \frac{1}{r}\frac{2G}{c^4}\ddot{I}_{ij}^{TT}(t - r/c) \tag{2.13}$$

in the TT gauge. The quadrupole moment is introduced as

$$I_{ij}^{TT}(t) = \int d\mathbf{x}\, \rho(t, \mathbf{x}) \left(x_i x_j - \frac{1}{3} r^2 \delta_{ij} \right), \tag{2.14}$$

where ρ is mass density of the source.

Now we can estimate order of magnitude of the GW. The quadrupole moment can be approximated as $I \sim MR^2$, and hence $\ddot{I} \sim Mv^2$, where M is mass and v is velocity of the source. For example, when a bar with the length of L and the mass of M is rotating at the angular frequency of ω, the magnitude is

$$h \sim \frac{GML^2\omega^2}{rc^4}. \tag{2.15}$$

Assuming that $M = 10^3\,\mathrm{kg}$, $L = 10\,\mathrm{m}$, $\omega/2\pi = 10^2\,\mathrm{Hz}$ and noting that the distance must be greater than the GW wavelength ($r \gg c/\omega$), we can get the order of amplitude

$$h \ll \frac{GML^2\omega^3}{c^5} \sim 10^{-39}. \tag{2.16}$$

This magnitude is very tiny.

On the other hand, there are sources expected to produce much larger GWs than artificial one even though they have cosmological distance. Hereafter these sources are categorized with typical amplitude and frequency.

Compact binary coalescence

Compact binary is a binary system consisting of two compact stars such as neutron stars and black holes. They are rotating around each other and finally merge resulting in the emission of large GWs. The source of the first direct detection of GW is a black hole merger. After some detections of binary black hole mergers, a binary neutron star merger has been also detected. The GW from a binary neutron star was expected to be promising candidates of direct detection because the GW emission from the system already has been tested via the radio wave observation of change of the revolution period [37, 38].

Here we assume that mass of each star of the binary is the same as M. In point mass approximation for the stars, when the GW comes along the perpendicular axis, the amplitude of the GW can be written as

$$h = \pi^{2/3} \left(\frac{R_{\rm s}}{r} \right) \left(\frac{R_{\rm s} f_{\rm gw}}{c} \right)^{2/3}, \tag{2.17}$$

where $R_{\rm s} \equiv 2GM/c^2$ is the Schwarzschild radius for the mass of each star, r is distance between the source and observer, and $f_{\rm gw}$ is frequency of the GW. The particle limit can be applied roughly until their rotating orbit reaches an Innermost Stable Circular Orbit (ISCO) $r_{\rm ISCO} = 12GM/c^2$. At that time the GW frequency increases to

$$f_{\rm gw,ISCO} = \frac{1}{6\sqrt{6}\pi} \frac{c}{R_{\rm s}}. \tag{2.18}$$

Thus, the amplitude of the GW at ISCO is

$$h_{\rm ISCO} = \frac{1}{6} \frac{R_{\rm s}}{r}, \tag{2.19}$$

The amplitude just before coalescence is decided by ratio of the Schwarzschild

Event	Masses [$M_\odot$]	Red shift	Localization [deg^2]
GW150914	$35.6^{+4.8}_{-3.0} + 30.6^{+3.0}_{-4.4}$	$0.09^{+0.03}_{-0.03}$	179
GW151012	$23.3^{+14.0}_{-5.5} + 13.6^{+4.1}_{-4.8}$	$0.21^{+0.09}_{-0.09}$	1555
GW151226	$13.7^{+8.8}_{-3.2} + 7.7^{+2.2}_{-2.6}$	$0.09^{+0.03}_{-0.04}$	1033
GW170104	$31.0^{+7.2}_{-5.6} + 20.1^{+4.9}_{-4.5}$	$0.19^{+0.07}_{-0.08}$	924
GW170608	$10.9^{+5.3}_{-1.7} + 7.6^{+1.3}_{-2.1}$	$0.07^{+0.02}_{-0.02}$	396
GW170729	$50.6^{+16.6}_{-10.2} + 34.3^{+9.1}_{-10.4}$	$0.48^{+0.19}_{-0.20}$	1033
GW170809	$35.2^{+8.3}_{-6.0} + 23.8^{+5.2}_{-5.1}$	$0.20^{+0.05}_{-0.07}$	340
GW170814	$30.7^{+5.7}_{-3.0} + 25.3^{+2.9}_{-4.1}$	$0.12^{+0.03}_{-0.04}$	87
GW170817	$1.46^{+0.12}_{-0.10} + 1.27^{+0.09}_{-0.09}$	$0.01^{+0.00}_{-0.00}$	16
GW170818	$35.5^{+7.5}_{-4.7} + 26.8^{+4.3}_{-5.2}$	$0.20^{+0.07}_{-0.07}$	39
GW170823	$39.6^{+10.0}_{-6.6} + 29.4^{+6.3}_{-7.1}$	$0.34^{+0.13}_{-0.14}$	1651

Table 2.1: Observed GW events [8].

radius of the component and the distance from observer. Typical amplitude and frequency are

$$h_{\rm ISCO} = 1 \times 10^{-21} \left(\frac{M}{30\,{\rm M}_\odot} \right) \left(\frac{400\,{\rm Mpc}}{r} \right), \tag{2.20}$$

$$f_{\rm gw,ISCO} = 24\,{\rm Hz} \left(\frac{30\,{\rm M}_\odot}{M} \right). \tag{2.21}$$

This GW sources which has been observed are listed in Table 2.1. The third event GW170608 came from the farthest distance, corresponding to the redshift of $z \sim 0.2$. The black holes of the fourth event GW170608 are the lightest ones observed by the GW. The binary neutron star event GW170817 has the best record of the signal to noise ratio and the localization. The best localization is due to not only the near event but also the fact that the GW came from the blind spot of Virgo and it was not able to observe the GW.

Supernova

One of the promising source except for compact binary coalescence is supernova explosion. For example, a type II supernova is typical. Massive stars heavier than around $10\,{\rm M}_\odot$ make the iron core, which has the highest bind-

ing energy of all atoms, at the center with supported by electron degeneracy pressure in the final phase of star evolution. Finally, after gravity beats the degeneracy pressure, gravitational collapse occurs and the outer matters fall into the center. The collapse is stopped by neutron degeneracy. It causes bounce of falling objects and making shock waves expanding out of the star. This is observed as a supernova.

These phenomena are expected to follow drastic change of the gravitational potential, especially the quadrupole moment. The amplitude of the GW from supernova is approximately given by

$$h \sim \frac{G}{rc^4}\left(\ddot{I}_{22} - \ddot{I}_{33}\right), \tag{2.22}$$

where

$$I_{22} = \frac{2}{5}MR^2\left(1 - \frac{e^2}{2}\right),\ I_{33} = \frac{2}{5}MR^2, \tag{2.23}$$

M, R, and e are the mass, radius, and eccentricity of the proto-neutron star, respectively. Assuming that $M = 1\,\mathrm{M}_\odot$, $R = 10\,\mathrm{km}$, and $e = 0.1$, time scale of this event can be considered as the free-fall time scale

$$\tau_\mathrm{f} = \sqrt{\frac{3\pi}{32}\frac{1}{G\rho}}, \tag{2.24}$$

where $\rho \sim 10^{18}\ \mathrm{kg/m^3}$ is the density of nuclear. Therefore, typical frequency and amplitude of the GW from supernova are obtained by

$$f_\mathrm{gw,sn} \sim \frac{1}{2\pi\tau_\mathrm{f}} \sim 3 \times 10^3\,\mathrm{Hz}, \tag{2.25}$$

$$h_\mathrm{sn} \sim 2 \times 10^{-21}\left(\frac{10\,\mathrm{kpc}}{r}\right). \tag{2.26}$$

Pulsar

Pulsar is a rotating neutron star emitting radio wave, which is observed as short pulses when the axis of the emission and the sight direction of the observer are overlapped. It is also one of promising candidates of the observation.

Although there is no GW emission if the neutron star is rotating axis-symmetrically, it produces the GW with ellipticity $\epsilon = (I_{11} - I_{22})/I_{33}$. The

amplitude of the GW is written as

$$h = \frac{4\pi^2 G I_{33} f_{\mathrm{gw,pu}}^2}{rc^4}\epsilon. \tag{2.27}$$

Here we assume that mass and radius of the neutron star is $M = 1\,\mathrm{M}_\odot$ and $R = 10\,\mathrm{km}$, respectively. By observation of radio wave, it is known that typical frequency of the GW from pulsars is

$$f_{\mathrm{gw,pu}} = 10\,\mathrm{Hz} - 1\,\mathrm{kHz}, \tag{2.28}$$

which is double of the rotating frequency. The amplitude is calculated as

$$h_{\mathrm{pu}} \sim 8 \times 10^{-26} \left(\frac{f}{1\,\mathrm{kHz}}\right)^2 \left(\frac{10\,\mathrm{kpc}}{r}\right) \left(\frac{\epsilon}{1 \times 10^{-6}}\right). \tag{2.29}$$

Early universe

It is a kind of final goal for the GW astronomy to hear the early universe. In the usual electro-magnetic wave observation such as cosmic microwave background (CMB) search, we can only see up to the recombination which occurred around 0.38 million years after the Big Bang. It is because electro-magnetic waves cannot avoid interacting with the radiation field and losing the information on the previous era. On the other hand, gravity is so weak that GW can avoid the interaction. It is the unique probe for information at the early universe such as the energy scale of the inflation.

Amplitude of the GW from the early universe is characterized by one of cosmological parameters, Ω_{GW}, like

$$h = \sqrt{\frac{3H_0^2\Omega_{\mathrm{GW}}}{4\pi^2 f^3}}, \tag{2.30}$$

where $H_0 \sim 67\,\mathrm{km/s/Mpc}$ is Hubble constant. Here we assume Ω_{GW} does not have dependence on frequency. The value is estimated to be $\Omega_{\mathrm{GW}} \sim 10^{-16}$. According to Eq. (2.30), the GW at lower frequency has larger amplitude. In the frequency range below 0.1 Hz, however, there are superposed GWs from binary white dwarfs in our galaxy. This prevents us from detecting the GW

from the early universe. Therefore, the best frequency for detection is

$$f_{\rm gw,eu} \sim 0.1\,{\rm Hz}, \tag{2.31}$$

and the amplitude is written as

$$h_{\rm gw,eu} \sim 2\times 10^{-25}\sqrt{\frac{\Omega_{\rm GW}}{1\times 10^{-16}}}\left(\frac{0.1\,{\rm Hz}}{f}\right)^{\frac{3}{2}}. \tag{2.32}$$

2.1.3 Interferometric GW detectors

Ultra-high sensitivity is required to detect GWs because it has so tiny amplitude as shown in the previous section. In the 1960s and the 1970s, it was proposed that a Michelson interferometer consisting of suspended mirrors can be used as a GW detector [35, 36]. A Michelson interferometer as a GW detector was expanded to Fabry–Perót cavities. Here, we describe the response to the GW of the detector.

Mechanical response

At first, the geodesic equations are considered. Taking difference between two nearby geodesics parametrized by x^μ and ξ^μ, we can get equations on spatial part of ξ^μ as

$$\begin{aligned}\ddot{\xi}^i &= -R^i_{0j0}\xi^j\left(\frac{dx^0}{d\tau}\right)^2 \\ &= \frac{1}{2}\ddot{h}^{TT}_{ij}\xi^j\end{aligned} \tag{2.33}$$

in a proper detector frame. This means that the effect of the GW can be regarded as classical force

$$F_i = \frac{m}{2}\ddot{h}^{TT}_{ij}\xi^j \tag{2.34}$$

to a point particle whose mass is m.

We consider a Michelson interferometer where end mirrors reflecting laser light are located on $(\xi_x, \xi_y) = (L, 0), (0, L)$. End mirrors are mechanical oscillators such as pendula with angular resonant frequency of $\omega_{\rm m}$ and mechanical dissipation of $\gamma_{\rm m}$. When the GW with the plus polarization propagates to

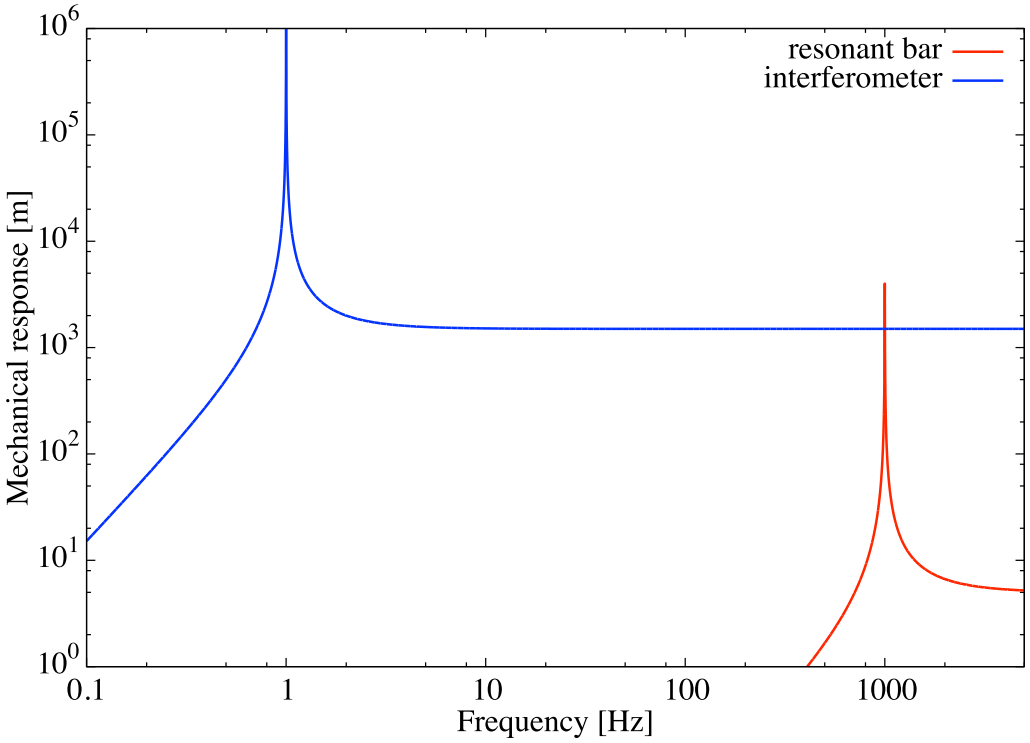

Figure 2.2: Mechanical response of the bar-type and interferometer-type GW detectors. Parameters of the resonant bar are $\omega_{\rm m}/2\pi = 1\,{\rm kHz}$, $\gamma_{\rm m} = \omega_{\rm m}/1000$, $L = 10\,{\rm m}$. Those of the interferometer are $\omega_{\rm m}/2\pi = 1\,{\rm Hz}$, $\gamma_{\rm m} = \omega_{\rm m}/1000$, $L = 3\,{\rm km}$.

z-direction, the equation of motion of the x arm mirrors, whose mass is m, is given by

$$m\left(\ddot{\xi}_x + \gamma_{\rm m}\dot{\xi}_x + \omega_{\rm m}^2\xi_x\right) = \frac{m}{2}\ddot{h}_+\xi_x, \tag{2.35}$$

where the right hand can be approximated as $\ddot{h}_+\xi_x \simeq \ddot{h}_+ L + \mathcal{O}(h^2)$. In frequency domain, Eq. (2.35) can be written as

$$\left(\omega_{\rm m}^2 + i\gamma_{\rm m}\omega - \omega^2\right)\xi_x = -\frac{1}{2}h_+ L\omega^2. \tag{2.36}$$

Therefore, the transfer function from strain of the GW to coordinate change (the mechanical response) of the end mirror is shown in

$$\frac{\xi_x}{h_+} = \frac{L}{2}\frac{\omega^2}{\omega^2 - \omega_{\rm m}^2 - i\gamma_{\rm m}\omega}, \tag{2.37}$$

which means that the response is flat above the mechanical resonant frequency of the mirror, while the mirror cannot be moved by the lower-frequency GW.

Fig. 2.2 shows the absolute value of the mechanical response of two types of the GW detector. One is a resonant bar type. It was developed in 1960s as the first GW detector by Weber. For a while from that time, this type of the detector was in the main stream. The test mass is a rigid heavy bar. It has a high sensitivity around the frequency of the bar resonance. The advantage of the bar detector is measuring GWs on one frequency coming from pulsars. The other is an interferometer type described later. It is in the recent main stream. The test masses are pendula, whose typical resonant frequencies are low. The merit is that the pendula can be placed on a faraway place, so we can set very large L. Moreover, the sensitivity range is the same as the GW frequency band from binary compact stars.

Under this discussion, it is assumed that the GW frequency is much larger than the inverse of time needed for the GW to propagate through the arm, $\omega \ll c/L$. The effect of the GW on mirror motions is cancelled while propagating when the frequency is higher than that.

Optical response

Next, we describe the response of an interferometer to the coordinate change of the end mirror. In a Michelson interferometer we can measure phase shift of laser light caused by differential motion of end mirrors. Moreover, a Fabry–Perót cavity can enhance the phase shift. We show a schematic picture of a Fabry–Perót Michelson interferometer in Fig. 2.3.

A Fabry–Perót cavity consists of two facing mirrors. When the input mirror has small transmission and the cavity round trip length is near integer times of laser wave length $\lambda_{\rm L}$, power of the light is enhanced dramatically. This state is called resonance. Here we introduce a parameter, finesse written by $\mathcal{F}$, which characterizes sharpness of the cavity resonance. The cavity is resonating under both situations where the wave length is $1/n$ and $1/(n+1)$ times of the cavity length, where n is a integer. The frequency difference of the laser light is called FSR,

$$\nu_{\rm FSR} = \frac{c}{2L}. \tag{2.38}$$

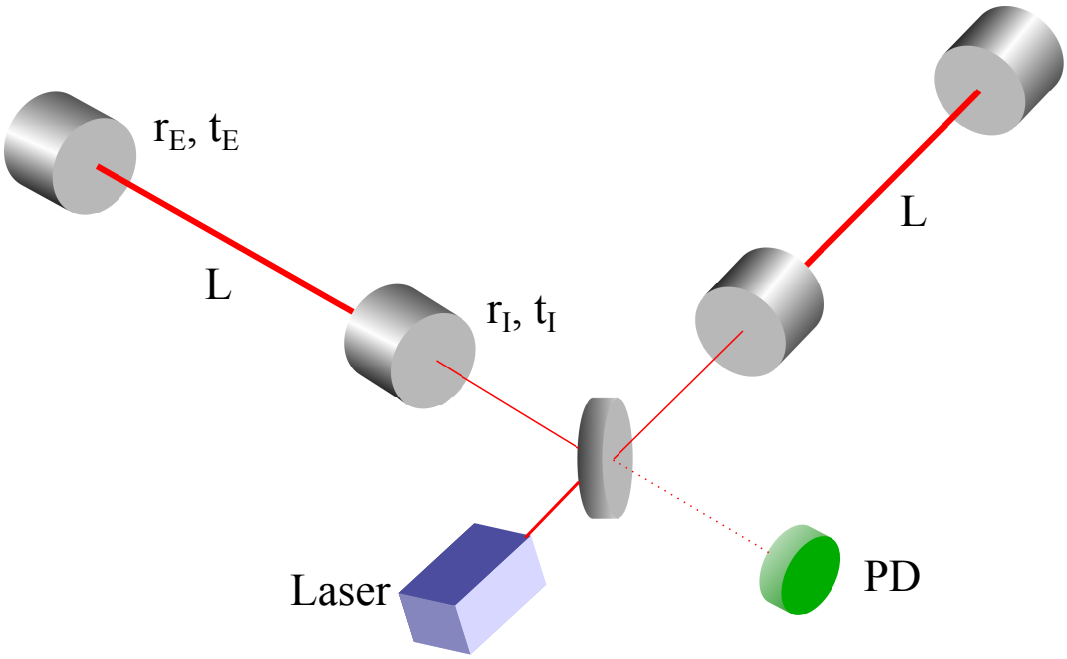

Figure 2.3: A schematic picture of a Fabry–Perót Michelson Interferometer. Two Fabry–Perót cavities replace the end mirrors of an usual Michelson interferometer.

On the other hand, laser light is enhanced even if the wave length is not just integer times but near that. This frequency width is defined as full width of the half maximum of the resonance peak,

$$\nu_{\mathrm{FWHM}} = \frac{1 - r_{\mathrm{I}} r_{\mathrm{E}}}{2\pi\sqrt{r_{\mathrm{I}} r_{\mathrm{E}}}} \frac{c}{L}, \tag{2.39}$$

where $r_{\mathrm{I}} \simeq 1$ and $r_{\mathrm{E}} \simeq 1$ are the reflectivity of the input and end mirror respectively. Finesse is the ratio of these parameters,

$$\mathcal{F} = \frac{\nu_{\mathrm{FSR}}}{\nu_{\mathrm{FWHM}}} = \frac{\pi\sqrt{r_{\mathrm{I}} r_{\mathrm{E}}}}{1 - r_{\mathrm{I}} r_{\mathrm{E}}}, \tag{2.40}$$

showing enhancement factor of the cavity.

The reflectivity of a Fabry–Perót cavity r_{FP} is given by

$$r_{\mathrm{FP}} = -r_{\mathrm{I}} + t_{\mathrm{I}}^2 r_{\mathrm{E}} \sum_{n=1}^{\infty} (r_{\mathrm{I}} r_{\mathrm{E}})^{n-1} e^{-i\omega_{\mathrm{L}} \Delta t_n}, \tag{2.41}$$

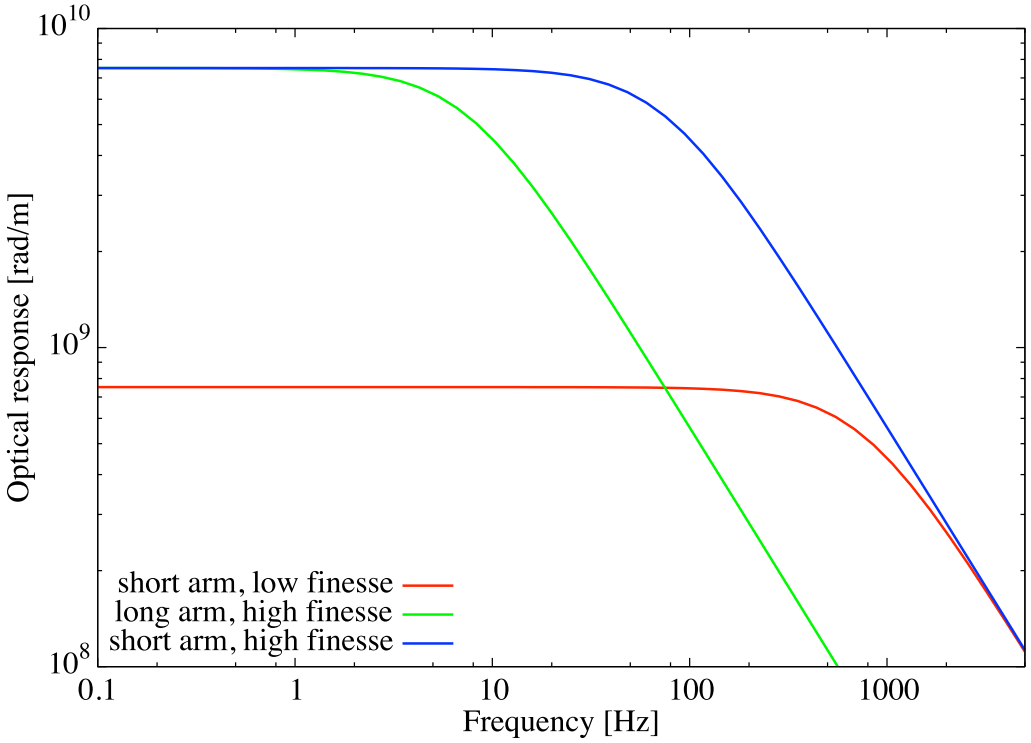

Figure 2.4: Optical response of the Fabry–Perót Michelson interferometer at the different finesse and arm length. Short and long arms mean $L = 1\,\mathrm{km}$ and $L = 10\,\mathrm{km}$, and high and low finesses mean $\mathcal{F} = 100$ and $\mathcal{F} = 1000$, respectively.

where t_I and Δt_n are transmissivity of the input mirror and time taken for laser light to go and return by n times in the cavity. This time can be written as

$$\Delta t_n = \frac{2L}{c}n + \frac{2}{c}\sum_{m=1}^{n}\delta L\left[t - \frac{L}{c}(2m-1)\right], \tag{2.42}$$

where δL is change of cavity length caused by the GW. By using a Fourier transformation, this can be rewritten as

$$\Delta t_n = \frac{2L}{c}n + \frac{2}{c}\int_{-\infty}^{\infty}\delta L\frac{1-e^{-2i\eta n}}{e^{i\eta}-e^{-i\eta}}e^{i\omega t}d\omega, \tag{2.43}$$

where $\eta = L\omega/c$. We assume that $r_\mathrm{E} = 1$ and the resonance condition $2L\omega_\mathrm{L}/c = 2\pi n$ is satisfied. It is enough to calculate under the 1st order

approximation of $\omega_{\rm L}\delta L/c$ because the displacement is much smaller than the wave length of the laser light, $\delta L \ll \lambda_{\rm L}$. In frequency domain, and hence, the reflectivity is calculated as

$$\begin{aligned} r_{\rm FP} &\simeq -r_{\rm I} + t_{\rm I}^2 \sum_{n=1}^{\infty} r_{\rm I}^{n-1} \left[1 - i\frac{2\omega_{\rm L}}{c}\delta L \frac{1 - e^{-2i\eta n}}{e^{i\eta} - e^{-i\eta}} \right] \\ &\simeq 1 - i\frac{4\pi(1+r_{\rm I})}{\lambda_{\rm L}} \frac{e^{-i\eta}}{1 - r_{\rm I}e^{-2i\eta}} \delta L. \end{aligned} \tag{2.44}$$

The phase shift of the cavity is expressed as $\Delta\phi_{\rm FP} = \arg r_{\rm FP}$. The GW frequency is low enough ($\eta \ll 1$), and the finesse can be approximated as $\mathcal{F} \simeq \pi\sqrt{r_{\rm I}}/(1-r_{\rm I}) \simeq \pi/(1-r_{\rm I})$. Therefore, the optical response from the mirror displacement to the phase shift of the Fabry–Perót Michelson Interferometer is

$$\frac{|\Delta\phi_{\rm FP}|}{\delta L} \simeq \frac{8\mathcal{F}}{\lambda_{\rm L}} \frac{1}{\sqrt{1 + (f/f_{\rm p})^2}}, \tag{2.45}$$

where

$$f_{\rm p} \simeq \frac{c}{4L\mathcal{F}} = \frac{\nu_{\rm FWHM}}{2} \tag{2.46}$$

is called a cavity pole. This means that the optical response gets worse above the cavity pole because the fast motion is averaged while laser light makes many round trips in the cavity.

In Fig. 2.4, the optical responses of the Fabry–Perót Michelson interferometer are plotted. The sensitivity is higher with a longer arm length at the low frequency, but gets worse at the high frequency because the cavity pole is lower. Considering that with the mechanical response proportional to the arm length, the total response is the same at the high frequency even with the long arm.

Total response

Combining the mechanical (Eq. (2.37)) and optical (Eq. (2.45)) response, we can get the transfer function from strain of the GW to phase shift of the Fabry–Perót Michelson interferometer $|\Delta\phi_{\rm FPMI}|$. Noting that the GW effect contributes to both arms differentially which can be measured by the Michelson interferometer, the phase shift is twice as large as that with only one cavity,

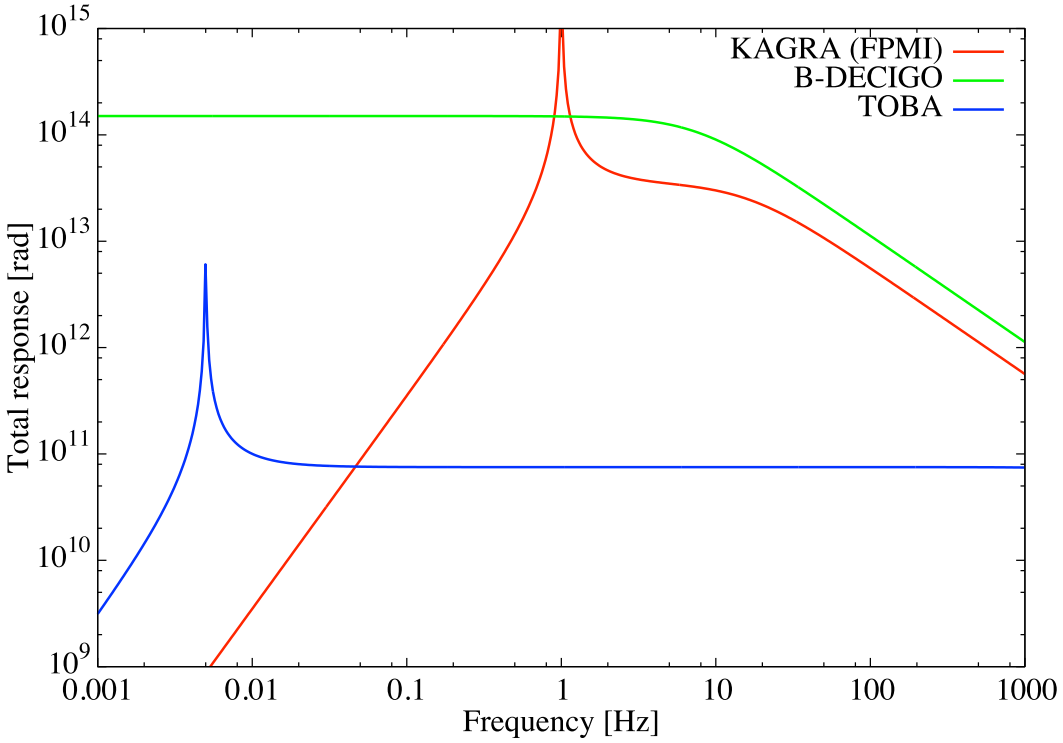

Figure 2.5: Total responses of the Fabry–Perót Michelson interferometer to the GW strain. The responses combining the mechanics and optics of KAGRA, B-DECIGO, and TOBA are shown in the red, green, and blue lines, respectively.

$\Delta\phi_{\mathrm{FPMI}} = 2\Delta\phi_{\mathrm{FP}}$. The total response is given by

$$\frac{|\Delta\phi_{\mathrm{FPMI}}|}{h_+} \simeq \frac{8\mathcal{F}L}{\lambda_{\mathrm{L}}} \frac{\omega^2}{\omega^2 - \omega_{\mathrm{m}}^2} \frac{1}{\sqrt{1 + (f/f_{\mathrm{p}})^2}} \tag{2.47}$$

with ignoring the mechanical dissipation.

In Fig. 2.5, this total response is shown on some GW detectors. Parameters of KAGRA are used in the plot of ground-based GW detectors, $\mathcal{F} = 1550$, $L = 3\,\mathrm{km}$, and $\lambda = 1064\,\mathrm{nm}$. In fact, ground-based detectors have multiple suspension system, but here one pendulum whose mechanical resonant frequency is $\omega_{\mathrm{m}}/2\pi = 1\,\mathrm{Hz}$. For example, the typical amplitude of GWs from binary coalescence is around $h \sim 10^{-21}$ as shown in the previous subsection, which is enhanced up to phase shift of $\sim 10\,\mathrm{nrad}$ by the ground-based detectors above the mechanical resonant frequency.

It should be noted that typical GW detectors like KAGRA has the signal recycling mirror between the BS and the PD enhancing the frequency band. The plot only shows the response of the Fabry–Perót Michelson interferometer with the same arm cavities as KAGRA.

A detector with the highest sensitivity is B-DECIGO where $\mathcal{F} = 100$, $L = 100\,\mathrm{km}$, $\lambda = 532\,\mathrm{nm}$. Deci-hertz gravitational wave observatory (DECIGO) is a GW detector in space targeting GWs from the early universe [41, 42]. B-DECIGO (called pre-DECIGO previously) is its outpost plan with shorter arms of 100 km [43]. In the case of spaceborne detectors, suspension system is not needed and the test masses are perfect free masses, $\omega_\mathrm{m}/2\pi = 0\,\mathrm{Hz}$. The target frequency of the GW is around 0.1 Hz.

Another detector which has high sensitivity around 0.1 Hz is TOBA where $\mathcal{F} = 1000$, $L = 10\,\mathrm{m}$, $\lambda = 1064\,\mathrm{nm}$. Torsion bar antenna (TOBA) is a new type of the GW detector [44]. It is a suspended torsion pendulum which rotates due to the GW. TOBA cannot have large arm length because it consists of a massive bar. However, the mechanical resonant frequency can be much lower than that of a usual pendulum down to $\omega_\mathrm{m} = 5\,\mathrm{mHz}$. Then it has much higher sensitivity compared with conventional ground-based GW detectors around 0.1 Hz range.

In this section, we describe theories on GWs and detectors focusing on how the amplitude of the GW is small even if it comes from the most drastic phenomena in the universe, and how we can enhance the effect and detect them with the Fabry–Perót cavities. There are various types of GW detectors, their sensitivities are limited by many noises, especially quantum noises of laser light, which are discussed in the next section.

2.2 Noises in GW detectors

Suspended mirrors of a GW detector are moved by many noise sources. These noises hide the GW signals, so we have to reduce them. The required level of noise reduction is very high because of the tiny amplitude of the GW.

First of all, power spectral density is introduced to discuss measured amplitude of noises in frequency domain. Next, we show quantum noise of laser light, which is one of the most fundamental noises, followed by another fun-

damental noise, thermal noise of the detector. Moreover, we introduce other technical noises such as seismic noise and laser frequency noise.

2.2.1 Power spectral density

Power spectral density is an useful value to evaluate the amplitude of fluctuation. It shows how the fluctuation at each frequency component contributes to averaged square of the interested value [39].

Here we define Fourier transformation of $x(t)$ as

$$\begin{aligned} X(\omega) &= \frac{1}{2\pi}\int_{-\infty}^{\infty} x(t)e^{-i\omega t}dt, \\ x(t) &= \int_{-\infty}^{\infty} X(\omega)e^{i\omega t}d\omega. \end{aligned} \tag{2.48}$$

With function defined on the interval $[-T/2, T/2]$ as

$$x_T(t) = \begin{cases} x(t) & |t| \leq T/2 \\ 0 & |t| > T/2, \end{cases} \tag{2.49}$$

single-sided power spectral density is given by

$$S_n(f) = \lim_{T\to\infty} \frac{2}{T} \left|2\pi X_T(f)\right|^2, \tag{2.50}$$

where

$$X_T(f) = \frac{1}{2\pi}\int_{-T/2}^{T/2} x_T(t)e^{-i2\pi ft}dt. \tag{2.51}$$

Then, we get the following equation on averaged square of $x(t)$,

$$\langle x^2(t)\rangle = \int_0^{\infty} S_n(f)df. \tag{2.52}$$

This means that the amplitude of fluctuation contributing to the averaged square at each frequency is $S_n(f)$.

In actual experiments, we cannot measure the value in infinity time. Therefore, usually the whole time-series data is divided to many set, the power spectral density is calculated at each data, and the average is taken. The more the

average is taken, the closer the experimental result gets to the real value. The statistical relative error σ_n is given by

$$\sigma_n = \frac{1}{\sqrt{n_{\mathrm{av}}}}, \tag{2.53}$$

where n_{av} is the average numbers. In this thesis, we adopt the Hanning window and half overlap for calculation of power spectra.

Moreover, we can describe the mean square with the measurement time T. If the spectral density does not depend on frequency, Eq. (2.52) can be written as

$$\langle x^2(t)\rangle = \frac{1}{2}S_n \int_{-\infty}^{\infty} df = \frac{1}{2}S_n \delta(t=0). \tag{2.54}$$

In the measurement in finite time T, the Dirac delta is replaced by

$$\delta(t) = \begin{cases} 1/T & |t| \leq T/2 \\ 0 & |t| > T/2. \end{cases} \tag{2.55}$$

Therefore, $\delta(t=0) = 1/T$ and we get

$$\langle x^2(t)\rangle = \frac{1}{2T}S_n. \tag{2.56}$$

An unit of the spectral density is the square of the unit of measured value over Hz. In order to make correspondence to the root mean square (RMS) of the value, the square root of the spectral density $h_n(f) = \sqrt{S_n(f)}$ is also used. In the case of the strain of the GW, the unit of $h_n(f)$ is $1/\sqrt{\mathrm{Hz}}$.

Typical strain of the GW is around $h \sim 10^{-21}$, which corresponds to $h_n \sim 10^{-22}\,[1/\sqrt{\mathrm{Hz}}]$ at 100 Hz because the integrating frequency range extends roughly from 50 Hz to 150 Hz, $\Delta f \sim 100$ Hz. On the other hand, the signal to noise ratio (SNR) of the the GW signal is decided by the ratio of power of the root mean square. Thus, required strain sensitivity of the detector is around $h_n \sim 10^{-23}$ at 100 Hz to detect the GW signal at the SNR of around 10.

2.2.2 Quantum noise

Quantum noise results from vacuum fluctuation of laser light. For simplicity, here we discuss fluctuation of photon number of laser light semi-classically and regard it as quantum noise. Strict quantum description derives the same result. Frequency region above $\omega_{\rm m}$ is considered.

The laser power P measured during the measurement time T is

$$P = \frac{1}{T} N_p \hbar \omega_{\rm L}, \tag{2.57}$$

where N_p is the photon number incident on the PD during the time of T. A number of photon follows the Poisson distribution. The RMS can be written as $\Delta N_p = \sqrt{N_p}$. Therefore, the power fluctuation is

$$\Delta P = \frac{\hbar \omega_{\rm L}}{T} \sqrt{N_p} = \sqrt{\frac{\hbar \omega_{\rm L} P}{T}}. \tag{2.58}$$

In addition, the quantum efficiency of PD is assumed to be 1 in this section.

Shot noise

Shot noise is one of readout noises caused by phase fluctuation of laser light. The phase fluctuation is given by $\Delta\phi = \Delta P/P$. By using Eq. (2.56) and (2.58), the spectral density of the phase fluctuation is given by

$$h_\phi = \sqrt{2T\Delta\phi} = \sqrt{\frac{2\hbar\omega_{\rm L}}{P}}. \tag{2.59}$$

Based on Eq. (2.47), this fluctuation can be expressed as the strain sensitivity of shot noise,

$$h_{\rm shot}(f) = \frac{1}{4\mathcal{F}L} \sqrt{\frac{\pi c \hbar \lambda_{\rm L}}{P_{\rm bs}}} \sqrt{1 + (f/f_{\rm p})^2}, \tag{2.60}$$

where $P_{\rm bs}$ is laser power just before the beam splitter. In the case of KAGRA parameters, the amplitude of shot noise is

$$h_{\rm shot}(f) \sim 6 \times 10^{-25}\,{\rm Hz}^{-1/2} \left(\frac{1550}{\mathcal{F}}\right) \left(\frac{3\,{\rm km}}{L}\right) \sqrt{\frac{670\,{\rm W}}{P_{\rm bs}}} \sqrt{1+\left(\frac{f}{16\,{\rm Hz}}\right)^2}, \tag{2.61}$$

and $h_{\rm shot}(f = 100\,{\rm Hz}) = 4 \times 10^{-24}\,{\rm Hz}^{-1/2}$. Input power and power recycling gain are 67 W and 10 respectively in KAGRA design sensitivity. A power recycling cavity consists of the Michelson interferometer as a compound mirror and a recycling mirror. The power recycling gain is the enhanced ratio after the power recycling mirror.

Radiation pressure noise

Radiation pressure noise results from force fluctuation acting on mirrors of the detector. The force fluctuation comes from the power fluctuation of the laser light.

First, we calculate enhancement factor $N_{\rm cav}$ of the intra-cavity power $P_{\rm circ}$ compared with the input power to the cavity $P_{\rm in}$. In terms of the electric field, the field in the cavity $E_{\rm cav}$ can be written with the input field $E_{\rm in}$ as

$$E_{\rm cav} = E_{\rm in} t_{\rm I} \sum_{n=0}^{\infty} r_{\rm I}^n \tag{2.62}$$

when the cavity is on resonance. The absolute square of the coefficient is the enhancement factor in terms of power. It is calculated as

$$N_{\rm cav} \simeq \frac{2\mathcal{F}}{\pi}. \tag{2.63}$$

Next, we consider the force noise due to the radiation pressure fluctuation. The force RMS is given by $\Delta F = 2\Delta P_{\rm circ}/c$, and the intra-cavity power fluctuation is $\Delta P_{\rm circ} = (\mathcal{F}/\pi)\Delta P_{\rm bs}$ by Eq. (2.63). With Eq. (2.56) and (2.58), the force spectral density is written as

$$h_F = \frac{2\mathcal{F}}{\pi c}\sqrt{2\hbar\omega_{\rm L} P_{\rm bs}}. \tag{2.64}$$

In free mass regime, this force spectrum can be rewritten as the displacement spectrum,

$$h_x(f) = \frac{1}{m(2\pi f)^2}\frac{2\mathcal{F}}{\pi c}\sqrt{2\hbar\omega_{\rm L}P_{\rm bs}}\frac{1}{\sqrt{1+(f/f_{\rm p})^2}}, \tag{2.65}$$

noting that the effect of radiation pressure is cancelled above the cavity pole. By using Eq. (2.37), the strain sensitivity of radiation pressure noise can be described as

$$h_{\rm radp}(f) = \frac{16\mathcal{F}}{m(2\pi f)^2 L}\sqrt{\frac{\hbar P_{\rm bs}}{\pi c\lambda_{\rm L}}}\frac{1}{\sqrt{1+(f/f_{\rm p})^2}}, \tag{2.66}$$

where the effect that the detector consists of 4 mirrors is concerned.

In KAGRA parameters, we get

$$h_{\rm radp}(f) \sim 7\times10^{-24}\,{\rm Hz}^{-1/2}\left(\frac{23\,{\rm kg}}{m}\right)\left(\frac{\mathcal{F}}{1550}\right)\left(\frac{3\,{\rm km}}{L}\right)\left(\frac{100\,{\rm Hz}}{f}\right)^2 \times\sqrt{\frac{P_{\rm bs}}{670\,{\rm W}}}\left(1+\left(\frac{f}{16\,{\rm Hz}}\right)^2\right)^{-1/2}, \tag{2.67}$$

and $h_{\rm radp}(f = 100\,{\rm Hz}) = 1\times10^{-24}\,{\rm Hz}^{-1/2}$. KAGRA consists of 4 sapphire mirrors whose mass is 23 kg.

Total quantum noise

Total quantum noise $h_{\rm qu} = \sqrt{h_{\rm shot}^2 + h_{\rm radp}^2}$ is given by

$$h_{\rm qu} = \frac{1}{\sqrt{2}}h_{\rm SQL}\sqrt{\frac{1}{\mathcal{K}}+\mathcal{K}}, \tag{2.68}$$

where

$$h_{\rm SQL} = \sqrt{\frac{8\hbar}{m\omega^2L^2}}, \tag{2.69}$$

$$\mathcal{K} = \frac{8P_{\rm bs}\omega_L}{m\omega^2L^2}\frac{1}{\omega^2+\omega_{\rm p}^2}, \tag{2.70}$$

and $\omega_{\rm p} = 2\pi f_{\rm p}$. Therefore, the total strain sensitivity cannot beat so called the standard quantum limit (SQL), $h_{\rm qu} \geq h_{\rm SQL}$ even if the laser power is

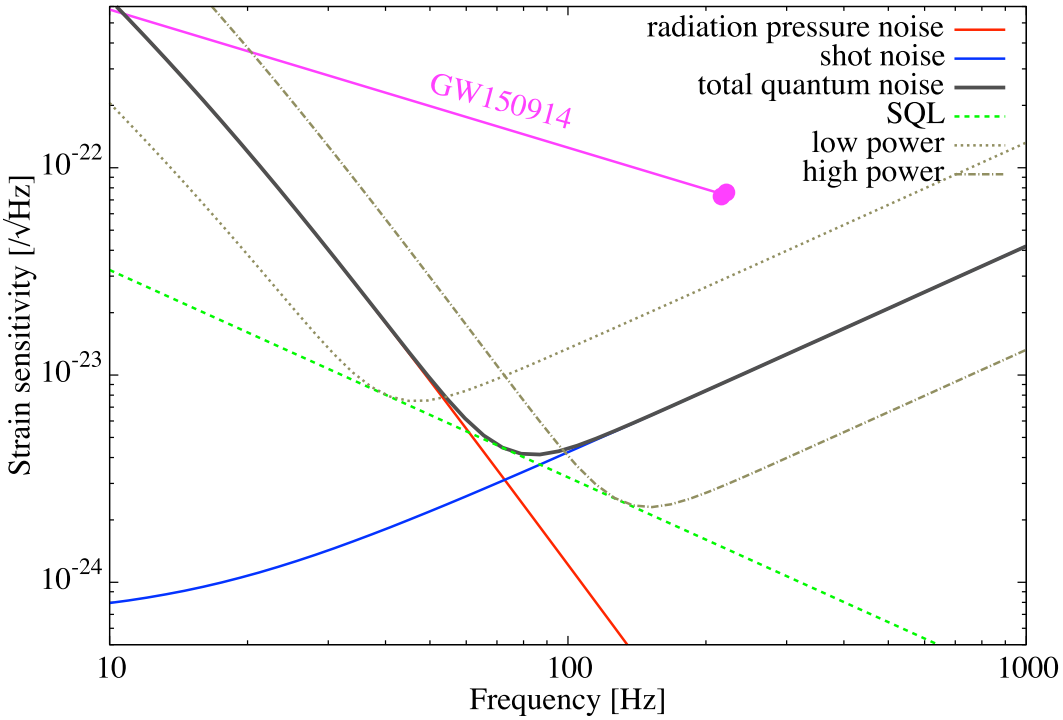

Figure 2.6: Total quantum noises of KAGRA with the Fabry–Perót Michelson interferometer. We show the radiation pressure noise, the shot noise, and the total quantum noises at the designed power of $P_{\rm bs} = 670\,{\rm W}$. Total quantum noises when the power is 1/10 times and 10 times are also shown as the black dotted lines. They cannot beat the green dotted line, SQL. The magenta line and dots show the inspiral and merger of the first event GW150914.

changed. Fig. 2.6 shows three strain sensitivities of quantum noises in KAGRA at each laser power with the design power centered. Similarly here, KAGRA is assumed to be the Fabry–Perót Michelson interferometer. Actually there is a signal recycling mirror with adopting the configuration of resonant sideband extraction. Therefore, the radiation pressure noise is smaller and the effective cavity pole is higher.

This sensitivity is high enough to detect the inspiral and merger of the first GW event shown in the figure. The frequency dependence of the inspiral is $f^{-2/3}$. In this description in the log-log plot, the signal to noise ratio is calculated as the area surrounded by the inspiral and the strain sensitivity of the detector. That of the first event is over 10.

With just increasing or decreasing the laser power, we cannot realize sensitivity beyond the SQL. However, some methods to beat the SQL have been proposed and a part of them has been already realized. We will see the methods and experiments in the next section.

Here we describe quantum noise of the GW detector such as KAGRA. In next subsection, another fundamental noise, thermal noise is discussed.

2.2.3 Thermal noise

After a mechanical mode of an oscillator is excited, the oscillation amplitude gets smaller in finite time. It is because the oscillator is coupled with thermal bath and energy dissipation to the thermal bath occurs. According to the fluctuation dissipation theorem (FDT) [45–47], the oscillator receives fluctuation from the thermal bath corresponding to this energy dissipation in the equilibrium. The amplitude of the fluctuation is proportional to temperature of the thermal bath and to the energy loss in one period of the ringdown oscillation.

In this subsection, we pick up two thermal noises such as suspension and mirror thermal noise. Suspension system can be regarded as a link between the oscillator and the thermal bath. Substrate of the mirror and the coating material have internal losses and the energy dissipates as heat. In order to decrease these thermal noises, test masses in KAGRA are cooled to cryogenic temperature of around 20 K, and the material of sapphire is used as the mirror substrate and the suspension fibers because it has low internal loss at cryogenic temperature. The detail about the thermal noise in KAGRA is described in Appendix, where the suspension thermal noise with the temperature gradient is focused on in particular.

Suspension thermal noise

In frequency domain, an equation of motion on one mechanical mode can be written as

$$\left(-m\omega^2 + i\Gamma_{\mathrm{m}}\omega + k_{\mathrm{m}}\right) x(\omega) = F(\omega), \tag{2.71}$$

where $k_{\mathrm{m}} = m\omega_{\mathrm{m}}^2$ is the mechanical spring constant and $\Gamma_{\mathrm{m}} \equiv m\gamma_{\mathrm{m}}(\omega)$ shows the mechanical decay of the mode. The decay of the mode after excitation x_0

is given by

$$x(t) = x_0 e^{-\gamma_{\rm m} t/2}. \tag{2.72}$$

This decay rate can be written by Q-value $Q_{\rm m} = \omega_{\rm m}/\gamma_{\rm m}(\omega_{\rm m})$ and by loss angle $\phi_{\rm m}(\omega) = \gamma_{\rm m}(\omega)\omega/\omega_{\rm m}^2$. When one period of the oscillation $t = 2\pi/\omega_{\rm m}$ passes, the amplitude decreases by $\pi\phi_{\rm m}(\omega_{\rm m})$.

In FDT, power spectrum of thermal noise in force is given by [48]

$$S_{f,{\rm th}}(\omega) = 4k_{\rm B}T_{\rm th}{\rm Re}\left[\frac{F(\omega)}{i\omega x(\omega)}\right], \tag{2.73}$$

where $T_{\rm th}$ is the temperature of the thermal bath. Therefore, the spectral density of suspension thermal noise can be described as $h_{f,{\rm sust}}(\omega) = \sqrt{4k_{\rm B}T_{\rm th}\gamma_{\rm pend}m}$, where $\gamma_{\rm pend}$ is the decay rate of the pendulum mode.

Here we introduce two dissipation models. One is viscous model, where the mode has friction and the oscillation is decayed by force proportional to the velocity. The other is structure model, where the energy loss is due to internal loss of the material. Frequency dependence of the decay rate and loss angle can be written as differently,

$$\gamma_{\rm m} = \frac{\omega_{\rm m}}{Q_{\rm m}},\ \phi_{\rm m}(\omega) = \frac{\omega}{Q_{\rm m}\omega_{\rm m}}\ : viscous, \tag{2.74}$$

$$\gamma_{\rm m}(\omega) = \frac{\omega_{\rm m}^2}{Q_{\rm m}\omega},\ \phi_{\rm m} = \frac{1}{Q_{\rm m}}\ : structure. \tag{2.75}$$

Thermal noise due to residual gas or magnet damping follows viscous model and the decay rate is constant. On the other hand, leading thermal noise of GW detectors introduced in this section is structural and the loss angle is constant. Then, above frequency of pendulum mode the displacement spectral density of suspension thermal noise is

$$h_{x,{\rm sust}}(\omega) = \sqrt{\frac{4k_{\rm B}T_{\rm th}\omega_{\rm pend}^2\phi_{\rm pend}}{m\omega^5}}, \tag{2.76}$$

KAGRA suspension consists of multiple pendula, but here we assume one pendulum whose resonant frequency is $\omega_{\rm pend}/2\pi = 1\,{\rm Hz}$. Sapphire fibers of KAGRA have the loss angle of $\phi_{\rm pend} \sim 1\times10^{-8}$ and the averaged temperature

of $T_{\rm th} = 19\,{\rm K}$. The strain sensitivity of suspension thermal noise is given by

$$h_{\rm sust}(\omega) = \frac{2}{L}\sqrt{\frac{4k_{\rm B}T_{\rm th}\omega_{\rm pend}^2\phi_{\rm pend}}{m\omega^5}}, \tag{2.77}$$

because 4 mirrors move independently. The concrete value is

$$h_{\rm sust}(f) \sim 3\times10^{-25}\left(\frac{3\,{\rm km}}{L}\right)\left(\frac{f_{\rm pend}}{1\,{\rm Hz}}\right)\sqrt{\frac{T_{\rm th}}{19\,{\rm K}}}\sqrt{\frac{\phi_{\rm pend}}{10^{-8}}}\sqrt{\frac{23\,{\rm kg}}{m}}\left(\frac{100\,{\rm Hz}}{f}\right)^{5/2}. \tag{2.78}$$

Mirror thermal noise

Elastic modes of mirror substrate have their internal loss resulting in substrate thermal noise. Moreover, dielectric coatings for mirrors also have the loss and contribute to coating thermal noise. Resonant frequencies of elastic modes are much higher than frequency region for observation, so the frequency dependence of the strain sensitivity is $f^{-1/2}$. The displacement can be calculated by summarizing infinite elastic modes of the mirror, but the other simple method for calculation of mirror thermal noise was proposed by Levin [49].

As a general formalism for FDT, displacement power spectrum of thermal noise can be described as

$$S_x(\omega) = \frac{8k_{\rm B}T_{\rm th}}{\omega^2}\frac{W_{\rm diss}}{F_0^2}, \tag{2.79}$$

where $W_{\rm diss}$ is an averaged dissipation energy when the oscillating force, whose amplitude is F_0, is applied to the surface of the mirror. This dissipation energy is given by

$$W_{\rm diss} = U_{\rm max}\omega\phi_{\rm m}, \tag{2.80}$$

where $U_{\rm max}$ is the maximum energy of elastic deformation while the force is applied.

In the case of the substrate, this energy is [50]

$$U_{\rm max} = \frac{1-\sigma_0^2}{2\sqrt{\pi}E_0 w_0}F_0^2, \tag{2.81}$$

where σ_0 is the Poisson ratio, E_0 is the Young's modulus of the substrate, and w_0 is the beam radius on the mirror. Then, the strain sensitivity of the substrate Brownian thermal noise can be written as

$$h_{\rm subt}(f) = \frac{2}{L}\sqrt{\frac{2k_{\rm B}T_{\rm th}}{\pi^{3/2}f}\frac{1-\sigma_0^2}{E_0 w_0}\phi_{\rm sub}}, \tag{2.82}$$

where $\phi_{\rm sub}$ is the loss angle of the substrate. A bulk of sapphire has very low loss at cryogenic temperature. Here $\phi_{\rm sub} = 1 \times 10^{-8}$ is assumed.

Next, we consider coating thermal noise. A dielectric multilayer is required to realize the high reflectivity of the mirror for GW detectors. Typically two materials which have different reflective index are laminated alternately. These layers have the internal loss and result in the thermal noise. By using the Levin's approach similarly, the strain sensitivity of coating thermal noise is [51]

$$\begin{aligned} h_{{\rm coat},i}(f) = &\frac{\sqrt{2}}{L}\sqrt{\frac{2k_{\rm B}T_{\rm th}}{\pi^2 f}\frac{d_{{\rm I},i}+d_{{\rm E},i}}{E_0^2 E_i w_0^2}\phi_{{\rm coa},i}} \\ &\times\sqrt{\frac{E_i^2(1+\sigma_0)^2(1-2\sigma_0)^2 + E_0^2(1+\sigma_i)^2(1-2\sigma_i)}{(1-\sigma_i^2)}}, \end{aligned} \tag{2.83}$$

where $i = 1, 2$ shows two materials for the coating, for example SiO_2 and Ta_2O_5, respectively, $d_{{\rm I},i}$ and $d_{{\rm E},i}$ are the thickness of each material on the input and end mirrors, E_i and σ_i is the Young's modulus and the Poisson ratio of each material. The total sensitivity is $h_{\rm coat}(f) = \sqrt{h_{{\rm coat},1}^2 + h_{{\rm coat},2}^2}$.

Another significant thermal noise is due to a thermo-elastic effect. When the substrate is deformed by an external force, temperature gradient arises and the distribution is relaxed at a time scale given by the thermal conductivity of the substrate. This energy loss is thermo-elastic damping. The strain sensitivity of the thermo-elastic noise is given by [52, 53]

$$h_{\rm thel}(f) = \frac{2}{L}\sqrt{\frac{4k_{\rm B}T_{\rm th}^2\alpha_0^2(1+\sigma_0)^2 w_0}{\sqrt{\pi}\kappa_0}J(\Omega_{\rm c})}, \tag{2.84}$$

$$J(\Omega_{\rm c}) = {\rm Re}\left[\frac{e^{i\Omega_{\rm c}/2}(1-i\Omega_{\rm c})}{\Omega_{\rm c}^2}\left({\rm Erf}\left[\frac{\sqrt{\Omega_{\rm c}}(1+i)}{2}\right]-1\right)\right] + \frac{1}{\Omega_{\rm c}^2} - \sqrt{\frac{1}{\pi\Omega_{\rm c}^3}}, \tag{2.85}$$

where α_0 is the thermal linear expansion, κ_0 is the thermal conductivity, and $\Omega_c = f/f_{cut}$ is the frequency normalized by cut off frequency of thermal relaxation, $f_{cut} = \kappa_0/(\pi C_0 w_0^2)$, where C_0 is the specific heat per unit volume. The frequency dependence of the thermo-elastic noise is $f^{-1/4}$ at $f \ll f_{cut}$ and f^{-1} at $f \gg f_{cut}$.

In KAGRA parameters, the relation of the amplitude of each mirror thermal noise around observation frequency region is $h_{coat} > h_{thel} > h_{subt}$. Here we show the concrete value of the coating thermal noise as an example. The mirror temperature is set to $T_{th} = 22\,\mathrm{K}$ in the design sensitivity. The coatings are multilayers of SiO_2 ($i = 1$) and Ta_2O_5 ($i = 2$). The Young's modulus and the Poisson ratio of each material are $E_0 = 400\,\mathrm{GPa}$, $E_1 = 73.2\,\mathrm{GPa}$, $E_2 = 140\,\mathrm{GPa}$, $\sigma_0 = 0.29$, $\sigma_1 = 0.16$, and $\sigma_2 = 0.23$. The input mirror has a little transmissivity, on the other hand the reflectivity of the end mirror is almost one. Therefore, the coating thickness of mirrors are different, $d_{I,1} = 2.2\,\mu\mathrm{m}$, $d_{I,2} = 1.4\,\mu\mathrm{m}$, $d_{E,1} = 3.9\,\mu\mathrm{m}$, $d_{E,2} = 2.6\,\mu\mathrm{m}$. The loss angle of each coating are $\phi_{coa,1} = 3 \times 10^{-4}$ and $\phi_{coa,2} = 5 \times 10^{-4}$. The beam radius on the mirrors is $w_0 = 3.5$ cm. Then the strain sensitivity of coating thermal noise in KAGRA is

$$h_{coat}(f) \sim 2 \times 10^{-24} \left(\frac{3\,\mathrm{km}}{L}\right) \left(\frac{3.5\,\mathrm{cm}}{w_0}\right) \sqrt{\frac{T_{th}}{22\,\mathrm{K}}} \sqrt{\frac{100\,\mathrm{Hz}}{f}}. \tag{2.86}$$

This is the largest noise except for quantum noise around 100 Hz in KAGRA, but better than that of other GW detectors because of the cryogenic operation.

2.2.4 Other technical noises

In previous subsection, we described two fundamental noises of GW detectors such as quantum noise and thermal noise. GW detectors have so many other noises. In this subsection they are shown, especially with picking up seismic noise and laser frequency noise.

Seismic noise

The ground always moves due to activities of the earth. The mirror motion is excited not only by the earthquake but also by continuous shaking. The

displacement of the seismic noises typically

$$\sqrt{S_{\rm seis}(f)} \sim 10^{-7} \left(\frac{1\,{\rm Hz}}{f}\right)^2 {\rm m}/\sqrt{\rm Hz}. \tag{2.87}$$

For example, at 100 Hz the ground moves by $\sim 10^{-11}\,{\rm m}/\sqrt{\rm Hz}$. When we realize the strain sensitivity of $\sim 10^{-24}$, reduction of ten orders of magnitude is needed.

In order to isolate the mirrors from the seismic noise, we make use of a character of multiple suspension system. An equation of motion of one pendulum whose spring constant is $k_{\rm m} = m\omega_{\rm m}^2$ can be written as

$$m\ddot{x} = -k_{\rm m}(x - X), \tag{2.88}$$

where x and X are coordinates of the pendulum and the ground. In frequency domain the transfer function from the ground motion to the pendulum displacement is given by

$$\frac{x}{X} = \frac{\omega_{\rm m}^2}{\omega_{\rm m}^2 - \omega^2}. \tag{2.89}$$

This means that the seismic noise is reduced by f^{-2} above the resonant frequency. In the same way, multiple pendula with n stages have attenuating factor of f^{-2n}. In KAGRA, 8-stage pendula are used for the vibration isolation system and the seismic noise is suppressed enough not to limit the sensitivity.

Laser frequency noise

Laser light has fluctuation of the frequency and it can be a significant noise. When the optical cavity is on resonance, the round trip length is n times of the wave length of the laser, so $2L = nc/f_{\rm L}$ is satisfied. If the cavity is shorter by ΔL, the corresponding laser frequency gets higher by Δf, and hence $2(L - \Delta L) = nc/(f_{\rm L} + \Delta f)$ holds. Subtracting these equations and assuming $L \gg \Delta L$ and $f_{\rm L} \gg \Delta f$, we can get the relation of the displacement and frequency change of the cavity as

$$\frac{\Delta L}{L} = \frac{\Delta f}{f_{\rm L}}. \tag{2.90}$$

In principle this noise contributes to the common signal, not to the differential signal, so does not limit the sensitivity of the detector with common mode rejection. However, the common mode rejection ratio is not infinite, and the frequency noise is the issue. To realize the sensitivity of $h \sim 10^{-24}$, we have to suppress the frequency noise to $\Delta f \sim 10\,\mathrm{nHz}/\sqrt{\mathrm{Hz}}$ with assuming the common mode rejection ratio is 100. However, typical fluctuation of laser frequency is around $\Delta f \sim 100\,\mathrm{Hz}/\sqrt{\mathrm{Hz}}$ at 100 Hz. Therefore, we need to reduce it by 10 orders of magnitude. Multistage frequency stabilization is applied at a reference cavity with input optical table, an input mode cleaner of laser light to the interferometer, and a summation signal of both arms.

Other noises

There are so many other noises in real detectors. Here we introduce noises which were relatively large in O1 of advanced LIGO in Livingston.

The strain sensitivity of advanced LIGO was limited by shot noise above 100 Hz. Around 10 Hz, coupling noise resulting from control of the angular degrees of freedom was dominant. The angular control is necessary for suppressing the residual angular motion due to seismic noise and eliminating Sidles–Sigg instability of the arm cavities [54]. The control couples with the GW signal port.

Measured noise between 15 Hz to 100 Hz was not explained well. A part of noise was actuator noise caused by excitation due to the dark noise of the actuator driver. Coupling noise from control of signal recycling cavity length was relatively large. Residual gas noise was also the issue. It is divided by two types. One is a kind of thermal noise caused by collision of the mirrors and gas molecules randomly. This effect is enhanced by the effect that the molecules kick more times than usual because of a narrow gap between the test mass and the recoil mass. It is called squeezed film damping. The other is a kind of phase noise induced by intersection of molecules across the beam in the cavity.

In this section various noises of GW detectors are shown. Next, we focus on quantum noise and discuss how it can be reduced.

2.3 Quantum noise reduction

Quantum noise is the most fundamental noise in the GW detector, and limits the sensitivity around almost all frequency region. Therefore, the reduction of quantum noise contributes the most directly to improving the sensitivity and to observation of more GW events. It seems difficult to reduce quantum noise, especially to beat the SQL because it derives from the Heisenberg's uncertainty principle. However, some methods have been proposed to suppress quantum noise below the SQL.

We introduce two methods for reduction of quantum noise. The first is injection of squeezed light, whose vacuum field is squeezed to one direction of two quadratures of the laser light. This method is changing the vacuum field causing the quantum noise. Second, a homodyne detection is used. In this scheme we change the readout quadrature of the output laser light.

2.3.1 Input squeezing

Quantum noise can be described as the vacuum field fluctuation of the laser light. First of all, the vacuum state of the laser light is introduced [55].

Vacuum state

A quantized electromagnetic field $E(t)$ is given by

$$E(t) = i\sum_k \sqrt{\frac{\hbar\omega_k}{2\epsilon_0}}\left[\hat{a}_k u(\mathbf{r})e^{-i\omega_k t} - \hat{a}_k^\dagger u(\mathbf{r})^* e^{i\omega_k t}\right], \tag{2.91}$$

where ϵ_0 is the dielectric constant of vacuum, ω_k is the angular frequency of each mode, and $u(\mathbf{r})$ is the spatial mode function. $\hat{a}_k$ is the annihilation operator of the mode and satisfies

$$[\hat{a}_k, \hat{a}_{k'}] = [\hat{a}_k^\dagger, \hat{a}_{k'}^\dagger] = 0,\ [\hat{a}_k, \hat{a}_{k'}^\dagger] = \delta_{kk'}. \tag{2.92}$$

Here we focus on one mode of the laser light frequency. The quadrature

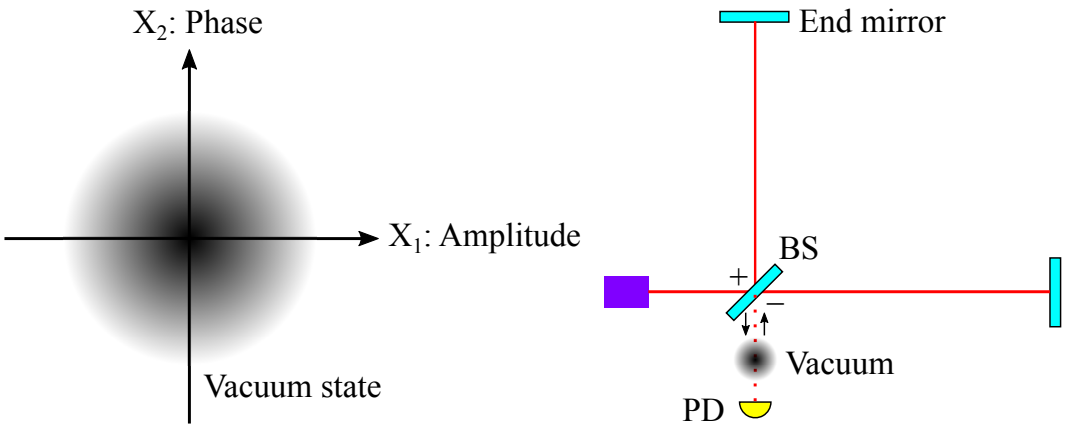

Figure 2.7: Schematic pictures of the vacuum state and the incidence to the Michelson interferometer. We describe the amplitude and phase of the laser light as the horizontal and vertical axis. This vacuum fluctuation enters the Michelson interferometer and causes the quantum noise.

operators are defined as

$$\hat{X}_1 = \hat{a} + \hat{a}^\dagger,\ \hat{X}_2 = -i(\hat{a} - \hat{a}^\dagger), \tag{2.93}$$

where $\hat{X}_1$ and $\hat{X}_2$ are the amplitude and phase quadrature respectively. The commutation relation of these quadratures is

$$[\hat{X}_1, \hat{X}_2] = 2i, \tag{2.94}$$

and the Heisenberg's uncertainty principle is

$$\Delta X_1 \Delta X_2 \geq 1. \tag{2.95}$$

Even without the coherent amplitude of laser light, the vacuum field has this fluctuation. This is shown with a ball picture on the quadrature plane. Quantum noise on the differential signal of the Michelson interferometer can be considered to be caused by injection of the field from the anti-symmetric port of the beam splitter. The amplitude and phase quadrature corresponds to radiation pressure noise and shot noise respectively.

In Fig. 2.7, we show the schematic pictures of the vacuum state of laser light and its incidence to the interferometer. The vacuum has the same fluctuation

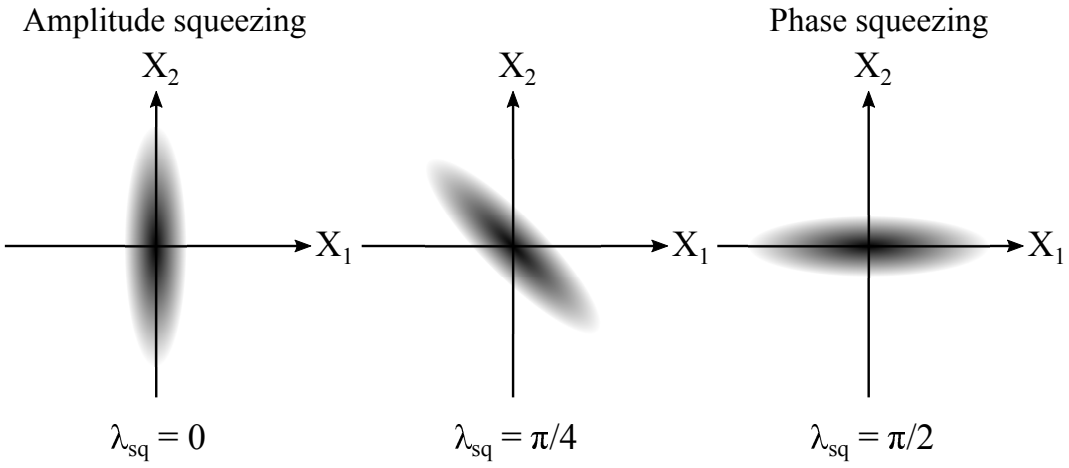

Figure 2.8: Schematic pictures of the squeezed vacuum state at different squeezing angles. We describe the squeezed states of 6 dB at three squeezing angles, $\lambda_{\rm sq} = 0$, $\pi/4$, and $\pi/2$. The states of $\lambda_{\rm sq} = 0$ and $\pi/2$ are called amplitude and phase squeezing respectively.

in the amplitude and phase quadrature. Here we define the amplitude and phase directions as the horizontal and vertical ones. The field from the anti-symmetric port has the differential effect [56].

Squeezed state

A squeezed state of laser light has smaller deviation on one quadrature than that of the vacuum state. For example, in order to keep the uncertainty principle Eq. (2.95), the modified deviation of two quadratures is given by

$$\Delta X_1 = z,\ \Delta X_2 = 1/z, \tag{2.96}$$

where z is positive and real number.

The squeezing factor is described with the unit of dB. For example, when $z = 2$, the deviation of the fluctuation is $V_{\rm dev} = 1/4$. This value corresponds to $-10 \log_{10} V_{\rm dev} \simeq 6\,{\rm dB}$, which is called 6 dB squeezing. Moreover, the parameter of

$$r = -\frac{1}{2} \log_e V_{\rm dev} \tag{2.97}$$

is also used. It is also called the squeezing factor. A squeezed direction is

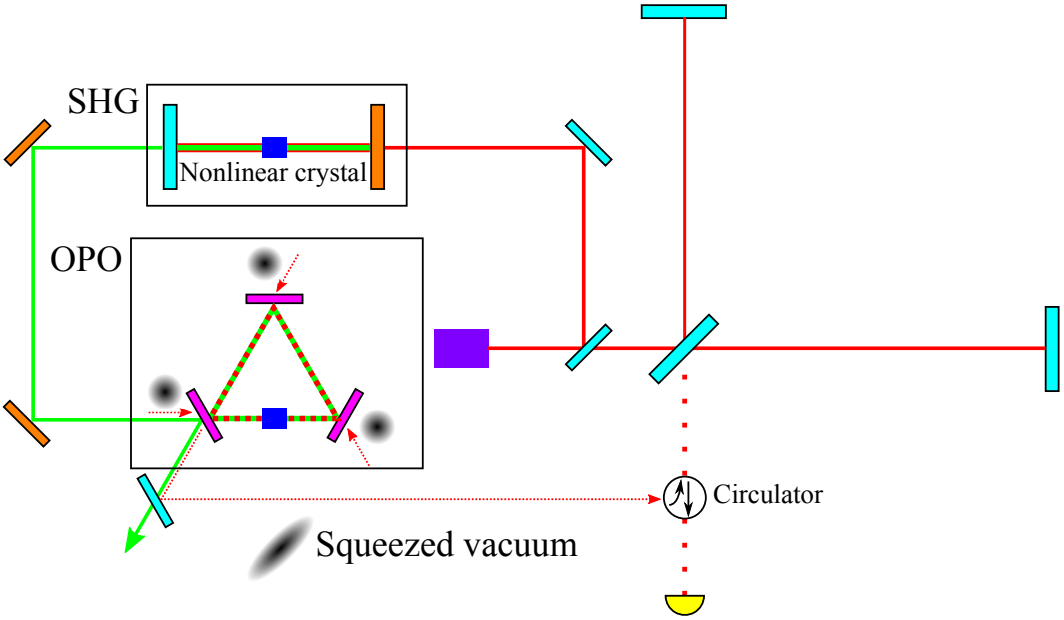

Figure 2.9: A schematic picture of generation of the squeezed light and its injection. The SHG and OPO contain the nonlinear crystals in the cavities. Orange mirrors are dichroic ones which have the high reflectivity of the green light and the high transmissivity of the red light. The circulator has the system of PBSs and changing the polarization of the light, so it can reflect the light from one direction and transmit from the perpendicular direction.

expressed as a squeezing angle $\lambda_{\rm sq}$. $\lambda_{\rm sq} = 0$ and $\pi/2$ means the amplitude and phase squeezing respectively. We show squeezed states of 6 dB at different squeezing angles with the ball pictures in Fig. 2.8.

The squeezed light used in the GW detectors is generated by an optical parametric oscillation (OPO) [58]. OPO consists of a cavity containing a nonlinear optical crystal inside. With second harmonic as a pump light, the output of fundamental light is squeezed due to a $\chi^{(2)}$ nonlinear interaction, down conversion effect of the crystal. The second harmonic (typically green light) can be made by a cavity which is called a second harmonic generation (SHG). The SHG has also the nonlinear crystal, and the up conversion effect occurs with the fundamental light resonating in the cavity.

We can make the squeezed vacuum with the SHG and OPO. The quantum noise of the Michelson interferometer can be reduced by injecting the generated squeezed light to the interferometer from the anti-symmetric port. In Fig. 2.9,

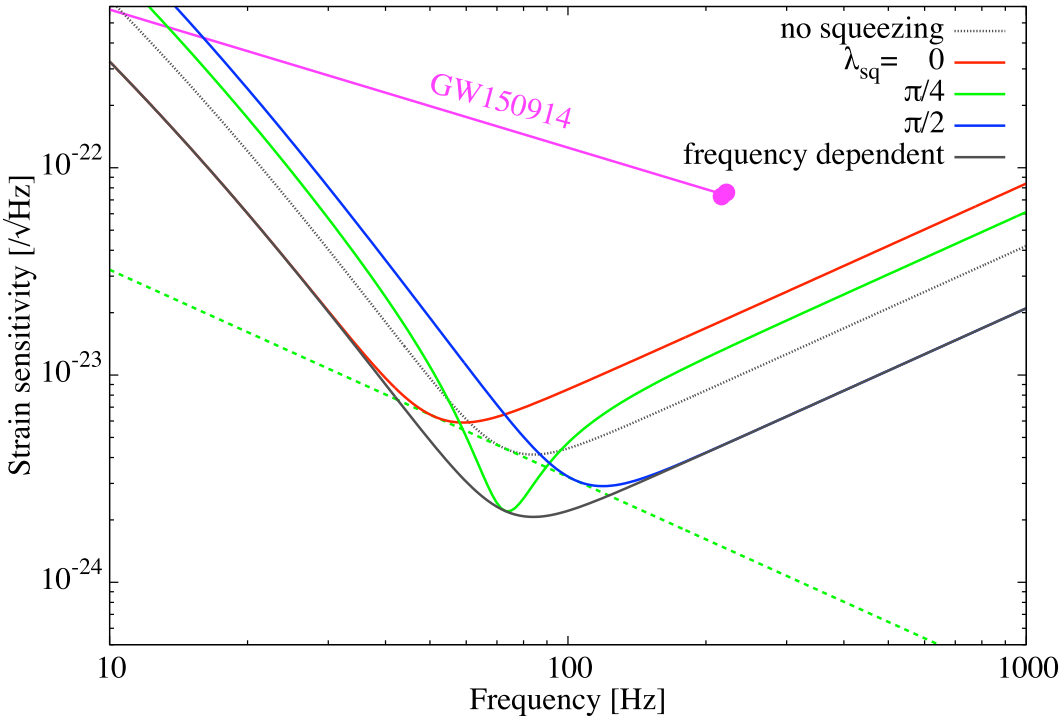

Figure 2.10: Quantum noises at different squeezing angles in frequency independent squeezing and frequency dependent squeezing. The red, green, and blue line show the quantum noises at $\lambda_{\rm sq} = 0$, $\pi/4$, and $\pi/2$. The blue line shows the sensitivity of frequency dependent squeezing. The squeezing level is 6 dB in all cases.

we show a schematic picture of generation of the squeezed light and its injection to the interferometer.

Frequency independent squeezing

We can adjust the squeezing angle by controlling the OPO system. The squeezing factor is determined by the loss in the OPO. Here we discuss how the strain sensitivity of detectors is changed when the squeezed vacuum, which is independent of the frequency, is injected. The strain sensitivity without input squeezing is shown in Eq. (2.68). The power spectrum is changed by squeezed

light to [57]

$$S_{\rm sq} = \frac{h_{\rm SQL}^2}{2}\left(\frac{1}{\mathcal{K}} + \mathcal{K}\right)\left(\cosh 2r - \cos[2(\Phi - \lambda_{\rm sq})]\sinh 2r\right), \tag{2.98}$$

where $\Phi = \mathrm{arccot}\mathcal{K}$.

The dependence of the strain sensitivity at KAGRA parameters on the squeezing angle is plotted in Fig. 2.10. When $\lambda_{\rm sq} = \pi/2$ (the phase squeezing), the spectrum can be written as

$$S_{\rm sq}(\lambda_{\rm sq} = \pi/2) = \frac{h_{\rm SQL}^2}{2}\left(\frac{1}{\mathcal{K}e^{2r}} + \mathcal{K}e^{2r}\right). \tag{2.99}$$

In other words, the squeezing effect is the same as increasing the input power to the interferometer by a factor of $1/V_{\rm dev}$. In the case of $\lambda_{\rm sq} = \pi/4$, the sensitivity is below the SQL. It is because the amplitude and phase fluctuation of the vacuum is no longer independent. On the other hand, the sensitivity is worse at the frequency outside the best region.

Frequency dependent squeezing

When we realize $\lambda_{\rm sq}(\omega) = \Phi(\omega) = \mathrm{arccot}\mathcal{K}(\omega)$, that is, we give the optimal frequency dependence to the squeezing angle at Eq. (2.98), the sensitivity is given by [57]

$$S_{\rm sq} = \frac{h_{\rm SQL}^2}{2}\left(\frac{1}{\mathcal{K}} + \mathcal{K}\right)e^{-2r}. \tag{2.100}$$

Therefore, quantum noise at all frequency range gets smaller than the original by a factor of e^{-2r}.

The frequency dependence of the squeezing angle is as follows. At low frequency, we need to suppress radiation pressure noise, so the amplitude squeezing ($\lambda_{\rm sq} = 0$) is necessary. On the other hand, shot noise can be reduced by the phase squeezing ($\lambda_{\rm sq} = \pi/2$) at high frequency. At the SQL frequency where $\mathcal{K} = 1$, the angle of $\lambda_{\rm sq} = \mathrm{arccot}1 = \pi/4$ is needed. In order to make such squeezed vacuum, we have to prepare the frequency independent phase squeezing and rotate the angle at low frequency by 90°.

Such a rotation can be made by a cavity whose pole is near the SQL

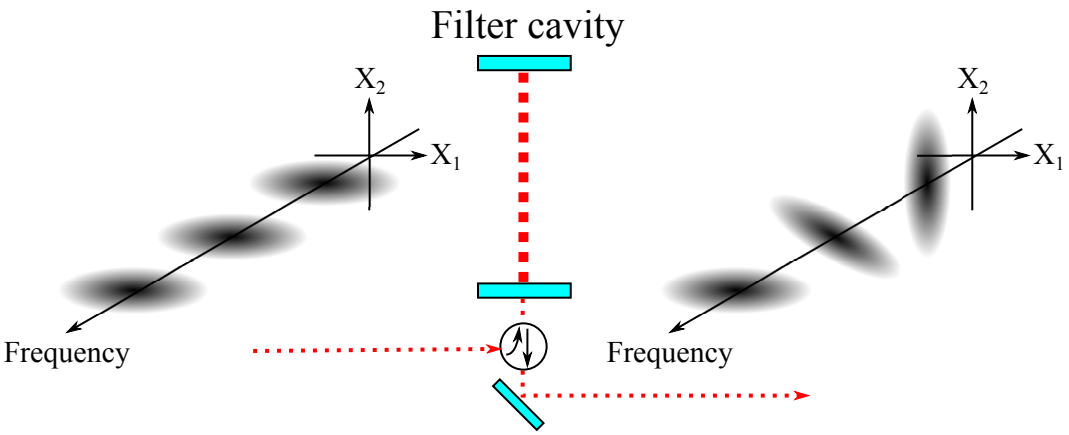

Figure 2.11: A schematic picture of a filter cavity and generation of the frequency dependent squeezed vacuum. The injected frequency independent squeezed state is shown at the left. The reflection from the filter cavity has the frequency dependence of the squeezing angle on the frequency.

frequency of the GW detectors. This cavity is called a filter cavity. We give the detuning of the cavity pole frequency and input the phase squeezing vacuum to the filter cavity. Then, the low frequency component of the vacuum enters the filter cavity and high frequency one is reflected off directly because of the cavity pole. The squeezing angle at low frequency is rotated by $-90°$ and becomes the amplitude squeezing. The strain sensitivity at all frequency range is changed to be better when the frequency dependent squeezed vacuum is injected. In Fig. 2.11, we show the schematic picture of the filter cavity and generation of the frequency dependent squeezed vacuum.

We can understand the effect of the filter cavity with a phasor diagram in Fig. 2.12. Each frequency component can be considered to be a sideband of the career. Actually there is no career in the vacuum state in the squeezed light but we can assume the virtual one. The sidebands move randomly for the career in the vacuum state, however, the upper and lower sidebands act with correlation in the squeezed state.

As shown later with Eq. (3.14), when the career frequency is detuned by the cavity line width to the red direction, the phase of the reflected career is shifted by $-90°$. Sidebands at low frequency compared with the cavity line width have the same shift as the career, so the squeezing angle gets the rotation

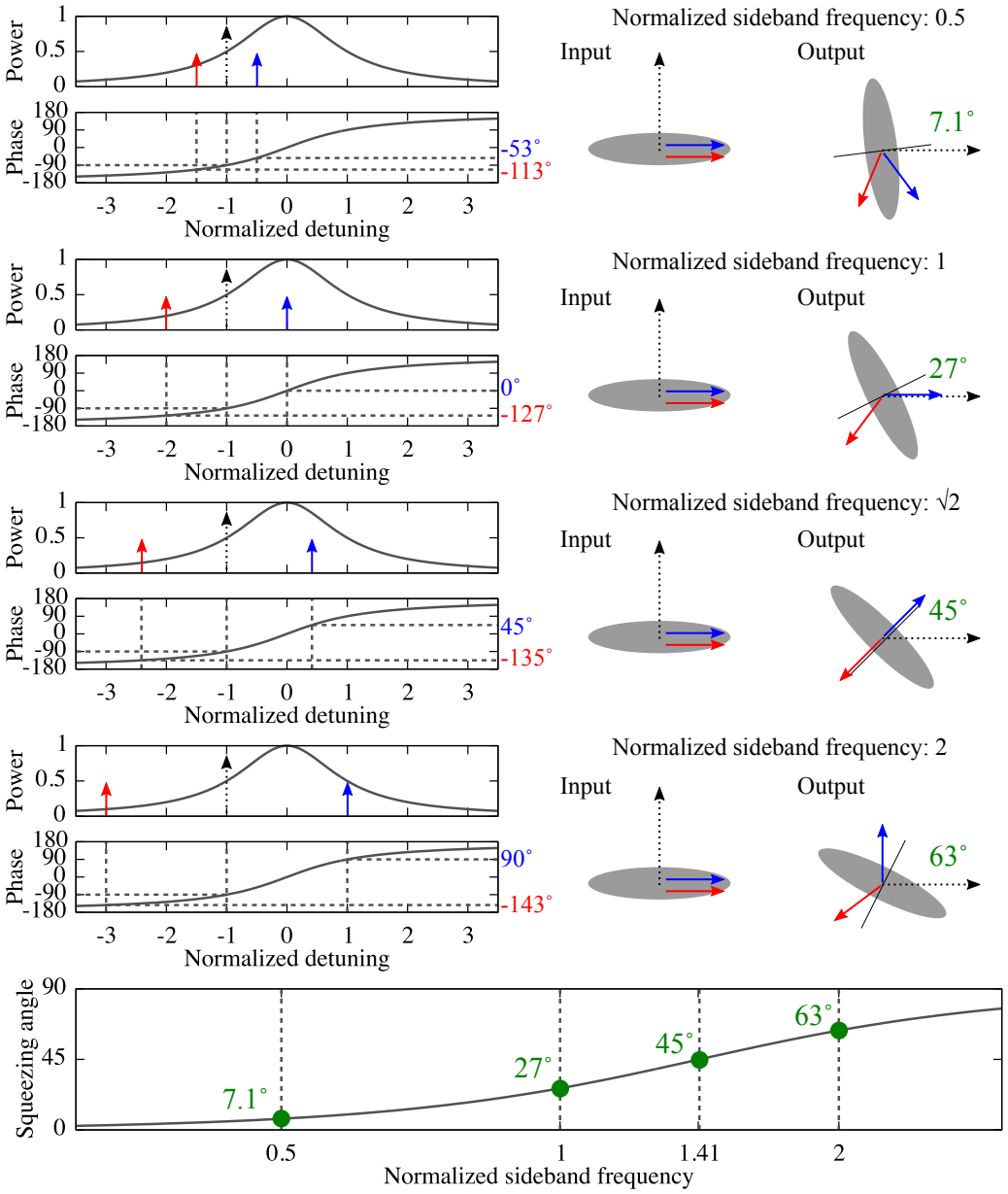

Figure 2.12: Dependence of the rotation angle on the sideband frequency. The dotted black arrow shows the virtual career and the blue and red arrows show the upper and lower sideband. At the bottom we show the dependence of the squeezing angle of the vacuum state out of the filter cavity on the sideband frequency normalized by the detuning.

by around $-90°$. On the other hand, the upper and lower sidebands at high frequency get different phase shift. The shift of the upper and lower sidebands are $-180°$ and $180°$ respectively, so the angle is not changed.

Around the frequency near the cavity line width, the rotation angles are varying. When the sidebands frequency is $\sqrt{2}$ times larger than the line width, their phase shift are $-135°$ and $45°$. In that case, the rotation angle is $-45°$ and the squeezing angle becomes $45°$. As mentioned in the previous section, $\lambda_{\rm sq} = \pi/4$ is required at the SQL frequency. Thus, the pole of the filter cavity has to be the SQL frequency over $\sqrt{2}$. In KAGRA, the SQL frequency is ~ 70 Hz, and hence the cavity pole has to be $\sim 50\,$Hz. It is so low frequency for the optical cavity. The filter cavity is required to be enough long and to have high finesse with low optical loss.

2.3.2 Homodyne detection

In the previous subsection, we discuss reducing the quantum noise with the active action of injection of the squeezed light. Here the change of readout method to evade the quantum noise is described. To be exact, this is not quantum noise reduction because the shot noise can not be reduced, but we can beat the SQL with the method.

The usual PD can measure the amplitude quadrature of the laser light. With the Michelson interferometer, the phase quadrature can be measured. Moreover, with the method of homodyne detection, we can take the arbitrary angle of the quadrature plane for the measurement. The basical set up for homodyne detection is shown in the left of Fig. 2.13. We see the interference between target light and local oscillator (LO) light at various phases by changing the optical path length of the local light. The measurement phase is called a homodyne phase labeled by ξ. The amplitude and phase measurement means $\xi = 0$ and $\pi/2$ respectively.

Ponderomotive squeezing

The amplitude of quantum noise in the interferometer also can be described with a ball picture [57]. Assuming the input field is the vacuum state, the shape of the output field turns to be an ellipse at low frequency, that is, radi-

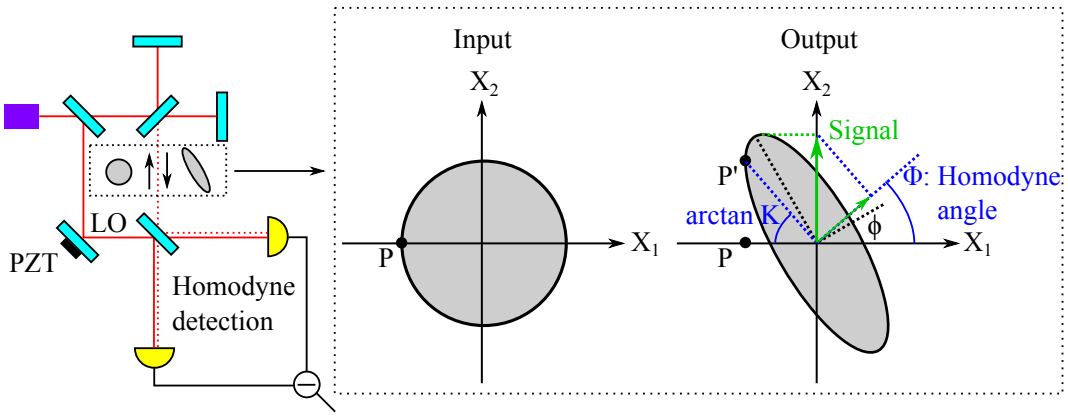

Figure 2.13: A schematic picture of the homodyne detection and the ponderomotive squeezing. The output from the interferometer and the LO light are combined at the BS and the signals of two PDs are subtracted. The homodyne angle can be changed by shifting the phase of the LO light with changing the the length of the optical path by the PZT. In the right the input and output field are shown. P moves to P' due to the ponderomotive squeezing. Here we should note that the optimal angle of the homodyne detection Φ and the squeezing angle of the output field ϕ are different. They are related by $2\tan\Phi = \tan 2\phi$, thus always $\Phi > \phi$ is satisfied. These values get close as they approach to zero.

ation pressure noise dominant regime. It is because the amplitude fluctuation of the vacuum affects the additional phase fluctuation by $\mathcal{K}$. This is a kind of squeezing effect and called ponderomotive squeezing. Combining the homodyne detection and selecting the appropriate homodyne angle, we can evade the radiation pressure noise.

It is understood by a picture in the right of Fig. 2.13. After the vacuum field enters the interferometer, the amplitude fluctuation causes the phase fluctuation with its radiation pressure and the vacuum circle is squeezed ponderomotively. The measurement value is decided by the projection of the signal and noises to the homodyne angle axis. For example, we consider that the amplitude of the signal and noise are the same in usual phase measurement $\xi = \pi/2$. When we do homodyne detection whose angle is Φ, the signal amplitude becomes larger than that of the noise.

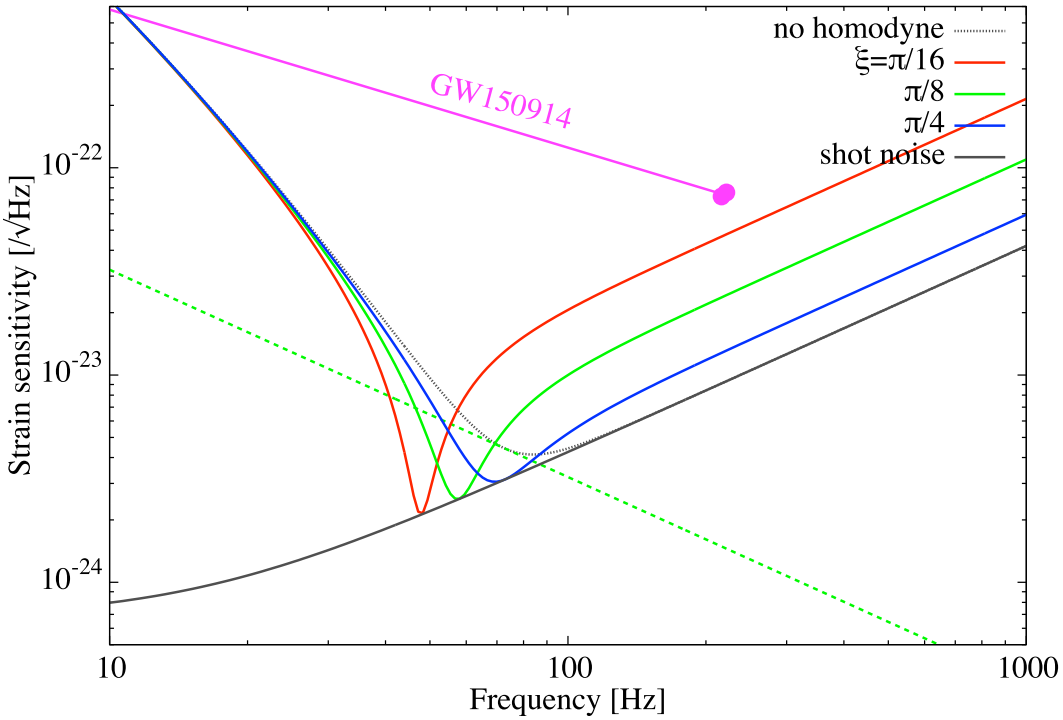

Figure 2.14: Quantum noises at different homodyne angles with the ponderomotive squeezing. The red, green, and blue lines show the quantum noises at the homodyne angles of $\xi = \pi/16$, $\pi/8$, and $\pi/4$ respectively. At one frequency the radiation pressure noise is cancelled and the sensitivity reaches the shot noise.

The strain sensitivity is changed to

$$S_{\rm po} = \frac{h_{\rm SQL}^2}{2\mathcal{K}} \left[1 + (\cot\xi - \mathcal{K})^2\right]. \tag{2.101}$$

When we do the usual phase measurement $\xi = \pi/2$, $S_{\rm po} = S_{\rm qu}$. In Fig. 2.14, the sensitivities in KAGRA parameters at different homodyne angles are shown. At the SQL frequency, $\mathcal{K} = 1$ and the optimal homodyne angle is $\xi = \pi/4$. The sensitivity of the total quantum noise beats the SQL and reaches the shot noise limit at the SQL frequency. In this measurement the mirror oscillates due to the radiation pressure noise actually, but we do not observe it by choosing the appropriate angle. Therefore, this method is also called back action evasion.

Moreover, if we set the frequency dependent homodyne angle as $\xi(\omega) =$

$\mathrm{arccot}\mathcal{K}(\omega) = \Phi(\omega)$, the radiation pressure noise can be evaded at all frequencies, which is called variational readout. Only the shot noise is left in the strain sensitivity. This situation can be realized with an output filter cavity to rotate the ponderomotively squeezed vacuum from the interferometer. We note that this frequency dependent angle is the same as the optimal squeezing angle at the frequency dependent squeezing except for the sign. That is to say, in order to do the variational readout, we have to prepare the same filter cavity and do the homodyne detection at $\xi = \pi/2$.

Detuned signal recycling cavity

In advanced GW detectors, a signal recycling mirror is used for enhancing the GW signal. The mirror is placed after the anti-symmetric port of the beam splitter. The cavity with the signal recycling mirror and the power recycling Michelson interferometer as a compound mirror is kept on anti-resonance. This condition is called resonant sideband extraction (RSE). The system raises the effective cavity pole of the arm cavities and avoids decreasing of the sensitivity at high frequency. The highest sensitivity gets worse with this method considering only the quantum noise, however, it is still effective due to the other noises at low frequency in terms of the binary compact star range.

On the other hand, it has been proposed that the highest sensitivity gets better at the cost of the high sensitivity range with the detuned signal recycling cavity. The homodyne detection is combined with making use of the detuned cavity. The strain sensitivity of quantum noise is given by [59]

$$S_{\mathrm{dsr}} = \frac{h_{\mathrm{SQL}}^2}{2\mathcal{K}} \frac{(C_{11}\cos\xi' + C_{21}\sin\xi')^2 + (C_{12}\cos\xi' + C_{22}\sin\xi')^2}{\tau^2 |D_1\cos\xi' + D_2\sin\xi'|^2}, \tag{2.102}$$

with

$$\begin{aligned} C_{11} = C_{22} &= (1+\rho^2)\left(\cos 2\phi + \frac{\mathcal{K}}{2}\sin 2\phi\right) - 2\rho\cos 2\beta, \\ C_{12} = -\tau^2(\sin 2\phi + \mathcal{K}\sin^2\phi),\ C_{21} &= \tau^2(\sin 2\phi - \mathcal{K}\cos^2\phi), \\ D_1 = -(1+\rho e^{2i\beta})\sin\phi,\ D_2 &= -(-1+\rho e^{2i\beta})\cos\phi, \end{aligned} \tag{2.103}$$

where ρ and τ are the amplitude reflectivity and transmission of the signal

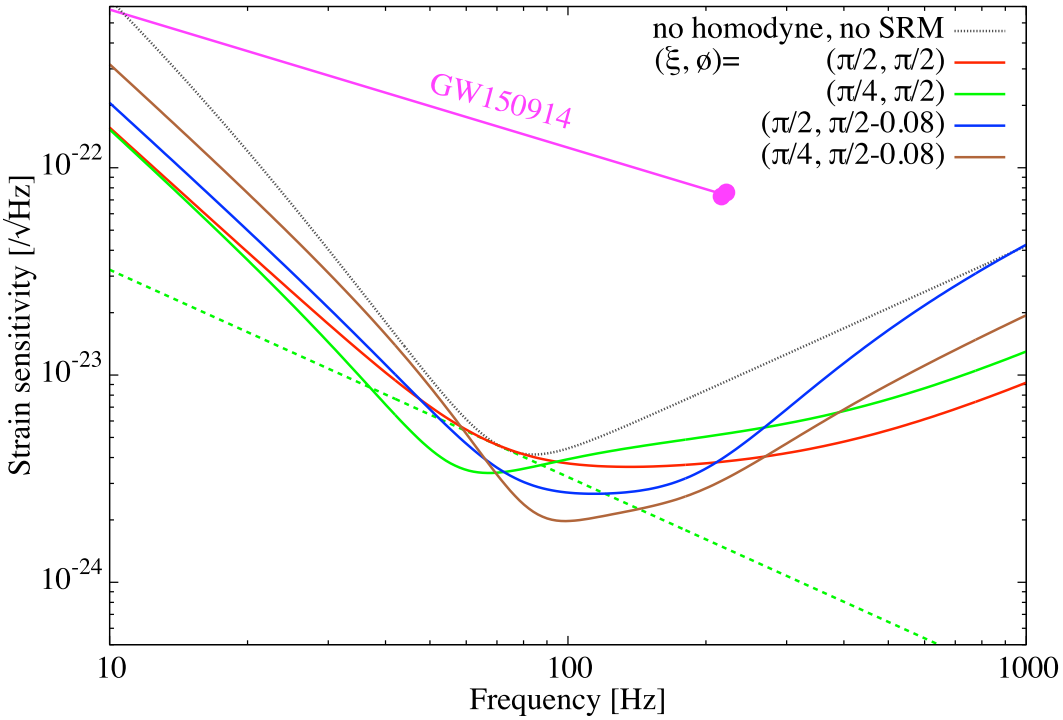

Figure 2.15: Quantum noises at different homodyne angles and detunings. The red and green lines show the sensitivities at the homodyne angles of $\xi = 0$ and $-\pi/4$ on the anti-resonance of the signal recycling cavity. The blue and brown lines show the sensitivities with the detuning of 0.08 rad from the anti-resonance.

recycling mirror ($\rho = 0.92$ in KAGRA), $\beta = \mathrm{atan}(\omega/\omega_\mathrm{p})$ is the phase shift in the arm cavity, and ϕ is the detuning phase. $\phi = \pi/2$ is satisfied in the RSE condition. The homodyne angle ξ' in this equation is defined differently from the usual one ξ. It can be calculated as $\xi = \xi' + \phi$.

The strain sensitivity curves of quantum noise are shown with some detuning phases and homodyne angles in Fig. 2.15. With the signal recycling cavity on the anti-resonance (the RSE condition), the effective cavity pole is decreased. The sensitivity is improved in almost all frequency ranges. It is especially useful in the detector with low cavity pole such as KAGRA. Moreover, we can realize the better maximum sensitivity even below the SQL with the detuning from the anti-resonance. This improving is also useful in KAGRA because the cryogenic system has better sensitivity around 100 Hz due to the

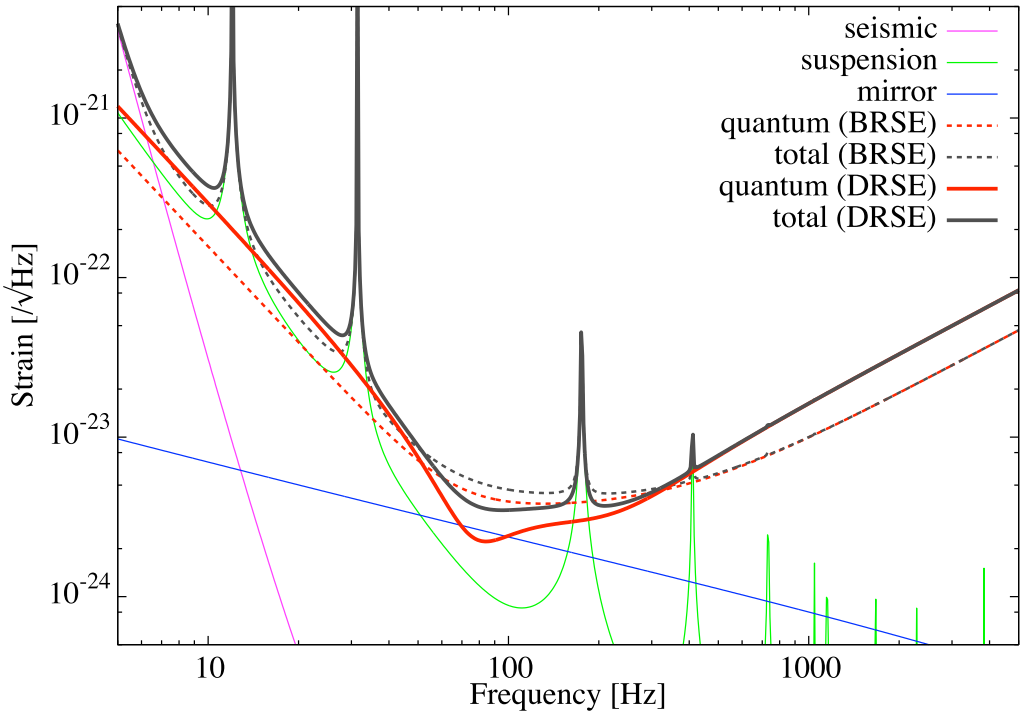

Figure 2.16: BRSE and DRSE sensitivities of KAGRA. The magenta, green, blue, and red lines show the displacement noises due to the seismic, suspension thermal, mirror thermal, and quantum noises. The total noise is given by the black line. The solid (dotted) lines mean the strain sensitivity of DRSE (BRSE).

low mirror thermal noise and we can dig the sensitivity more deeply.

2.3.3 Motivations for reduction of quantum noises

Scientific motivations for reduction of quantum noises are written in this subsection with KAGRA design sensitivities as an example. Fig. 2.16 shows the design sensitivities of KAGRA with two configurations. One is broadband RSE (BRSE) type without the homodyne detection or the detuning of the signal recycling cavity. The other is detuned RSE (DRSE) type with the homodyne phase of 135.1° and the detuning phase of 86.5°. Other detailed parameters are described in Appendix B. With these techniques, the total sensitivity of KAGRA is improved by a factor of about 2 around 100 Hz.

This leads to enhancement of an inspiral range for binary neutron stars from 128 Mpc to 153 Mpc. The inspiral range $\mathcal{R}$ is defined by

$$\mathcal{R} = \frac{0.442}{\rho_{\rm SN}} \sqrt{\frac{5}{6}} \frac{GM_{\rm c}}{\pi^{2/3} c^2} \left[\int_{f_{\rm min}}^{f_{\rm max}} \frac{f^{-7/3}}{S_{\rm n}(f)} df \right]^{1/2}, \tag{2.104}$$

where $\rho_{\rm SN}$ is the signal to noise ratio of GW detection, $M_{\rm c}$ is the chirp mass of the binary, and $S_{\rm n}(f)$ is the square of the strain sensitivity of the detector. The factor of 0.442 is a sky average constant. In the case of calculation related to KAGRA, we set that $\rho_{\rm SN} = 8$, $f_{\rm min} = 10\,{\rm Hz}$, and $f_{\rm max}$ is the ISCO frequency in Eq. 2.18. The improvement factor of the inspiral range for binary neutron stars is 1.2.

The factor seems to be small, but it has significant impacts in the case of GW detectors. The covered volume by the detectors is determined by the third power of the inspiral range. Thus, the volume is expanded by a factor of $1.2^3 \simeq 1.7$. That is to say, detection number becomes 1.7 times larger. Moreover, typical signal to noise ratio of GWs gets bigger by the same factor. They contributes to 1.7 times smaller errors of astrophysical parameters estimated by GWs such as the Hubble constant. Also, Estimation accuracy of the number of binary compact stars is improved by $\sqrt{1.7} \simeq 1.3$.

As described above, the dominant noises are quantum noises in GW detectors and the reduction is meaningful even with a small factor. The second dominant noise around 100 Hz is the coating thermal noise, which is low because of the cryogenic operation of KAGRA. It is more important to reduce quantum noises around 100 Hz in order to get the better sensitivity compared with other GW detectors. Considering the KAGRA configuration, one of the goals is reducing quantum radiation pressure noise by half for demonstration of the reduction in GW detectors. The demonstration should be done by experiments on the table-top scale ahead of the actual detectors, and the first step is observing the quantum radiation pressure noise on a mechanical oscillator.

In this section, we discuss how to reduce quantum noise in GW detectors with some techniques. Next, experimental previous works on quantum noise are introduced, and left works are shown.

2.4 Previous works

Many experiments have been done to test the reduction methods introduced in the previous section. We need to check that the methods can be actually applied to the real GW detectors. The testing process has two steps: first, observing the quantum noise, and second, reducing that.

In this section we describe previous works on quantum noise reduction. Here, in particular, works at detector-band frequency are focused on. Observation and reduction of shot noise has been reported by many experiments including both the table-top scale and the real detectors. However, on radiation pressure noise, there is only one experiment with success of observation at $\sim 10^4$ Hz, and the measurement at detector-band frequency has not been realized yet.

2.4.1 Generation and injection of squeezed light

We review works on generation of squeezed light at table-top scale firstly, and next on injection of squeezed light to the real interferometers like the GW detectors with confirmation of shot noise reduction.

Generation of squeezed light at table-top scale

Caves proposed that the quantum noise in GW detectors can be reduced with squeezed light in 1981, and the first success of making the squeezed light was done by Slusher *et al.* [60] in 1985. After that the squeezing level has been progressed with time, up to 15 dB squeezing by Vahlbruch *et al.* [61] at MHz region, where the field of laser light has almost the vacuum state without any suppression of the classical amplitude and phase noise.

At the audio-band frequency, it is technically difficult to produce the squeezed states because of the classical noises of the laser source. The first locked squeezed state at audio frequency was done by McKenzie *et al.* [62], where the squeezing was realized down to 100 Hz in 2006. In 2012, 10 dB squeezing around 10 Hz was reported by Stefszky *et al.* [63]. The squeezing over 10 dB is not realistic well due to the optical loss especially in the context of GW detectors, so we can say generation of squeezed light is already developed

enough.

In 2015, the frequency dependent squeezing was realized by Oelker *et al.* [64] at audio-band. They succeeded in rotating the squeezing angle at 1.2 kHz by 90° with keeping the squeezing level of 2 dB. The rotation frequency of the squeezed vacuum should be below 100 Hz to improve the quantum noise of advanced detectors, but this demonstration is the significant first step for reduction of quantum noise at all frequency range.

Shot noise reduction at an interferometer

The first measurement of reduction of shot noise at a detectors-like interferometer was reported by Goda *et al.* [65] in 2008. They improved the sensitivity beyond the shot noise limit. Squeezed light was injected to a simple signal recycling Michelson interferometer, where the shot noise was reduced by about a half between 40 kHz and 100 kHz.

At a large detector scale, reduction of shot noise was demonstrated in 2011 by GEO600 in Hannover [66]. GEO600 is a prototype GW detector for the second generation with the arms of 600 m and the signal recycling Michelson interferometer. It has a role of testing the advanced technique such as quantum noise reduction. With the input of squeezed light, the shot noise was reduced by 3.5 dB above 1 kHz.

Moreover, the demonstration at km-scale detectors was done at LIGO Hanford in 2013 [67]. In this experiment, the sensitivity of initial LIGO Hanford was improved by 2 dB above 500 Hz. There was no noise excess at low frequency at the demonstration in both sites.

As we show the previous works in this subsection, it has much progress to generate the squeezed light with the enough squeezing level and to reduce the shot noise even at the real GW detectors. There is a plan to install the squeezer and reduce the shot noise in advanced LIGO at O3.

2.4.2 Towards measurement of radiation pressure noise

In contrast to experiments on shot noise, there is still room for improvement on experimental research of radiation pressure noise. It has been observed for the radiation pressure noise to be dominant with such light mechanical

oscillators as below ng scale, and in a part the back action evasion also has succeeded as we describe the details in the next chapter. Their frequency region is mainly MHz. It is much higher than the detector-band frequency. However, the reduction of radiation pressure noise below 1 kHz has not been realized yet, even the measurement of it either. Here we show experimental works trying to measure the radiation pressure noise.

Lighter mirrors and cavities with higher finesse than the real detectors are used in order to enhance the radiation pressure noise. Sakata *et al.* [16] developed a Fabry–Perót Michelson interferometer with a 20-mg suspended mirror. Due to the suspension of a single wire, the Sidles–Sigg instability [54] occurred and they could not realize enough intra-cavity power to measure the radiation pressure noise. This instability was caused by the negative spring of the rotational mode of the test mass. When the mirror tilts, the torque of the intra-cavity power works with enhancing the tilt. The method to avoid this instability was developed by controlling the rotational mode of the other heavier mirror which was a pair of the test mass [68, 69].

Neben *et al.* [18] tried to measure radiation pressure noise on 1-g suspended mirrors constructing a Fabry–Perót Michelson interferometer. They suspended test masses with two suspension fibers to avoid the Sidles–Sigg instability. However, thermal noise of bonding between the mirror and the suspension fibers was the issue and radiation pressure noise was much below the measured displacement.

Sub-gram scale cantilever flexures were developed by Nguyen *et al.* [21]. Their test masses were made of Aluminum and Niobium. The sensitivity was also limited by the thermal noises of the fundamental modes of the cantilevers.

Westphal *et al.* [17] is planning to reach the SQL sensitivity with 100-g test masses in a 10-m Fabry–Perót Michelson interferometer. The plan of Gräss *et al.* [19] is testing back action evasion with a speed meter consisting of 1-g mirrors. In the speed meter, the relative velocity of the test mass can be measured with laser light traveling in the clockwise and the counter clockwise direction in a Sagnac interferometer.

In our group, a 5-mg suspended mirror in a triangular cavity was developed [20]. The negative rotational spring by the Sidles–Sigg instability turns to be positive in the case of the triangular cavity because of the one more

sign flip at reflection. We succeeded in storing the intra-cavity power of 7 W. The power was around 50 times higher than that in the case of linear cavity. The displacement sensitivity was limited by the laser frequency and intensity noise. Even though the suspension thermal noise was estimated to be smaller than the radiation pressure noise over 325 Hz, that frequency was not radiation pressure dominant band for the real GW detectors.

The sensitivity of advanced LIGO in O1 was close to the radiation pressure noise compared with above experiments [70]. The signal (radiation pressure noise) to noise (sum of the other noises) was ~ 0.1 around 40-50 Hz.

In 2018 at last, Cripe *et al.* [71] reported the first observation of radiation pressure noise at wide frequency band. Their test mass was a 50-ng cantilever. The signal to noise ratio was over 1 between 10 kHz and 50 kHz. The result is a benchmark for radiation pressure experiments. The frequency region was lower than MHz region, however, it was far from the detector band.

We summarize the noise to radiation pressure ratio of above previous works in Fig. 2.17. Many experiments have not succeeded in observing the quantum radiation pressure noise. Around the detector band, the most sensitive test mass is that of LIGO at O1. The 50-ng cantilever is the unique oscillator driven by radiation pressure, but the frequency region is different from around 100 Hz.

2.5 Summary of this chapter

Gravitational waves bring us information which is not accessible with electromagnetic waves. Future detectors' sensitivities are designed to be limited by quantum radiation pressure noise. This noise is caused by the vacuum fluctuation coupled with the laser light inside the arm cavities. It is important to observe the noise ahead of the actual detectors and confirm the reduction method. Displacement noises of previous works aiming at observation of the radiation pressure noise were higher than the target by more than one order of magnitude.

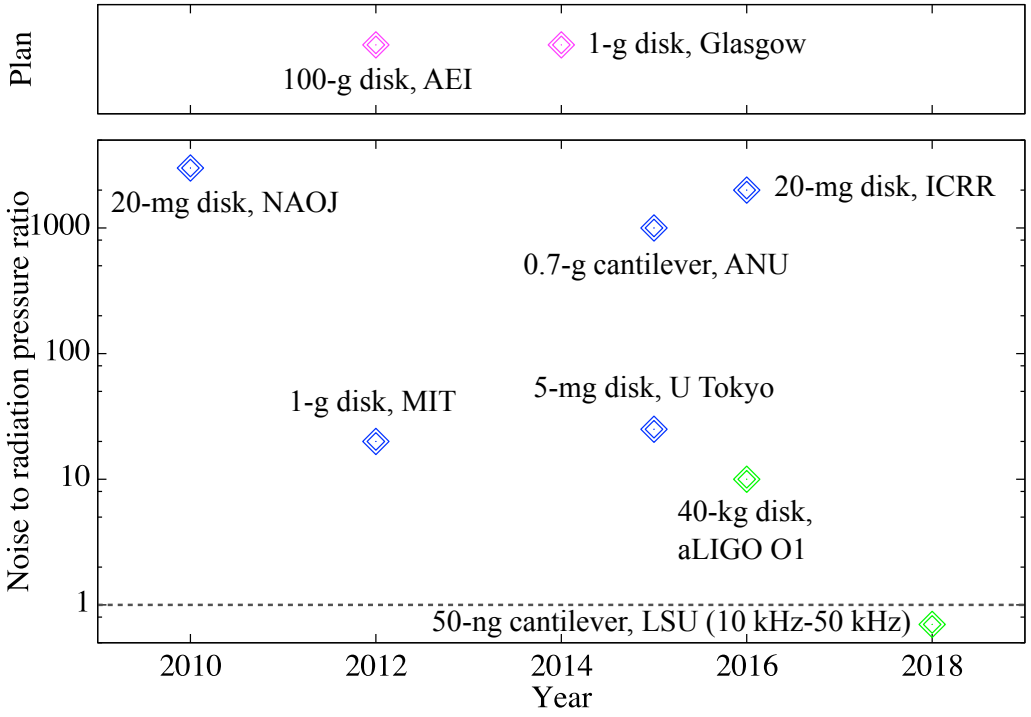

Figure 2.17: The noise to radiation pressure ratio of previous works. We describe the results of ongoing experiments (the 100-g suspended disk by Westphal *et al.* from AEI [17] and the 1-g suspended disk by Gräss *et al.* from Glasgow [19]) as magenta points, done works (the 20-mg suspended disk by Sakata *et al.* from NAOJ [16], the 1-g suspended disk by Neben *et al.* from MIT [18], the 0.7-g cantilever by Nguyen *et al.* from ANU [21], the 5-mg suspended disk by Matsumoto *et al.* from U Tokyo [20], and the 20-mg suspended disk by Nagano *et al.* from ICRR [68]) as blue points, and different types (the sensitivities of aLIGO O1 [70] and the 50-ng cantilever by Cripe *et al.* from LSU [71]) as green dots.

Chapter 3

Radiation pressure fluctuation in optomechanics

Optomechanics describes interactions between mechanical modes of oscillators and optical modes of laser light. The origin of the interaction is radiation pressure of the light. Photon of the laser light gives momentum to the mechanical oscillator at the hitting, when the oscillator feels the pressure. In this chapter, we describe the radiation pressure effect and its quantum fluctuation from a viewpoint of optomechanics.

First, background of optomechanics is introduced in Section 3.1, followed by theories of a optomechanical Hamiltonian, an optical cavity, an optical spring, and radiation pressure fluctuation in Section 3.2. Next, we introduce phonon number and optomechanical cooling of the oscillator in Section 3.3. At the last in Section 3.4, previous works in optomechanics are discussed.

3.1 Background

One of the most fundamental goals of optomechanics is to realize macroscopic quantum states such as superposition of massive oscillators and to test the principle of quantum mechanics. In this section, the fundamental motivation and application of optomechanics are shown.

3.1.1 Massive superposition

Quantum mechanics can be well applied to microscopic physics in the scale of atoms and molecules. On the other hand, how about the macroscopic scale? In 1935, Schrödinger did a thought experiment whether a cat is in the superposition states of alive or dead state [72]. From a viewpoint of quantum correlation length, many experiments have been demonstrated and behaved in the quantum mechanics. However, a truly Schrödinger's cat state, that is to say, the superposition of such the massive degree of freedom as kg scale has not been realized yet.

It is pointed out that quantum mechanics might not hold in strong gravitational fields. It is because the gravity can not be quantum, or there exists the gravitational decoherence [73]. Diósi [74] and Penrose [75] pointed out that the gravity causes wave function collapse. Ghirardi *et al.* [76] proposed continuous spontaneous localization (CSL) model, where the localization of the wave function is always occurring. In these theories the energy dissipation of a massive degree of freedom due to the localization can be observed as a kind of classical noise, which is detectable with feasible techniques. The CSL model attracts much attention because it can be tested experimentally on the two parameters space, the correlation length r_{CSL} and the collapse rate λ_{CSL}. The force noise spectrum due to the CSL effect is given by [77]

$$S_{\mathrm{f,CSL}} = \frac{4\pi\hbar^2\rho m}{m_0^2 d}\lambda_{\mathrm{CSL}} r_{\mathrm{CSL}}^2, \tag{3.1}$$

where ρ and m are the density and mass of the oscillator, m_0 is the nucleon mass, and d is the characteristic length of the oscillator. Some experiments have set the bounds on the CSL parameters [79–83].

In addition to the test of the CSL model, it is also an outstanding goal to create superposition states of massive oscillators and to observe the behavior after that, for example, to measure the decoherence time of the superposition. Optomechanics can be a great test bench for making such states. In the next subsection, we describe how optomechanics can be applied to test the macroscopic quantum mechanics.

3.1.2 Application of optomechanics

Optomechanics provides the platform to search for massive superposition states with the effect cooling of mechanical modes drastically. Similarly to laser cooling of trapped atoms, the laser light in the optical cavity can suppress the motion of mirrors of the cavity by the radiation pressure. It is possible to cool the mechanical mode even to its quantum ground state.

Marshall *et al.* [24] proposed the method of making superposition state of a macroscopic mirror if we can prepare the mirror cooled almost to the ground state. The cooled mirror is used as an end mirror of Fabry–Perót Michelson interferometer. A single photon is injected to the interferometer. If the mirror is fixed, the entangled state of which arms the photon exists in, $|\psi\rangle = (|0\rangle_A|1\rangle_B + |1\rangle_A|0\rangle_B)/\sqrt{2}$, is observed. When the one end mirror is in its ground state $|0\rangle_m$, time evolution of the wave function is given by

$$|\psi(t)\rangle = \frac{1}{\sqrt{2}}\left[|0\rangle_A|1\rangle_B|0\rangle_m + e^{i\zeta^2(\omega_{\rm m}t-\sin\omega_{\rm m}t)}|1\rangle_A|0\rangle_B|\zeta(1-e^{-i\omega_{\rm m}t})\rangle_m\right], \quad (3.2)$$

where $\zeta = (\omega_{\rm L}/L\omega_{\rm m})\sqrt{(\hbar/2m\omega_{\rm m})}$, $\omega_{\rm m}$ and m are the angular resonant frequency and mass of the end mirror respectively, L is the cavity length, and $\omega_{\rm L}$ is the angular frequency of the single photon. After a one period of the mirror the interference visibility of photon is revived if the entangled state holds. If decoherence occurs, the visibility goes to zero, so we can measure the decoherence time of the system. This entangled state involves the translational mode of the center of the end mirror mass.

Also from a viewpoint of a GW detector, the field of optomechanics is developed. The sensitivity of the detector can reach the SQL. It means that the system can test the quantum behavior of a massive mirror whose mass is even over kg scale. Ebhardt *et al.* [84] proposed that the entanglement of two mirrors can be generated with a power recycling Michelson interferometer and measurement of common and differential modes, whose sensitivities are reaching the SQL. Due to the quantum correlation, the wave function of the system $\Psi(x^E, x^N) = \psi^c[(x^E + x^N)/2]\psi^d[(x^E - x^N)/2]$ cannot be separable, where x^E and x^N are the position of two end mirrors, ψ^c and ψ^d are the wave function of the common and differential mode. The entanglement can be

shown by calculating the logarithmic negativity of the system to be over zero.

Furthermore, optomechanical demonstration of macroscopic quantum state has been proposed such as measurement-induced superposition with pulse laser and a quantum tomography [85].

Before moving to the next section, the formula of the SQL is noted. In the previous chapter we discuss only the free mass SQL. However, the true SQL in the force spectrum is described as [86]

$$S_{\mathrm{f,SQL}} = \frac{2\hbar}{|\chi_{\mathrm{m}}(\omega)|} + 2\hbar\omega_{\mathrm{m}}\gamma_{\mathrm{m}}m, \tag{3.3}$$

where $\chi_{\mathrm{m}} = 1/[m(\omega_{\mathrm{m}}^2 - \omega^2 + i\gamma_{\mathrm{m}}\omega)]$ is the susceptibility of the oscillator. The suspended cavities like a GW detector can reach the SQL at free mass range $\omega \gg \omega_{\mathrm{m}}$. On the other hand, the optomechanical device can be cooled to the SQL at $\omega = \omega_{\mathrm{m}}$, which means the ground state cooling. The second term of Eq. (3.3) shows the mechanical zero-point fluctuation. The displacement due to the zero-point fluctuation is the same as that of the first term at $\omega = \omega_{\mathrm{m}}$.

3.2 Theories on optomechanics

Optomechanical effects are enhanced by optical cavities consisting of mechanical oscillators. It is clear to apply the optomechanical description to the cavities and the effect such as an optical spring. In this section, we describe optomechanical theories of the Hamiltonian, the optical cavity, the optical spring, and quantum radiation pressure fluctuation.

3.2.1 Optomechanical Hamiltonian

The starting points are the Hamiltonian of the optomechanical system and deriving the characteristics of the optical cavity. We denote the creation and annihilation operators of the laser photon as $\hat{a}^\dagger$ and $\hat{a}$, those of the phonon of the mechanical mode as $\hat{b}^\dagger$ and $\hat{b}$, respectively. The Hamiltonian of the optomechanical system can be shown as

$$\hat{\mathcal{H}} = \hbar\omega_{\mathrm{c}}(x)\hat{a}^\dagger\hat{a} + \hbar\omega_{\mathrm{m}}\hat{b}^\dagger\hat{b}, \tag{3.4}$$

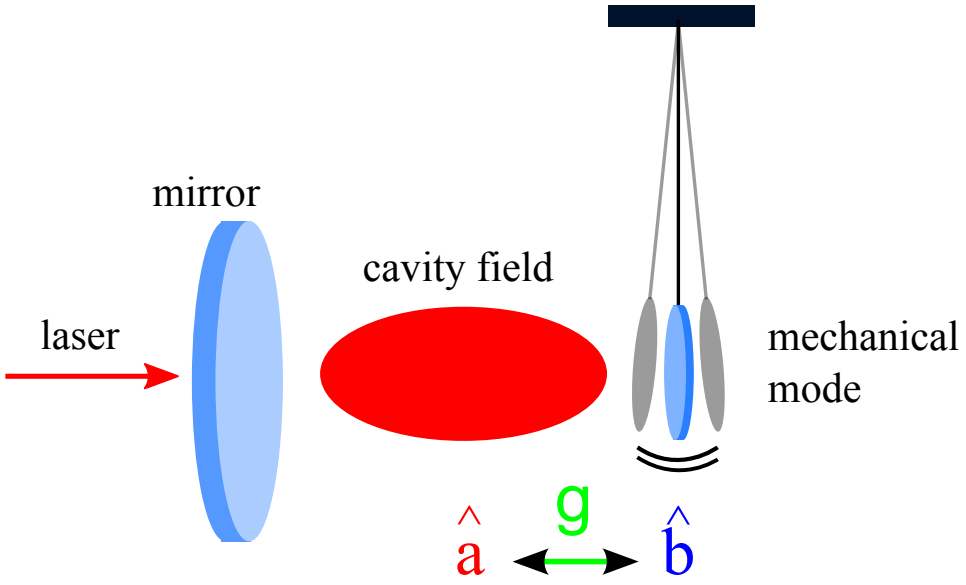

Figure 3.1: A conceptual scheme of optomechanics. The cavity consists of facing mirrors. One of them has a mechanical mode $\hat{b}$. The mode couples with the photon field in the cavity $\hat{a}$. Their coupling constant is g called the optomechanical coupling constant.

where $\omega_{\rm c}(x)$ is the angular resonant frequency of the photon in the cavity and the function of the oscillator position x.

It is assumed that the tiny fluctuation of the oscillator around one resonance of the cavity even though there are other resonances the wave length away. In other words, $x \ll \lambda_{\rm L}$ is assumed. In this approximation, the resonant frequency of the cavity is changed linearly by x,

$$\omega_{\rm c}(x) = \omega_0 - gx, \tag{3.5}$$

where ω_0 is the angular resonant frequency of the cavity at the natural position of the oscillator, g is the optomechanical coupling constant. The constant can be written as

$$g = \frac{2\omega_0 \cos\beta}{L_{\rm r}}, \tag{3.6}$$

where β is the incident angle of the light and $L_{\rm r}$ is the round trip length of the cavity.

In Fig. 3.1, the conceptual scheme of optomechanics is shown. The photon

of the laser light in the cavity and the phonon of the mechanical oscillator are coupled via the optomechanical coupling constant.

3.2.2 Optical cavity

In this subsection we describe the optical cavity. Time evolution of the annihilation operator of the photon is given by

$$\dot{\hat{a}} = -\frac{i}{\hbar}[\hat{a}, \hat{\mathcal{H}}] - \kappa\hat{a} + \sum_l \sqrt{2\kappa_l}\hat{A}_l. \tag{3.7}$$

The first term comes from the Heisenberg equation, the second term shows the total transmission including the loss of the intra-cavity field, and the third term is the input of the photon at each port ($\kappa = \sum_l \kappa_l$). $\hat{A}_l$ [Hz] is the driving field of the each port.

Substituting Eq. (3.4) for Eq. (3.7), and considered in the rotating frame at the laser frequency ω_{L} (*i.e.* $\hat{a} \to \hat{a}e^{-i\omega_{\mathrm{L}}t}$), we get

$$\dot{\hat{a}} = -[\kappa - i(\omega_{\mathrm{L}} - \omega_0 + gx)]\hat{a} + \sum_l \sqrt{2\kappa_l}\hat{A}_l. \tag{3.8}$$

Then, the time-dependent parameters are divided to the time-averaged value and the fluctuation component,

$$\hat{a} = \bar{a} + \delta\hat{a},\ x = \bar{x} + \delta x,\ \hat{A}_l = \bar{A}_l + \delta\hat{A}_l. \tag{3.9}$$

In the first order approximation, the equations for each component can be written as

$$0 = -(\kappa - i\Delta)\bar{a} + \sqrt{2\kappa_{\mathrm{in}}}\bar{A}_{\mathrm{in}}, \tag{3.10}$$

$$\delta\dot{\hat{a}} = -(\kappa - i\Delta)\delta\hat{a} + ig\bar{a}\delta x + \sum_l \sqrt{2\kappa_l}\delta\hat{A}_l, \tag{3.11}$$

where $\Delta = \omega_{\mathrm{L}} - \omega_0 + g\bar{x}$ represents the detuning between the laser frequency and the resonant frequency of the cavity. The index of "in" means the input port of the cavity.

The power of reflection and transmission of the cavity can be calculated by

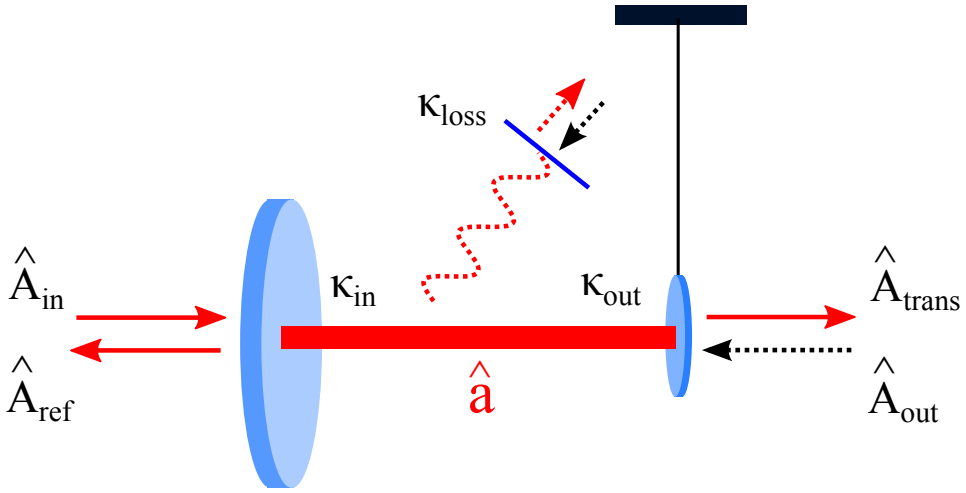

Figure 3.2: Definition of the indices of the driving field and the input and output ports. The input $\hat{A}_{\rm in}$ and output $\hat{A}_{\rm ref}$ of the input mirror $\kappa_{\rm in}$, and the output $\hat{A}_{\rm trans}$ of the end mirror $\kappa_{\rm out}$ has large coherence amplitude. Actually there is loss from the cavity of $\kappa_{\rm loss}$ with small amplitude. The input fields from the output port $\hat{A}_{\rm out}$ and the loss port are in the vacuum states.

these equaitons. The input-output relation is given by [55]

$$\begin{aligned}\hat{A}_{\rm in} + \hat{A}_{\rm ref} &= \sqrt{2\kappa_{\rm in}}\hat{a},\\ \hat{A}_{\rm out} + \hat{A}_{\rm trans} &= \sqrt{2\kappa_{\rm out}}\hat{a},\end{aligned} \tag{3.12}$$

where the each index is shown in Fig. 3.2. Here the loss of the cavity is neglected. With Eq. (3.10), the averaged amplitude of the photon number of the cavity is written as

$$\bar{a} = \frac{\sqrt{2\kappa_{\rm in}}}{\kappa - i\Delta}\bar{A}_{\rm in}. \tag{3.13}$$

Substituting Eq. (3.13) and $\bar{A}_{\rm out} = 0$ for Eq. (3.12),

$$\begin{aligned}\bar{A}_{\rm ref} &= \left(-1 + \frac{2\kappa_{\rm in}}{\kappa - i\Delta}\right)\bar{A}_{\rm in},\\ \bar{A}_{\rm trans} &= \frac{\sqrt{4\kappa_{\rm in}\kappa_{\rm out}}}{\kappa - i\Delta}\bar{A}_{\rm in}\end{aligned} \tag{3.14}$$

are satisfied. Therefore, the power of the reflection $P_{\rm ref} = \hbar\omega_{\rm L}|\bar{A}_{\rm ref}|^2$ and the

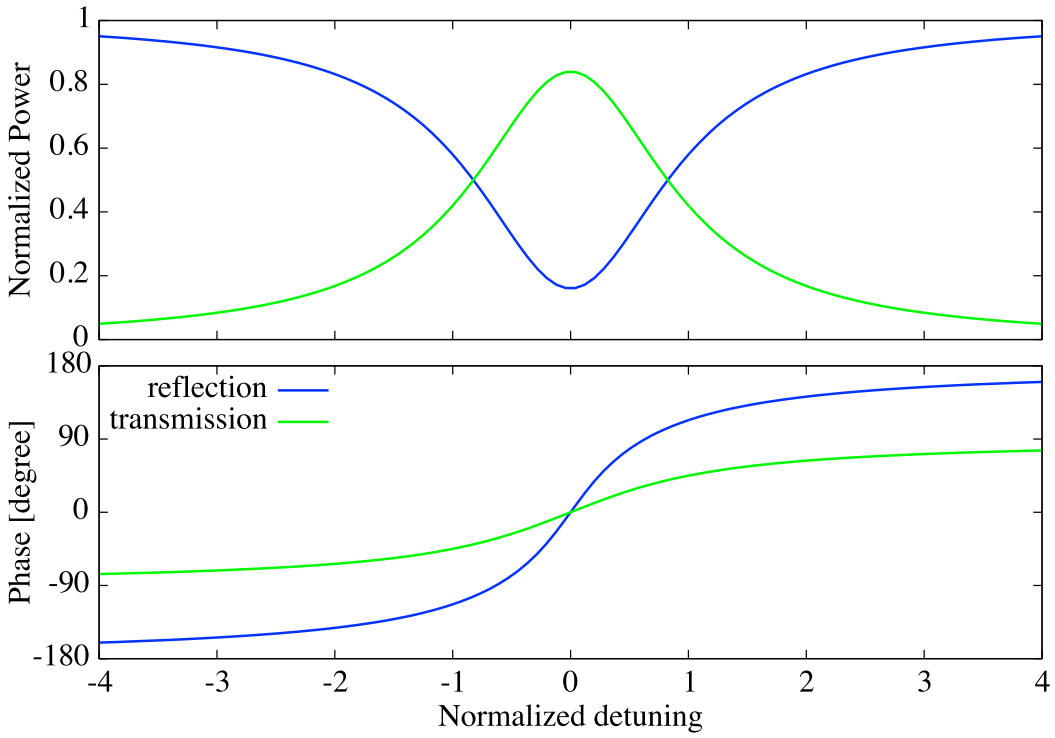

Figure 3.3: Normalized power and phase of the reflection and transmission on the normalized detuning. The blue and green lines show the reflection and transmission respectively. Here we assume $\kappa_{\mathrm{in}}/\kappa = 0.7$ and $\kappa_{\mathrm{out}}/\kappa = 0.3$, an over coupled cavity.

transmission $P_{\mathrm{trans}} = \hbar\omega_{\mathrm{L}}|\bar{A}_{\mathrm{trans}}|^2$ can be described as

$$P_{\mathrm{ref}} = \left[1 - \frac{4\kappa_{\mathrm{in}}}{\kappa}\left(1 - \frac{\kappa_{\mathrm{in}}}{\kappa}\right)\frac{1}{1+\delta^2}\right]P_{\mathrm{in}}, \tag{3.15}$$

$$P_{\mathrm{trans}} = \frac{4\kappa_{\mathrm{in}}\kappa_{\mathrm{out}}}{\kappa^2}\frac{1}{1+\delta^2}P_{\mathrm{in}}, \tag{3.16}$$

where the input power is $P_{\mathrm{in}} = \hbar\omega_{\mathrm{L}}|\bar{A}_{\mathrm{in}}|^2$ and $\delta = \Delta/\kappa$ is the detuning normalized by the cavity line width.

In Fig. 3.3, the normalized power and phase of the reflection and transmission are plotted as a function of the normalized detuning. It should be noted that the phase of the reflection changes from $-\pi$ to π, totally by 2π with the over coupled cavity. The dependence of the power is Lorentzian and the half width half maximum can be written as $\kappa = 2\pi f_{\mathrm{p}}$ with the cavity pole

in Eq. (2.46). Then the finesse of the cavity is also written by the κ as

$$\mathcal{F} = \frac{\pi c}{\kappa L_{\rm r}}. \tag{3.17}$$

At the last, the formula of the intra-cavity power is introduced. With the round trip time $\tau_{\rm r} = L_{\rm r}/c$ of the laser light in the cavity, the intra-cavity power is given by

$$\begin{aligned} P_{\rm circ} &= \frac{\hbar\omega_{\rm L}}{\tau_{\rm r}}|\bar{a}|^2 \\ &= \frac{2\mathcal{F}}{\pi}\frac{\kappa_{\rm in}}{\kappa}\frac{1}{1+\delta^2}P_{\rm in}. \end{aligned} \tag{3.18}$$

The enhanced factor of $P_{\rm circ}/P_{\rm in}$ is around the $\mathcal{F}$. The characteristic of the cavity changes with the value of $\kappa_{\rm in}/\kappa$ as below.

$$\begin{aligned} 1/2 < \kappa_{\rm in}/\kappa < 1 &: \textit{over coupling} \\ \kappa_{\rm in}/\kappa = 1/2 &: \textit{critical coupling} \\ 0 < \kappa_{\rm in}/\kappa < 1/2 &: \textit{under coupling} \end{aligned} \tag{3.19}$$

When the cavity is the critical coupling, the reflection is nothing $P_{\rm ref} = 0$. The intra-cavity power is large with high coupling factor. In the context of arm cavities of the GW detectors, the over-coupling limit of $\kappa_{\rm in}/\kappa = 1$ is assumed.

3.2.3 Optical spring

In the previous subsection the characteristics of the optical cavity is shown. In this subsection, we derive the spring effect with the detuned optical cavity, which is called an optical spring [87].

Fig. 3.4 shows a qualitative description of the optical spring. Here a detuned optical cavity with a mechanical oscillator is considered. The radiation pressure force in the cavity balances the restoring force of the oscillator. When it slightly moves as the cavity length gets shorter, the intra-cavity power increases due to being near on resonance, and hence the radiation pressure pushes back, and vice versa.

The quantitive description is as follows. The operator of the radiation

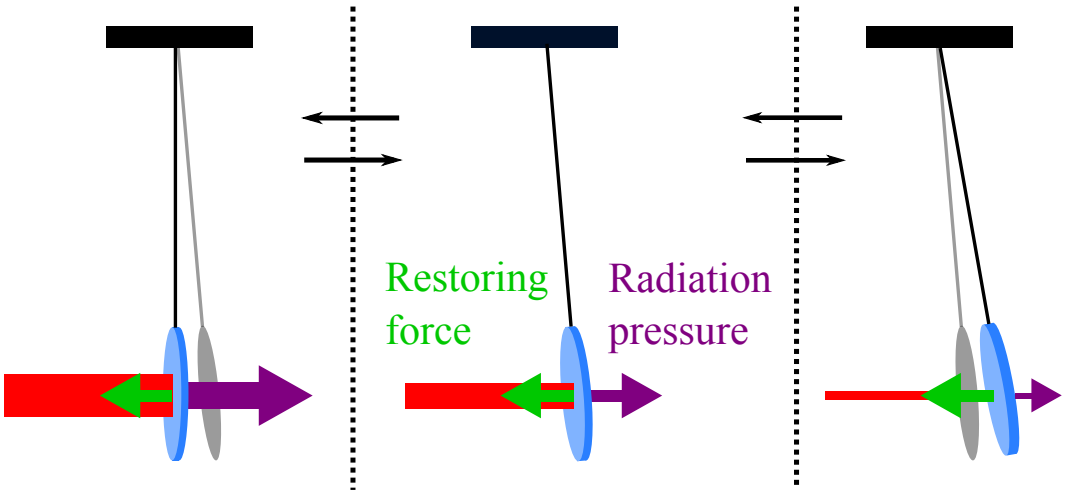

Figure 3.4: A qualitative description of the optical spring. The green and purple arrows show the restoring force of the mechanical mode and the radiation pressure. The detuning is positive $\delta > 0$.

pressure is given by differentiating the Hamiltonian by time,

$$\begin{aligned} \hat{F}_{\mathrm{rad}} &= \left| \frac{d\hat{\mathcal{H}}_{\mathrm{SYS}}}{dx} \right| \\ &= \hbar g \hat{a}^\dagger \hat{a}. \end{aligned} \tag{3.20}$$

The averaged component can be represented as

$$\begin{aligned} \bar{F}_{\mathrm{rad}} &= \hbar g |\bar{a}|^2 \\ &= \frac{2\cos\beta}{c} P_{\mathrm{circ}}, \end{aligned} \tag{3.21}$$

with Eq. (3.18) and (3.6).

In the first order approximation, the fluctuation component of the radiation pressure is written as

$$\delta\hat{F}_{\mathrm{rad}} = \hbar g(\bar{a}\delta\hat{a}^\dagger + \bar{a}^*\delta\hat{a}). \tag{3.22}$$

In Fourier domain, the fluctuation of the annihilation operator, Eq. (3.11), can be written as

$$\delta\hat{a}(\omega) = \chi_{\mathrm{c}}(\omega) \left(ig\bar{a}\delta x + \sum_l \sqrt{2\kappa_l}\delta\hat{A}_l \right), \tag{3.23}$$

in the definition of Eq. (2.48). The susceptibility of the optical cavity is defined as

$$\chi_{\rm c}(\omega) = \frac{1}{\kappa + i(\omega - \Delta)}. \tag{3.24}$$

Noting that

$$\delta\hat{a}(t)^\dagger = \int_{-\infty}^{\infty} \delta\hat{a}(-\omega)^\dagger \exp(i\omega t) d\omega, \tag{3.25}$$

we substitute Eq. (3.23) for Eq. (3.22) and get

$$\begin{aligned}\delta\hat{F}_{\rm rad} &= i\hbar g^2 |\bar{a}|^2 \left[\chi_{\rm c}(\omega) - \chi_{\rm c}^*(-\omega)\right] \delta x \\ &\quad + \hbar g \sum_l \sqrt{2\kappa_l} \left[\bar{a}^* \chi_{\rm c}(\omega) \delta\hat{A}_l + \bar{a}\chi_{\rm c}^*(-\omega)\delta\hat{A}_l^\dagger\right].\end{aligned} \tag{3.26}$$

The first term

$$\delta F_{\rm opt} \equiv i\hbar g^2 |\bar{a}|^2 [\chi_{\rm c}(\omega) - \chi_{\rm c}^*(-\omega)]\delta x \tag{3.27}$$

is the force produced by the displacement δx of the oscillator, in other words, the effect of the optical spring. The spring constant is described as

$$\begin{aligned}K(\omega) &= -\frac{\delta\hat{F}_{\rm rad}}{\delta x} \\ &= 2\hbar g^2 |\bar{a}|^2 \frac{\Delta}{(\kappa + i\omega)^2 + \Delta^2},\end{aligned} \tag{3.28}$$

with Eq. (3.24).

The slow varying condition: $\omega \ll \kappa$ is focused on in order to discuss the characteristics of the optical spring. This is a good approximation when the oscillator is massive with the low resonant frequency and the cavity length is not so long. Substituting Eq. (3.13) for Eq. (3.28), the spring constant can be written as

$$\begin{aligned}K(\omega) &\simeq \frac{16\omega_{\rm L}\mathcal{F}^2 P_{\rm in}\cos^2\beta}{\pi^2 c^2} \frac{\kappa_{\rm in}}{\kappa} \frac{\delta}{(1+\delta^2)^2} \left[1 - \frac{2i\omega}{\kappa(1+\delta^2)}\right] \\ &\equiv K_{\rm opt} + i\Gamma_{\rm opt}\omega.\end{aligned} \tag{3.29}$$

The real and imaginary parts correspond to the restoring force and the damping respectively. Their dependence on the detuning is plotted in Fig. 3.5. The

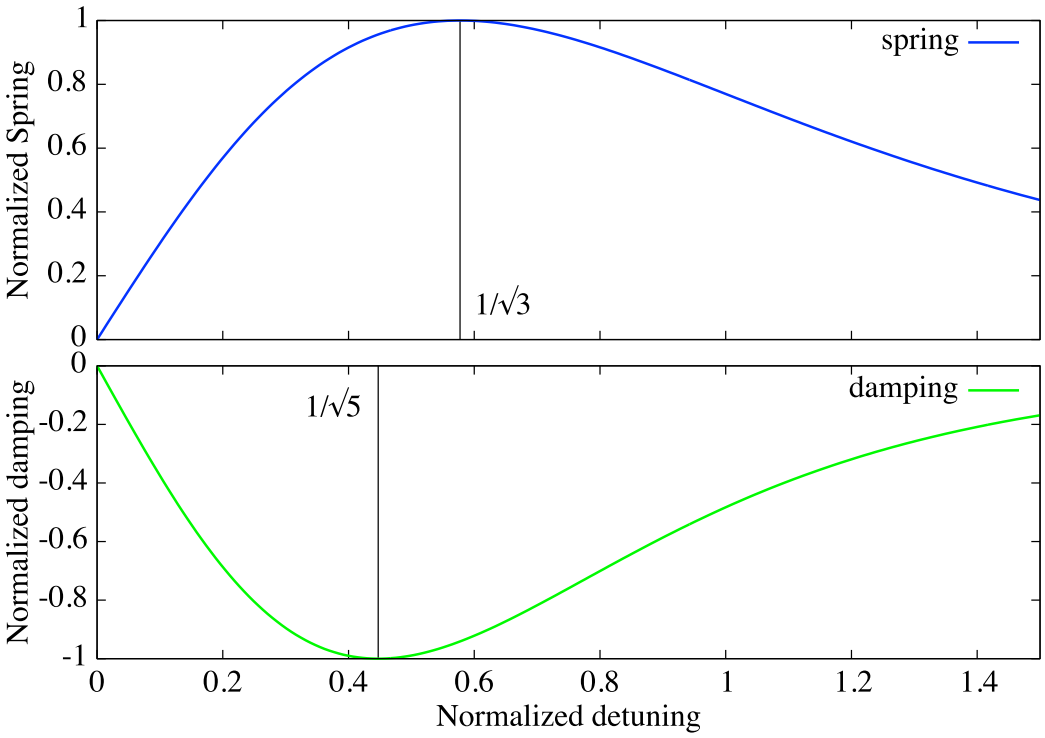

Figure 3.5: Dependence of the normalized spring and damping on the normalized detuning. The blue and green line show the spring and damping constant respectively. The detuning taking their maximum values are shown as black lines.

detuning of each constant at the maximum is slightly different, $\delta = 1/\sqrt{3}$ at the spring and $\delta = 1/\sqrt{5}$ at the damping. The sign of them is always opposite.

3.2.4 Quantum radiation pressure fluctuation

In this subsection, we describe the quantum radiation pressure fluctuation in the optical cavity. It is the main theme of the thesis. In Eq. (3.10), $\kappa_{\rm in}$ out of κ_l is only taken into account at the average component. On the other hand, all of the fluctuation components are considered in Eq. (3.11). It is because only the input field has the coherent amplitude, and the vacuum fluctuation is entered from any ports of the cavity. Exactly writing, the avelaged value of

the vacuum fluctuation operator is given by

$$\begin{aligned}\langle \delta\hat{A}_l^\dagger(t)\delta\hat{A}_m(t')\rangle &= N(\omega_{\rm c}),\\ \langle \delta\hat{A}_l(t)\delta\hat{A}_m^\dagger(t')\rangle &= [N(\omega_{\rm c})+1]\delta_{lm}\delta(t-t'),\end{aligned} \tag{3.30}$$

where

$$N(\omega_{\rm c}) = \frac{1}{e^{\hbar\omega_{\rm L}/k_{\rm B}T_{\rm th}}-1} \tag{3.31}$$

is the photon number driven by the thermal bath. Even at toom temperature $T_{\rm th} = 300$ K, the energy scale of the photon $\omega_L/2\pi \sim 300$ THz is much higher than that of the thermal bath ($\hbar\omega_{\rm L}/k_{\rm B}T_{\rm th} \gg 1$). Therefore, we can suppose that $N(\omega_{\rm c}) \simeq 0$ and

$$\begin{aligned}\langle \delta\hat{A}_l^\dagger(t)\delta\hat{A}_m(t')\rangle &\simeq 0\\ \langle \delta\hat{A}_l(t)\delta\hat{A}_m^\dagger(t')\rangle &\simeq \delta_{lm}\delta(t-t').\end{aligned} \tag{3.32}$$

This fluctuation contributes to the operator of the radiation pressure as the second term of Eq. (3.26),

$$\delta\hat{F}_{\rm qrp}(\omega) = \hbar g\sum_l \sqrt{2\kappa_l}\left[\bar{a}^*\chi_{\rm c}(\omega)\delta\hat{A}_l + \bar{a}\chi_{\rm c}^*(-\omega)\delta\hat{A}_l^\dagger\right]. \tag{3.33}$$

This is the quantum radiation pressure fluctuation. The single-sided power spectrum in the force is given by

$$\begin{aligned}S_{\rm f,qrp} &= \langle \delta\hat{F}_{\rm qrp}(\omega)\delta\hat{F}_{\rm qrp}(-\omega)\rangle + \langle \delta\hat{F}_{\rm qrp}(-\omega)\delta\hat{F}_{\rm qrp}(\omega)\rangle\\ &= 2\hbar^2 g^2\kappa|\bar{a}|^2\left[|\chi_{\rm c}(\omega)|^2 + |\chi_{\rm c}(-\omega)|^2\right]\\ &\simeq \frac{32\hbar\omega_{\rm L}\mathcal{F}^2 P_{\rm in}\cos^2\beta}{\pi^2 c^2}\frac{\kappa_{\rm in}}{\kappa}\frac{1}{(1+\delta^2)^2}.\end{aligned} \tag{3.34}$$

In the context of the GW detectors, this fluctuation is called the radiation pressure noise. In optomechanics, however, observation of the quantum radiation pressure fluctuation is one of the benchmarks to reach the quantum ground state.

The quantum fluctuation is discussed here, and there is also a classical noise of the laser amplitude. The classical fluctuation causing the displacement of

the mirror is called the classical radiation pressure noise. The relative shot noise level of the laser power is defined as

$$B_{\mathrm{rsnl}} = \sqrt{\frac{S_{\mathrm{p,las}}}{S_{\mathrm{p,shot}}}}, \tag{3.35}$$

where $S_{\mathrm{p,las}}$ and $S_{\mathrm{p,shot}}$ is the power spectrum of the laser intensity noise and the shot noise, whose units are W^2/Hz. The ratio between the quantum fluctuation and classical radiation pressure noise in the force spectrum can be written as

$$\frac{S_{\mathrm{f,crp}}}{S_{\mathrm{f,qrp}}} = \frac{\kappa_{\mathrm{in}}}{\kappa} B_{\mathrm{rsnl}}^2. \tag{3.36}$$

In this section, we show the theoretical description of the bases in optomechanics such as the optical cavity, the optical spring, and the quantum radiation pressure fluctuation, including the background. In the next section, the optomechanical cooling is introduced.

3.3 Optomechanical cooling

The optomechanical interaction can be used to suppress the mechanical motion with the radiation pressure. In that way the effective temperature of the mode is cooled even to its quantum ground state and to observe the zero-point fluctuation. The ground state cooling is one of the necessary conditions to realize the entangled state of the mechanical motion.

In this section, at first, phonon number of the mechanical mode is introduced with focusing on the thermal phonon and radiation pressure phonon. That is followed by the cooling method in the two cases. They are the sideband cooling in a good cavity and the feedback cooling in a bad cavity.

3.3.1 Phonon number

Here we introduce the concept of the phonon number, especially the thermal phonon number and the radiation pressure phonon. Total phonon number can

be defined as

$$n_{\rm pn} \equiv \langle \hat{b}^\dagger \hat{b} \rangle - \frac{1}{2}, \tag{3.37}$$

with the creation and annihilation operators of the mechanical mode in Eq. (3.4). This value shows how the energy of the mechanical mode is large compared with the zero-point fluctuation in the unit of one quantum of the mode $\hbar\omega_{\rm m}$. With the total mean square of the displacement of the mechanical mode $\langle x^2 \rangle$ [m^2], the phonon number can be written as

$$n_{\rm pn} = \frac{m\omega_{\rm m}}{\hbar}\langle x^2 \rangle - \frac{1}{2}. \tag{3.38}$$

When the mode is in the ground state, the mean square is $\langle x^2 \rangle = \hbar/2m\omega_{\rm m}$, and hence the phonon number is zero $n_{\rm pn} = 0$.

The total phonon can be separated by the origin. We define the photon due to the thermal noise, the quantum radiation pressure fluctuation, and the others as $n_{\rm th}$, $n_{\rm rp}$, and $n_{\rm ot}$ respectively. The sum of these phonon is equal to the total phonon number,

$$n_{\rm pn} = n_{\rm th} + n_{\rm rp} + n_{\rm ex}. \tag{3.39}$$

In order to observe the zero-point fluctuation, each phonon number is less than 1. The method is discussed how fundamental phonon of $n_{\rm th}$ and $n_{\rm rp}$ can be reduced below 1.

Thermal phonon

First, the thermal phonon number is calculated. According to the law of equipartition of energy, the energy of $k_{\rm B}T_{\rm th}/2$ is distributed to one mechanical mode,

$$\frac{1}{2}m\omega_{\rm m}^2\langle x^2 \rangle_{\rm th} = \frac{1}{2}k_{\rm B}T_{\rm th}, \tag{3.40}$$

where $\langle x^2 \rangle_{\rm th}$ is the mean square of the displacement due to the thermal noise, and hence

$$\langle x^2 \rangle_{\rm th} = \frac{k_{\rm B}T_{\rm th}}{m\omega_{\rm m}^2} \tag{3.41}$$

is satisfied. This can be obtained by integrating the displacement power spectrum of the thermal noise at all frequencies,

$$\langle x^2 \rangle_{\rm th} = \int_{-\infty}^{\infty} \frac{S^{(2)}_{\rm f,th}(\omega)}{|m(\omega_{\rm m}^2 - \omega^2 + i\gamma_{\rm m}\omega)|^2}, \tag{3.42}$$

where $S^{(2)}_{\rm f,th}(\omega) = 2k_{\rm B}T_{\rm th}m\gamma_{\rm m}(\omega)$ is the double-sided power spectrum in the force of the thermal noise. Substituting Eq. (3.41) in Eq. (3.38), the thermal phonon number is given by

$$n_{\rm th} \simeq \frac{k_{\rm B}T_{\rm th}}{\hbar\omega_{\rm m}}, \tag{3.43}$$

where the energy scale of the thermal bath is much larger than that of the quantum of the mode, $k_{\rm B}T_{\rm th} \gg \hbar\omega_{\rm m}$.

For example, in the case of a suspended mirror at room temperature ($\omega_{\rm m}/2\pi = 1$ Hz, $T_{\rm th} = 300$ K), the thermal phonon is $n_{\rm th} \sim 6 \times 10^{12}$, so we need the cooling by 12 orders of magnitude to the ground state. If we prepare the high-frequency resonator such as $\omega_{\rm m}/2\pi = 10$ MHz at cryogenic temperature $T_{\rm th} = 100$ mK, the phonon is $n_{\rm th} \sim 200$. Therefore, the required cooling factor is reduced to around 2 orders.

fQ condition

In optomechanics, the parameter of the frequency times the Q-value of the mechanical mode is important for the ground state cooling. It is not until the mechanical mode satisfies so called *fQ* condition described as below that the ground state cooling is meaningful.

When the mechanical damping rate of the susceptibility increases from $\gamma_{\rm m}$ to $\gamma_{\rm eff}$ with some method, the effective temperature of the mode is reduced to

$$T_{\rm eff} = \frac{\gamma_{\rm m}}{\gamma_{\rm eff}} T_{\rm th}, \tag{3.44}$$

and the thermal phonon number is also reduced by this factor. The effective temperature can be decreased by increasing the effective damping rate, but it must be smaller than the resonant frequency to keep the coherent oscillation during its one period, $\gamma_{\rm eff} < \omega_{\rm m}$. Under this condition, the thermal phonon

number has the lower limit of [88]

$$\begin{aligned} n_{\mathrm{th}} &= \frac{k_{\mathrm{B}} T_{\mathrm{eff}}}{\hbar \omega_{\mathrm{m}}} \\ &> \frac{k_{\mathrm{B}} T_{\mathrm{th}}}{\hbar \omega_{\mathrm{m}}} \frac{\gamma_{\mathrm{m}}}{\omega_{\mathrm{m}}} = \frac{k_{\mathrm{B}} T_{\mathrm{th}}}{\hbar \omega_{\mathrm{m}} Q_{\mathrm{m}}}. \end{aligned} \tag{3.45}$$

Thus, the condition that n_{th} can be lower than 1 with keeping one coherent amplitude is given by

$$f_{\mathrm{m}} Q_{\mathrm{m}} > 6 \times 10^{12} \left(\frac{T_{\mathrm{th}}}{300\,\mathrm{K}} \right). \tag{3.46}$$

This is called the fQ condition.

It can be derived from a perspective of decoherence rate of the mechanical quantum coherence. Here we consider the interaction between the mechanical oscillator and the thermal bath. Time evolution of the phonon number can be written as

$$\dot{n}_{\mathrm{pn}}(t) = -\gamma_{\mathrm{m}}(n_{\mathrm{pn}} - n_{\mathrm{th}}). \tag{3.47}$$

Assuming that the oscillator is in the quantum ground state at $t = 0$, $\dot{n}_{\mathrm{pn}}(t = 0) = \gamma_{\mathrm{m}} n_{\mathrm{th}}$ is satisfied. The phonon number increased after one period is given by

$$n_{+} = \frac{\dot{n}_{\mathrm{pn}}(t = 0)}{\omega_{\mathrm{m}}} = \frac{n_{\mathrm{th}}}{Q_m}, \tag{3.48}$$

which must be below one in order to keep the ground state during the one period. In other words, the period number until the phonon number is over one should be above one,

$$n_{\mathrm{osc}} = \frac{1}{n_{+}} > 1. \tag{3.49}$$

We can observe the coherent oscillation at the quantum ground state at least one time in this condition without being prevented by the thermal decoherence. This condition can be described as

$$f_{\mathrm{m}} Q_{\mathrm{m}} \frac{h}{k_{\mathrm{B}} T_{\mathrm{th}}} > 1, \tag{3.50}$$

which is equivalent to the fQ condition.

At room temperature $fQ > 6 \times 10^{12}$ is necessary and it is difficult to realize with the usual pendulum like a suspended mirror. Nevertheless, the optical spring enables the pendulum to satisfy the fQ condition. With the optical spring constant in Eq. (3.29), the effective resonant frequency of the mode is given by

$$\omega_{\rm eff}^2 = \omega_{\rm m}^2 + \frac{K_{\rm opt}}{m}. \tag{3.51}$$

When the resonant frequency increases, not only the energy of the one phonon increases but also the effective temperature can be dramatically decreased. The condition for the coherent oscillation is changed to $\gamma_{\rm eff} < \omega_{\rm eff}$. The damping model of the pendulum is structural, and hence the original mechanical damping rate also decreases because of the dependence of $1/f$ in Eq. (2.75),

$$\gamma_{\rm m}(\omega_{\rm eff}) = \frac{\omega_{\rm m}^2}{Q_{\rm m}\omega_{\rm eff}}. \tag{3.52}$$

Therefore, the mitigated fQ condition is given by

$$f_{\rm m}Q_{\rm m} > 6 \times 10^{12} \left(\frac{T_{\rm th}}{300\,{\rm K}}\right) \left(\frac{\omega_{\rm m}}{\omega_{\rm eff}}\right)^3. \tag{3.53}$$

The usual pendulum can satisfy the condition if the resonant frequency increases from $\omega_{\rm m}/2\pi = 2$ Hz to $\omega_{\rm eff}/2\pi = 400$ Hz and the mechanical Q-value is $Q_{\rm m} = 1 \times 10^6$ at room temperature. With the feasible parameter, even the suspended mirror can be cooled to the ground state in terms of the thermal phonon.

Fig. 3.6 shows the cooling with the increased resonant frequency in both cases of viscous and structure damping. The shaded areas equivalent to their thermal phonon number are dramatically reduced. The fQ conditions are mitigated by factors of $(\omega_{\rm m}/\omega_{\rm eff})^2$ and $(\omega_{\rm m}/\omega_{\rm eff})^3$ when thermal noise of the oscillator is viscous and structural respectively. In the case of the viscous damping, the mitigated fQ condition is not satisfied yet. On the other hand, the structure damping satisfies the requirement. There is a possibility of the ground state cooling only in the structure damping. It can be explained by the fact that only structural thermal noise beats the free mass SQL at the resonant frequency.

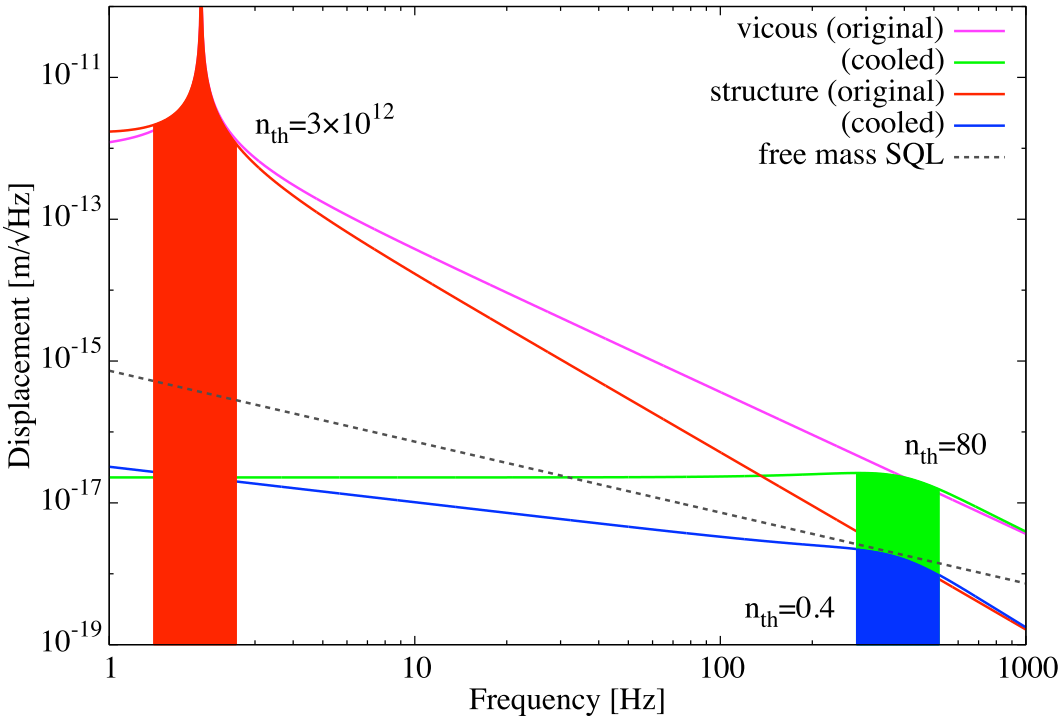

Figure 3.6: Cooling of the mechanical oscillator with the increased resonant frequency. The original Q-value, mass, original and increased resonant frequency are $Q_{\rm m} = 10^6$, $m = 10\,{\rm mg}$, $\omega_{\rm m}/2\pi = 2\,{\rm Hz}$ and $\omega_{\rm eff}/2\pi = 400\,{\rm Hz}$. The magenta and red lines show the original thermal noises of the oscillator following the viscous and structure damping. The green and blue lines show the thermal noises in each case with the increased resonant frequency. We can get the thermal phonon number experimentally by calculating the shaded area.

Radiation pressure phonon

Next, the radiation pressure phonon is discussed. The phonon is increased by the displacement due to the quantum radiation pressure fluctuation. With the integration of the displacement, we can get the phonon number driven by the quantum radiation pressure fluctuation.

Without the slow varying approximation, the optical damping $\Gamma_{\rm opt} = m\gamma_{\rm opt}$

is decided by

$$\begin{aligned}\Gamma_{\rm opt} &= {\rm Im}\left[\frac{K(\omega)}{\omega}\right]_{\omega=\omega_{\rm eff}} \\ &= -2\hbar g^2|\bar{a}|^2\frac{2\kappa\Delta}{[\kappa^2+(\omega_{\rm eff}-\Delta)^2][\kappa^2+(\omega_{\rm eff}+\Delta)^2]},\end{aligned} \tag{3.54}$$

with Eq. (3.28). Here it is assumed that the total damping rate of the system is determined by the optical damping rate and the sign is positive ($\Delta < 0$). The mean square of the displacement can be described as

$$\langle x^2\rangle_{\rm rp} = \int_{-\infty}^{\infty}\frac{S^{(2)}_{\rm f,qrp}(\omega)}{\left|m(\omega_{\rm eff}^2-\omega^2+i\gamma_{\rm opt}\omega)\right|^2}, \tag{3.55}$$

where $S^{(2)}_{\rm f,qrp}(\omega) = 2\hbar^2g^2\kappa|\bar{a}|^2|\chi_{\rm c}(\omega)|^2$ in Eq. (3.34) is the double-sided power spectrum in the force of the quantum radiation pressure fluctuation. Then, the phonon number of the fluctuation is calculated as [89]

$$n_{\rm rp} = -\frac{1+(\delta+\omega_{\rm eff}/\kappa)^2}{4\delta\omega_{\rm eff}/\kappa}. \tag{3.56}$$

The minimum value of the $n_{\rm rp}$ is given by

$$n_{\rm rp} \geq \left(\frac{\kappa}{2\omega_{\rm eff}}\right)^2\frac{2}{1+\sqrt{1+(\kappa/\omega_{\rm eff})^2}}, \tag{3.57}$$

for the normalized detuning of $\delta = -\sqrt{1+(\omega_{\rm eff}/\kappa)^2}$. The magnitude correlation between the effective resonant frequency and the cavity line width is important for the phonon number of the radiation pressure.

3.3.2 Sideband and feedback cooling

In the previous section we introduce the phonon number caused by the thermal noise and the radiation pressure fluctuation. From a viewpoint of the thermal phonon, it is necessary only to prepare the mechanical oscillator and the mode which satisfies the fQ condition and to give the large damping rate by any method. On the other hand, the effective method to reduce the radiation

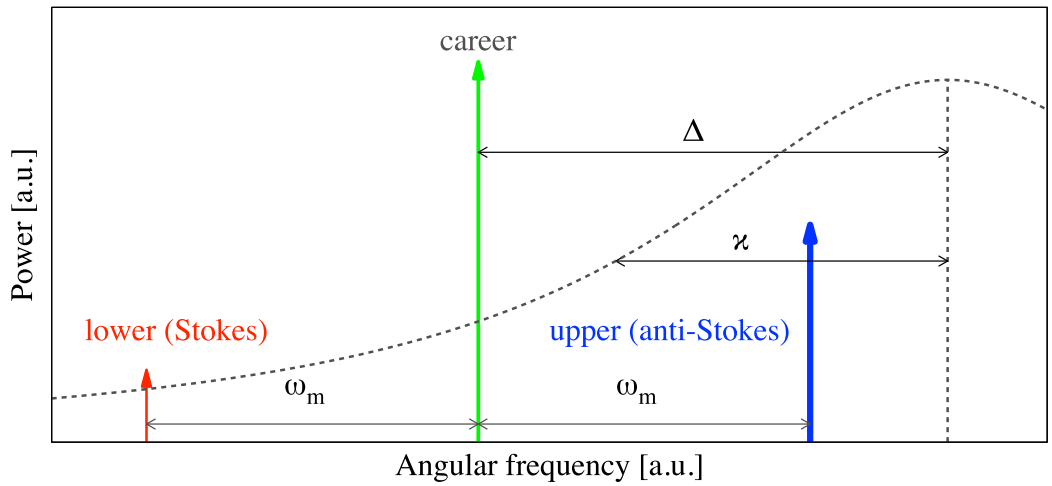

Figure 3.7: Configuration of the sideband cooling. The green, red, and blue arrows show the career, lower sideband (Stokes), and upper sideband of the light, respectively. The detuning is negative and the amplitude is optimized $\Delta = -\sqrt{2}\kappa$, and the resonant frequency is equal to the line width $\omega_{\rm m} = \kappa$. In this stuation the power of the upper sideband subtracted by that of the lower sideband is maximum.

pressure phonon differs depending on which is larger the mechanical resonant frequency and the cavity line width. Two cooling methods are introduced in this subsection [23]. One is a sideband cooling which is valid in the case of the resonant frequency is larger than the cavity line width [28–30]. The other is a feedback cooling which is valid in vice versa [90, 92].

Sideband cooling in good cavity

Sideband cooling is a passive cooling using the detuned laser light. With Eq. (3.57), we can realize $n_{\rm rp} < 1$ only with the laser light if $\omega_{\rm m} \gtrsim \kappa$ is satisfied. Moreover, the radiation pressure phonon can be suppressed close to zero in $\omega_{\rm m} \gg \kappa$. This condition is called *good cavity* limit.

The real part (restoring) and imaginary part (damping) of the optical spring constant in Eq. (3.28) has the opposite sign. Thus, the positive restoring force and the positive damping are not compatible. However, mechanical oscillators with the resonant frequency of MHz region is so stiff that their restoring force keeps positive even in the positive damping ($\Delta < 0$). When the input power

increases with the negative detuning, the damping rate also increases and the oscillation peak is suppressed.

The situation can be described with a sideband picture of the cavity and laser light. The upper and lower sidebands of the career are generated by the mechanical resonance. The upper sideband absorbs the energy of the oscillation (anti-Stokes for a Raman process) and the lower sideband gives the energy (Stokes). In the good cavity condition, these sidebands are enough far to affect the optomechanical system differently. As shown in Fig. 3.7, the upper sideband is close to the resonance of the cavity and the lower one is far. Therefore, the anti-Stokes effect is dominant and the mechanical energy is absorbed, in other words, the mode is cooled.

Feedback cooling in bad cavity

In contrast, when the cavity line width is larger than the resonant frequency $\kappa \gtrsim \omega_{\rm eff}$, the radiaton pressure phonon is

$$n_{\rm rp} \gtrsim \frac{\kappa}{2\omega_{\rm eff}}. \tag{3.58}$$

This means that the phonon cannot be suppressed below 1 only with the laser light. The condition is called *bad cavity* limit.

The small cooling performance is because the two sidebands are too close to cause the different effect to the cavity. In this case, however, a feedback cooling can be used. In the feedback cooling, the mechanical motion is measured, filters give the appropriate amplitude and phase to the error signal and generate the feedback signal, and that is sent to the actuator related to the optomechanical system. A schematic picture is shown in Fig. 3.8. An example of the filter is a high-pass filter. The signal proportional to the velocity can be made from the displacement signal with the high-pass filter. The limit of the feedback cooling is determined by the sensing noise for the displacement signal.

In both cases of the good and bad cavity, the total phonon number below 1 can be realized with the sideband and feedback cooling, including the thermal phonon and radiation pressure phonon. The cooling limit in each case is calculated to be almost the same level in the previous work [23].

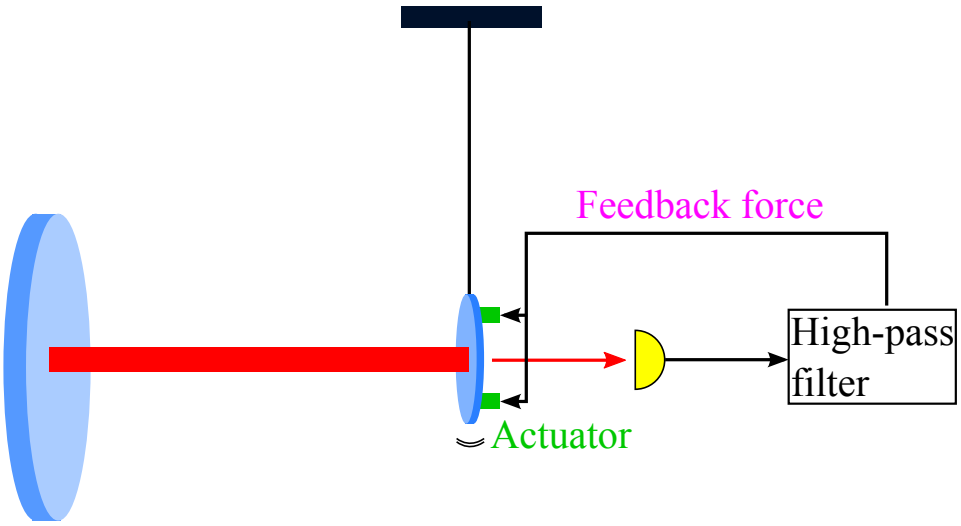

Figure 3.8: A schematic picture of the feedback cooling. The displacement of the oscillator is measured with the PD. The signal enters in the filter, which is assumed high-pass filter here, and the signal is changed to be proportional to the velocity of the oscillator. Then, the feedback force is generated and added via a some actuator.

3.4 Previous works

Theories on optomechanics are described until the last section. Here we introduce previous woks, especially about the experimental optomechanics and the current status. The cooling level is evaluated by the phonon number $n_{\rm pn}$ or the effective temperature $T_{\rm eff}$. Their relation is given by

$$n_{\rm pn} = \frac{k_{\rm B} T_{\rm eff}}{\hbar \omega_{\rm eff}}. \tag{3.59}$$

3.4.1 Ground state cooling and beyond

One of the goals of optomechanics is generating macroscopic superposition states. Mechanical oscillators are enough massive to test it because such states have been realized only at the molecular scale. Towards the ground state cooling from a viewpoint of the fQ condition and the good cavity, high resonant frequency is favorable. Therefore, the optomechanical devices with the fg-ng scale resonator have been searched well.

Radiation pressure fluctuation measurement

The research of optomechanics is aimed at the ground state cooling of the mechanical mode, and in terms of that the quantum radiation pressure fluctuation is the noise. On the other hand, its measurement is regarded as one of the benchmarks because it can show that the other classical noises are below the quantum fluctuation of the laser light. We introduce two previous works emphasizing observation of quantum radiation pressure fluctuation with a mechanical oscillator.

Purdy *et al.* [26] reported observation on a 7-ng membrane in 2013. Their membrane is a square plane with 40-nm thickness, 0.5-mm side length, and has a mechanical resonant frequency of 1.55 MHz. It is located in an optical cavity whose line width is 0.89 MHz (a good cavity) at the base temperature of 4.9 K. Two laser lights are entered into the cavity, the signal beam and the meter beam. The signal beam around on the cavity resonance drives the mechanical motion by its quantum radiation pressure fluctuation. The meter beam is for the sideband cooling and the displacement sensing of the position of the membrane. They observed the fluctuation at the signal to noise ratio over 1 and measured the $\sqrt{P}$ dependence of the displacement spectrum on the input power. The correlation measurement of the amplitude and phase of two beams was also done.

Another experiment is referred in the GW detector's chapter, demonstrated by Cripe *et al.* The 55-ng cantilever is used for broadband observation of the radiation pressure fluctuation. The cavity line width is 500 kHz and the mechanical resonant frequency is originally 876 Hz and increased up to 100 kHz due to the positive restoring force of the optical spring, so it is a bad cavity. The detuning is heating side, in other words having the negative damping effect, but the cavity length is controlled by feedback. Even though the radiation pressure fluctuation is observed only at the mechanical resonance in the other experiments, they realized the broadband measurement.

Ground state cooling

Some mechanical oscillators were already cooled to its quantum ground state. In 2011, Teufel *et al.* [28] reported the ground state cooling of a microme-

chanical resonator. The oscillator is 100-nm-thick aluminum membrane with a diameter of 15 μm, and the mass is 48 pg. The cavity line width is around 200 kHz and the mechanical resonant frequency is 10.56 MHz, so the good cavity level is extremely high. They operated the experiment at the cryogenic temperature of 20 mK and achieved the sideband cooling down to the phonon number of 0.34.

Also in 2011, Chan *et al.* [29] demonstrated the ground state cooling of a nanomechanical oscillator. The oscillator is a patterned silicon nanobeam at μm scale, whose mass is 311 fg. The mechanical resonant frequency and the cavity line width are 3.68 GHz and 500 MHz respectively. The temperature of the system is 20 K. They made use of the sideband cooling in the good cavity condition and reached the phonon number of 0.85.

In 2016, the Purdy group demonstrated not only the ground state cooling of the membrane but also reached the backaction limit in the paper of Peterson *et al* [30]. The backaction limit comes from the radiation pressure phonon n_{rp} in Eq. (3.57). They suppressed thermal phonon number enough, adjusted the optimal detuning of the cavity, and finally reached the radiation pressure phonon number of 0.20.

Squeezing

Above three groups also demonstrated the squeezing of the laser light with their mechanical oscillators. The quantum fluctuation is the noise for observing the zero-point fluctuation. Therefore, the squeezing to reduce the quantum noise is effective.

In 2016, the Teufel group reported the improvement of the displacement sensitivity of the resonator with injection of the squeezed light in the paper of Clark *et al* [93]. They succeeded in observing the 3 dB reduction of the quantum noise with amplitude squeezing light under the radiation pressure dominant regime. They also measured the quantum radiation pressure fluctuation at the high signal to noise ratio, and realized the quantum non-demolition measurement by 13 dB with upper and lower sidebands of two lights.

In 2013, the Chan group demonstrated the ponderomotive squeezing of 0.4 dB with the homodyne detection in the paper of Safavi-Naeini *et al* [92].

The measurement bandwidth is a few MHz around the mechanical resonant frequency of 28 MHz.

Purdy *et al.* [94] also demonstrated the ponderomotive squeezing of 1.7 dB using their membrane in 2013. The realization is due to the strong radiation pressure fluctuation overwhelming the thermal noise.

Entanglement

After cooling the resonator to the quantum ground state, the next goal is generating entangled states of the mechanical mode. Even the entangled state of mechanical oscillators have been reported recently.

Mechanical resonators whose entangled states are demonstrated are as follows: the pg-scale membrane of Teufel group by Palomaki *et al.* [31] in 2013, the sub-pg-scale nano beam by Riedinger *et al.* [32] in 2018, and a pg-scale drum-type oscillator similar to the Teufel group's one by Ockeloen-Korppi *et al.* [33] also in 2018.

3.4.2 Massive scale above microgram

As shown in the previous subsection, recent progress of optomechanics is drastic especially with the mass scale below ng. On the other hand, however, demonstration in massive regime above μg scale is still challenging. It is because isolating the mechanics from the thermal bath and interacting strongly with laser light are difficult in such heavy scale.

Neuhaus *et al.* tried the ground state cooling of a mm-scale micropillar. The mass was 34 μg, which is much heavier than resonators cooled to the ground state ever. The mechanical resonant frequency was 3.58 MHz and the cavity line width was 16.3 MHz, so the cavity was bad cavity, but they used the sideband cooling whose backaction limit was $n_{\mathrm{rp}} = 2.4$. This large line width came from the short cavity length of 58 μm. The shortness was in order to narrow the beam waist on the mirror and avoid clipping loss. The mechanical Q-value was 7×10^7, satisfying the fQ condition. The achieved lowest phonon number was 20. It was limited by the heating of the pillar through absorbed laser light. The effective temperature was originally 50 mK at the base increasing up to 4 K at the maximum laser input.

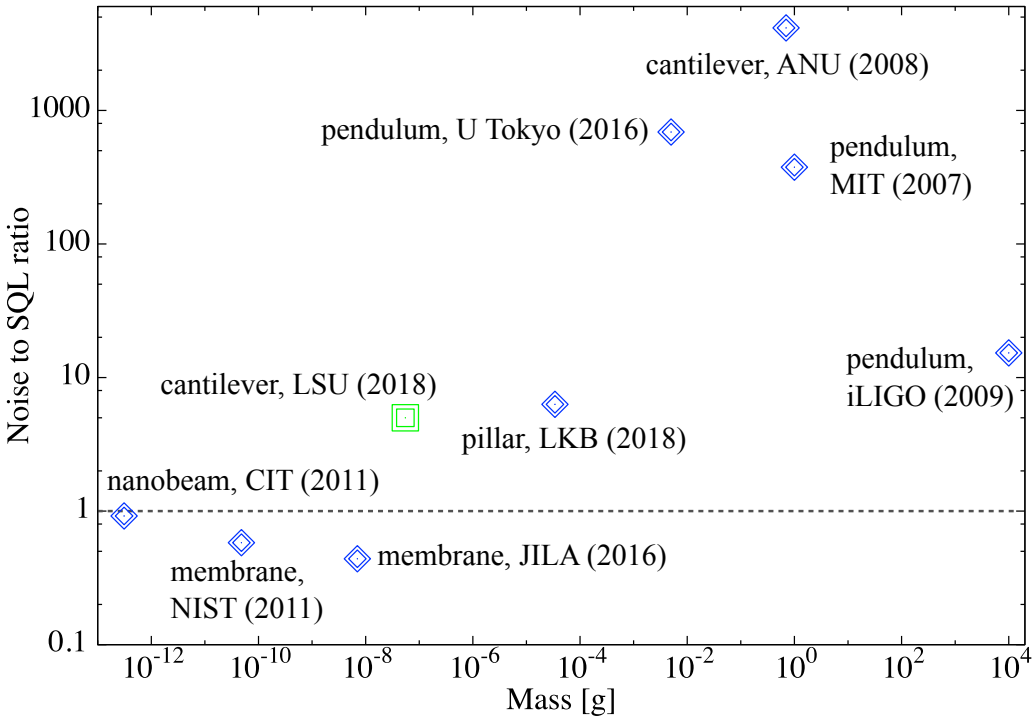

Figure 3.9: The noise to SQL ratio of previous works. We represent the results of cooling experiments (the nanobeam by Chan *et al.* from CIT [29], the membrane by Teufel *et al.* from NIST [28] and by Peterson *et al* from JILA [30], the pillar by Neuhaus *et al.* from LKB, the pendulum by Coribitt *et al.* from MIT [98] and by Matsumoto *et al.* from U Tokyo [95], the cantilever by Mow-Lowry *et al*from ANU [96], and the iLIGO test mass [99]) as blue rhomboids, and works for radiation pressure measurement (the cantilever by Cripe *et al.* from LSU [71]) as a green square.

Above mg-scale, oscillators which is used to observe the quantum radiation pressure noise from a viewpoint of the GW detector has been also demonstrated in the context of the cooling. In mg-scale, Matsumoto and Komori *et al.* [95] were cooling the pendulum mode of the 5-mg suspended mirror. A pendulum had the low resonant frequency such as 1 Hz, but it could be increased with the optical spring. We generated the optical spring increasing the resonant frequency from 2.14 Hz to 660 Hz and combined the feedback cooling. The effective temperature of the mode decreased down to 15 mK ($n_{\rm pn} = 4.7 \times 10^5$). The limiting factor was the frequency noise of the laser light.

The 1-g cantilever was cooled by Mow-Lowry *et al* [96]. They also made use of the feedback cooling and realized the effective temperature of 70 mK ($n_{\mathrm{pn}} = 1.7 \times 10^7$) without any excess noise at off resonance frequency. The thermal noise limited the cooling ability. Coribitt *et al.* performed the cooling of the 1-g suspended mirror with two methods. One was a double optical spring. They injected two laser light detuned differently and realized the positive restoring force and damping [97]. The other was the feedback cooling with an optical spring [98]. The achieved effective temperature is 0.8 K and 6.9 mK ($n_{\mathrm{pn}} = 1.4 \times 10^5$) respectively, both of which were limited by the frequency noise of the laser light.

Finally, even a kg-scale oscillator was demonstrated as the optomechanical cooling [99]. In the first generation of LIGO, the test mass of 10 kg was cooled to the effective temperature of 1.4 μK ($n_{\mathrm{pn}} = 230$) with the feedback cooling at the increased resonant frequency of 133 Hz. The sensitivity was limited by the shot noise around the resonant frequency, but it could reach the ground state if the sensitivity would be improved to the SQL at the frequency.

The noise to SQL ratio of representative previous works is summarized in Fig. 3.9. It is equal to $\sqrt{n_{\mathrm{pn}}}$ for the cooling experiments. Below ng scale, zero point fluctuation of some oscillators was observed and the quantum behaviors were tested on various ways as shown above. Those on μg and kg scales reached close to their quantum limits. However, mg- and g-scale oscillators are still far from the SQL.

3.5 Summary of this chapter

The interaction between the mechanical oscillation and the radiation pressure of the laser light can be described in optomechanics. Using the optomechanical effect, we can cool the oscillator to its quantum ground state and search for macroscopic quantum mechanics. It is important to test quantum behavior with oscillators on various mass scales. One of the necessary conditions for the ground state cooling is observing quantum radiation pressure fluctuation acting on the test mass. Compared with light mass scales between fg and μg, mg- and g-scale oscillators is far from their quantum limit.

Chapter 4

Experimental setup

It is important to observe quantum radiation pressure fluctuation around the frequency band of the GW detectors, especially between 10 Hz to 100 Hz with a suspended mirror in terms of more detection of the GW and the optomechanics on various mass scales. System of a torsion pendulum having two optical cavities on both edges is devised in order to observe that. In this chapter we describe the experimental setup to realize the observation.

In Section 4.1, the concept of our torsion pendulum and the advantages are shown with the design sensitivity of our experiment. Next, in Section 4.2, we discuss the main system including the cavities and the torsion pendulum. Moreover, we describe the associated system such as frequency and intensity stabilization of the laser light for realizing observation of quantum radiation pressure fluctuation in Section 4.3.

4.1 Concept and design

our goal is observing quantum radiation pressure fluctuation with a torsion pendulum. The target frequency band is between 10 Hz to 100 Hz where the sensitivities of actual GW detectors are limited by the quantum radiation pressure noise. In order to achieve the observation, a torsion pendulum is used. The advantages of the torsion pendulum are described in this section.

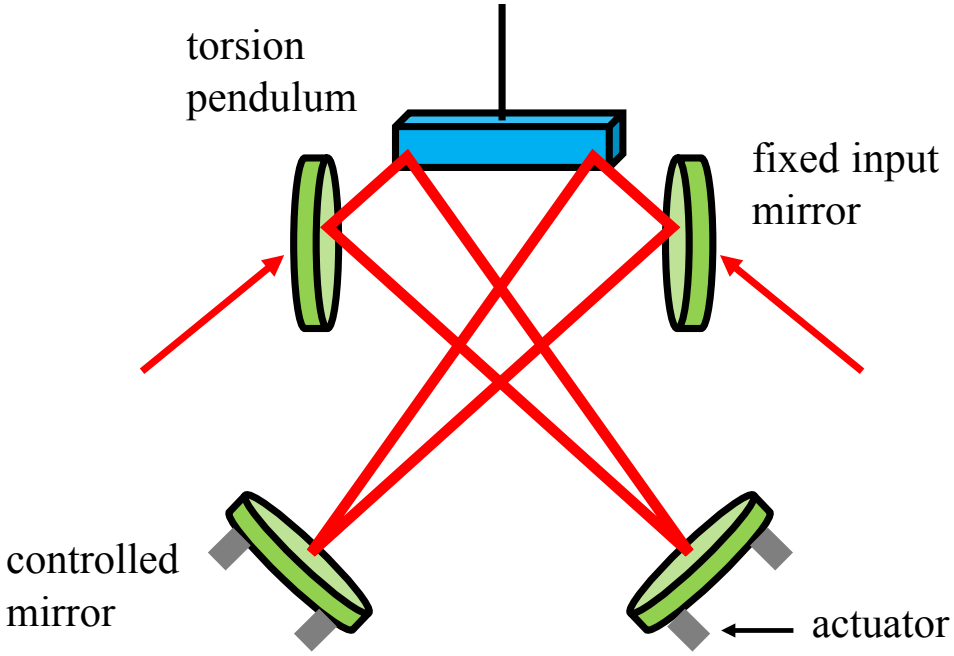

Figure 4.1: A schematic picture of two cavities with a torsion pendulum. The blue rectangular solid is the torsion pendulum as a test mass. The input mirrors are close to the torsion pendulum, whose incident angle is around 45°. Actuators are attached to the controlled mirrors. In our case the actuator consists of coil-magnets

4.1.1 A torsion pendulum consisting of cavities

One of the most fundamental issues for measuring quantum radiation pressure fluctuation is thermal noise related to the system, especially the suspension thermal noise of the targeting mechanical mode. In order to overwhelm the thermal noise, it is advantageous to use as light a mirror as possible because the mechanical susceptibility gets larger.

In our group a mg-scale suspended mirror (5 mg) is developed in optomechanical experiments [20, 95]. The mirror size is a mm scale (4 mm diameter). That is the smallest of mirrors which can be treated by hand. It is technically difficult to make such a small mirror with a negative curvature, so it must be flat and cannot avoid the Sidles–Sigg instability in a linear cavity [16]. In order to head off the instability, we use a triangular cavity. The negative spring constant in the rotational mode of the tiny mirror gets positive with the triangular

cavity because there is one more sign flip at the reflection [100].

In the previous experiment with the 5-mg suspended mirror, the quantum radiation pressure fluctuation was estimated to be larger than the suspension thermal noise above several 100 Hz. It was because we succeeded in realizing high intra-cavity power of 7 W with the triangular cavity and the suspension with an ultra thin wire of 3 μm diameter. The thin wire contributed to the low suspension thermal noise with the gravitational dilution [48]. However, the suspension thermal noise was larger than radiation pressure fluctuation between 10 Hz to 100 Hz, and the frequency and classical radiation pressure noise of the laser light were dominant noise sources. We need to reduce those noises.

Then, we come up with the idea of two cavities consisting of a torsion pendulum. Fig. 4.1 shows a schematic picture of the setup. The torsion pendulum is widely used to do precise measurement with its high susceptibility due to the low resonant frequency of the rotational mode. Each cavity contains three mirrors to keep the optomechanical stability of the rotational mode like the previous triangular cavity. The input mirrors are fixed and the end mirrors have actuators to control the cavity length. Here we describe how those noises can be suppressed .

Low suspension thermal noise

Here the suspension thermal noise is shown again in Eq. (2.76),

$$S_{\mathrm{x,sust}} = \frac{4k_{\mathrm{B}}T_{\mathrm{th}}\omega_{\mathrm{m}}^2\phi_{\mathrm{m}}}{m\omega^5}, \tag{4.1}$$

where ω_{m} is the angular resonant frequency and ϕ_{m} is the loss angle of the mechanical mode. Typically reducing the loss angle (increasing the Q-value) is aimed to suppress the thermal noise. The dependence on the loss angle is linear to the power spectrum of the thermal noise. In contrast, the spectrum is proportional to the square of the resonant frequency.

In the tabletop-scale experiments, the resonant frequency and the Q-value of the pendulum mode are several Hz and the order of 10^5 at the most respectively. On the other hand, the Q-value of the torsion pendulum is the order of 10^3, but the resonant frequency can be easily below 0.1 Hz. Therefore

decreasing the resonant frequency is better even at the cost of the loss angle.

Common mode rejection

One of the other issues is the frequency and intensity noise of laser light. These are not fundamental noises but must be reduced to observe the quantum radiation pressure fluctuation.

When one cavity on one edge of the bar mirror is controlled to be on resonance, the DC radiation pressure pushes and rotates the bar-shaped mirror, resulting in the breakdown of the cavity resonance. Therefore, two cavities are necessary on both edges of the bar. In order to sense the rotational mode of the torsion pendulum, we have to subtract the signal of two cavities. The subtraction has the other advantages. The classical noise such as the frequency and intensity noise of the laser light, and vibration noise of the usual pendulum mode can be subtracted at the same time. In principle, all common noises can be evaded and we get only the independent or differential fluctuation.

This common mode rejection ratio is estimated to be above 10, so it can be expected to subtract the frequency and intensity noise by a factor of 10. Here we also assume the ratio of 10 on the translational noises such as the vertical thermal noise and the pendulum thermal noise.

Light effective mass

The rotational mode of the torsion pendulum has lighter effective mass than that of the usual pendulum mode. This fact enhances the sensitivity for tiny force with the higher susceptibility. Here we show what is the enhancement factor.

Assuming that the random force of F [N/$\sqrt{\text{Hz}}$] is added to the center of the usual pendulum whose mass is m, the displacement spectrum can be written as

$$x_{\text{pend}}(\omega) = \frac{F}{m\omega^2}\,[\text{m}/\sqrt{\text{Hz}}]. \tag{4.2}$$

In contrast, the situation is different when the same random forces are added to both edges of a rigid body whose length is L. The differential component of force is $F/\sqrt{2}$ [N/$\sqrt{\text{Hz}}$], so the torque fluctuation is $FL/\sqrt{2}$ [N·m/$\sqrt{\text{Hz}}$] and the rotation spectrum can be given by $FL/(\sqrt{2}I\omega^2)$, where $I = \alpha m L^2$

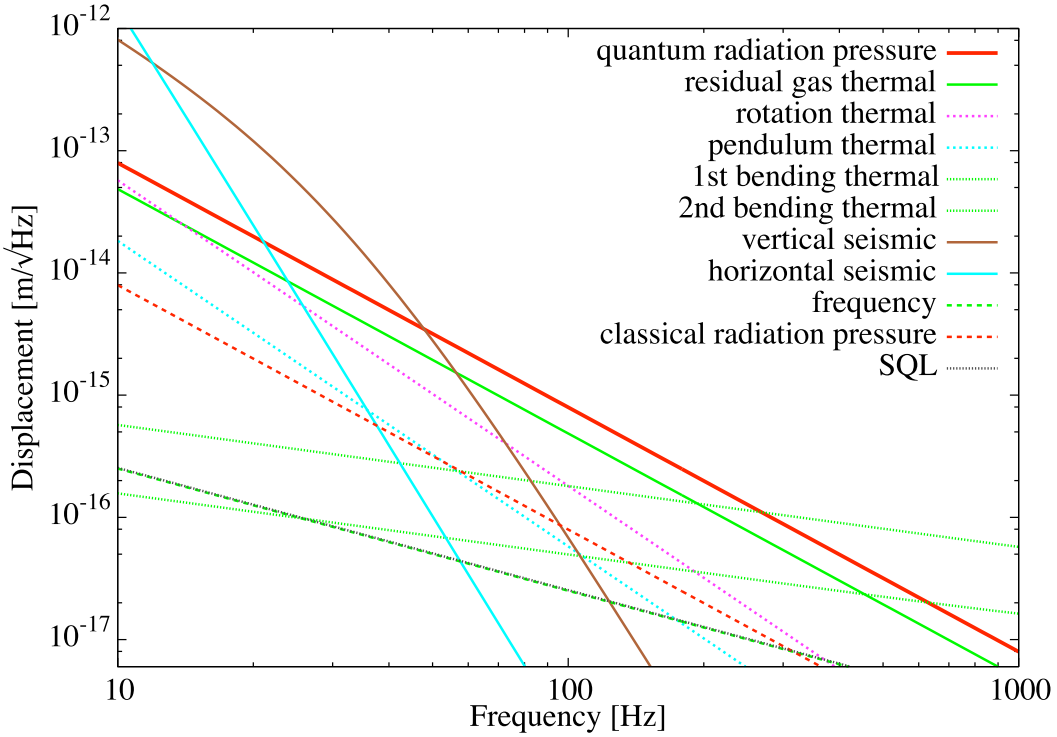

Figure 4.2: Design sensitivity of our setup. The red solid line represents the target quantum radiation pressure fluctuation.

is the moment of inertia and α differs depending on the shape of the object. Therefore, the differential displacement spectrum is written as

$$\begin{aligned} x_{\rm rot}(\omega) &= \frac{FL}{\sqrt{2}I\omega^2} \times L \\ &= \frac{1}{\sqrt{2}\alpha}\frac{F}{m\omega^2}\,[\mathrm{m}/\sqrt{\mathrm{Hz}}]. \end{aligned} \tag{4.3}$$

In the experiments the rotation is sensed as the differential displacement signal. Thus, the effective mass of the rotational mode is lighter by a factor of $\sqrt{2}\alpha$ than that of the usual pendulum mode. This high sensitivity is tolerant of the sensing noise including the vibration noise to the pendulum. In the case of the simple bar, $\alpha = 1/12$, so the enhancement factor is $6\sqrt{2}$.

Property	Requirement
Rotational Q-value	$Q_{\mathrm{rot}} > 2 \times 10^3$
Pendulum Q-value	$Q_{\mathrm{pend}} > 5 \times 10^4$
Vertical transfer function	$0.01 \left(\frac{100\,\mathrm{Hz}}{f}\right)^2$
Frequency noise [Hz/$\sqrt{\mathrm{Hz}}$]	$1 \left(\frac{100\,\mathrm{Hz}}{f}\right)$
Relative shot noise level	$B_{\mathrm{rsnl}} < 6$
Pressure [Pa]	$\sim 3 \times 10^{-4}$

Table 4.1: Requirement of the experimental parameters.

4.1.2 Design sensitivity

We aim at observing quantum radiation pressure fluctuation acting on the bar-shaped mirror with these advantages. The design sensitivity is shown in Fig. 4.2. It is difficult to isolate the test mass from the vertical seismic noise on table-top scale experiments, so our target sensitivity is set to be 50-100 Hz. In this band, the signal to noise ratio is more than 1.

Requirement of experimental parameters is set in order to realize this sensitivity and not to cover the radiation pressure. It is summarized in Table 4.1. The vertical transfer function means the transfer function from the vertical seismic noise to displacement of the test mass. Details of noises in Fig. 4.2 and the measured results of parameters in Table 4.1 are described in the following subsections: the thermal noises and Q-values in Subsection 4.2.1, the seismic noises and transfer function in Subsection 4.2.3, the frequency noise in Subsection 4.3.2, the intensity noise in Subsection 4.3.3, and the vacuum system in Subsection 4.3.5.

4.1.3 Whole setup

In this subsection, the whole setup to observe quantum radiation pressure fluctuation is shown. Fig. 4.3 shows the conceptual design of the experimental setup. The set up can be separated to 4 parts, the input optics, the stabilization and alignment, the main cavities, and the auxiliary optics.

In the input optics, we give phase and amplitude modulation to the Nd:YAG laser light whose wave length is 1064 nm, which is followed by the frequency

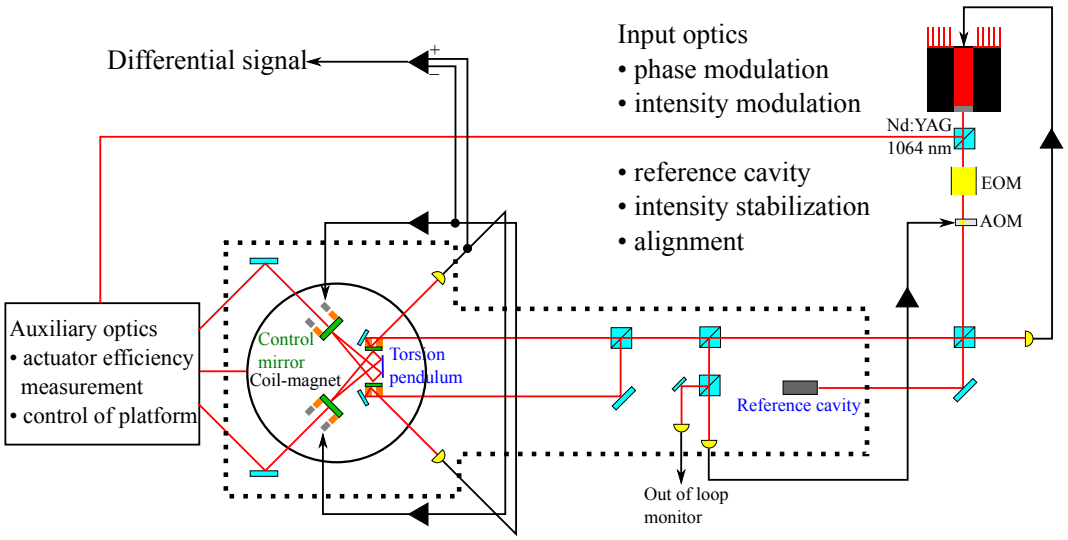

Figure 4.3: A conceptual design of the whole experimental setup. The paths of the laser light and the electrical signal are described as red and black solid lines respectively. Black triangles show each filter circuit. Black dotted line shows the area in vacuum.

and intensity stabilization of the laser light. The frequency is stabilized by the rigid reference cavity and feedback to the laser system. With picking off the laser light toward the main cavities, the intensity signal is used for the intensity stabilization with the AOM. After the adjustment of the beam path, the light enters the main cavities. The reflection is measured and used as the feedback signal to the coil-magnet actuator on the controlled mirror. We get the rotation fluctuation by subtraction of the two error signals of the cavity length. Quantum radiation pressure fluctuation can be observed by analyzing them. Using the auxiliary system, we measure the actuator efficiency and control a platform of the main cavities.

4.2 Main setup

The main setup is described in this section. After focusing on the test mass of the torsion pendulum, schematic pictures of the main cavities system such as double pendula for the bar mirror and the controlled mirror.

Figure 4.4: Shapes of the bending modes of the bar mirror whose length is 15 mm. The left (right) shows the first (second) bending mode. These are results from the finite element analysis by COMSOL. The red area means that the amplitude of the oscillation is large, and the blue area shows the node.

4.2.1 A torsion pendulum

Our test mass is a bar-shaped mirror used as a torsion pendulum to observe quantum radiation pressure fluctuation. The mass of the bar mirror should be as light as possible to enhance the radiation pressure. In order to reduce the suspension thermal noise of the rotational mode, the test mass has to be suspended by the ultra thin wire. The bar is fixed to the wire with ultraviolet curing resin.

Substrate

Sigma-koki company produced the thin bar-shaped mirror. The substrate is made of fused silica. One side of the mirror has a high reflective coating.

A longer bar mirror has higher signal to noise ratio between the radiation pressure fluctuation and the suspension thermal noise. A thinner and lower one is lighter, so it has higher susceptibility. However, the thermal noise of the bending mode of the bar can be an issue because the resonant frequency of the bending mode is low in the case of too long bar. Also, it is technically difficult to handle the very thin and long mirror. Moreover, it cannot be too low because the low height results in the larger clipping of the beam and the low finesse of the cavity.

The following aspects are selected: the length is 15 mm, the height is 1.5 mm, and the thickness is 0.2 mm. The resulting mass is 10.3 ± 0.5 mg. The theoretical resonant frequencies of the first and second bending mode are

Figure 4.5: A photograph of the bar mirror from the front and side views. Our test mass seems to be warped at the mirror coating. The curvature is measured to be around 200 mm.

5.26 kHz and 14.5 kHz respectively. The mode shapes are shown in Fig. 4.4. This thermal noises of these modes should be enough small not to cover the quantum radiation pressure fluctuation. The contribution of the bar thermal noise to the sensitivity of the main cavities can be estimated with the displacement spectrum around the first and second resonance of the bending modes. The detailed result is represented in Sec. 5.3.

Photographs of the substrate are shown in Fig. 4.5. The curvature of the produced mirror is around -200 mm even though it should be flat. This value is measured by the beam profiling of the reflection from the bar mirror. The convex surface seems to be caused by the coating (high-reflection coating of over 99.99% at the incident angle of 43°) of the thin and long substrate. It is required to use a more concave mirror as the controlled mirror to construct the optical cavity with the test mass.

Suspension fiber

In order to suppress the suspension thermal noise, as thin a suspension fiber as possible is favorable because the thin wire has a small restoring force of the rotational mode and contributes to reducing the low resonant frequency, resulting in the low thermal noise. The restoring force of a wire related to the rotational mode is given by

$$K_{\mathrm{rot}} = \frac{\pi G_{\mathrm{w}} \phi_{\mathrm{w}}^4}{32 l_{\mathrm{w}}}, \tag{4.4}$$

Property	Carbon fiber	Tungsten
Young's modulus [GPa]	294	345
Tensile strength [GPa]	5.9	3.8
Density [10^3 kg/m^3]	1.81	19.3
Minimum thickness [μm]	5-7	2.5

Table 4.2: Properties of the carbon fiber and the tungsten wire. The tensile strength is the value at the diameter of $\sim 10\,\mu$m.

where $G_{\rm w}$ is the shear modulus, $\phi_{\rm w}$ is the diameter, and $l_{\rm w}$ is the length of the wire, respectively. As shown in this equation, the dependence of the wire diameter is very sharp, the fourth order. It is the most important how thin wire we use.

In the previous experiment of the 5-mg suspended mirror, a tungsten wire whose diameter is $3\,\mu$m. This thickness is the thinest in wires in the market. However, we use a double pendulum system on the test mass for reducing the residual amplitude of the pendulum mode at locking the cavity and two pendula should be aligned, so the metal wire, which has the residual shear, is not preferable. A carbon fiber is used as the suspension fiber for the test mass.

Carbon fibers are made from an acrylic fiber or a pitch carbonized at high temperature. The advantages are low weight, high stiffness, high tensile strength, high temperature tolerance, high chemical resistance and low thermal expansion. The carbon fiber used in our experiments is offered by Toray industries. In Table 4.2, properties of the carbon fiber are shown with compared to tungsten. The Young's modulus is similar, but the tensile strength of carbon fiber is almost twice than that of tungsten. Moreover, the density is smaller by one order. It is advantageous from a view point of the suspension thermal noise. The suspension thermal noise of the pendulum mode gets worse over the frequency of the violin mode [101]. The violin mode frequency is inversely proportional to square root of the density, so the low density wire avoids making the suspension thermal worse.

Q-value of the carbon fiber

It is necessary to measure the Q-value of the carbon fiber to estimate the suspension thermal noise of the rotational and pendulum mode. Here the

Property	Q-value measurement	Test mass
Bar material	Aluminum	Fused silica
Bar length (designed) [mm]	15	15
Height (designed) [mm]	1.5	1.5
Thickness (designed) [mm]	0.2	0.2
Mass [mg]	12.0 ± 0.1	10.3 ± 0.1
Wire length [mm]	18 ± 1	22 ± 1
Resonant frequency [mHz]	97.1 ± 0.1	90 ± 1

Table 4.3: Properties of the torsion pendulum for the Q-value measurement and the test mass.

results of the Q-value measurement are represented.

A carbon fiber and an aluminum bar are combined as a torsion pendulum. Their properties are listed in Table 4.3, where those of the test mass are also shown for the comparison. The Q-value is measured by an optical lever and a position sensitive detector (PSD). The PSD can sense the position of the reflection beam spot from the bar, so the rotational and pendulum mode can be measured by the signal along the horizontal and vertical axis respectively.

First, the ringdown oscillation of the rotational mode is measured after the excitation. The result is shown in Fig. 4.6. The resonant frequency is $97.1 \pm 0.1\,\mathrm{mHz}$, that is, the period is $10.30 \pm 0.01\,\mathrm{s}$. The time series data of the envelope $y(t)$ is fitted by a function of

$$y(t) = a \exp\left(-\frac{\omega_{\mathrm{rot}} t}{2b}\right) + c, \tag{4.5}$$

where a, b, c are the fitting parameters and $\omega_{\mathrm{rot}}/2\pi = 97.1\,\mathrm{mHz}$. The b is the Q-value of the rotational mode. It is estimated to be $Q_{\mathrm{rot}} = (2.6 \pm 0.2) \times 10^3$, which satisfies the requirement. The error comes from the values changed by the selection of the start and end time of the fitting.

Next, we measure the power spectrum density of signals along each axis of the PSD in the equilibrium state to estimate the Q-value of the rotational and pendulum mode. Assuming that the added force spectrum is the same in the equilibrium state, the displacement spectrum around the resonant frequency

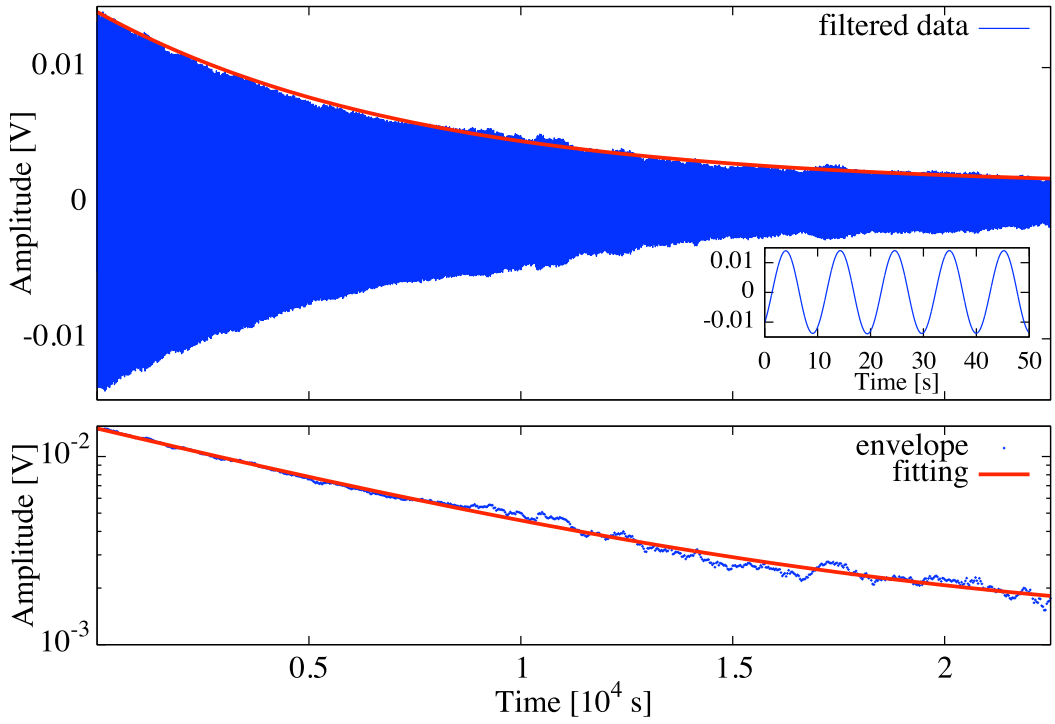

Figure 4.6: Ringdown oscillation of the rotational mode. The blue line at the upper figure indicates the raw data cleaned by a sharp butterworth filter. The green line shows the fitting of the envelope data. The data is averaged every 30 second.

can be written as

$$\sqrt{S_{\rm x}} \propto \left|\omega_{\rm m}^2 - \omega^2 + i\omega_{\rm m}^2/Q_{\rm m}\right|^{-1}. \tag{4.6}$$

The fitting results in log-scale of the displacement spectrum of rotation and pendulum modes are shown in Fig. 4.7. The measurement time is not long enough to reconstruct the sharp spectrum, so the number of frequency bins is short even at $n_{\rm av} = 3$. Therefore, we can get the lower limits of each Q-value such as $\mathrm{Q}_{\rm rot} \gtrsim 3.2 \times 10^3$, $\mathrm{Q}_{\rm pend} \gtrsim 8.2 \times 10^4$. The requirement of the pendulum Q-value is also satisfied.

The rotational Q-value is a little higher than the estimated one by the ringdown measurement. However, the ringdown measurement has the dependence of peak shear strain at the excitation and the estimated Q-value is lower when the excitation is larger [102]. Therefore, it is consistent that the estimated

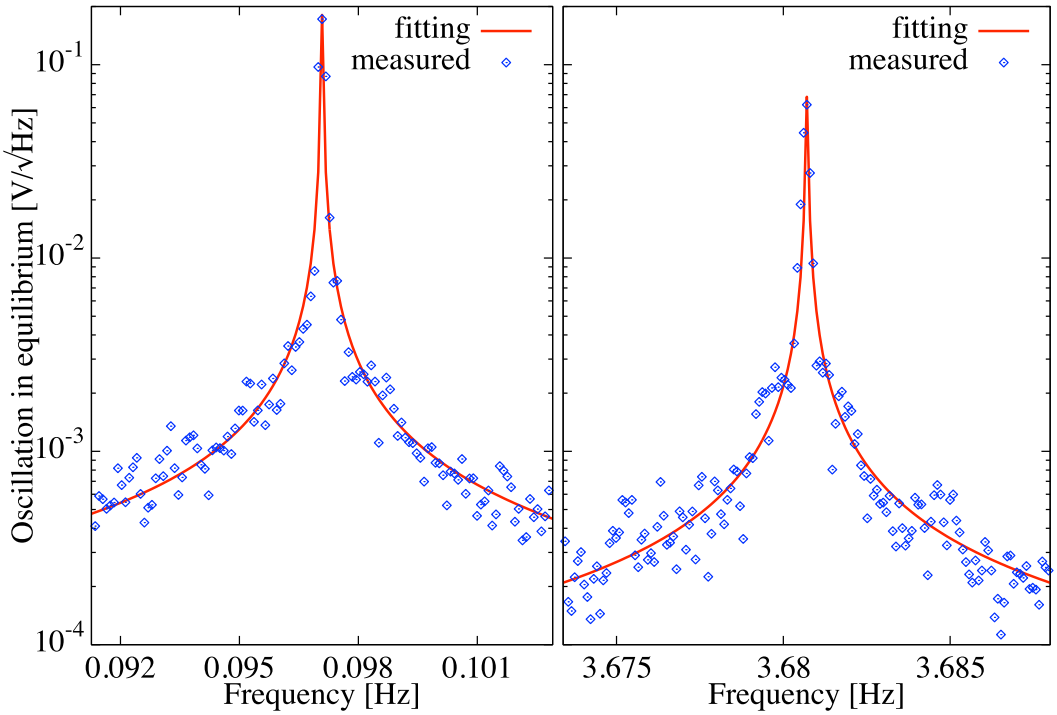

Figure 4.7: Power spectrum density of the displacement signals of the rotation and pendulum modes. The blue dots show the measured spectrum data and the red lines represent the fitting results around each resonant frequency. $n_{\rm av} = 3$.

value without the excitation is larger. This rotational Q-value is higher than that of the 3-μm tungsten wire ($Q_{\rm rot} = 1.9 \times 10^3$) [20].

The pendulum Q-value is also consistent in terms of gravitational dilution of the pendulum mode [48]. The gravitational dilution is the effect enhancing the Q-value compared with the intrinsic one of the thin wire. It is because the energy is lost at whole area on the wire in the rotational mode, on the other hand the energy loss occurs only near the clamp point in the pendulum mode. The dilution factor $Q_{\rm pend} = \alpha_{\rm dil} Q_{\rm rot}$ in the single fiber suspension is given by

$$\alpha_{\rm dil} = \frac{l_{\rm w}}{\phi_{\rm w}^2} \sqrt{\frac{128mg}{\pi E_{\rm w}}}, \tag{4.7}$$

where g is the gravitational acceleration and $E_{\rm w}$ is the Young's modulus of the wire. In our case the dilution factor is $\alpha_{\rm dil} \sim 60$, so the pendulum Q-value

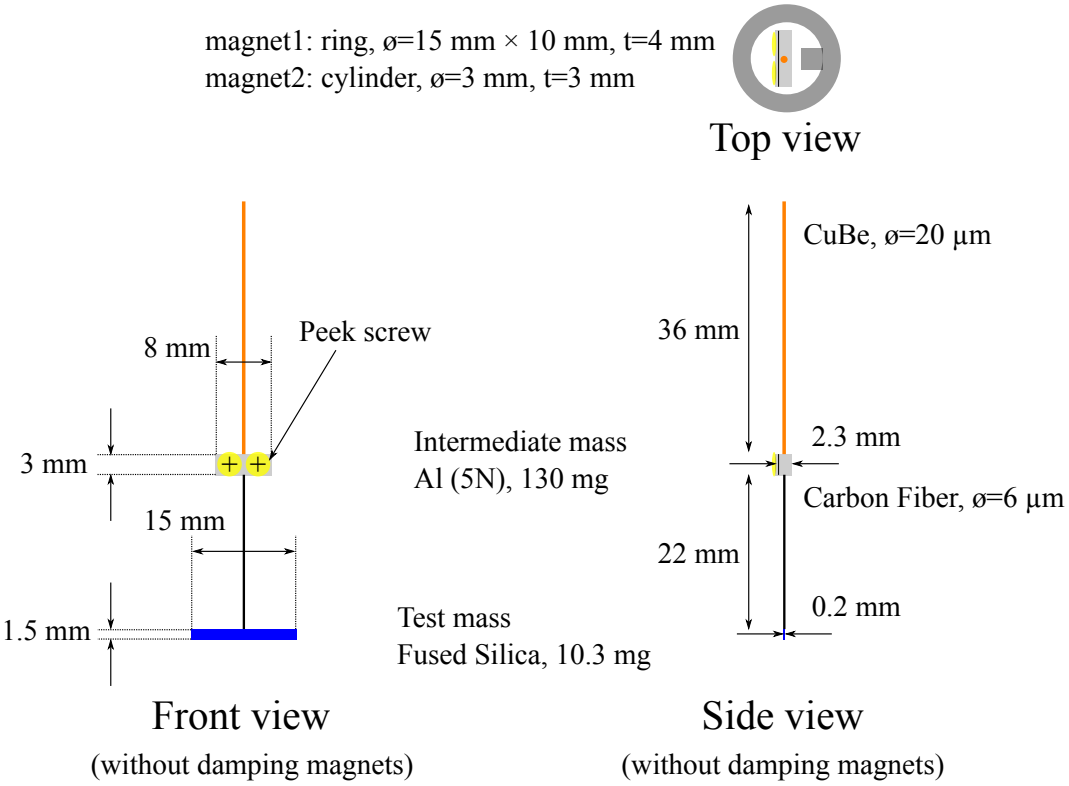

Figure 4.8: Top, front, and side view of the suspension of the test mass. For the clean description, there is no damping magnet in the front and side views.

has potential to be enhanced up to $Q_{\mathrm{pend}} \sim 1.5 \times 10^5$. The difference between the theoretical and measured values can be regarded to show the clamp loss. The clamp method using a pure aluminum bar is common in the Q-value measurement and the main experiment, so the Q-values are similar.

4.2.2 Main cavities

In this subsection, the setup for main cavities is described. As shown in Fig. 4.1, the main cavities consist of aone torsion pendulum (the test mass), and two fixed input mirrors and two suspended controlled mirrors with coil-magnet actuators.

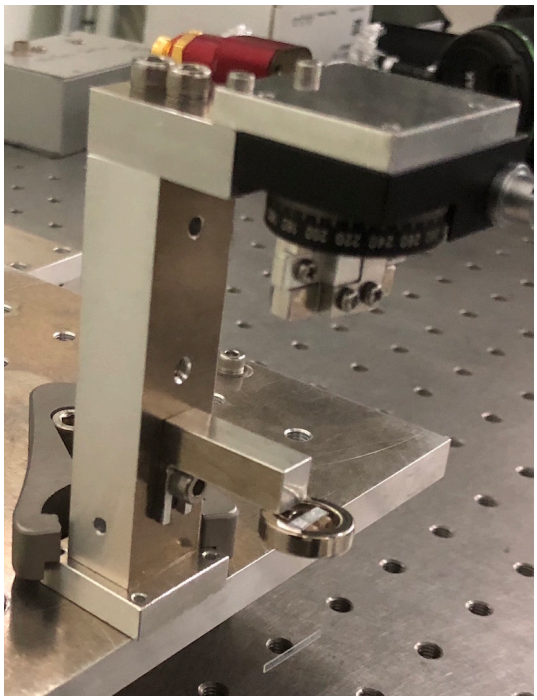

Figure 4.9: A photograph of the suspension for the test mass. This consists of the pillar, the rotational stage with the picomotor, the damping magnet, the intermediate mass made of pure alminum, and the bar mirror.

Suspension for the test mass

In order to lock the cavities, it is necessary to suppress the residual oscillation of the pendulum mode caused by seismic noise. All components of the cavities are located on a double-suspended platform to reduce the seismic noise. Moreover, similarly to the platform, the residual motion can be suppressed by the intermediate mass which is damped by a magnet.

Fig. 4.8 shows top, front, and side views of the suspension of the test mass. The intermediate mass is damped by Nd magnets for reducing the residual amplitude of the test mass due to the seismic noise. The intermediate mass of usual aluminum is trapped by the magnetic field, so we use high-purity aluminum of 99.999% (5N). The carbon fiber is clamped by the pure aluminum of a 2-mm main body and a 0.3-mm lid with peek (not metal) screws, which is also used to avoid the magnetic trap. The mass is $129.5 \pm 0.1\,\mathrm{mg}$. This value should be the same as the test mass in terms of the optimal damping, but that

heavier mass is necessary for the intermediate mass to be equipped with the clamp system.

The damping is done by ring and cylinder magnets given by Magfine company. The ring magnet is fixed to a pole for this suspension, and the cylinder magnet is attached by the magnetic force to the ring one. It can be realized because the ring magnet has the magnetic field to the radial direction. These two magnets damp two horizontal pendulum modes of the intermediate mass.

The intermediate mass is suspended by a CuBe fiber adhering with curing of Locktite. The CuBe fibers are produced by Tokusai company. The diameter is 20 μm and the length is 36 ± 1 mm. CuBe fibers have relatively large intrinsic Q-value [102] and small Young's modulus of 130 GPa in metallic material. At the top the CuBe fiber is clamped by a stainless steel jig.

A photograph of this whole suspension for the test mass is shown in Fig. 4.9. It is fixed to a rotation stage of Sigma-koki. The stage is used to adjust the rotation angle of the bar mirror. A picomotor of Newport model 8353 is fixed to the rotation stage for remote control from outside the vacuum chamber.

Input mirrors

Here two input mirrors for the main cavities are introduced. They are fixed to the platform, which is a suspended alminum plate including the main cavities. These can be main noise sources of vibration noise such as the residual seismic noise of the platform and thermal noises of components on the platform and mechanical modes of the input mirror holder. It is because they are not isolated by suspension and these vibrations can directly contribute to the cavity length change.

Properties of the input mirrors are shown in Table 4.4. These are also produced by Sigma-koki company. We place a special order of mirror holder used for the input mirror of the cavity with an oblique incidence to Newport. The holders are equipped with picomotors of Newport model 8353-V also for remote control of the alignment. The front surface of the input mirrors are close to the test mass, where the distance is below 1 cm.

The reflectivity and transmissivity of the mirrors are set to be 99.8% and 0.2% respectively. The finesse of the cavity is determined to be several thou-

Property	Value
Substrate	Fused silica
Diameter [mm]	12.7 (half inch)
Thickness [mm]	3
Curvature	∞ (flat)
Front surface reflectivity	99.8%
Rear surface reflectivity	<0.2%
Incident angle [degree]	43

Table 4.4: Properties of the input mirrors.

sand. This finesse can realize the enough intra-cavity power to measure quantum radiation pressure fluctuation. Also, we know that the suspended cavity with the finesse of a few thousand can be locked without local control.

Suspension for the controlled mirrors

Finally suspension for the controlled mirrors is shown. The mirrors control the cavity length with coil-magnet actuators. These are also suspended for vibration isolation and enough actuating range. Therefore, it is necessary to construct double-pendulum system and damp the intermediate mass similarly to the test mass.

In Fig. 4.10, the suspension for the controlled mirrors are shown from top, front, side, and back views. The controlled mirror consists of a half-inch curved mirror made of fused silica and brass body with 2 small magnets for the actuation. The mirror is concave and the curvature is 150 mm. The curvature is decided by the requirement of a stable cavity with the convex test mass. The reflectivity is 99.99% at the incident angle of 0° although the actual incident angle is a few degree. They are produced by Lattice Electro Optics. The brass has the hole for the mirror of 12.9 mm. It is buried and attached to the body with ultra-violet curing resin. The mass of the controlled mirror is 63 g. This value is heavier than that of the test mass by more than 3 orders of magnitude. Therefore, the cavity can be considered to have only one pendulum. At the right and left edges of the controlled mirror, there are two Nd magnets. These are a part of the coil-magnet actuator.

The intermediate mass is made of copper, whose mass is 60 g. Copper

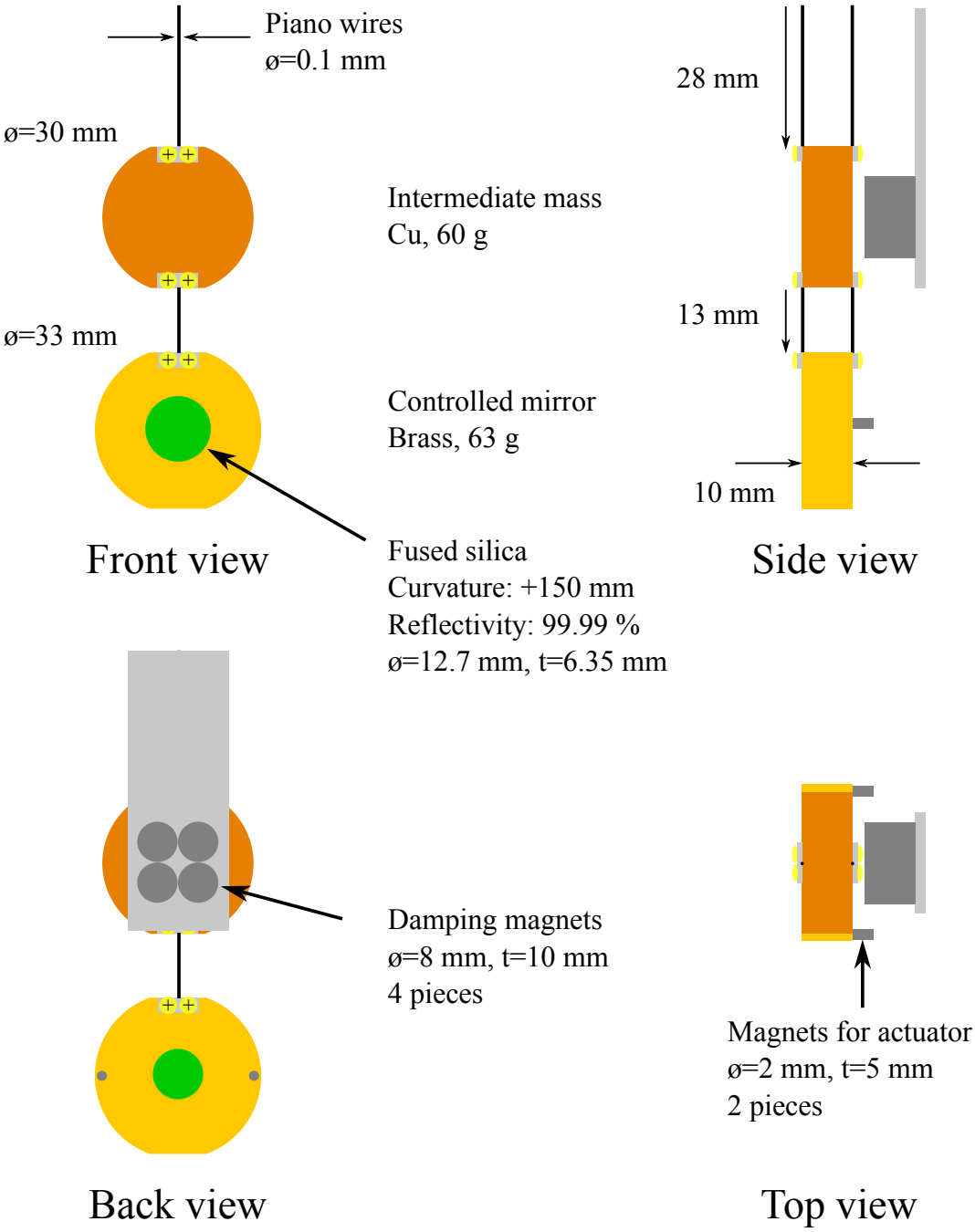

Figure 4.10: Top, front, side, and back view of the suspension for the controlled mirrors. The green circle shows the curved mirror for the cavity buried in the brass body.

is one of metals with the lowest electrical resistivity as well as silver. The damping magnets also produced by Magfine are supported by the aluminum plate like a cantilever. Four pieces magnets are used with alternate magnetic poles because loops of the magnetic fields are closed and they do not largely affect the other system.

These masses are suspended by piano wires of 0.1 mm diameter of Niraco. A piano wire has some advantages for the suspension compared with a tungsten wire as explained at the next subsection. The clamps for the intermediate mass and the controlled mirror are done by an aluminum thin plate and peek screws. Both masses are suspended by 2 wires for the remote alignment with stages of Sigma-koki controlling the pitch and yaw direction. At the top of the suspension, the piano wires are clamped to stages with picomotors of Newport model 8353. The back stage can move to horizontal direction and the front stage can move to vertical direction. They change the pitch and yaw modes of the controlled mirror. All setup for these suspension is fixed to pillars of thick aluminum plate and the pillars are fixed to the platform.

4.2.3 Vibration isolation

Vibration isolation system of the platform is needed to reduce the residual seismic motion of the suspended mirrors and suppress the vibration noise of the fixed input mirror which is directly coupled with the displacement noise of the cavity. In this subsection the vibration isolation of the platform is described.

First, we show top, front, and side views of the platform in Fig. 4.11. There are the test mass suspension, the controlled mirrors suspension, the input mirrors, and the coil-magnet actuators on the platform. Pillars for the controlled mirrors suspension are 200 mm tall. From the top and center of the pillars, the platform is suspended by single piano wire, which is included in double suspended system. In the previous experiment we suspend the platform with 3 tungsten wires. It is treated easily, however, the resonant frequency of the pitch and bounce modes of the platform can be almost the same, introducing the large seismic noise. Moreover, in our case, the low frequency sensitivity is important and the pitch motion of the platform directly contributes to the

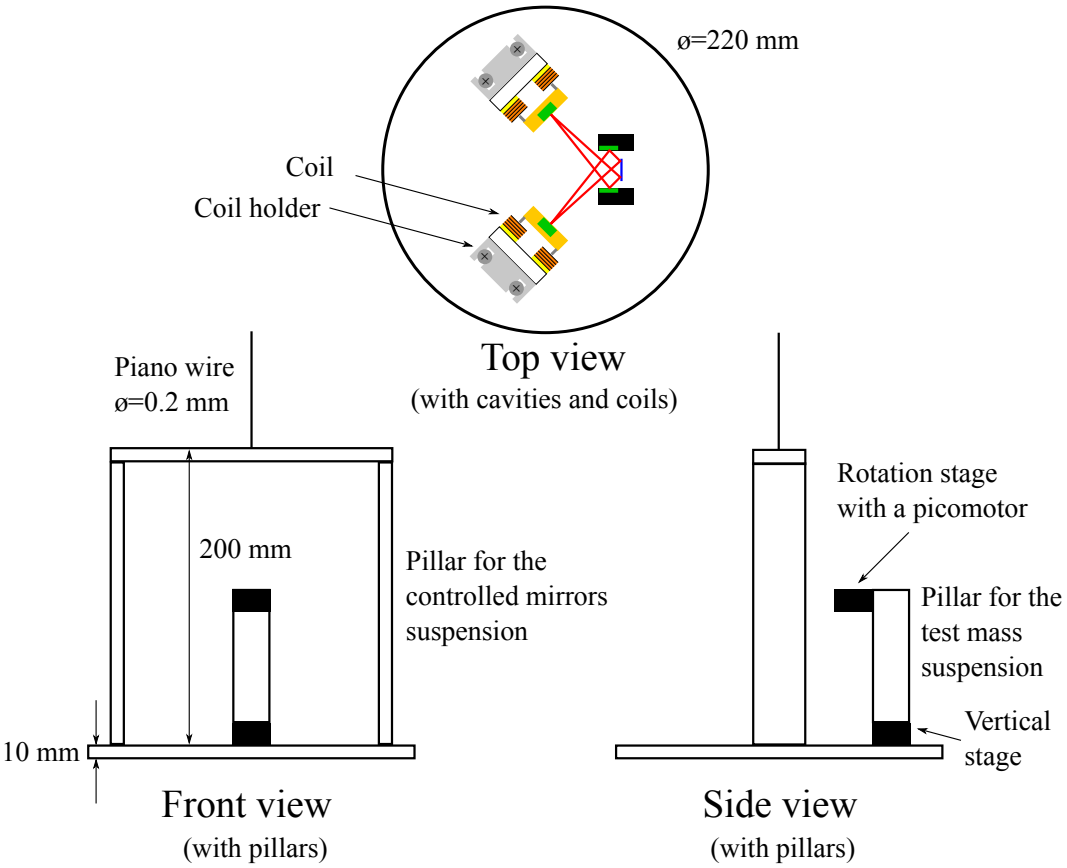

Figure 4.11: Top, front, and side views of the platform. For clear description, we show the top view without pillars and the front and side views without cavity mirrors or coils. The vertical and horizontal stages for the alignment of the controlled mirrors are also omitted.

input mirror and changes the two cavity length differentially. Therefore, the single wire suspension is adopted to avoid the issues. A photograph of the platform is shown in Fig. 4.12.

Our vibration isolation system for the main cavities is shown from top, front, and side views in Fig. 4.13. We construct the building on the 3 viton rubbers suspending the double pendulum and the damping mass. The building consists of a floor, a roof, and 3 poles made of alminum. A magnetized stainless steel as the 4.5-kg damping mass is suspended from the roof by 3 piano wires, and a copper as the 1.8-kg intermediate mass is suspended by a single piano wire. The 2.6-kg platform is suspended from the intermediate mass. The

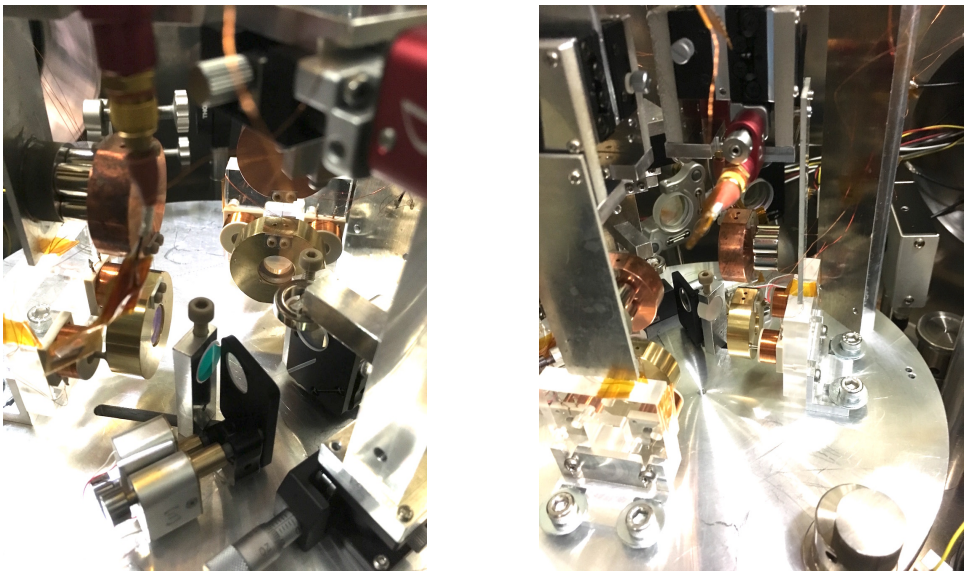

Figure 4.12: A photograph from the front and back views of the platform. There are the test mass suspension, the input mirror holders, the controlled mirror suspensions, and the coil-magnet actuators.

Property	Piano	Tungsten
Young's modulus [GPa]	206	345
Tensile strength [GPa]	3.1	2.8
Density [10^3 kg/m^3]	7.85	19.3
Minimum thickness [μm]	80	2.5

Table 4.5: Properties of the piano wire and the tungsten wire. The tensile strength is the value at the diameter of $\sim$0.1 mm.

damping mass has 8 Nd magnets to damp the intermediate mass with the hole of the diameter of 70 mm and the depth of 15 mm in order to bring the suspension point close to the center of mass to reduce the resonant frequency of the pitch mode. The mass of the building is 14 kg including other optics on the floor.

All piano wires have the diameter of 0.2 mm. They are favorable to tungsten wires in terms of small Young's modulus, large tensile strength, and low density as compared in Table 4.5. That contributes to reducing vertical seismic noise of the cavities. In general, it is more difficult to suppress the vertical seismic noise than the horizontal seismic noise because the bounce mode of the suspended

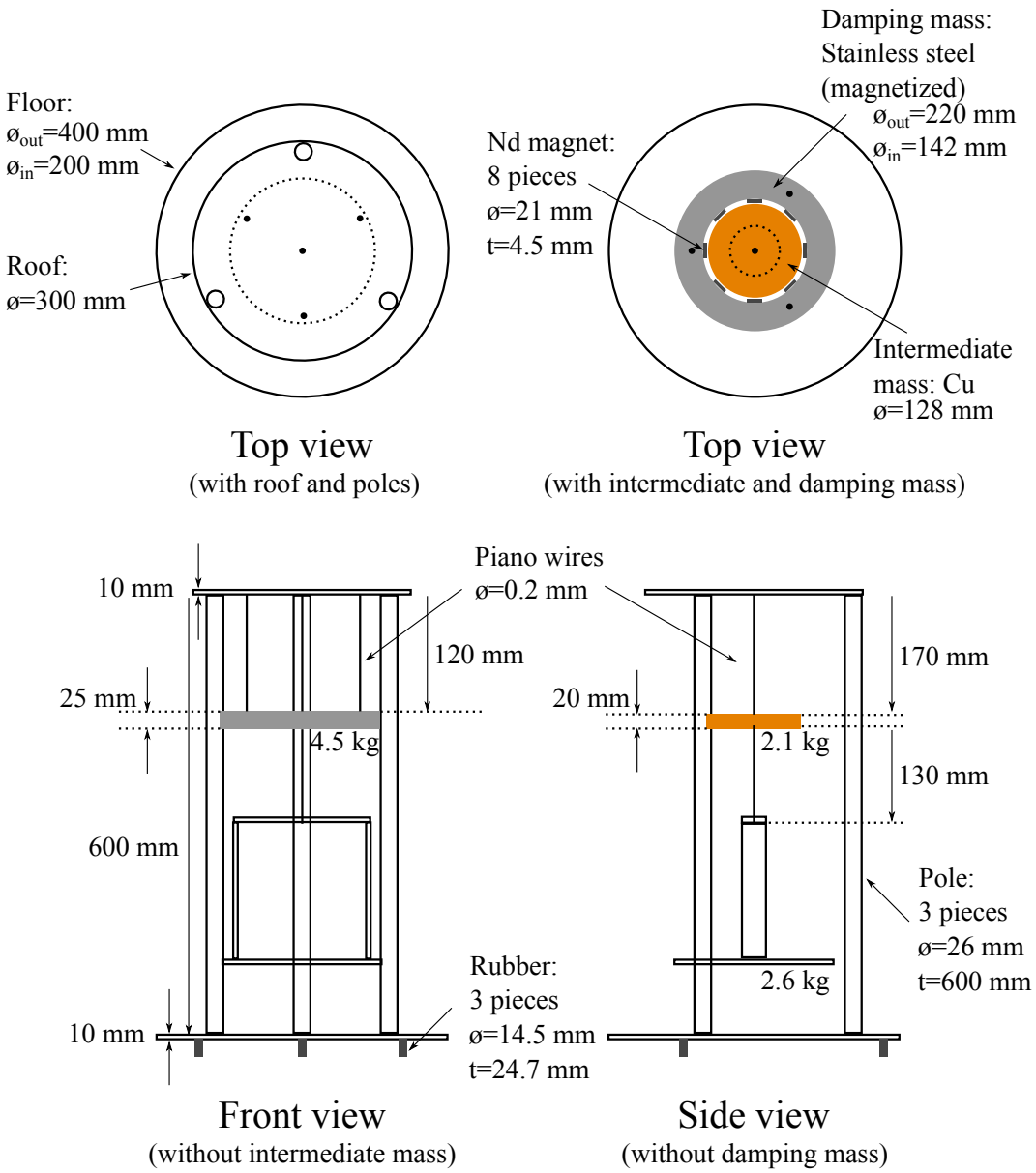

Figure 4.13: Top, front, and side views of the vibration isolation system for the main cavities. Similarly, we select which parts are shown for clear description. The poles and piano wires for the damping mass are located at the shape of an equilateral triangle, whose center are common.

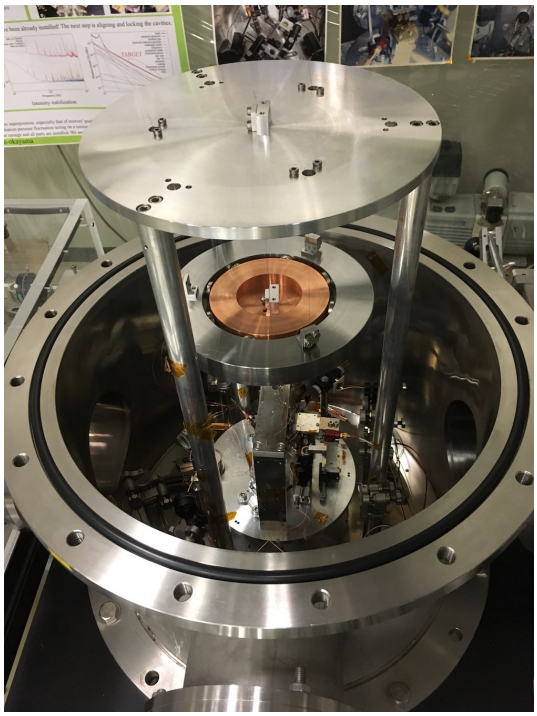

Figure 4.14: A photograph of the entire apparatus of the second chamber. The building suspends the damping mass, the intermediate mass, and the platform.

mass is much stiffer than the pendulum mode. The resonant frequency of the bounce mode can be low with a coil spring, but the internal eigen modes can be the issues. Therefore, softer and stronger wires, which enables suspension with thiner ones, should be used. Even though the piano wire cannot be as thin as several μm, it is one of the best wire to suspend kg-scale objects. A photograph of the building is shown in Fig. 4.14.

Measurement of the seismic noise

The seismic noise of the platform and vibration isolation ratio of our system are measured and estimated. First, the theoretical description is shown in a simple model for coupled oscillators. A conceptual scheme of our coupled oscillator is shown in Fig. 4.15. In our case, The coordinates of x_{b}, x_{d}, x_{i}, and x_{p} correspond to the displacement of the whole building, the damping mass, the intermediate mass, and the platform. The seismic motion is shown as X and the effective mass can be regarded as infinity. Equations of motion of the

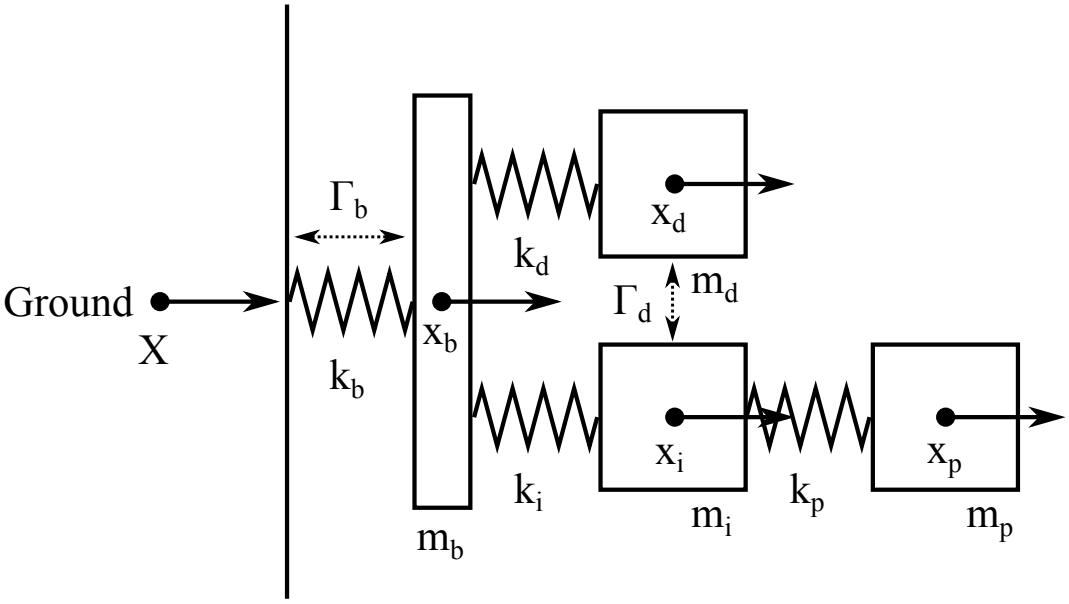

Figure 4.15: A conceptual scheme of our coupled oscillator. The position, mass, and spring constant of each object are labeled as x, m, and k respectively. The damping constant of the rubber and damping magnet are $\Gamma_{\rm b}$ and $\Gamma_{\rm d}$.

system are as follows:

$$\begin{cases} m_{\rm b}\ddot{x_{\rm b}} &= -k_{\rm b}(x_{\rm b}-X) - \Gamma_{\rm b}(\dot{x}_{\rm b}-\dot{X}) - k_{\rm i}(x_{\rm b}-x_{\rm i}) - k_{\rm d}(x_{\rm b}-x_{\rm d}) \\ m_{\rm i}\ddot{x_{\rm i}} &= -k_{\rm i}(x_{\rm i}-x_{\rm b}) - k_{\rm p}(x_{\rm i}-x_{\rm p}) - \Gamma_{\rm d}(\dot{x}_{\rm i}-\dot{x}_{\rm d}) \\ m_{\rm p}\ddot{x_{\rm p}} &= -k_{\rm p}(x_{\rm p}-x_{\rm i}) \\ m_{\rm d}\ddot{x_{\rm d}} &= -k_{\rm d}(x_{\rm d}-x_{\rm b}) - \Gamma_{\rm d}(\dot{x}_{\rm d}-\dot{x}_{\rm i}), \end{cases} \tag{4.8}$$

where the internal loss of the spring is ignored. These can be rewritten in frequency domain as

$$\begin{pmatrix} \alpha_{\rm b} & -k_{\rm i} & 0 & -k_{\rm d} \\ -k_{\rm i} & \alpha_{\rm i} & -k_{\rm p} & -i\Gamma_{\rm d}\omega \\ 0 & -k_{\rm p} & \alpha_{\rm p} & 0 \\ -k_{\rm d} & -i\Gamma_{\rm d}\omega & 0 & \alpha_{\rm d} \end{pmatrix} \begin{pmatrix} x_{\rm b}(\omega) \\ x_{\rm i}(\omega) \\ x_{\rm p}(\omega) \\ x_{\rm d}(\omega) \end{pmatrix} = \begin{pmatrix} k_{\rm b}+i\Gamma_{\rm b}\omega \\ 0 \\ 0 \\ 0 \end{pmatrix} X(\omega), \tag{4.9}$$

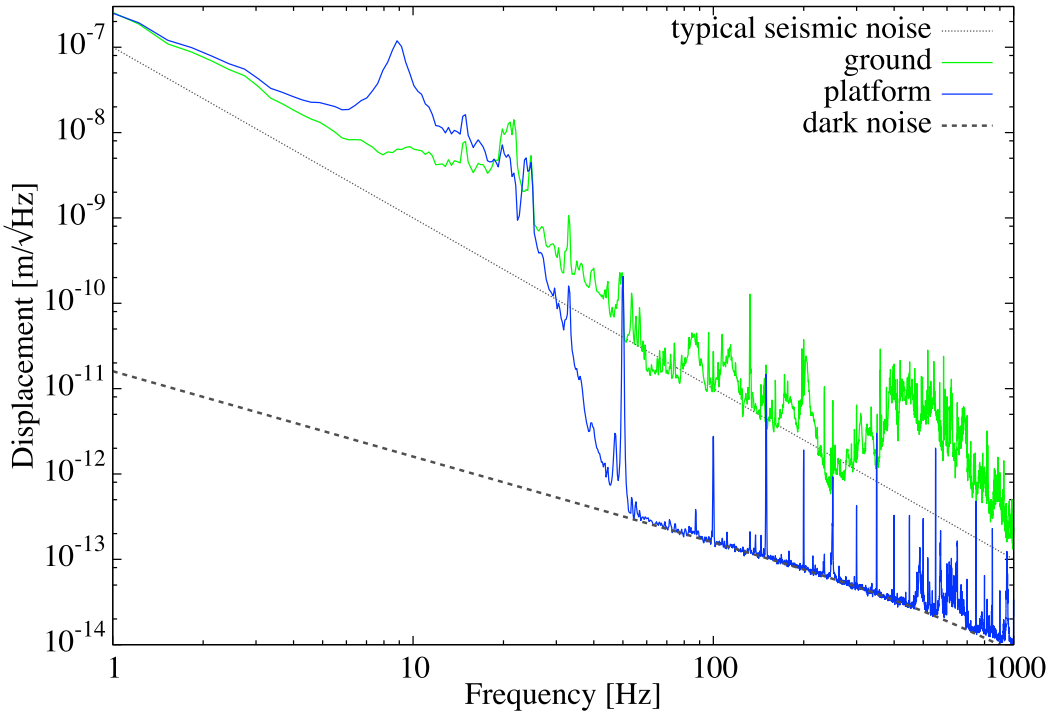

Figure 4.16: Vertical seismic noise on the ground and on the platform. The green and blue lines show the displacement spectrum on the ground and on the platform respectively. The thick dotted black line is the dark noise of the geophone. The typical seismic noise level is shown as the thin dotted line. Sharp spikes come from power supply and the harmonics.

where

$$\begin{cases} \alpha_{\mathrm{b}} &= -m_{\mathrm{b}}\omega^2 + k_{\mathrm{b}} + i\Gamma_{\mathrm{b}}\omega + k_{\mathrm{i}} + k_{\mathrm{d}} \\ \alpha_{\mathrm{i}} &= -m_{\mathrm{i}}\omega^2 + k_{\mathrm{i}} + k_{\mathrm{p}} + i\Gamma_{\mathrm{d}}\omega \\ \alpha_{\mathrm{p}} &= -m_{\mathrm{p}}\omega^2 + k_{\mathrm{p}} \\ \alpha_{\mathrm{d}} &= -m_{\mathrm{d}}\omega^2 + k_{\mathrm{d}} + i\Gamma_{\mathrm{d}}\omega. \end{cases} \tag{4.10}$$

The vibration isolation ratio of $x_{\mathrm{p}}(\omega)/X(\omega)$ can be calculated by the multiplication of the inverse matrix in the left side of Eq. (4.9) to the right side.

A similar setup to the main experiment is constructed to confirm the vibration isolation ratio. The vertical mode is focused on. The mode can be a larger issue than the other mode because of its high resonant frequency. The

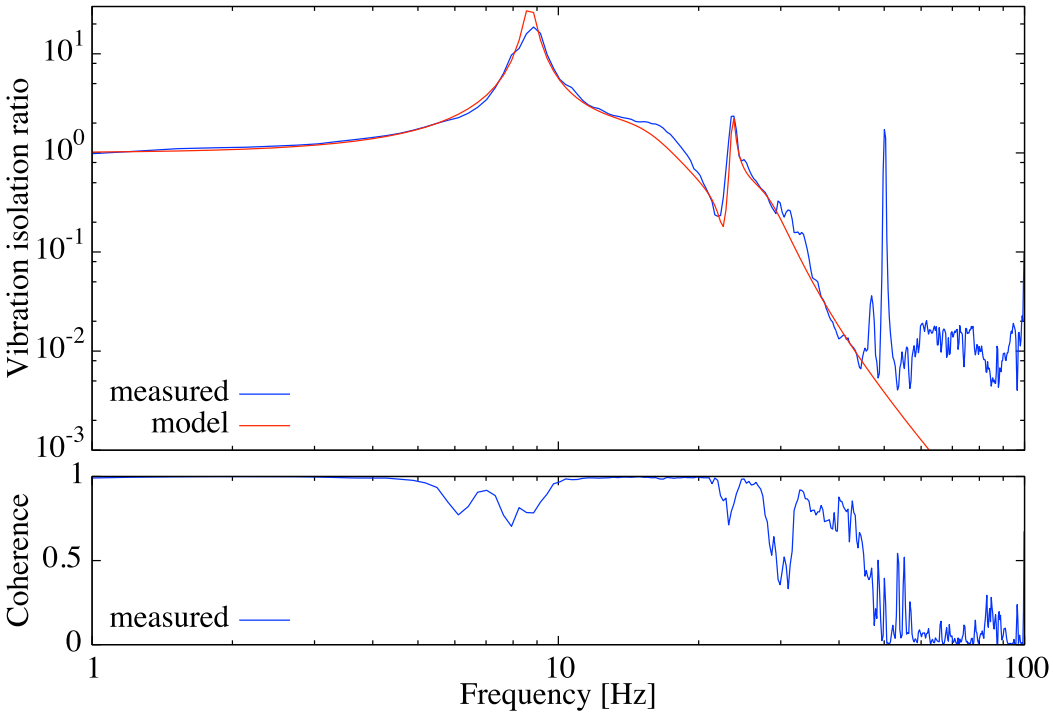

Figure 4.17: Vertical vibration isolation ratio of the platform. The upper blue line shows the result of getting the ratio of two spectra. The lower blue line expresses coherence of the two spectra. The modeled spectrum is also plotted as the red line.

different points are the number of suspension wires and the diameter. The intermediate mass and the platform are suspended by 3 piano wires of the 0.1 mm diameter. It is because a geophone used in the vibration measurement cannot be located at the center of the platform under the pillars for the controlled mirrors suspension, and wider space is needed.

The used geophones L4C are made by Sercel company. The calibration factor from the velocity of a target for measurement to the output voltage was measured to be $(2.6\pm0.3)\times10^2$ V/(m·s) above 1 Hz [103]. The displacement can be obtained by dividing the velocity by ω. Fig. 4.16 shows the displacement spectrum of the vertical seismic noise on the ground and on the platform. The noise level on the ground is larger than that of the typical amplitude of $10^{-7}/f^2\,\mathrm{m}/\sqrt{\mathrm{Hz}}$. Here the 'ground' means the place on a table for vacuum chambers. The broad peak around a few 100 Hz is considered to be caused

Property	Model	Main experiment
Young's modulus [GPa]	180	180
Mass of the platform [kg]	2.5	2.6
the intermediate mass [kg]	2.1	1.8
the damping mass [kg]	5.0	4.5
the building [kg]	14	14
Diameter of the piano wires [mm]	0.17	0.20
Wire length for the platform [mm]	240	130
the intermediate mass [mm]	190	170
the damping mass [mm]	170	120

Table 4.6: A parameter list of the suspension for the main cavities.

by the structure of the table and acoustic vibration. The sensitivity for the spectrum of the platform is limited by the dark noise of the geophone above 60 Hz. The vibration isolation succeeds over 30 Hz.

The calculated vertical vibration isolation ratio is shown in Fig. 4.17. This ratio is evaluated by dividing the measured spectrum on the platform by that on the ground. The theoretical model of the ratio is acquired by tuning the parameters of the suspension and calculating $x_{\mathrm{p}}(\omega)/X(\omega)$. Above 50 Hz there is almost no correlation between the two signals because of the dark noise of the geophone and the data and the modeling do not match. However, the model succeeds reconstruction of the measured structure of the spectrum below 50 Hz with the coherence over 0.5. It means that the suspension with 3 wires can be regarded as the single suspension effectively and this model can be used at the estimation of the seismic noise.

In Table 4.6, we compare the parameters related to the suspension for the main cavities at the model in this measurement and at the main experiment. The wire diameter of $0.1\sqrt{3}$ mm in the model is the effective value of the single suspension with 3 wires whose diameters are 0.1 mm.

The vibration isolation ratio at the main experiment is estimated and shown in Fig. 4.18 with the requirement. The vertical requirement is determined by assuming that the seismic noise level is typical and the displacement noise is smaller by 1/10 than that of radiation pressure fluctuation. It is also supposed that the coupling from vertical to horizontal mode is 1/100 and the common

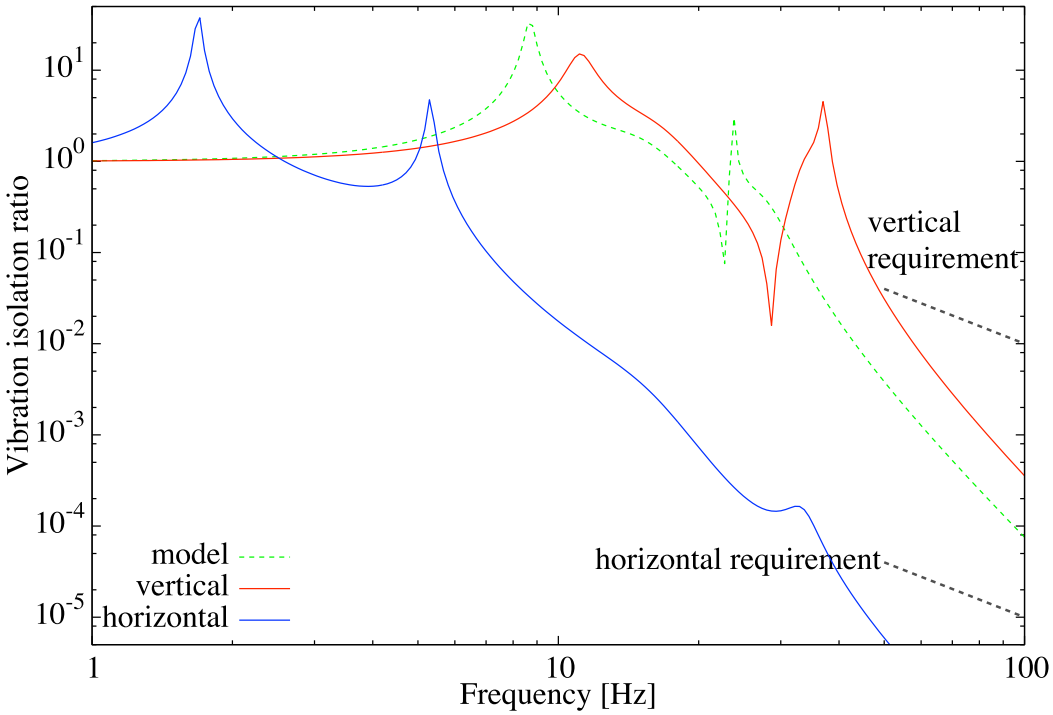

Figure 4.18: vibration isolation ratio estimated at the main experiment. The model curve in the previous figure is plotted again for the comparison as the green dotted line. The red and blue lines show the isolation ratio of the vertical and horizontal mode. The dotted black lines mean each requirement for observation of quantum radiation pressure fluctuation.

mode rejection ratio of the vertical vibration is 1/10. As shown in Table 4.6, the wire length at the main experiment is shorter and the dimeter is larger than that at the measurement of vertical seismic noise. Therefore, the red curve is above the green dotted one, but it still satisfies the requirement.

There are two components causing the horizontal seismic noise, the pitch and pendulum modes of the platform. Due to the high resonant frequency of several Hz, the pitch mode can become the larger problem. Here we set that $k_\mathrm{i} = m_\mathrm{i}\omega_\mathrm{i}^2$, $k_\mathrm{p} = m_\mathrm{p}\omega_\mathrm{p}^2$, where $\omega_\mathrm{i}/2\pi = \omega_\mathrm{p}/2\pi = 3\,\mathrm{Hz}$ to do pessimistic estimation, and the other parameters are the same as the model. The horizontal mode is coupled with the differential mode of the main cavities, and hence the requirement is much more strict than the vertical one. Even so, the horizontal isolation ratio is much smaller than the requirement. It can be confirmed that

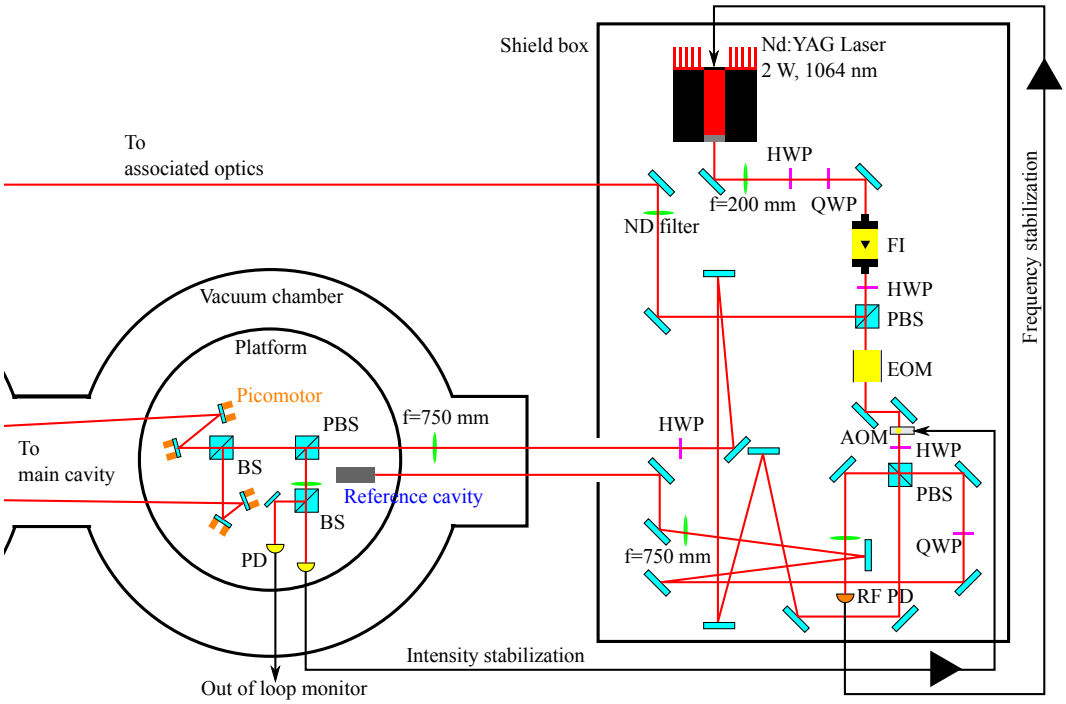

Figure 4.19: A schematic picture of the Input optics. Optics except for parts in the vacuum chamber is covered by a shield box made of acrylic plates.

our vibration isolation system enables reduction of seismic noises enough not to hide the radiation pressure fluctuation.

4.3 Sub setup

Sub setup is also important to achieve the observation. Before the main cavities the laser light is injected from the input optics with an EOM, AOM, and frequency and intensity stabilization. There is auxiliary optics for the main experiment such as the Michelson interferometer for measurement of actuator efficiencies of the coil-magnet actuators and optical lever to control the platform suspended by the single wire. A part of the system including the cavities are located in 2 vacuum chambers. They are introduced in this section.

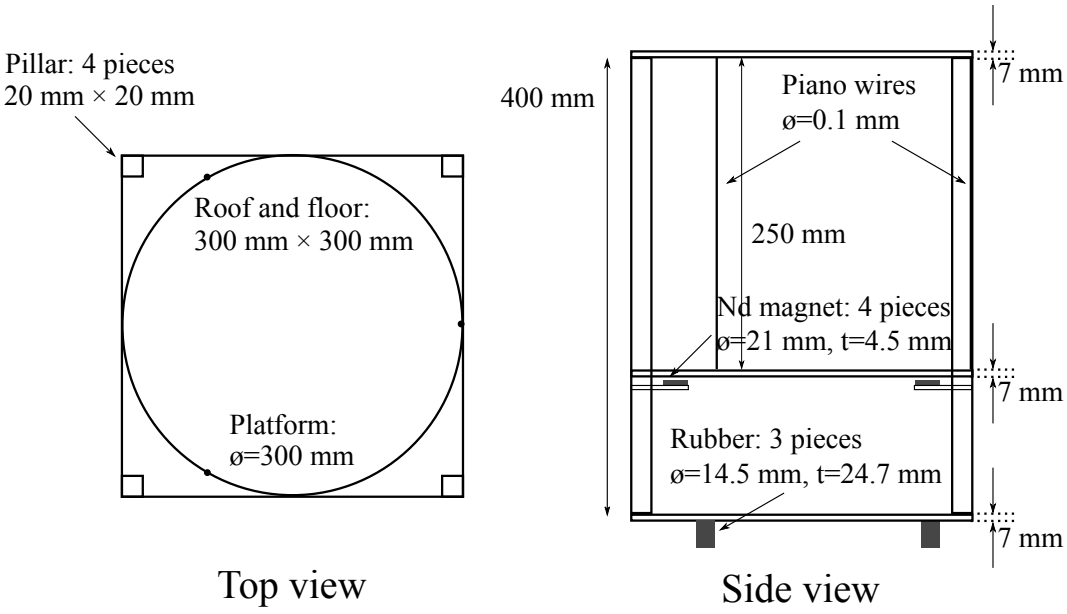

Figure 4.20: Top and side views of the vibration isolation system for the input optics and the frequency and intensity stabilization. The parts on the platform are not shown for the clear description.

4.3.1 Input optics

A schematic picture of the input optics is shown in Fig. 4.19. The light source (Mephisto 2000 NE) is Nd:YAG laser with the wave length of 1064 nm and the output power of 2 W produced by Innolight. The laser light goes through a FI to avoid return beam and is split to the light going to the associated optics and the main one. Phase of the main beam is modulated by an EOM and amplitude is modulated by an AOM whose first order light is used. Moreover, the light is divided by a PBS whose branching ratio is changed by a HWP. One is used for frequency stabilization with a reference cavity. The other enters the main cavity after the intensity stabilization with light picked off by another PBS. The length of the optical path is adjusted for mode matching of the cavities. Black triangle means each filter circuit of the stabilization.

The reference cavity, the PDs for the intensity stabilization, and steering mirrors for the alignment of the main cavities are on a platform. The platform has a vibration isolation system described in Fig. 4.20. It is suspended by a building on 3 rubbers. The building consists of a square floor and roof and

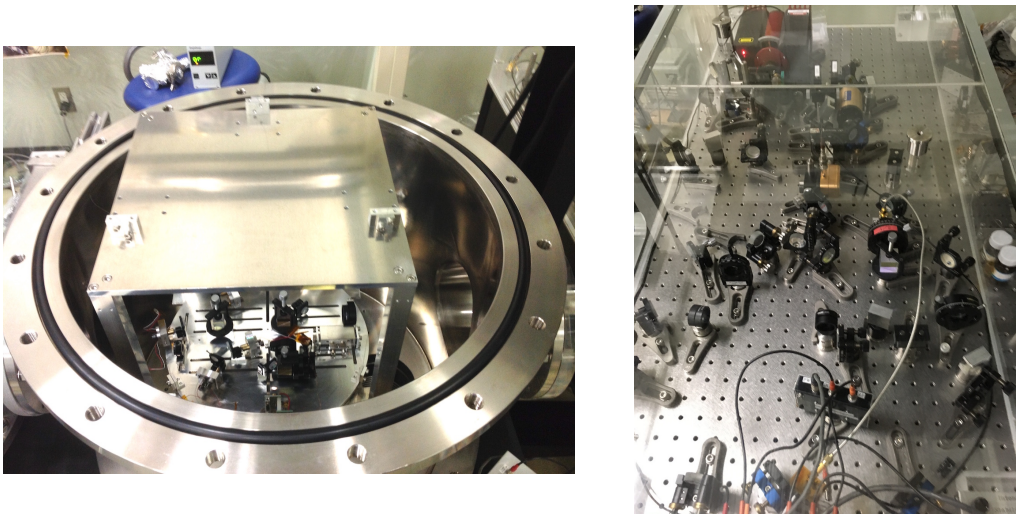

Figure 4.21: Photographs of the entire apparatus of the input optics. The building at the left suspends the platform including the reference cavity, the intensity stabilization system, and the steering mirrors for the cavity alignment.

4 pillars at the corners. The vibration isolation system is simpler than that of the platform for the main cavities. It is not a double but single pendulum, and the damping magnet is not fixed to the suspended damping mass but to the building. Three piano wires of the 0.1 mm diameter are used for the single suspension of the platform. These suspension points also form an equilateral triangle. Mirror holders after the last splitting of the beam have each 2 picomotors to do the alignment for the pitch and yaw directions. Optical and mechanical parts introduced at this paragraph are located in a vacuum chamber to eliminate the effect of the air and sound. Photographs of the input optics are shown in Fig. 4.21.

4.3.2 Frequency stabilization

Frequency noise of the laser light can be a large issue. As described in Eq. 2.90, the frequency noise of a linear cavity Δf [Hz/$\sqrt{\text{Hz}}$] contributes to the displacement noise as $\sqrt{S_{\text{x,freq}}} = L_{\text{r}}\Delta f/(2f_{\text{L}})$ [m/$\sqrt{\text{Hz}}$]. In the case of a triangular

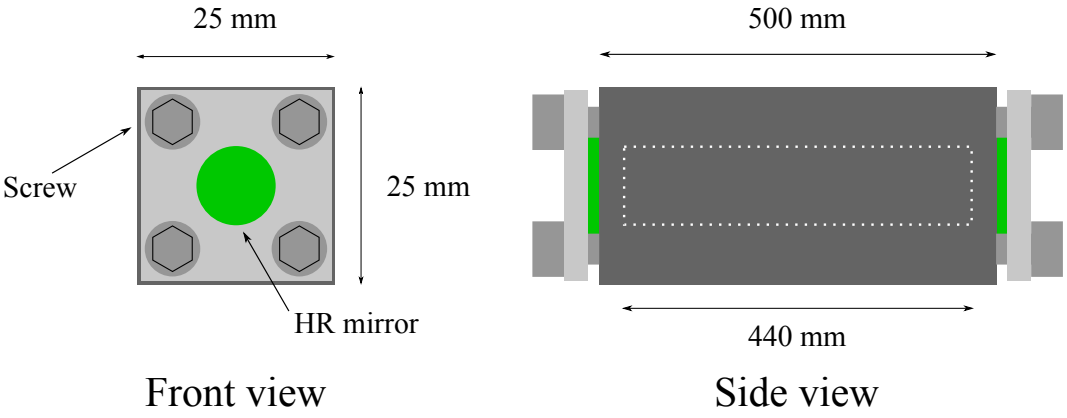

Figure 4.22: Top and side views of the reference cavity. The white dotted area whose diameter is 10 mm shows the space in the reference cavity.

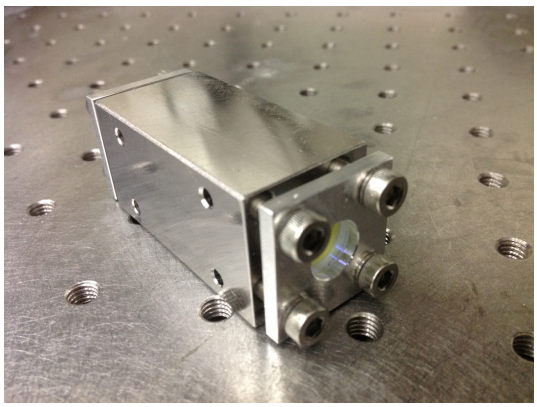

Figure 4.23: A photograph of the reference cavity.

cavity, these have the relation of

$$\sqrt{S_{\mathrm{x,freq}}} = \frac{2\pi\Delta f}{g}, \tag{4.11}$$

where g is the optimechanical coupling constant. Here the requirement of the frequency noise is set to be below the SQL of the test mass. It is enough small to observe the radiation pressure fluctuation.

The reference cavity is used to suppress the frequency noise of the laser source. When the displacement noise is much smaller than the corresponding frequency noise of the light, the frequency fluctuation is stabilized toward the displacement level of the reference cavity by the feedback control. Our

Property	Value
Spacer material	Super Invar
Cavity length [mm]	44
FSR [GHz]	3.4
Mirror substrate	Fused silica
Diameter [mm]	12.7 (half inch)
Thickness [mm]	6.35
Front surface reflectivity	∼99.994%
Rear surface reflectivity	<0.2%
Curvature [mm]	1000
Designed finesse	5.24×10^4
Measured finesse	6.14×10^4

Table 4.7: Properties of the reference cavity.

reference cavity consists of a rigid body made of super Invar, which has ultra low coefficient of thermal expansion, and two mirrors with the high reflection coating. A schematic picture , photograph, and properties of the reference cavity are represented in Fig. 4.22, Fig. 4.23, and Table 4.7. Two high reflection mirrors are buried by 3 mm in the hole at edges of the spacer. They are fixed to the spacer by screws.

The frequency stabilization is done with this reference cavity. We get Pound–Drever–Hall (PDH) signals from the reflection light of the cavity with the 15-MHz phase modulation by the EOM [104]. The EOM of Newport 4003 is a resonant type and the modulation index is 0.1 rad/V. In the frequency stabilization the signal amplitude of the 15-MHz modulation is 4 V and the demodulation signal is also 4 V. The used PD is Hamamatsu Photonics G10899 InGaAs photodiodes with the diameter of 1 mm, which can response at 15 MHz.

The filter includes low-pass filters and a high-pass filter to compensate the phase delay and keep the stable feedback control. It generates the feedback signals which go to the two actuators. Main one is the PZT attached to the cavity for the laser emission, and the other is the temperature of the laser crystal. The temperature actuator has larger dynamic range than the PZT. These actuator efficiencies are measured by the cavity scan. By changing the frequency of the laser light with shaking the input voltage to each actuator,

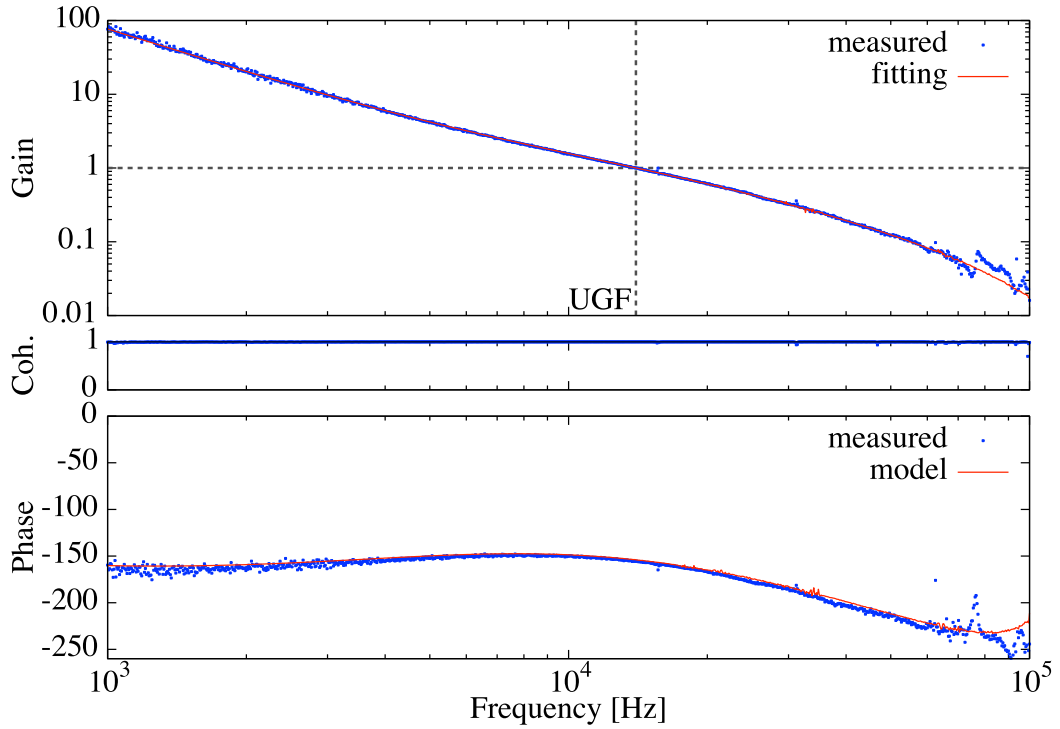

Figure 4.24: An openloop transfer function of the frequency stabilization. The blue dots show the measured data and the red line shows the fitting result with the gain. The unity gain and the frequency are described as the black dotted line.

the reflection power varies at the FSR of 3.4 GHz or the sideband frequency of 15 MHz. The coefficient of the frequency over the input voltage to the actuator can be obtained by using the FSR (temperature) or sideband (PZT) as the reference. The actuator efficiencies are estimated to be 2.65 ± 0.01 GHz/V at the temperature and 1.51 ± 0.01 MHz/V at the PZT.

An openloop transfer function of the frequency stabilization is shown in Fig. 4.24. The UGF is around 14 kHz and the phase margin at the frequency is 24°. The temperature actuator has much larger but slower efficiency, so the temperature control loop is dominant below ∼1 Hz and the PZT actuator is dominant in the shown frequency band. The fitting function is generated with the openloop gain divided by the measured filter gain. The fitting parameters are the whole gain and the cutoff frequency of the optical gain, which is the same as the cavity pole. The cavity pole and the finesse of the reference cavity

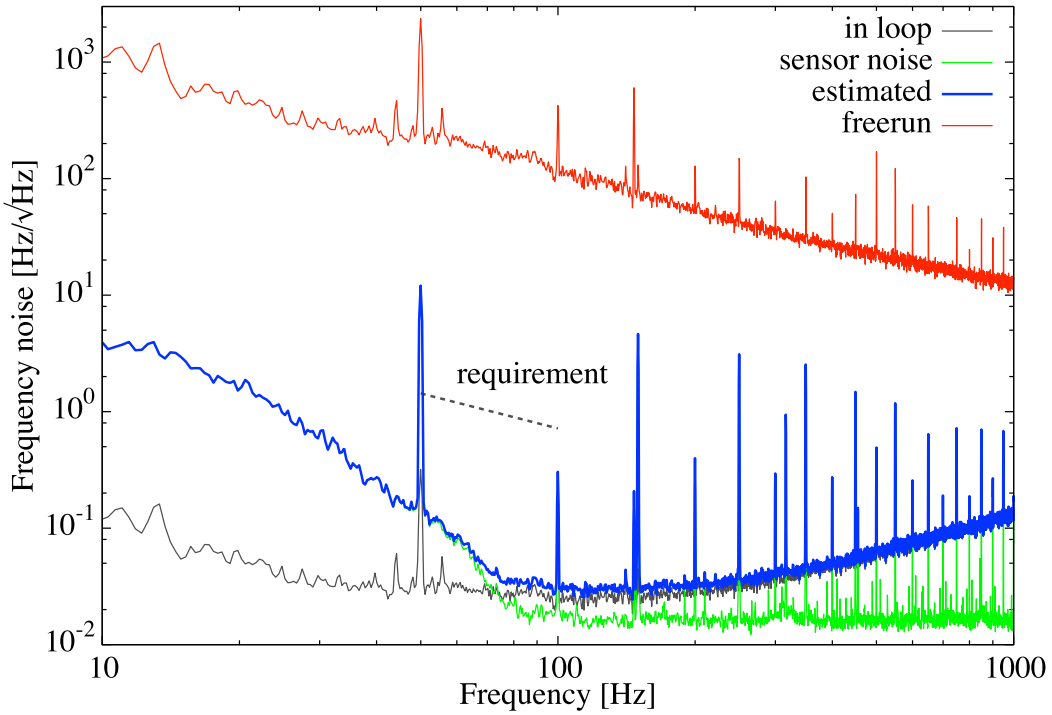

Figure 4.25: Frequency noise of the laser light. The red line shows the noise level of the freerun. The blue line is calculated by summation of the measured in loop signal (the black line) and the sensor noise (the green line). $n_{\mathrm{av}} = 44$.

are measured to be

$$f_{\mathrm{p}} = (2.71 \pm 0.02) \times 10^4\,\mathrm{Hz},\ \mathcal{F} = (6.30 \pm 0.04) \times 10^4, \tag{4.12}$$

respectively. These values are consistent with the calculated ones from the designed reflectivity of ∼99.994%. From the fitting result of the overall gain and the actuator efficiency of $1.51 \pm 0.01\,\mathrm{MHz/V}$, the optical gain below the cavity pole is calculated as $11.4 \pm 0.1\,\mathrm{V/MHz}$. The input power to the reference cavity is 1.5 mW at the measurement of the openloop transfer function and the frequency noise spectrum.

The frequency noise of the laser light is described in Fig. 4.25. The calibration is based on the optical gain and the openloop gain. The estimated freerun level is consistent with the typical spectrum of the NPRO laser source, which is roughly $10^4/f\,\mathrm{Hz}/\sqrt{\mathrm{Hz}}$. The estimation in the control loop only gives the

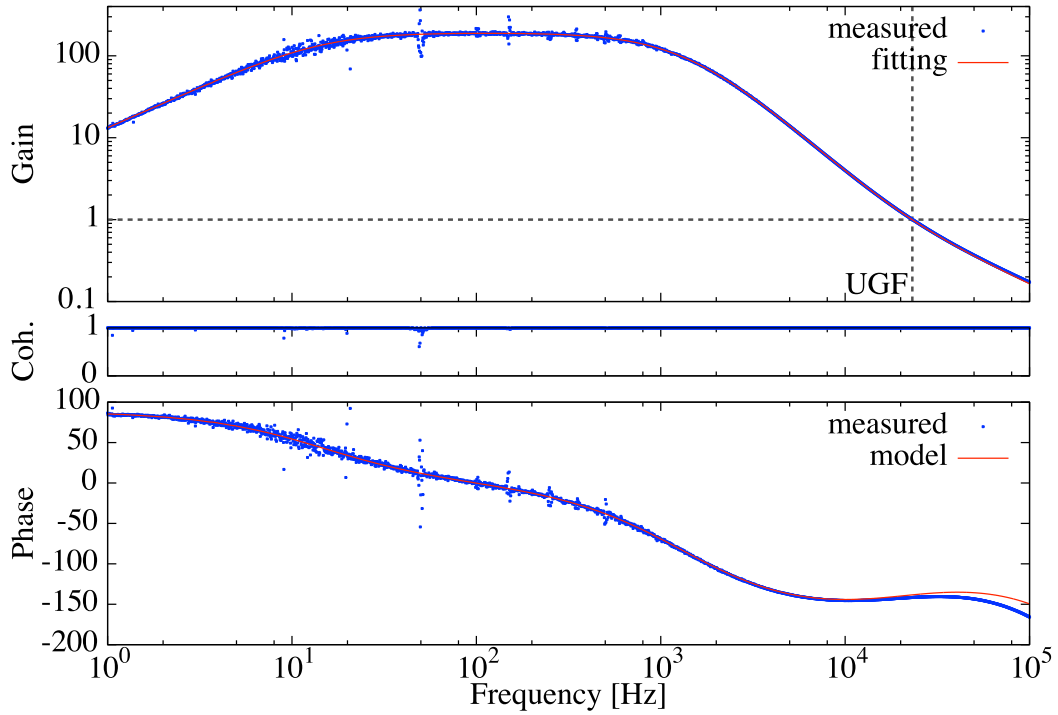

Figure 4.26: An openloop transfer function of the intensity stabilization. The blue dots show the measured data and the red line shows the fitting result with the gain.

lower limit of the real frequency noise. For example, it cannot be stabilized below the sensor noise. The sensor noise is measured by getting the PDH signal with the laser frequency far from resonance of the cavity. It can be considered that the structure is caused by the seismic noise. The thermal noises of spacer of the reference cavity and coating of the cavity mirror is also the issues, but they are smaller than the error signal. Here, It is assumed that the actual frequency noise represented by the blue line, which satisfies the requirement. As noted previously, the requirement is set not to cover the SQL of the test mass with the common mode rejection ratio of 1/10 at both arms.

4.3.3 Intensity stabilization

Intensity stabilization is also important because the classical radiation pressure noise and the amplitude fluctuation entering main PDs must be reduced to

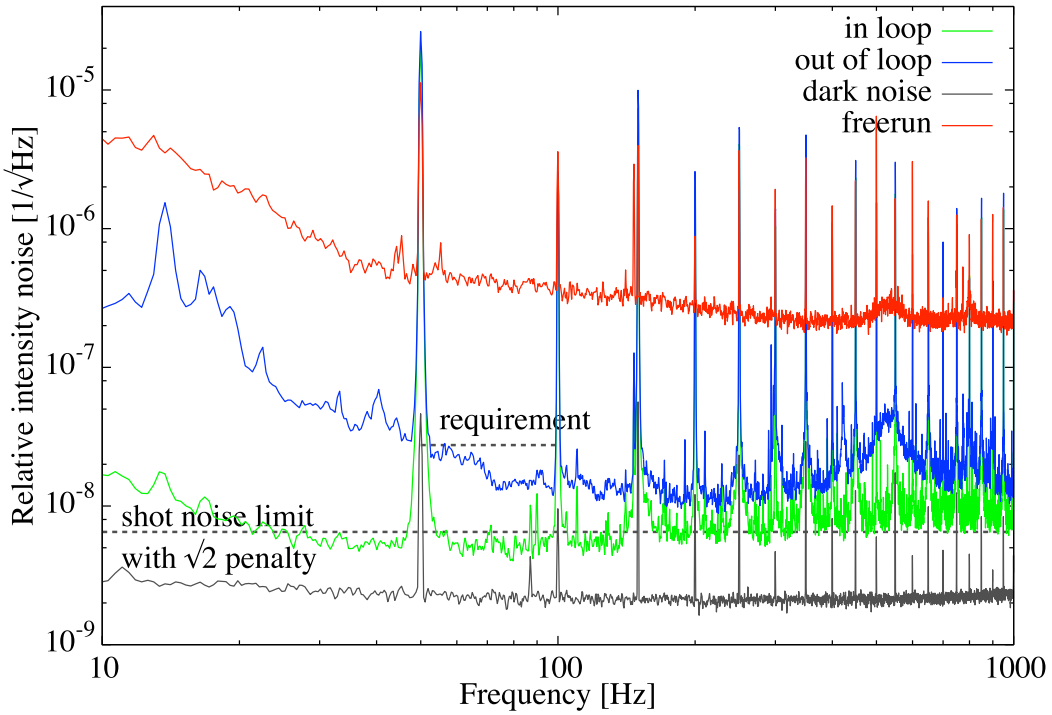

Figure 4.27: Intensity noise of the laser light. The relative intensity noise at the vertical axis means the voltage spectrum divided by the DC voltage. The spectrum of out of loop measurement is represented by the blue lines. The red, green, black solid lines correspond to the noise level of the freerun, error signal in the control loop, and dark noise of the PDs, respectively. $n_{\mathrm{av}} = 44$.

observe the quantum radiation pressure fluctuation. An AOM is used in order to do the stabilization. The AOM diffracts and shifts the laser light with the sound waves at radio frequency typically over MHz. When the sound waves are added to the AOM crystal, the input beam is sprit to the zeroth and first order lights. The divided ratio is determined by the amplitude of the radio wave, so it can be used for the actuator of the intensity stabilization.

Our AOM (Brimrose QZF-80-20) has the shift frequency of 80 MHz and the first order light is used as the main beam. The amplitude can be changed by the input voltage to the AOM driver. After the AOM, the main beam enters the first vacuum chamber and the light is picked off by a PBS, followed by one more junction at another BS before 2 PDs. One is used in the control loop of the intensity stabilization, and the other is for monitor out of the loop. These

PDs are Perkinelmer C30642 InGaAs photodiodes with the diameter of 2 mm.

In Fig. 4.26, an openloop transfer function of the intensity stabilization is shown. We have the UGF of 23 kHz and the phase margin of 38°. A high-pass filter is inserted in series at the filter circuit, and hence the offset to the AOM driver is not changed but the intensity fluctuation can be controlled at the measurement band. The responsibility of the PDs were measured to be 0.79 ± 0.08 A/W in the previous work [105]. The current voltage conversion is done by the resister of 390 Ω and the capacitor of 0.22 μF in parallel (the cutoff frequency of 1.86 kHz). With these parameters and the measurement of the transfer function of the circuit, we can estimate the actuator efficiency of the AOM driver to be 4.4 ± 0.4 mW/V.

We show intensity noise of the laser light in Fig. 4.27. The averaged DC voltage is 5.9 V, so the input power to each PD is calculated as around 19 mW. A broad peak around 500 Hz comes from the vibration of the AOM driver. A structure from 10 Hz to several 10 Hz is thought of due to the seismic noise. The freerun and dark noise signals of the two PDs have similar spectra. Thus, the averaged spectra of the two are shown.

The requirement of the intensity noise is determined as the classical radiation pressure noise becomes smaller than the quantum fluctuation by 1/10 with considering the displacement of common and rotational modes. Here we again note the relative shot noise level given in Eq. 3.35 As discussed at Sec. 4.1, the rotational mode has the effectively light mass. The ratio of the displacement in the two modes by common and differential radiation pressure noise is given by $B_{\rm rsnl}/6$. With the common mode rejection ratio is assumed to be 1/10, the requirement of the relative shot noise level is $B_{\rm rsnl} < 6$.

The relative intensity shot noise is given by

$$\sqrt{S_{\rm shot}} = \sqrt{\frac{2e}{\rho_{\rm PD} P_{\rm in}}}\ [1/\sqrt{\rm Hz}], \tag{4.13}$$

where $\rho_{\rm PD}$ is the responsibility of the PD and $P_{\rm in}$ is the input power. It is typically the order of $10^{-9}/\sqrt{\rm Hz}$ at the input power of a few 10 mW. On the other hand, the relative intensity noise $\sqrt{S_{\rm rin}}$ of the NPRO laser is around the order of $10^{-7}/\sqrt{\rm Hz}$. Thus, about 100-times stabilization is necessary toward the shot noise level. Even though the openloop gain is high enough, a noise

penalty cannot be avoided owing to the method picking the light off. Fluctuation of electrical fields at reflection δE_{r} and transmission δE_{t} of a BS can be described as

$$\begin{cases} \delta E_{\mathrm{r}} &= r_1 \delta b_{\mathrm{in}} + t_1 \delta \alpha_{\mathrm{as}} \\ \delta E_{\mathrm{t}} &= t_1 \delta b_{\mathrm{in}} - r_1 \delta \alpha_{\mathrm{as}}, \end{cases} \tag{4.14}$$

where r_1 and t_1 are the amplitude reflectivity and transmissivity of the BS, δb_{in} is the electrical field of the input light, and $\delta \alpha_{\mathrm{as}}$ is the vacuum field from anti-symmetric port of the BS. When we suppress the fluctuation as $\delta E_{\mathrm{r}} = 0$, $\delta b_{\mathrm{in}} = -t_1/r_1 \alpha_{\mathrm{as}}$ is satisfied. With substituting it, the measured transmission goes to

$$\delta E_{\mathrm{t}} = -\frac{\delta \alpha_{\mathrm{as}}}{r_1}. \tag{4.15}$$

It means that the relative shot noise level can never be below $1/r_1$. In our case the penalty factor is $\sqrt{2}$ because we use the BS of $r_1 = 1/\sqrt{2}$.

4.3.4 Auxiliary optics

In Fig. 4.28, we describe the auxiliary optics for the main cavities. It includes 2 CCD cameras for monitoring transmission light from the test mass, 2 PDs for getting the main amplitude signals, and steering mirrors with picomotors. These are located on the floor of the building for the suspension of the main cavities. Moreover, there are 2 asymmetric Michelson interferometers to measure the actuator efficiencies of the controlled mirrors, and the control system of the yaw mode of the platform with an optical lever and a coil-magnet actuator. Laser light for these system is injected from the back of the second vacuum chamber. Steering mirrors and lenses for mode matching of the beam in the Michelson interferometers are also on the floor of the building. A mirror with a magnet at its side for the optical lever and the control is attached to the edge of the platform. In Fig. 4.29, a photograph of the auxiliary optics is shown.

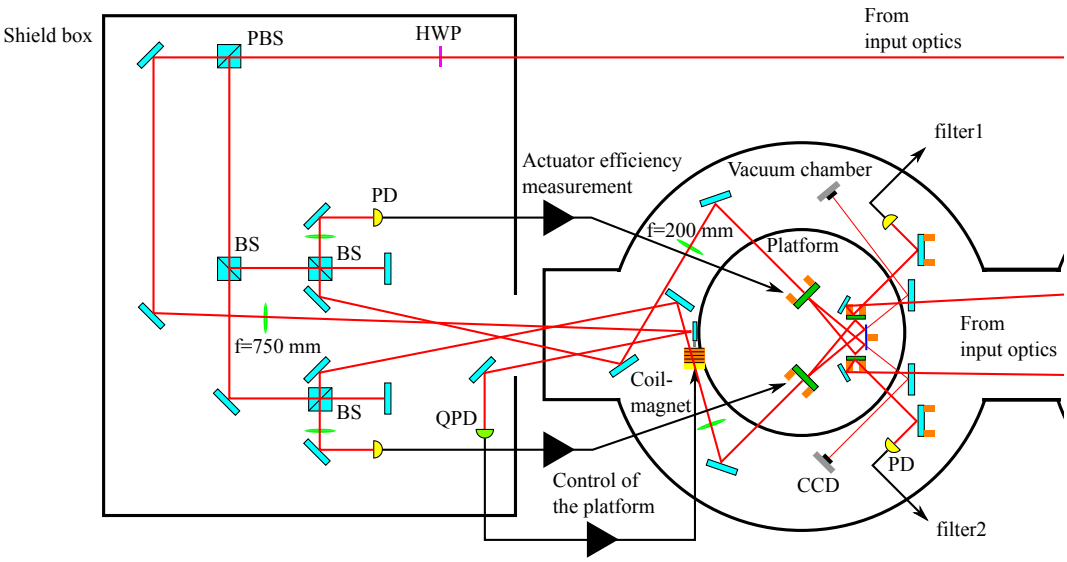

Figure 4.28: A schematic picture of the associated optics. The components on the platform are simplified. Similarly to the input optics, parts out of the vacuum chamber is in an acrylic shield box.

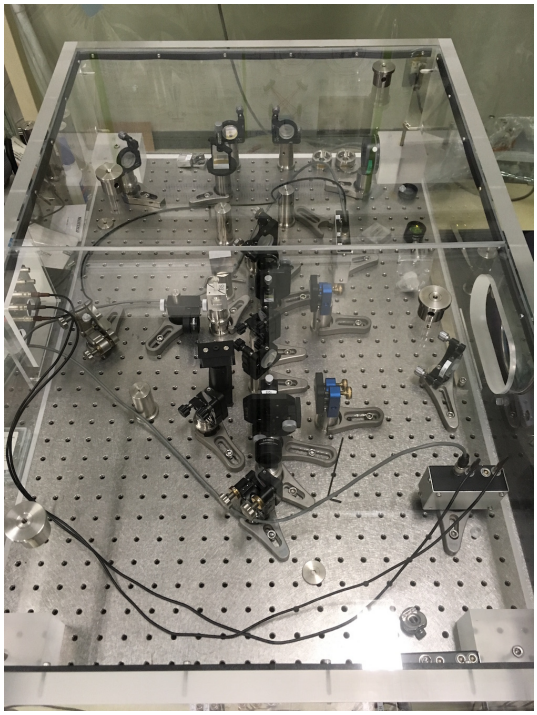

Figure 4.29: A photograph of the entire apparatus of the auxiliary optics.

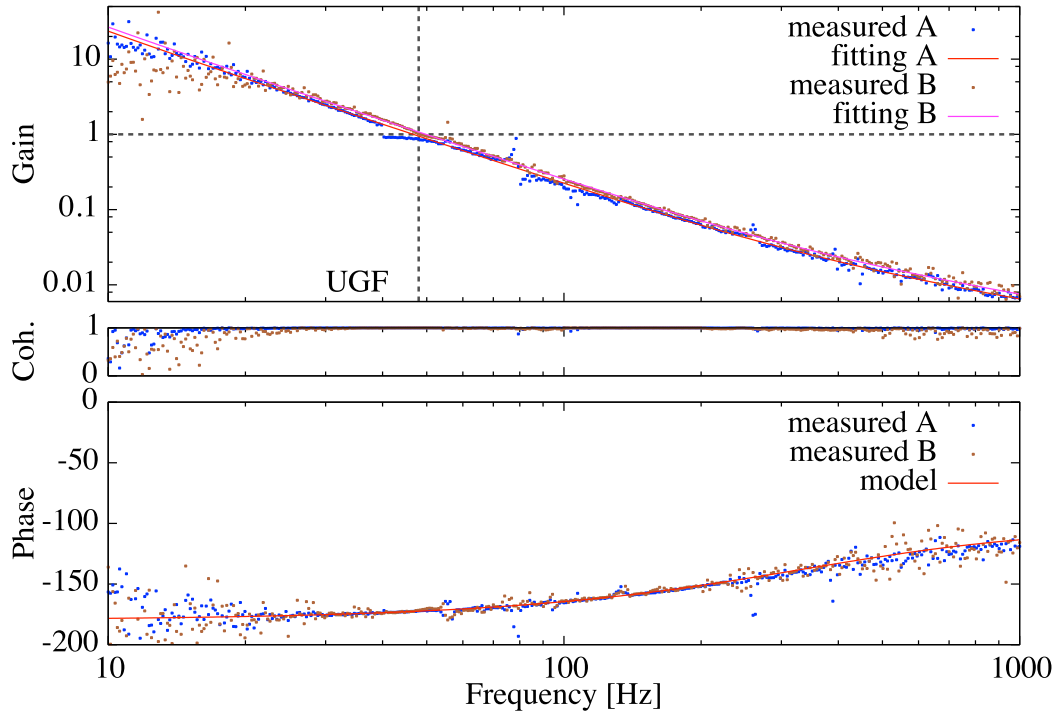

Figure 4.30: Openloop transfer functions of the control of the Michelson interferometers. The blue and brown dots show the measured data of each control and the red and magenta lines show the fitting result with the actuator efficiencies.

Actuator efficiency measurement

The actuator efficiencies of the 2 controlled mirrors should be measured for calibration from measured voltage to displacement of the main cavities. Each efficiency is measured by constructing the Michelson interferometer with a fixed mirror close to the BS in the shield box and the controlled mirror from whose back the light comes. The interferometers are locked in the mid fringe. Fig. 4.30 represents openloop transfer functions of the control of the Michelson interferometers. The actuator efficiency of force added to the controlled mirror per unit voltage (N/V) can be calculated by dividing the openloop transfer function by the sensor efficiency, the measured transfer function of measured filter and the susceptibility of the controlled mirror.

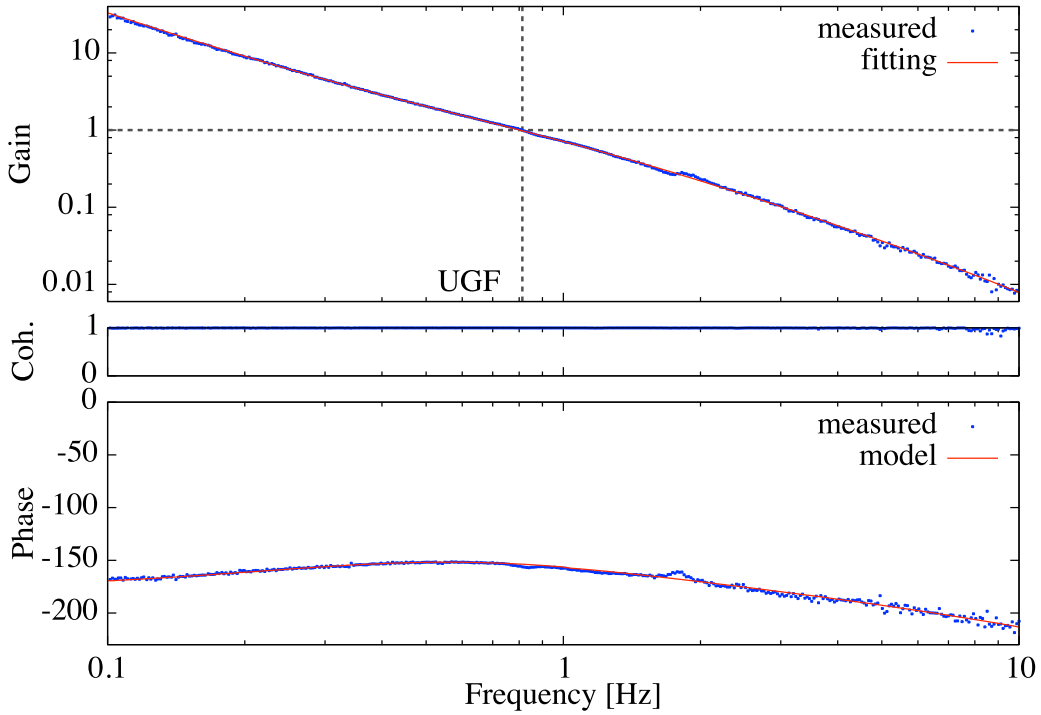

Figure 4.31: An openloop transfer function of the control of the yaw platform. The blue dots express the measured data and the red line shows the fitting result with the overall gain multiplied by the transfer function of the filter circuit.

The error signal of the Michelson interferometer is given by

$$V_{\mathrm{MI}}(x) = A \sin\left(\frac{4\pi}{\lambda_{\mathrm{L}}} x\right), \tag{4.16}$$

where A is the voltage amplitude and x is the displacement. The locked point is $x = 0$. Therefore, the sensor efficiency can be calculated as $V'_{\mathrm{MI}}(x = 0) = 4\pi A/\lambda_{\mathrm{L}}$ [V/m]. A can be measured by observing the error signal caused by the free oscillation of the controlled mirror. After measuring each sensor efficiency, we calculate the actuator efficiency at different frequencies and get the average. They are estimated to be $(3.7 \pm 0.4) \times 10^{-4}$ N/V and $(3.3 \pm 0.3) \times 10^{-4}$ N/V respectively. The errors derive from the standard devision of the data.

Control of the platform

The platform for the main cavity is suspended by a single wire. The resonant frequency of the rotational mode is around 10 mHz and it can be easily excited due to touch to the platform following the long time taking until it gets stable. Thus, it is necessary to control the yaw motion of the platform. We pick off a part of the laser light for the actuator efficiency measurement and use it as an optical lever. The beam reflects from the mirror attached to the edge of the platform and enters the QPD. The yaw motion of the platform is sensed by the horizontal signal of the QPD. The signal goes to the coil-magnet actuator for the feedback control.

In Fig. 4.31, an openloop transfer function of this control is shown. The UGF is around 0.8 Hz and the phase margin is about 25°. The reason of this slow control is for the actuator not to give the motion of the platform around several Hz. The resonant frequency of the yaw mode is around 15 mHz without any components on the platform, but it can be changed by the damping magnets for the control mirror. Actually, the stable position of the platform varies by whether the magnets are installed on the platform or not. It is also the reason why the damping magnets for the controlled mirror consist of 4 pieces. Susceptibility of the platform for magnetic field out of the platform is made to be as small as possible by combining 4 magnets with alternating N and S poles.

4.3.5 Vacuum system

As described in the previous figures, sensitive components are located in the vacuum chambers to avoid the effect of the residual gas. A schematic picture of the vacuum chambers and the table are represented in Fig. 4.32. The table is on 4 pieces of rubbers at each leg for vibration isolation. The input optics is in the right chamber and the main cavities are in the left one. Measurement of the pressure and vacuum leak is done via the port behind the right chamber. Signals for picomotors and coils go through the lead ports. Entrance windows for laser light have the anti-reflection coatings.

Two types of vacuum pumps for evacuation are used, although they are not drawn in the figure. The evacuation is done from the floor of the right

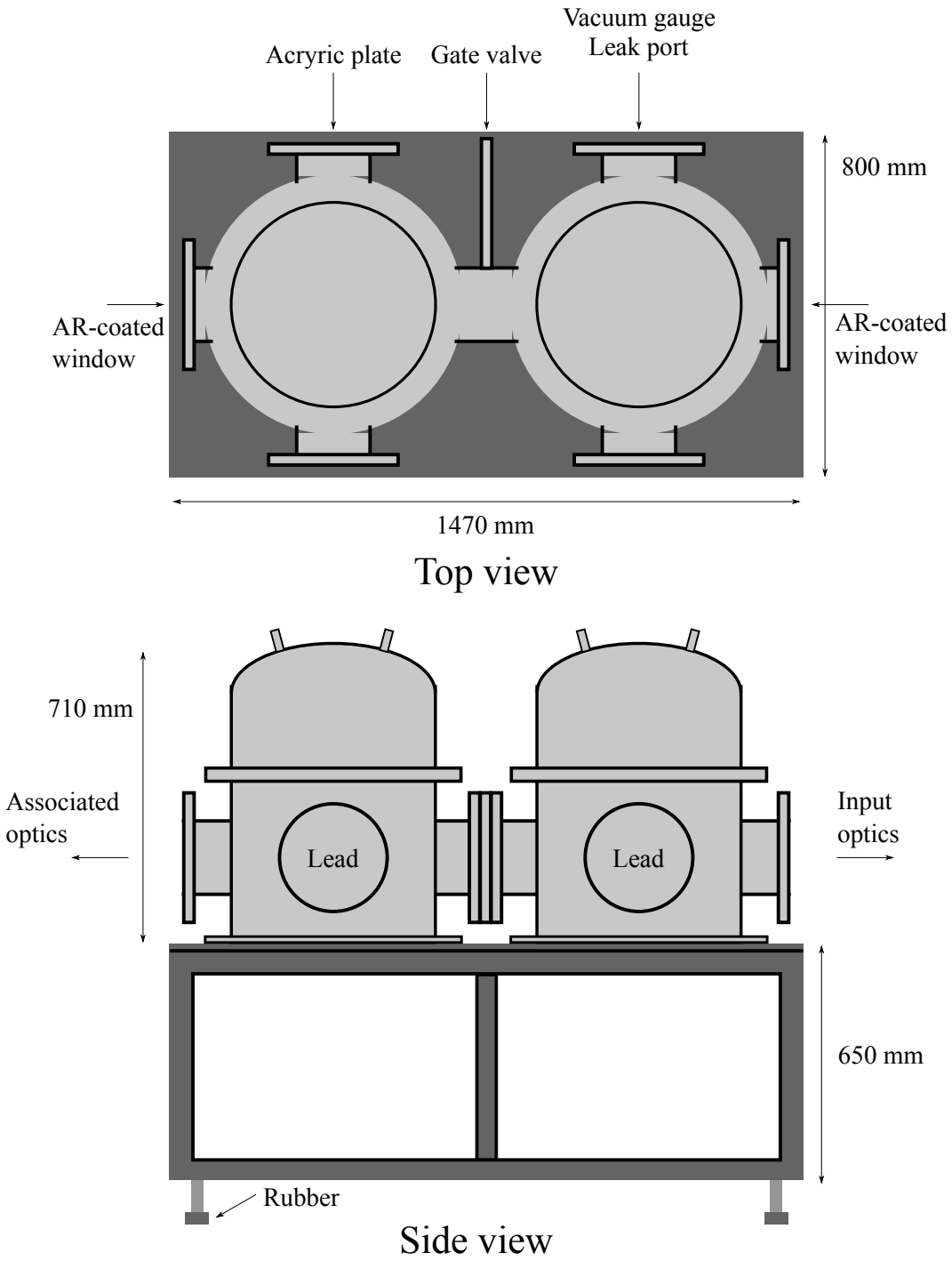

Figure 4.32: Top and side views of the vacuum chambers and the table.

chamber. One pump is an oil-sealed rotary one (Edwards RV12) for the rough evacuation. The other is a turbo-molecular pump (Osaka vacuum TG450F) for as low pressure as possible. The reached vacuum level goes below 2×10^{-4} Pa without any components in the chambers and 3×10^{-4} Pa with all parts inside for a few days.

The sound and the air flow are the issues at air pressure, and at low pressure thermal noise of the residual gas molecules hitting the test mass randomly can be the noise of the measurement. The dissipation of the residual gas is given by [48].

$$\gamma_{\mathrm{gas}} = \frac{P}{Ch\rho}\sqrt{\frac{m_{\mathrm{mol}}}{k_{\mathrm{B}}T_{\mathrm{th}}}}, \tag{4.17}$$

where P, h, ρ, and m_{mol} are the pressure, the thickness of the mass, the density of the mass, and the mass of dominant molecules, respectively. C is a dimensionless constant of order unity depending on the shape of the oscillator. It is viscous damping without frequency dependence of the dissipation because the force proportional to the velocity is added. In our experiment, the residual gas noise at the pressure of 2×10^{-4} Pa is smaller than the quantum radiation pressure fluctuation. Finally, we show a photograph of the entire apparatus of our setup in Fig. 4.33.

4.4 Summary of this chapter

A bar-shaped mirror as a torsion pendulum which has two optical cavities at both edges is designed in order to realize observation of quantum radiation pressure fluctuation. The rotational mode is measured by subtracting one of the displacement signals from the other. This setup has advantages such as the low suspension thermal noise, the common mode rejection, and the light effective mass. We show all setup designs and associated results.

Figure 4.33: A photograph of the entire apparatus of our setup. The apparatus consists of the input optical table, the first vacuum chamber including the intensity and frequency stabilization system, the second chamber containing the main cavities, and the associated optics from the front to the back. The time series data are recorded in a logger at the right top. We see outputs of the CCD cameras with a monitor for the cavities resonance.

Chapter 5

Experimental result

In the previous chapter, we describe the experimental setup and the associated system to observe the quantum radiation pressure fluctuation at 50-100 Hz. The stabilization of the laser frequency and intensity and the vibration isolation reach enough level for the goal. Here, the main result of the experiment is shown.

The displacement spectra of the torsion pendulum cavities are described in section 5.1. We discuss how the spectra are calibrated from the error signals to the displacement in section 5.2. In section 5.3, the displacement due to the quantum radiation pressure fluctuation is estimated with based on a theoretical equation and the bar thermal noises. Estimation and measurement errors are discussed and summarized in section 5.4.

5.1 Main result

First of all, we focus on our main results of the displacement spectra. Method of controlling the cavity length is also introduced here.

5.1.1 Displacement spectrum

In Fig. 5.1, we show the displacement spectra of the measured differential mode and the estimated quantum radiation pressure fluctuation acting on the test mass. The measured differential spectrum reaches $3 \times 10^{-15}\,\mathrm{m}/\sqrt{\mathrm{Hz}}$ between 60 Hz and 100 Hz. During this measurement, the quantum radiation pressure

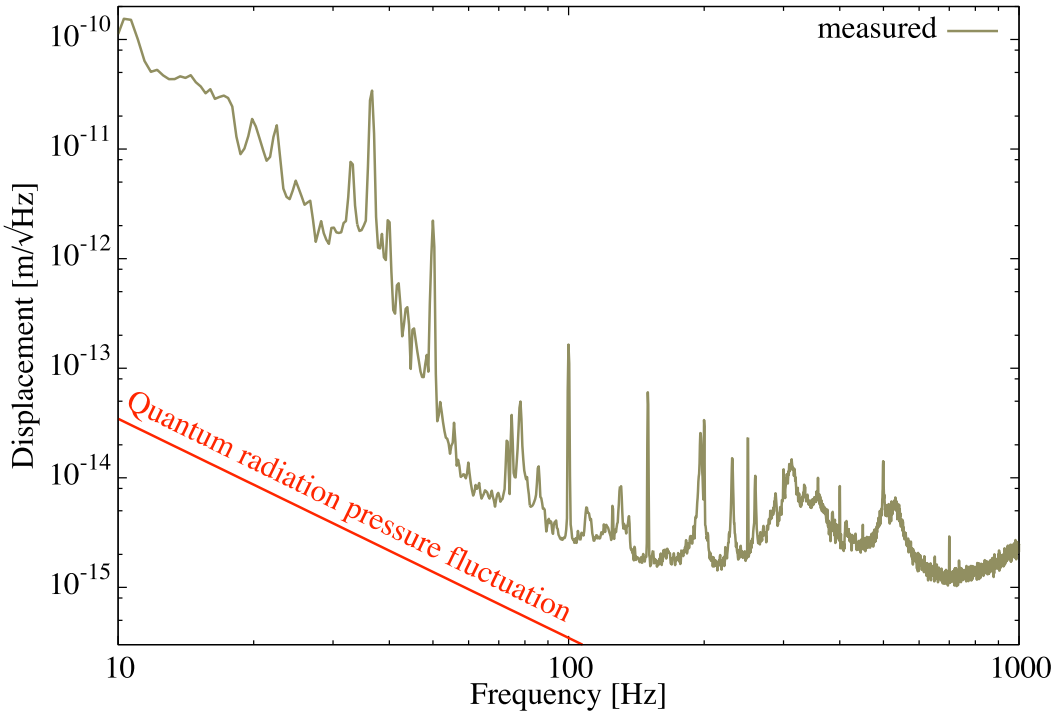

Figure 5.1: Differential displacement spectrum of the cavities. The gold line shows the measured spectrum, $n_{\mathrm{av}} = 44$. The estimated quantum radiation pressure fluctuation acting on the bar mirror is represented as the red line.

fluctuation contributes to the spectrum by $3.6 \times 10^{-16}\,\mathrm{m}/\sqrt{\mathrm{Hz}}$. The signal to noise ratio is estimated to be 0.14 ± 0.03. This value is the most highest signal to noise ratio for measurement of quantum radiation pressure fluctuation.

The displacement spectra of each cavity are described in Fig. 5.2. We get the differential signal by subtracting each voltage signal as

$$V_{\mathrm{diff}} = V_{\mathrm{B}} - 0.575 V_{\mathrm{A}}, \tag{5.1}$$

calculate the spectrum, and calibrate it with the calibration factor from voltage to displacement of the B cavity. The factor of 0.575 is determined from a view point of the common mode rejection. It gives the best common mode rejection ration of 0.05 to the peak height at 73 Hz. This peak is due to the vibration of the vacuum pump. The floor sensitivity is also improved the most with the factor of 0.575.

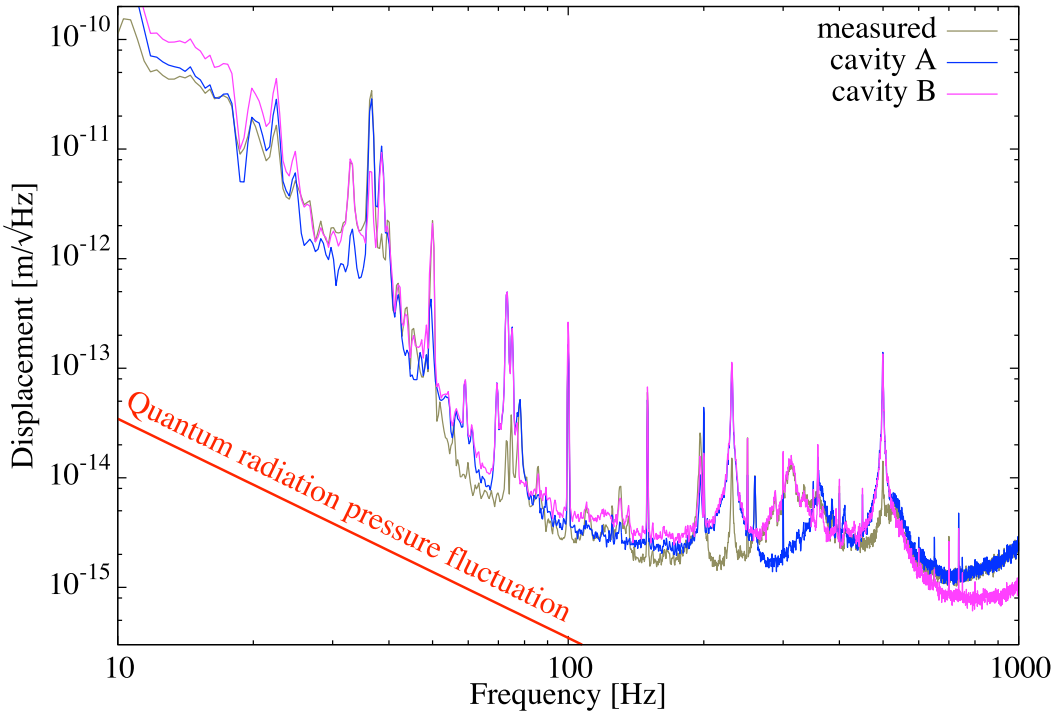

Figure 5.2: Displacement spectra of each cavity. The blue and magenta lines represent the spectra of the cavity A and B.

5.1.2 Control method

In the main experiment, we lock the cavity length at one side of a shoulder of the cavity Lorentzian where the restoring force of the optical spring is positive, and do not use the PDH method. The amplitude of the reflection from the cavity is detected by a PD (Hamamatsu G10899-03K). The offset is adjusted as the targeting point of the Lorentzian becomes zero before the filter. The filter circuits has phase compensation around 1 kHz. The feedback signal goes to a coil driver for the coil-magnet actuator, and the cavity length is controlled to keep the resonance.

It takes a period of time, typically several 10 s, to lock the cavities. When the one arm is locked, constant radiation pressure pushes the bar mirror and rotates it, resulting in breaking the lock. Therefore, the simultaneous locking is required. Both of initial locked points are far from the resonance peaks. They are not zero points of each error signal. After the initial lock, we change

the offset of the coil drivers and push the controlled mirrors to the zero points which are close to the peak. We need to take care of the filter gains during the adjustment of the locked points. It is because the optical gain gets larger as the locked point is close to the peak and the feedback control cannot help oscillating with the same filter gain owing to some oscillation sources.

This manipulation is done with looking at the error signals and videos of CCD cameras. A small rotation of the controlled mirror is caused by unbalance of actuator efficiencies at the right and left coil-magnets. That rotation can be judged by the CCD camera, and it is modified by differential offset to change its yaw mode manually. These cameras are also used at the adjusting the alignment of the cavities and improving the mode matching of the TEM00 modes.

5.2 Calibration

In this section we discuss the calibration from the voltage signal to the displacement. The calibration is one of the most important factors for observing the target signal. First, a block diagram for our feedback control system is described. Next, our experimental key technic of the optical spring is shown with the result of openloop transfer function measurements.

5.2.1 Block diagram

A block diagram of the transfer functions described in Fig. 5.3 can help clearer understanding. This diagram shows the control loop of one cavity and at which points noise sources are introduced. We have 2 loops in the block diagram. One corresponds to the optical spring, and the other is for the active feedback control of the cavity length. These openloop gains are defined as G_1 and G_2 respectively.

The error voltage signal is calibrated to the displacement. Especially, we consider the displacement x_{dis} when the measured force is added to the torsion pendulum as a free mass. The displacement of one cavity can be expressed by

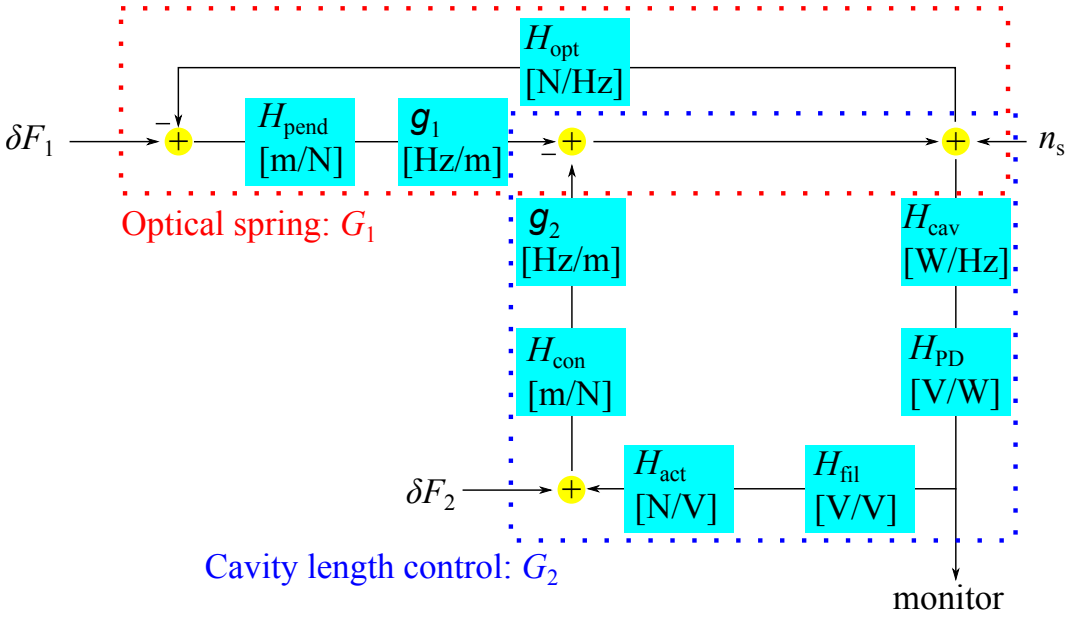

Figure 5.3: A block diagram of the control used in the main experiment. Each blue box with the unit shows the transfer function at each experimental component. $H_{\rm pend}$ [m/N] and $H_{\rm con}$ [m/N] mean the mechanical susceptibilities, and g_1 and g_2 are the optomechanical coupling constant of the test mass and the controlled mirror, respectively. $H_{\rm cav}$, $H_{\rm PD}$, $H_{\rm fil}$, and $H_{\rm act}$ show the optical, PD, filter, and actuator gain. The filter includes the circuit to change the offset of the error signal. δF_1 and δF_2 are force noises added to the test mass and the controlled mirror, and $n_{\rm s}$ is the sensing noise in the cavity such as the frequency noise.

the error signal $V_{\rm error}$ and the transfer functions as

$$x_{\rm dis} = \left| \frac{1+G_0}{G_0} \frac{g_2}{g_1} H_{\rm fil} H_{\rm act} H_{\rm con} \right| V_{\rm error}, \tag{5.2}$$

where $G_0 = G_2/(1+G_1)$ is the total openloop gain. Then, we obtain two displacement spectra of each cavity and the differential spectrum. The optomechanical coupling constants of g_1 and g_2 and the mechanical susceptibility of the controlled mirror $H_{\rm con}$ are decided by the mechanical design. The actuator efficiency $H_{\rm act}$ is already measured by the Michelson interferometer. Therefore, the filter and openloop transfer functions are required to be measured in order to calibrate the signal.

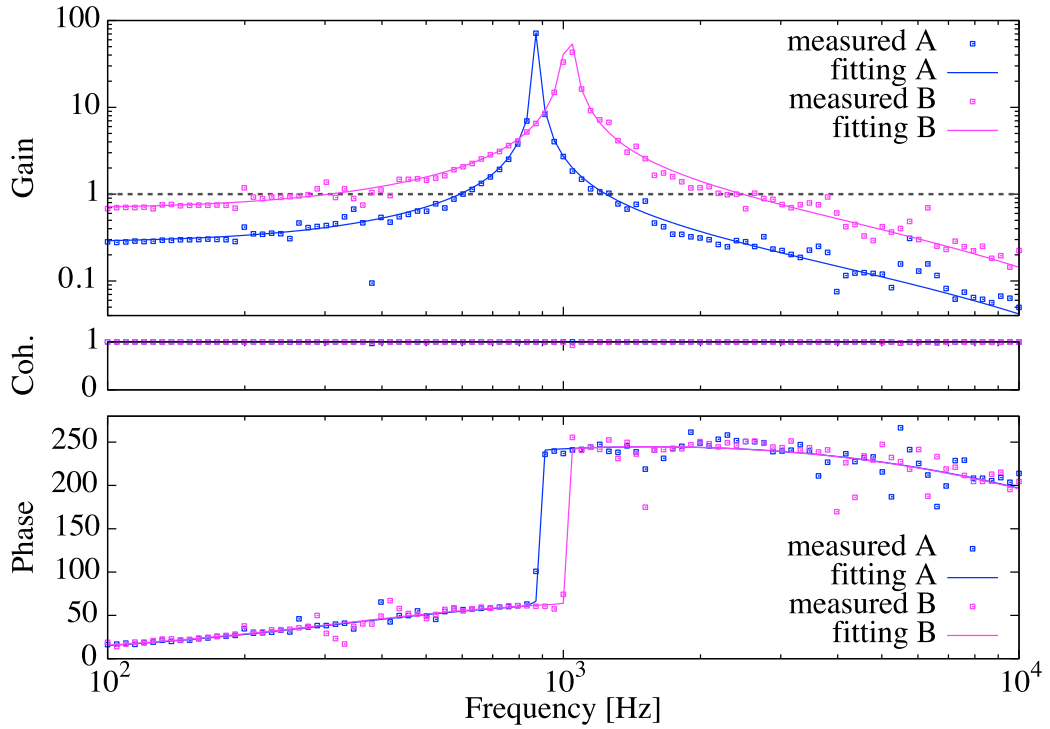

Figure 5.4: Openloop transfer functions of the cavity controls. The blue and brown dots show the measured data of each control and the red and magenta lines show the fitting result with the resonant frequencies and the optical gains.

5.2.2 Optical spring

We measure the openloop transfer function by injecting sine waves at various frequencies after the filter circuit and getting the ratio of signals just before and after the injection port. This openloop gain is equal to G_0 and includes the susceptibility of the optical spring. The optical spring constant is given by $K_{\rm opt} = H_{\rm opt} g_1 = m\omega_{\rm opt}^2$, where m is the mass of the torsion pendulum and $\omega_{\rm opt}$ is the angular resonant frequency due to the optical spring. In our configuration, the mechanical susceptibility $H_{\rm pend}$ and $H_{\rm con}$ can be approximated as those of free masses above 10 Hz, *i.e.*, $H_{\rm pend} \simeq -1/(m\omega^2)$ and $H_{\rm con} \simeq -1/(M\omega^2)$, where M is the mass of the controlled mirror. Hence, the total openloop gain is proportional to

$$G_0 \propto \frac{H_{con}}{1+G_1} \simeq \frac{1}{M(\omega_{\rm opt}^2 - \omega^2)}, \tag{5.3}$$

without the damping constant.

In Fig. 5.4, measured openloop transfer functions are represented on two cavities. We can observe the peak due to the optical spring at $0.88 \pm 0.02\,\mathrm{kHz}$ and $1.03 \pm 0.02\,\mathrm{kHz}$. The original mechanical resonant frequency of about 3 Hz is increased by a few 100 times higher. This strong optical springs realize the robust locking of the cavities. The frequency region whose gain is over unity is around the optical spring resonance. The difference between two resonant frequencies is due to the different finesse, detuning, mode matching, and input power of the two cavities. Moreover, we estimate the optical gain from the displacement of the bar mirror to the voltage signal from another fitting parameter. These values are $(6.3 \pm 0.6) \times 10^9\,\mathrm{V/m}$ and $(1.0 \pm 0.1) \times 10^{10}\,\mathrm{V/m}$.

5.3 Quantum radiation pressure fluctuation

Here, we discuss how the displacement caused by quantum radiation pressure fluctuation can be estimated. It is important at calculating the signal to noise ratio of the target. Our estimation method making use of the optical resonant frequency is tolerant of various systematic errors. Moreover, we can measure the beam spot position of the bar mirror using the resonance of the internal modes, and estimate the normalized detuning during the operation also using the optical resonant frequency.

5.3.1 Expression with optical spring

As described in Eq. 5.5, the theoretical force spectrum of quantum radiation pressure fluctuation

$$S_{\mathrm{f,qrp}} = \frac{32\hbar\omega_{\mathrm{L}}\mathcal{F}^2 P_{\mathrm{in}} \cos^2\beta}{\pi^2 c^2} \frac{\kappa_{\mathrm{in}}}{\kappa} \frac{1}{(1+\delta^2)^2}, \tag{5.4}$$

has a large systematic error of P_{in}. Experimentally, the effective input power includes the mode matching ratio of the input beam to the cavity. The alignment is slightly changed because of the DC radiation pressure, so it is difficult to estimate the precise mode matching ratio when the cavity is resonating.

Moreover, the PD responsibility has also large errors about 10%, and $\kappa_{\rm in}/\kappa$ of the cavity is not easy to be measured.

However, we find the method which is tolerant of these systematic errors with the optical spring resonant frequency. According to Eq. (3.29), the real part of optical spring constant is given by

$$K_{\rm opt} = \frac{16\omega_{\rm L}\mathcal{F}^2 P_{\rm in}\cos^2\beta}{\pi^2 c^2}\frac{\kappa_{\rm in}}{\kappa}\frac{\delta}{(1+\delta^2)^2}. \tag{5.5}$$

This spring constant can be written as $K_{\rm opt} = m\omega_{\rm opt}^2$, so substituting this to Eq. (5.4) we get a simple formula as follows:

$$S_{\rm f,qrp} = \frac{2\hbar}{\delta} m\omega_{\rm opt}^2. \tag{5.6}$$

Therefore, the differential displacement of the test mass due to quantum radiation pressure fluctuation is calculated as

$$\sqrt{S_{\rm x,qrp}} = \frac{12(L_{\rm A}+L_{\rm B})}{L^2\omega^2}\sqrt{\frac{2\hbar}{m}\left(\frac{L_{\rm A}^2\omega_{\rm opt,A}^2}{\delta_{\rm A}} + \frac{L_{\rm B}^2\omega_{\rm opt,B}^2}{\delta_{\rm B}}\right)}, \tag{5.7}$$

where $L_{\rm A}$ and $L_{\rm B}$ are the beam spot positions from the center of the bar, and the indices of A and B show each cavity. Our next step to estimate the displacement is measuring the beam spot positions on the bar mirror.

5.3.2 Beam spot position

We can measure the beam spot positions on the test mass with the resonance peaks of the bar bending modes. As described in Fig. 4.4, the test mass has the eigen modes of the substrate. In Fig. 5.5, we show displacement of position at the bar. The beam spot position decides the displacement of the modes. Therefore, the position can be calculated by getting the ratio of the peak hight of these two modes.

The spectra of the error signals around the bending modes are shown in Fig. 5.6. Measured resonant frequencies of the 1st and 2nd bending modes are 5.779 kHz and 15.91 kHz. The ratio of these frequencies are different from that of theoretical values only by 0.2%. The absolute values are higher by 10%,

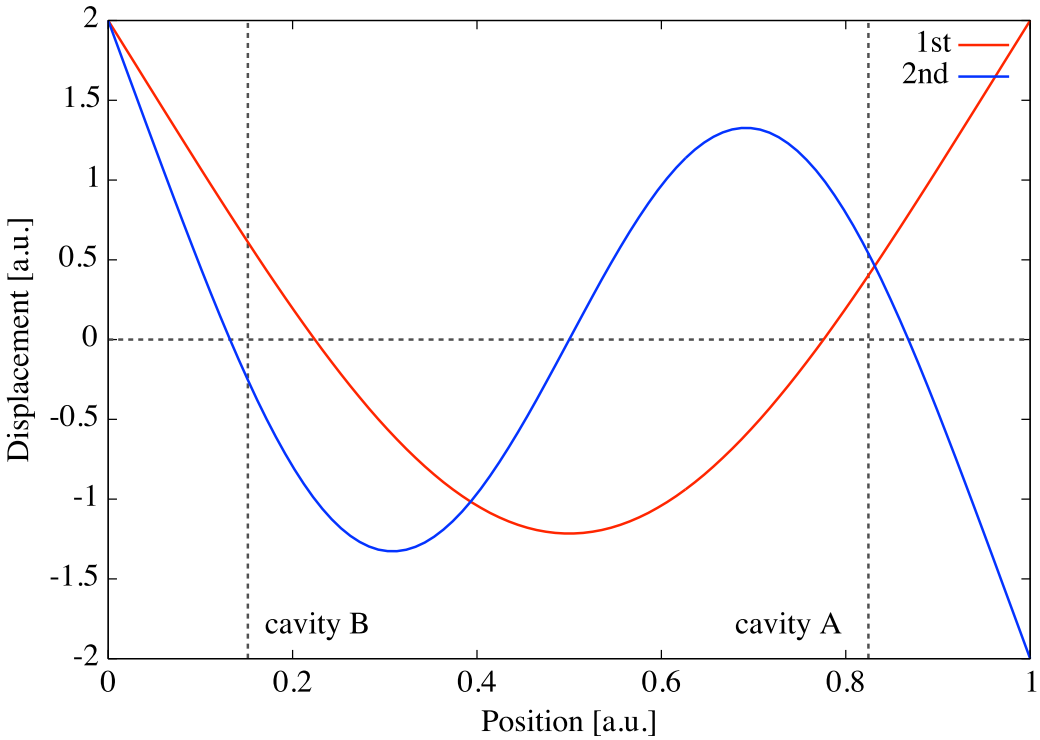

Figure 5.5: Displacement of position at the bar. The red and blue lines show the displacement of the 1st and 2nd bending modes. Both axises are normalized. The origin of the position is the left edge of the test mass, and the right edge corresponds to the position of 1. The vertical dotted lines mean measured positions of each cavity.

which can result from the larger Young's modulus by 20% or lower density of the substrate by 20%.

The fitting results, whose function is the mechanical susceptibility multiplied by a constant, are also described. The fitting parameters are the floor value and the Q-value of each mode. The estimated Q-values are $2 - 3 \times 10^3$. This low values for the substrate are due to a kind of feedback cooling with the filter circuit. Actually, the feedback control of the cavities are broken owing to the oscillation of the 1st bending mode when the filter gain is not large enough. With another fitting parameters of the floor value, we calculate the ratio of the displacement amplitude of the modes in order to corresponding the beam spot positions. The positions are estimated to be $L_{\mathrm{A}} = 4.82 \pm 0.05\,\mathrm{mm}$ and $L_{\mathrm{B}} = 5.22 \pm 0.04\,\mathrm{mm}$. That is to say, the effective bar length for the radiation

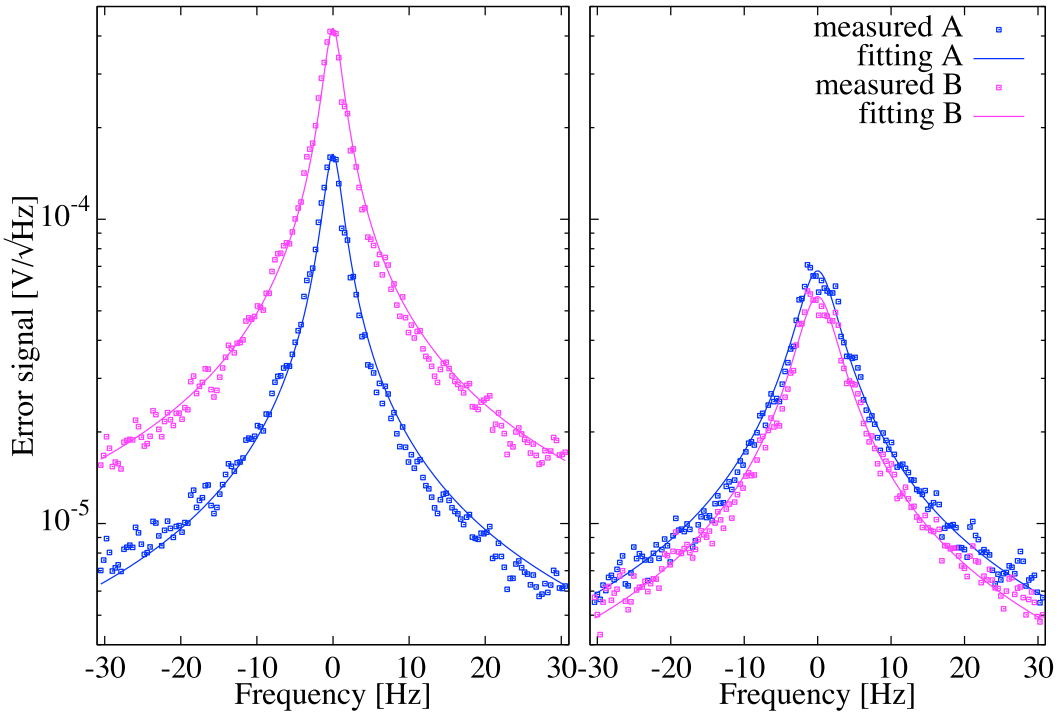

Figure 5.6: Error signals around the bending modes. The blue and magenta dots show the measured spectrum, and the blue and magenta lines represent the fitting result of each cavity. $n_{\mathrm{av}} = 44$. The origins of the frequency are at 5.779 kHz and 15.91 kHz, respectively.

pressure is $L_{\mathrm{A}} + L_{\mathrm{B}} = 10.0\,\mathrm{mm}$. The result of the position estimation is shown in Fig. 5.5 as vertical dotted lines.

5.3.3 Normalized detuning

Finally, we need to calculate the normalized detuning of the cavities during the operation. The normalized detuning is determined by comparing the reflection power with the result of the cavity scan. The result, however, can be changed with the cavity resonating because the radiation pressure pushes the mirror and gets the mode matching worse. Thus, it is difficult to estimate the precise detuning. Here the normalized detuning are calculated with the optical spring frequencies. The resonant frequencies are around their maximum theoretically predicted with the cavity optical parameters. It has the maximum at the

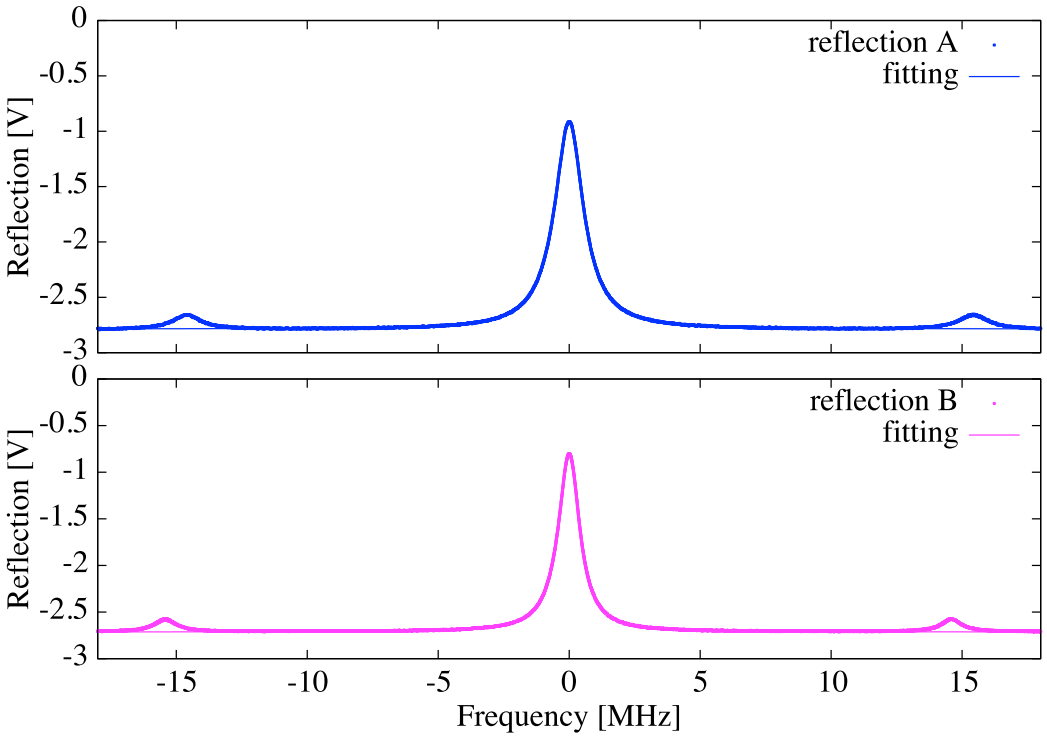

Figure 5.7: Cavity scans of the main cavities around the resonance peak. The blue and magenta dots show the measured data, and the lines show the fitting result of cavity A and B, respectively. The vertical axis expresses the actual voltage output of PDs measuring the reflection.

normalized detuning of $\delta = 1/\sqrt{3}$, so we can estimate it to be around $1/\sqrt{3}$.

The cavity parameters are measured by cavity scans. First, information around the resonance peak of the TEM00 mode gives the cavity line width. In Fig. 5.7, the result of the cavity scans around the peak is represented. The cavity is scanned spontaneously by the residual oscillation caused by seismic motion. The frequency reference is the 15-MHz sideband. The error of the estimated line width derives from the difference of the sideband interval which is due to changing speed of the pendulum oscillation.

Next, the scan across the FSR is used to measure the cavity FSR and mode matching ratio. The frequency reference for the FSR measurement is also the sideband, and the FSR value is averaged with some intervals. The FSR gives the cavity round trip length, and the ratio of the doubled cavity line width and the FSR is equal to the finesse. We get the mode matching ratio

Property	cavity A	cavity B
Finesse	$(3.0 \pm 0.3) \times 10^3$	$(2.4 \pm 0.2) \times 10^3$
Cavity line width [MHz]	0.67 ± 0.03	0.49 ± 0.02
FSR [GHz]	3.0 ± 0.3	3.4 ± 0.2
Round trip length [cm]	9.9 ± 0.9	8.9 ± 0.6
$\kappa_{\mathrm{in}}/\kappa$	0.65 ± 0.04	0.66 ± 0.04
Input power [mW]	18 ± 1	19 ± 1
Mode matching ratio	$77 \pm 3\%$	$75 \pm 3\%$

Table 5.1: List of measured parameters related to the cavities.

by dividing the TEM00 peak height by sum of the height of all peaks. The maximum effective input power to the cavity can be given by the calibrated reflection voltage with the impedance and responsibility of the PD multiplied by the mode matching ratio. Based on the mode matching ratio and the reflection voltage on resonance, the coupling rate of the injection, $\kappa_{\mathrm{in}}/\kappa$, can be calculated. Over and under coupling degenerate only with information of the reflection, but in our experiment the cavity can be concluded to be over coupling because the under coupling cavity with the measured finesse cannot realize the measured optical spring. These parameters are listed in Table 5.1.

We can predict the optical resonant frequencies with these parameters as shown in Fig. 5.8. This figure represents the estimated optical resonant frequency of normalized detuning including the error with the shaded area. The estimation error mainly results from that of the cavity finesse, which is a little less than 10%. When our cavities are under coupling, the assumed $\kappa_{\mathrm{in}}/\kappa$ is half and cannot reproduce those high resonant frequencies, so the cavity is over coupled. The normalized detuning exists in the overlapped region of the dotted line and shaded area. Each detuning is estimated to be $\delta_{\mathrm{A}} = 0.6 \pm 0.2$ and $\delta_{\mathrm{B}} = 0.6 \pm 0.3$.

With these measured parameters such as the optical resonant frequency, the beam spot position, and the normalized detuning, we can estimate the differential displacement caused by the quantum radiation pressure fluctuation described in Eq. (5.7). The estimated displacement spectrum is

$$\sqrt{S_{\mathrm{x,qrp}}} = (3.6 \pm 0.8) \times 10^{-15} \left(\frac{100\,\mathrm{Hz}}{f} \right)^2 \mathrm{m}/\sqrt{\mathrm{Hz}}, \tag{5.8}$$

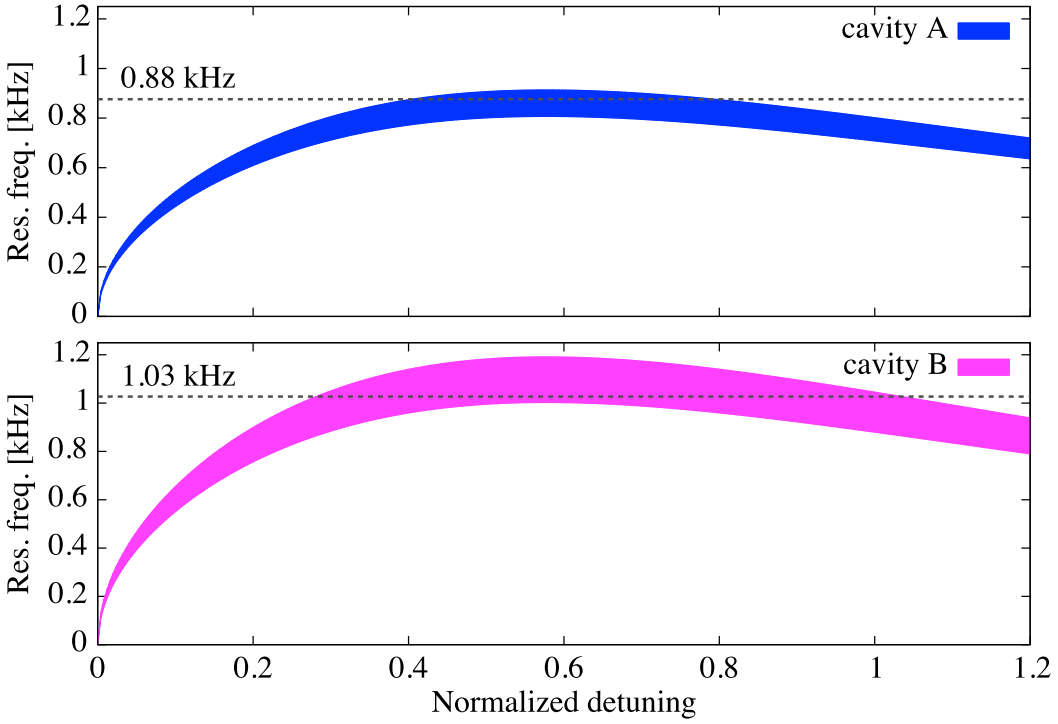

Figure 5.8: Optical resonant frequency of normalized detuning on the cavity. The blue and magenta areas show the predicted resonant frequencies including their errors. The horizontal dotted lines mean the measured resonant frequencies.

and the signal to noise ratio is 0.14 ± 0.03 between 60 Hz and 100 Hz. The error of the estimated normalized detuning has the largest contribution.

5.4 Summary of errors

In this section we summarize measurement errors of experimental parameters and discuss the estimation error of the signal to noise ratio.

- Calibration error for the displacement noise

  We calibrate the voltage signal to the displacement one based on Eq. (5.2). Dominant sources of the measurement error are H_{act} and V_{error}. The relative errors of the actuator efficiency and the measured voltage spectrum

Property	Relative error
Beam spot position	1%
Detuning	30-50%
Optical resonant frequency	2%
Displacement spectrum	20%

Table 5.2: Relative errors of parameters for estimation of radiation pressure fluctuation.

are 10% and 15% ($\simeq \sqrt{1/n_{\mathrm{av}}}$), respectively. The error of actuator efficiency comes from the fitting to calculate it. Those of other transfer functions are negligible because they are a few percent at the most.

- Estimation error of the radiation pressure fluctuation

  The displacement spectrum of the quantum radiation pressure fluctuation is estimated with Eq. (5.7). Parameters are the beam spot position, the detuning of the cavity, the optical resonant frequency. Relative errors for these parameters and the estimated displacement spectrum are shown in Table 5.2. A dominant parameter for the estimation error is the detuning. The other errors are derived from the fitting.

Relative errors for calibration of the measured data and estimation of the quantum radiation pressure fluctuation are 18% and 20%, respectively. The signal to noise ratio is estimated to be 0.14 ± 0.03 with the relative error of 27%.

5.5 Summary of this chapter

We show the main result of our experiments. Achieved signal to noise ratio of quantum radiation pressure fluctuation of 0.14 ± 0.03 is the highest one on the measurement around the detector band around 100 Hz and on the mass scales above mg. The estimation error of the cavity detuning is dominant in that of the signal to noise ratio. Our result is compared with previous works in Fig. 5.9.

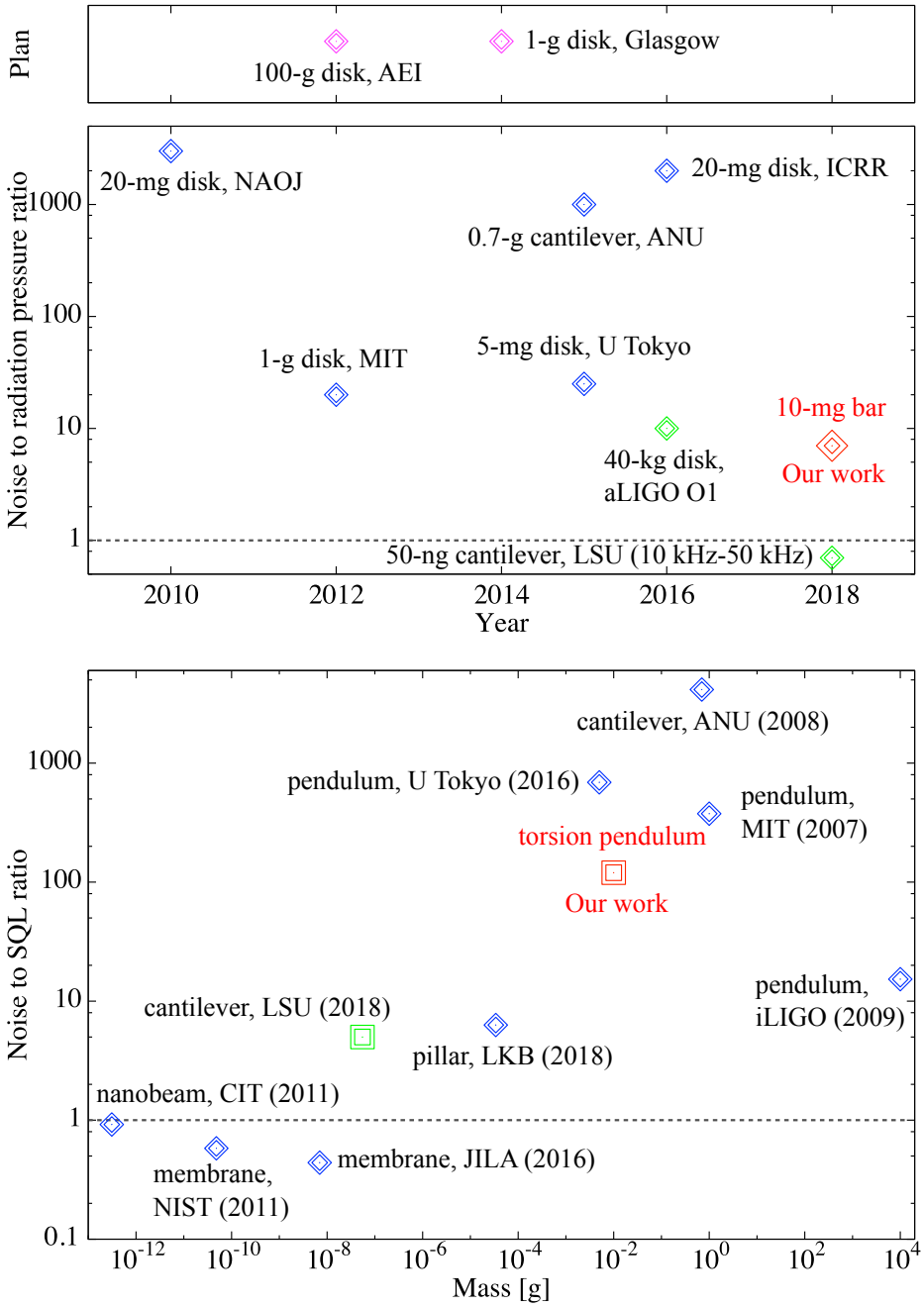

Figure 5.9: Comparison of our result with previous works. The red point means our result.

Chapter 6

Discussion

The results of our main experiment using the torsion pendulum cavities are described in the previous section. In the most sensitive band of 60-100 Hz, the signal to noise ratio of the quantum radiation pressure fluctuation is evaluated to be 0.14 ± 0.03. The displacement noise is about 7 times larger than the signal. In this chapter, we discuss the possible noise sources contributing to the measured displacement spectra.

6.1 Noise analysis

In this section various noise sources are analyzed. We evaluate the contribution of the thermal, seismic, electronic, and other noises to the displacement spectra.

6.1.1 Thermal noise

Important thermal noises on our experiment are separated to 3 types, the residual gas, suspension, and substrate thermal noise.

Residual gas noise

The effect of the residual gas is searched for by changing the pressure in the vacuum chamber and measuring the displacement noises. In Fig. 6.1, we represent 4 results at each pressure, 100 Pa, 1.3 Pa, 3.8×10^{-2} Pa, and the main

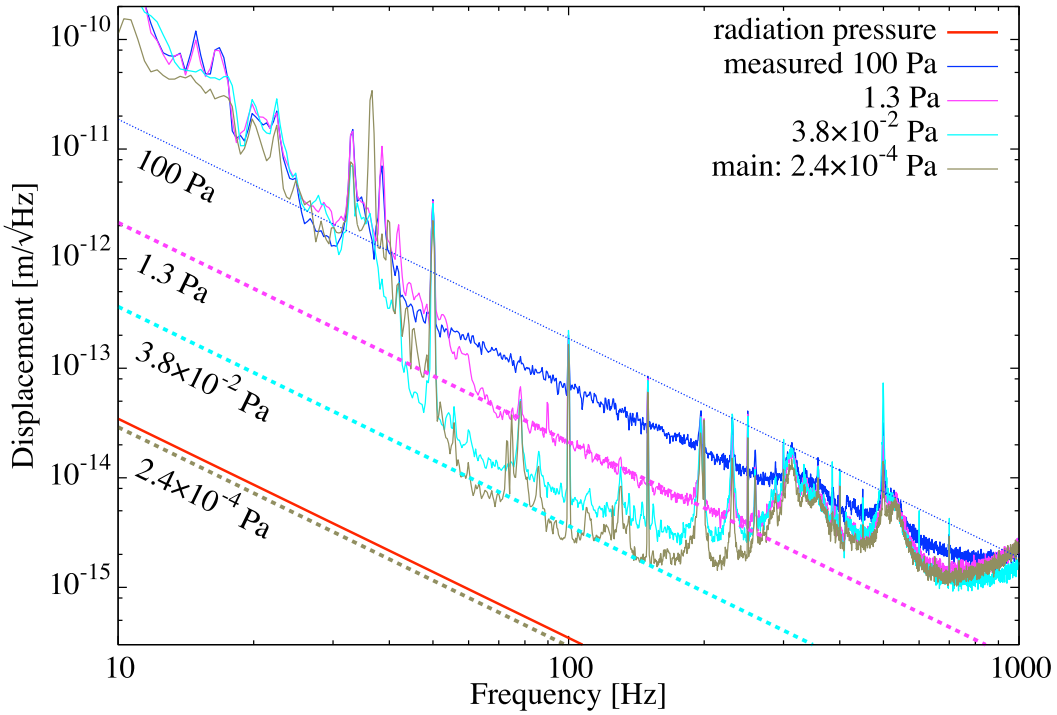

Figure 6.1: Displacement spectra at various pressure. The blue, magenta, cyan, and gold lines show the measured spectra at each pressure, $n_{\mathrm{av}} = 44$. The dotted lines mean the theoretical residual gas thermal noise corresponding to the pressure. The red line represents the quantum radiation pressure fluctuation.

one already shown (2.4×10^{-4} Pa). Theoretical residual gas noises are also described. This estimation is based on Eq. (4.17). The assumed molecules, temperature, and shape factor are water, $T_{\mathrm{th}} = 300$ K, and $C = 1$, respectively.

The line of $P = 1.3$ Pa explains the measured data well, and measured spectra at $P = 3.8 \times 10^{-2}$ Pa is consistent with the sum of the displacement noise shown as the gold line and the theoretical value. The 100 Pa line is larger than the measured data. It seems to be because the approximation of particle description of residual gas molecules cannot be applied anymore and the viscous effect is dominant at such high pressure. The estimated gas noise at $P = 2.4 \times 10^{-4}$ Pa is much smaller than the displacement noise, so it is not a dominant noise for the main result.

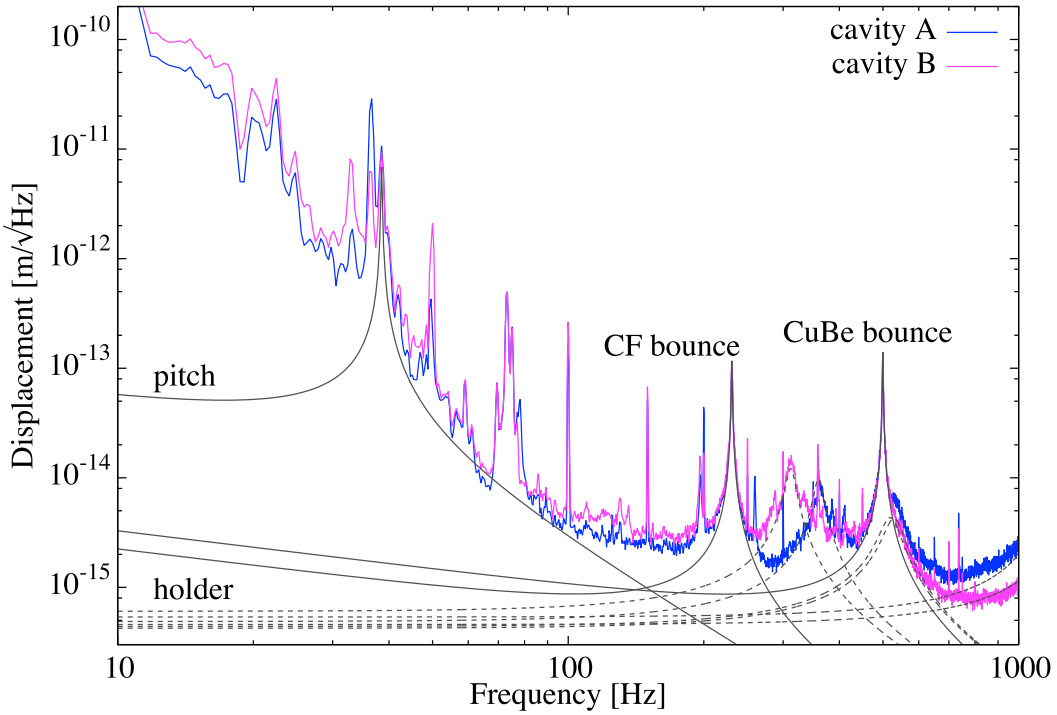

Figure 6.2: Estimated displacement spectra of the pitch and bounce modes, and the thermal noise of the input mirror holders. The blue and magenta lines show each cavity spectrum, and the black solid lines express 3 suspension thermal noises. The black dotted lines mean the holder thermal noises.

Suspension thermal noise

Suspension thermal noise is one of the largest obstacles for observation of quantum radiation pressure fluctuation. Our set up avoids it because the rotational suspension thermal noise is small due to the low mechanical resonant frequency. However, we find that the other suspension thermal noise of wires can be the issues.

In Fig. 6.2, we show the measured displacement spectra of each cavity and the estimated suspension thermal noise of the pitch mode of the test mass and bounce modes of the carbon fiber and CuBe wire. At frequencies of these resonant peaks, coherence between error signals of two cavities is almost 1 as

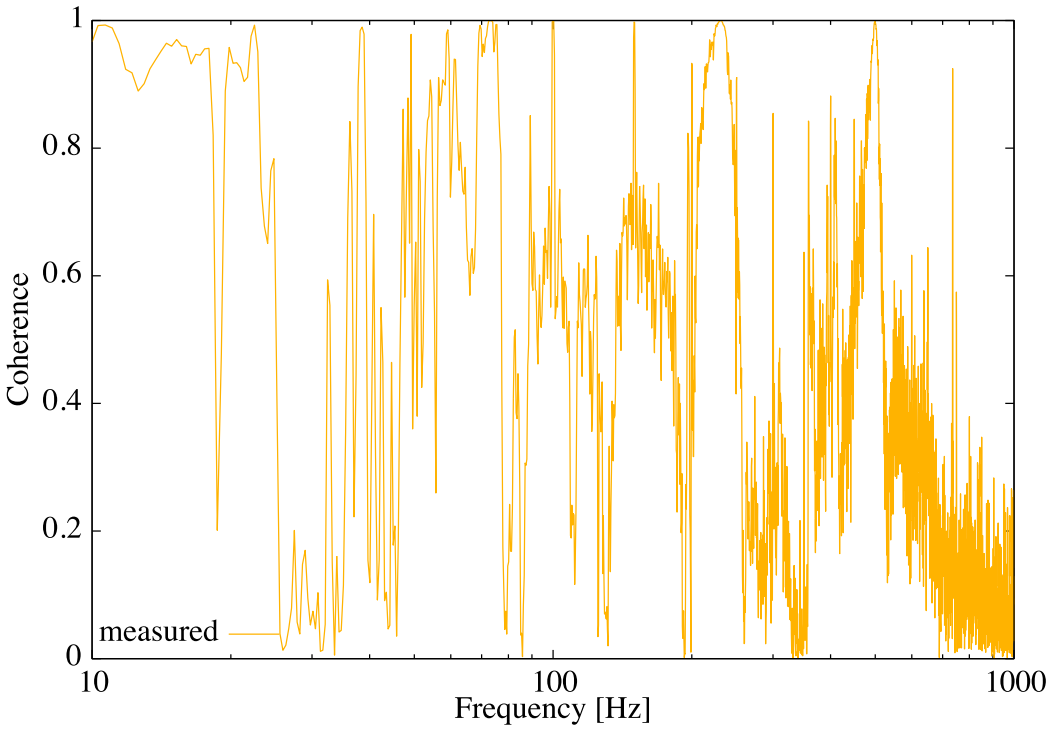

Figure 6.3: Measured coherence between the error signals from each cavity. The measured data is represented as the brown line.

shown in Fig. 6.3. The coherence $C(f)$ is defined as

$$C(f) = \frac{|S_{\rm ab}(f)|^2}{S_{\rm aa}(f)S_{\rm bb}(f)}, \tag{6.1}$$

where $S_{\rm ab}(f)$ is the correlation spectrum of the two signals, and $S_{\rm aa}(f)$ and $S_{\rm bb}(f)$ are the power spectra of each signal. When the signals are absolutely correlate (independent), the coherence is 1 (0). Therefore, these motions can be concluded to come from the oscillation of the test mass, which is a common mirror for the cavities.

Actually, these resonant frequencies are consistent with the estimated ones from the moment of inertia of the test mass and the length and Young's modulus of CF and CuBe fibers. The assumed Q-values and coupling constant from vertical motion to horizontal one (VHC) of the modes are listed in Table 6.1. The coupling from the pitch oscillation varies with the vertical beam

Property	Pitch	CF bounce	CuBe bounce
Frequency [Hz]	38.5	231	499
Q-value	250	250	300
VHC	NA	0.01	0.13
CMRR	0.16	0.13	0.1

Table 6.1: List of the assumed Q-values, the measured vertical horizontal coupling, and the common mode rejection ratio of the pitch and bounce modes.

spot position on the bar. It is required for us to adjust the positions with seeing the CCD cameras and move them near the center. The pitch Q-value is much lower than that of the pendulum mode because the energy loss occurs the adhesion point just above the test mass, which is much lossier than the energy loss of the bending wire. This pitch coupling and the bounce thermal noises limit the sensitivity of each cavity.

Dominant noises above a few 100 Hz are derived from thermal noises of the independent input mirror holders. Their estimated contributions are shown also in Fig. 6.2. These broad peaks only exist on each displacement spectrum. Therefore, the origin is not vibration of the test mass and the platform which should be common for two spectra. The different parts are the input mirrors and the controlled mirrors. The controlled mirror does not have the broad resonance peak around 100 Hz because it is a pendulum. The input mirror holder consists of the main bode with picomotors and the front panel including the mirror. These are connected by two coil springs. The resonance of the small coil spring can have the resonant frequency from several 100 Hz to kHz, and the low Q-value around 10.

Furthermore, we show the comparison of the spectra of the error signals with slightly different input mirror holders in Fig. 6.4. The error signal spectra for our main data are represented in the upper figure. On this measurement we use the holder whose front panel is made in the machine shop and it is constructed by ourselves. The different holder with almost the same structure is made by Newport based on 9761-K. That holder is used in the measurement shown in the lower figure. The resonant frequency of the marked peaks change slightly. Thus, we can judge that these peaks are generated by the input mirror holder.

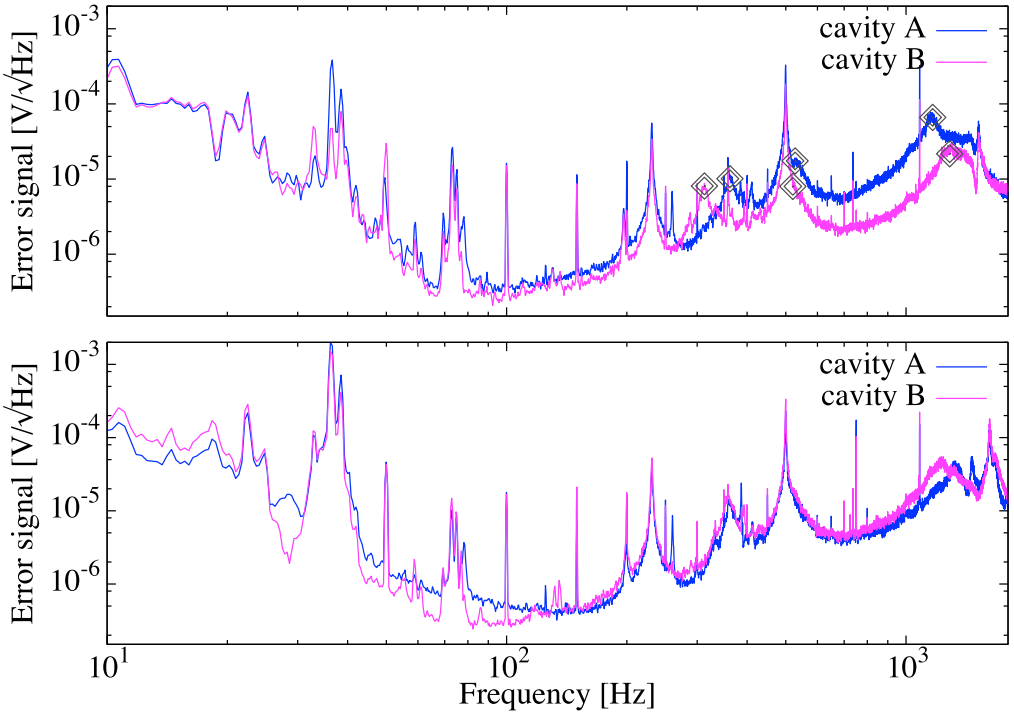

Figure 6.4: The comparison of the spectra of the error signals with different input mirror holders. The marked resonant peaks are caused by the input mirror holders. The upper spectra come from the main data, and the lower spectra is measured with the different holders.

Peak number	Frequency [Hz]	Q-value	Effective mass [g]
A1	360	20	300
B1	310	20	300
A2	530	10	250
B2	520	10	250
A3	1160	10	15
B3	1280	10	15

Table 6.2: List of the modeled resonant frequencies, Q-values, and effective masses of the input mirror holders.

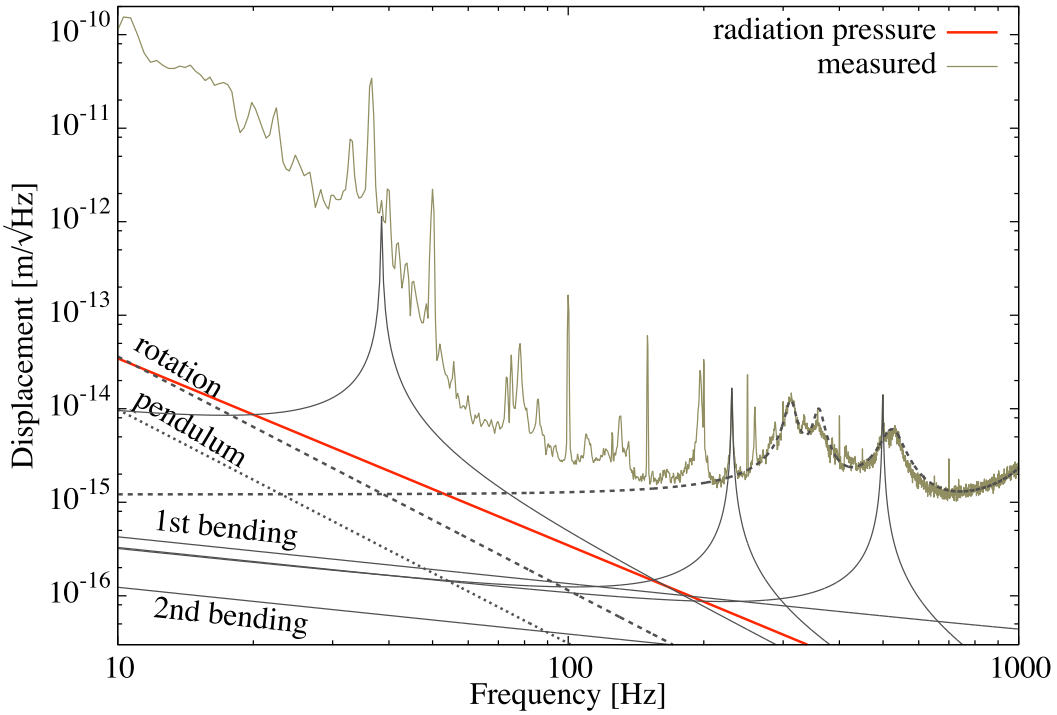

Figure 6.5: Estimated suspension and substrate thermal noises. Each noise source is put down with the line. The solid lines are based on the fitting, and the dotted lines are calculated by the results of Q-values measurement.

The modeled resonant frequencies, Q-values, and the effective masses for the thermal noise are listed in Table 6.2. The front panel of the input mirror holder has the mass of around 10 g. This is much lighter than the effective mass of two modes represented in the table. It is considered to be because the motions are parallel to the mirror surface, and the coupling factors to the direction of the cavity length are about 5. Here, these thermal noises are assumed to obey the viscous model [106].

In addition to the displacement spectra of the suspension thermal noises, the differential spectra of the pendulum and rotation suspension thermal noises are represented in Fig. 6.5. The common mode rejection ratio (CMRR) is optimized based on the vibration noise around 73 Hz, so those of the pitch, CF bounce, and CuBe are not as large as that of the 73 Hz peak. They are also listed in Table 6.1. The thermal noise of the pendulum mode, whose common

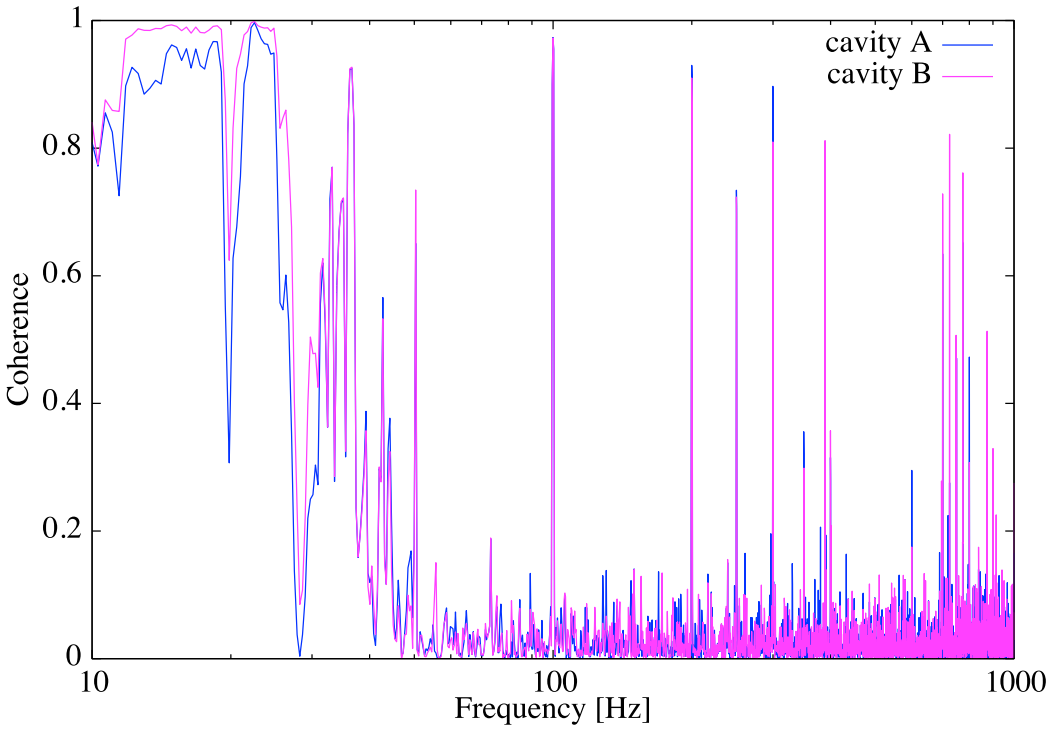

Figure 6.6: Measured coherence between the vertical seismic noise and each cavity displacement. The blue (magenta) line means the measured coherence between the geophone output and the cavity A (B) signal.

mode rejection ratio is assumed to be 0.1, and the rotational mode are much lower than the measured spectrum. We adopt their Q-values measured by the ringdown on the rotational mode and the monitor of the equilibrium state on the pendulum mode.

Substrate thermal noise

Thermal noise of the bending modes of the bar mirror causes the displacement not only at their resonant frequencies but also at the lower frequency band. The frequency dependence is $f^{-1/2}$ because it obeys the structure model. The voltage signals are calibrated by the same factor as that of the main experiment. Similarly to the pitch and bounce modes, the common mode rejection of the 1st mode is not large. The contribution of the 2nd mode is enhanced because the mode is differential. The fitting result is shown in Fig. 6.5. In

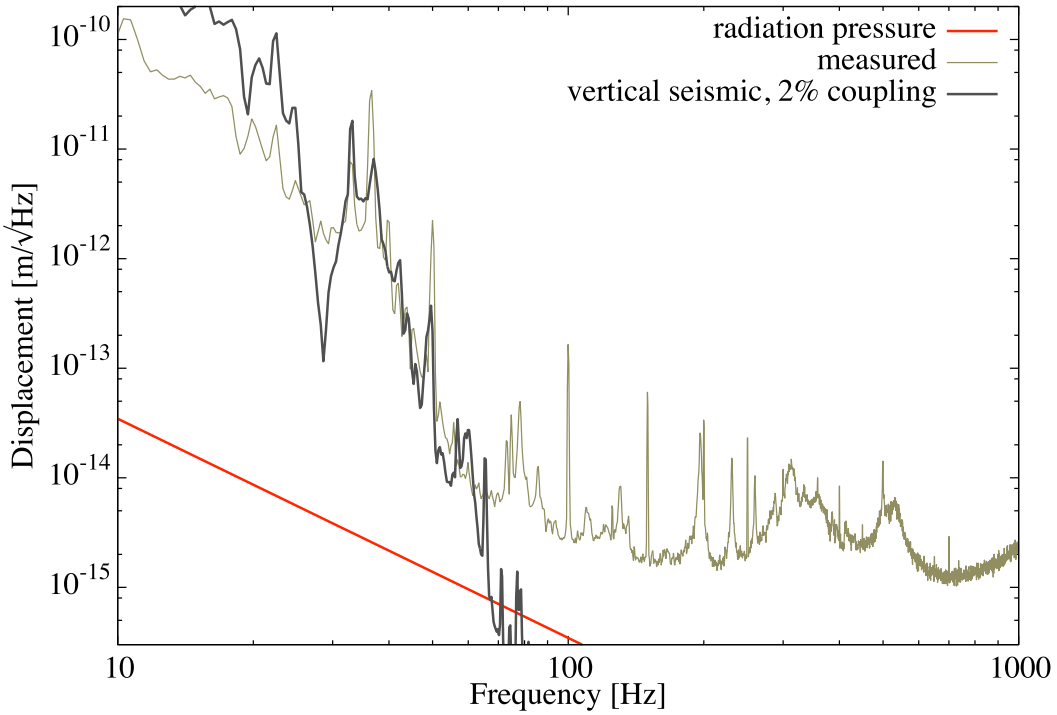

Figure 6.7: Contribution of the vertical seismic noise. The black line shows the displacement due to the vertical seismic noise of the platform multiplied by 0.02, which is estimated to be the coupling factor.

this figure, suspension thermal noises discussed in this subsection are summarized. Around the targeting frequency band, they are lower than the quantum radiation pressure fluctuation.

6.1.2 Seismic noise

The seismic noise, in particular, the vertical seismic noise is a dominant noise source below 50 Hz in our setup. It is confirmed by the coherence measurement between the vertical seismic noise and each cavity displacement, which is described in Fig. 6.6. The vertical seismic noise data comes from the output of the geophone on the table for the vacuum chamber. The contribution can be estimated from the result of vertical seismic noise on the chamber table multiplied by the transfer function to the platform described in Fig. 4.18.

In Fig. 6.7, we show contribution of the vertical seismic noise of the platform

to the measured spectrum. When the coupling factor including the common mode rejection is assumed to be 0.02, the measured displacement noise is explained between 30-50 Hz. The dip of the seismic noise around 30 Hz derives from the transfer function. It appears in the short measurement, but gets dull owing to some small glitches in the long measurement. Between 10 Hz and 30 Hz, the measured data has better sensitivity. The coupling of the seismic noise is considered to be smaller than 0.01 around this frequency range. Peaks at 37 Hz and 73 Hz are due to not the seismic noise but vibration of the turbo-molecular pump because they appear only with the pump on.

The common mode rejection ratio of the vertical seismic noise is around 0.5 below 50 Hz, which is worse those of the other common noises. It is because the optimization is not done based on that frequency band and the optimal factor at the subtraction is different from that for the 73 Hz peak. The difference is considered to be caused by the variance of transfer function from the vibration noise to the displacement signal.

6.1.3 Electric noises

One of the most significant technical noises is an electric noise such as the sensor, filter, and actuator ones whose unit is $\mathrm{V}/\sqrt{\mathrm{Hz}}$. The sensor noise V_{sens} contributes to the displacement spectrum as

$$x_{\mathrm{dis}} = \left| \frac{g_2}{g_1} H_{\mathrm{fil}} H_{\mathrm{act}} H_{\mathrm{con}} \right| V_{\mathrm{sens}}, \tag{6.2}$$

and the filter and actuator noises $V_{\mathrm{fil,act}}$ behave as

$$x_{\mathrm{dis}} = \left| \frac{g_2}{g_1} H_{\mathrm{act}} H_{\mathrm{con}} \right| V_{\mathrm{fil,act}}. \tag{6.3}$$

The estimated result is represented in Fig. 6.8. The sensor noise is measured by monitoring the reflection from the input mirror keeping cavities misaligned. We measure the filter and actuator noises with putting a terminator of 50 Ω into the input port and monitoring the voltage fluctuation of the output. These are not dominant noise sources but above the quantum radiation pressure fluctuation. Therefore, it is necessary to suppress the electric noises or enhance

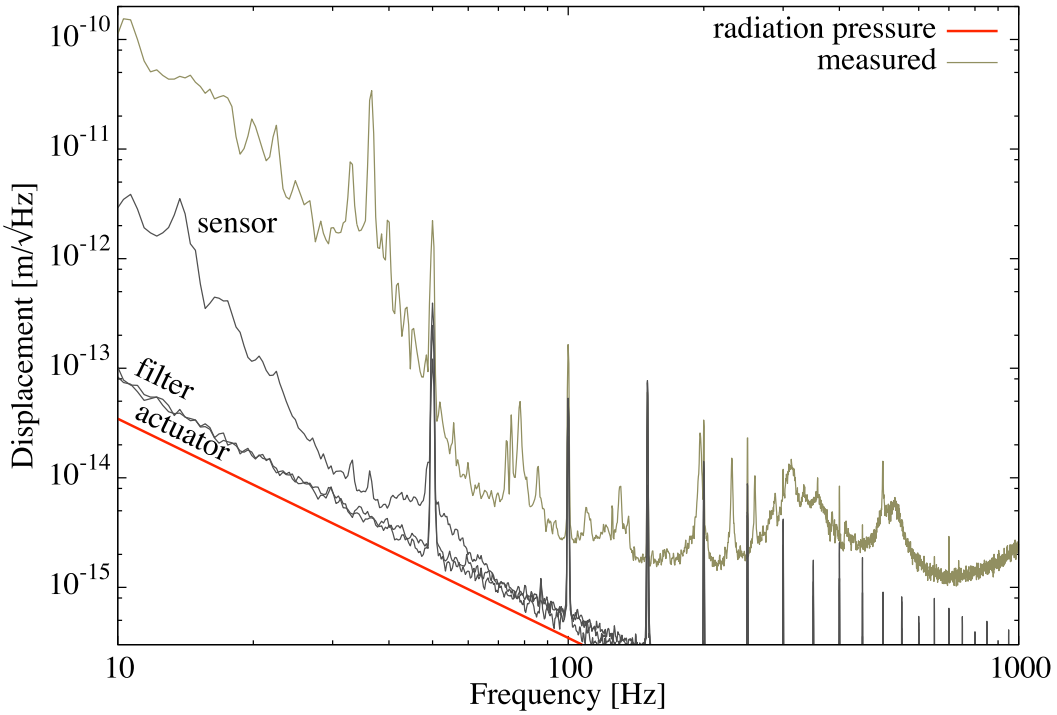

Figure 6.8: Contribution of the sensor, filter, and actuator noises. The black lines show each noise calibrated to the displacement.

the radiation pressure to realize the signal to noise ratio over 1.

6.1.4 Laser frequency and intensity noise

Here we estimate how the stabilized frequency and intensity (classical radiation pressure) noise contribute to the measured spectrum. As shown in Eq. (4.11), the frequency fluctuation Δf turns the displacement noise of

$$\sqrt{S_{\mathrm{x,freq}}} = \frac{2\pi\Delta f}{g_1}. \tag{6.4}$$

The classical radiation pressure noise is given by Eq. (3.36). The displacement spectrum can be written as

$$\sqrt{S_{\mathrm{x,crp}}} = \frac{\kappa_{\mathrm{in}}}{6\kappa} B_{\mathrm{rsnl}}^2 \sqrt{S_{\mathrm{x,qrp}}}. \tag{6.5}$$

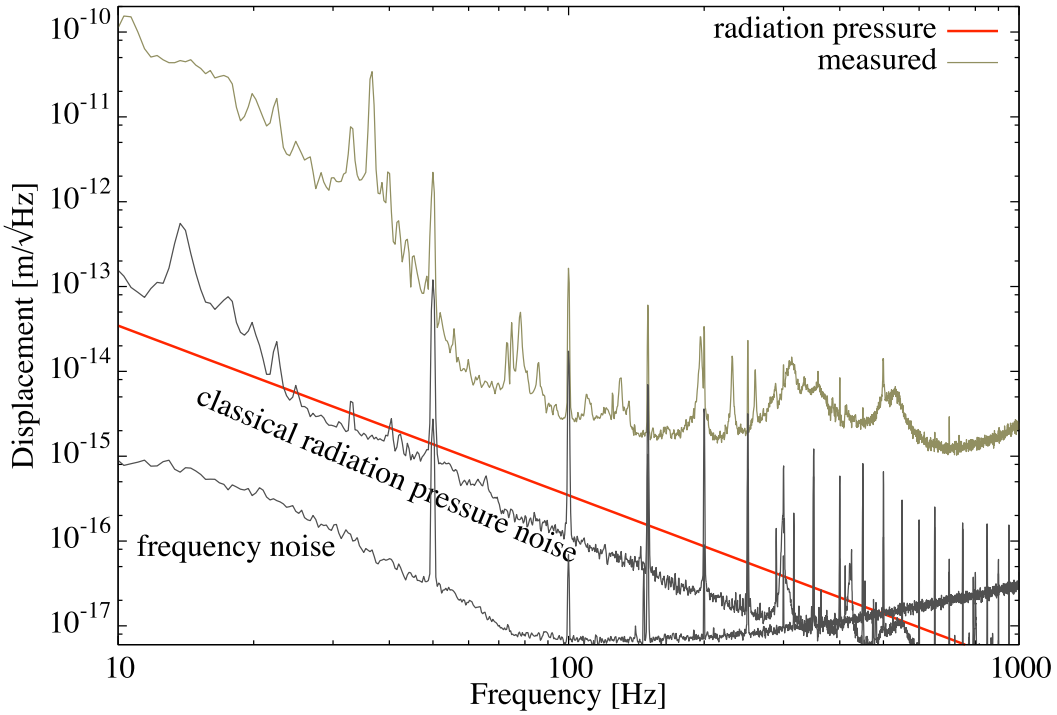

Figure 6.9: The displacement spectra due to the frequency and classical radiation pressure noises. The common mode rejection of the frequency noise is not assumed.

The factor of 6 comes from the effective mass ratio between the pendulum and rotational modes as described in Sec. 4.3.

In Fig. 6.9, we represent the displacement spectra due to the frequency and classical radiation pressure noises. They are much smaller than the measured spectrum even though the common mode rejection of the frequency noise is not considered. In fact, however, the frequency noise level is not confirmed because tit is estimated only from the in-loop error signal and the sensor noise for the stabilization.

The following is a summary of the above discussion of noises. The displacement spectrum of the estimated total noise is shown in Fig. 6.10. Around the most sensitive range of 50-150 Hz, the sum is lower than the measured data by a factor of about 2, so there are other contributions to the displacement noise. The vertical seismic noise can explain the measured spectrum below 50 Hz. Over 150 Hz, the thermal noise of the input mirror holders limit the

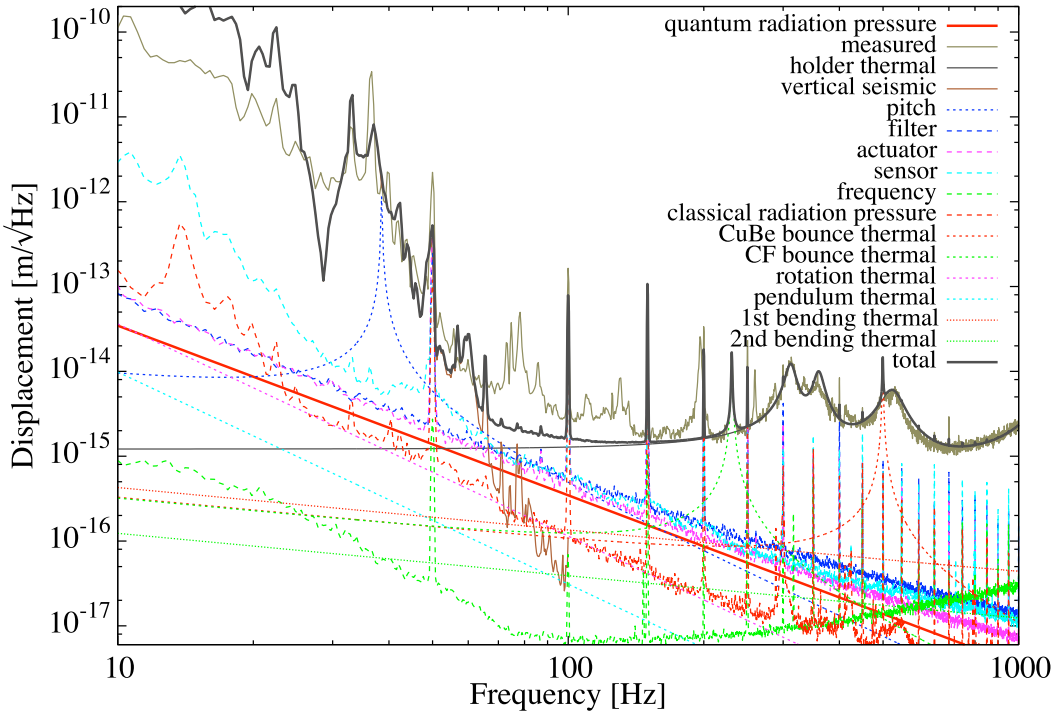

Figure 6.10: The displacement spectrum of the estimated total noise.

sensitivity.

6.1.5 Other possible noises

In this subsection we consider what noises can limit the sensitivity around the most sensitive region. One candidate is a scattering noise. In the case of a linear cavity, the light on the way and on the way back is superposed and enhanced. On the other hand, the light propagates on one way in the triangular cavity and the tiny light on the inverse direction can be generated by the scattering on the mirror surface. Also, our bar mirror does not have the anti-reflection coating on the rear surface resulting in the reflectivity of several percents. The reflection can couple with the main beam because the thickness of the mirror is as thin as the beam radius. Moreover, the small dust can attach to the surface and generate inhomogenous. Actually, we see tiny scattered light of the transmission on the CCD camera, and the sensitivity

around the sensitive band changes with the beam spot position as shown in Fig. 6.4. These scattering light has the possibility to behave as the floor noise around 50-150 Hz.

The other candidate is other vibration noise on the platform which directly couples with the cavity displacement because the input mirrors are fixed to it. In particular, the translation and pitch modes of the platform along the direction perpendicular to the input mirror surface causes the differential displacement of two cavities. Jagged structures around 80 Hz and 120 Hz seem to be caused by vibration noises. We have to also suspend the input mirrors to avoid these noises.

6.1.6 Common mode rejection

Here we summarize the discussion of the common mode rejection at our analysis. The reference to determine the subtraction factor is the peak of 73 Hz, which is caused by the vibration of the turbo-molecular pump. The rejection ratio is 0.05. With this subtraction factor, the common motions of the test mass such as the pitch and bounce thermal noises are reduced by a factor of about 0.1. It enables the differential sensitivity to reach the signal to noise ratio of 0.14 ± 0.03, which is limited by unknown independent noises. The ratio for the vertical seismic noise is 0.5. The small ratio is derived from the difference of the transfer path of the noise to the differential signal. The laser frequency and intensity noises are small enough to require the common mode rejection ratio.

6.2 Summary of this chapter

We discuss various noises which can limit the measured sensitivity, such as the thermal noises, electrical noises, seismic noise, and laser noises. The vertical seismic noise is dominant below 50 Hz. Above 150 Hz, the thermal noises of the input mirror holders limit the sensitivity. There are unknown noises between 50-150 Hz, but the scattering noise and the vibration noise of the platform are candidates.

Chapter 7

Future and conclusion

Quantum radiation pressure fluctuation can be observed with the signal to noise ratio over 1 using improved experimental designs. The future plans are described in Section 7.1, and the thesis is concluded in Section 7.2.

7.1 Future plan

In this section, we discuss future plans towards observation of quantum radiation pressure fluctuation with the signal to noise ratio above 1. One method is evolving our bar mirror cavities. The other is using a torsion pendulum like a dumbbell having mg-scale curved mirrors at both edges. In the future planning, it is assumed that the unknown noise is reduced, and the input mirror with the holder is replaced with a monolithic or suspended one so that their thermal noises disappear. Also, we focus on the vertical seismic, filter, actuator, pitch noises which can be the issue particularly in all noises described in Fig. 6.10.

7.1.1 Bar mirror

Here the upgrading plan for a short term is shown with the similar bar mirror. It is important to enhance the signal, quantum radiation pressure fluctuation. By changing the bar length from 15 mm to 10 mm, the mass decreases by 2/3 and the signal gets larger by 1.5. Further enhancement factor of 1.5 can be obtained with changing the beam spot positions closer to the edges, $L_{\mathrm{A,B}} =$

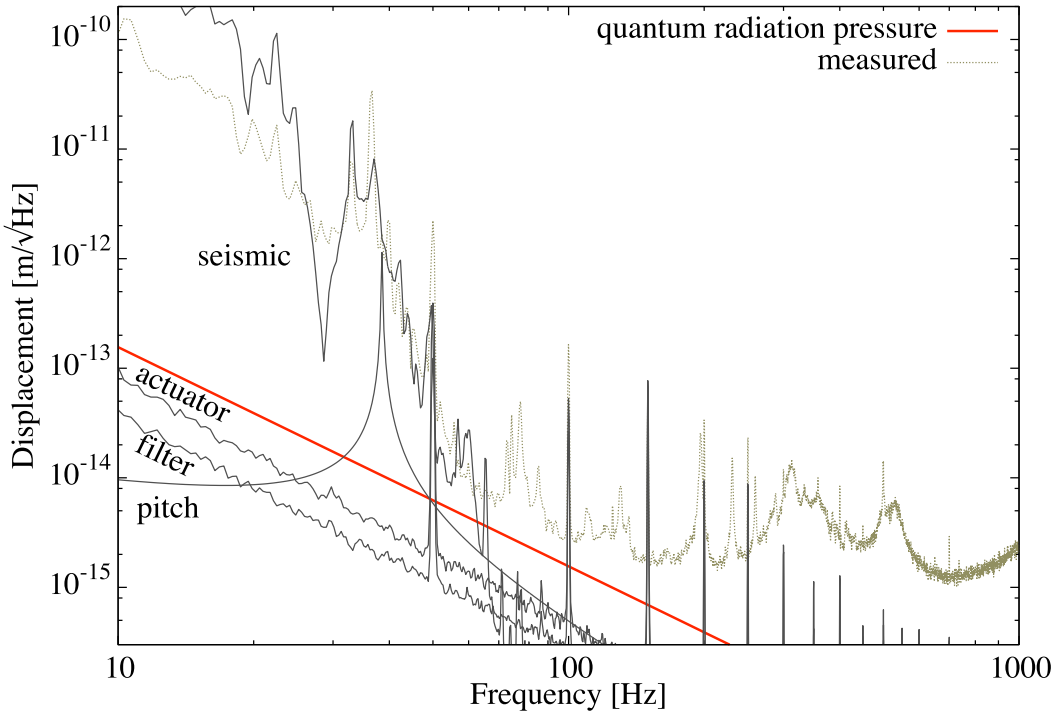

Figure 7.1: Improved displacement sensitivity with the bar mirror. The measured spectrum in the main experiment is plotted by the gold dotted line.

4 mm. Also, when we increase the finesse of cavities from current 3000 to 5000, the optical restoring force is approximately doubled. The quantum radiation pressure fluctuation is enhanced totally by 4.5.

We can decrease the filter gain to the half because the optical gain is also doubled and the openloop gain can keep with the half filter gain. Therefore, the filter noise gets half. In Fig. 7.1, the future displacement sensitivity for this upgrade is shown with noises whose contribution is critical. It is assumed that the classical radiation pressure noise is suppressed enough by distributing higher power to the PDs for the intensity stabilization. The other noises such as thermal noise of pendulum, rotation, bounce, and bending modes are much lower than those represented in the figure. Between 50-100 Hz, the signal to noise ratio is estimated to be over 1.

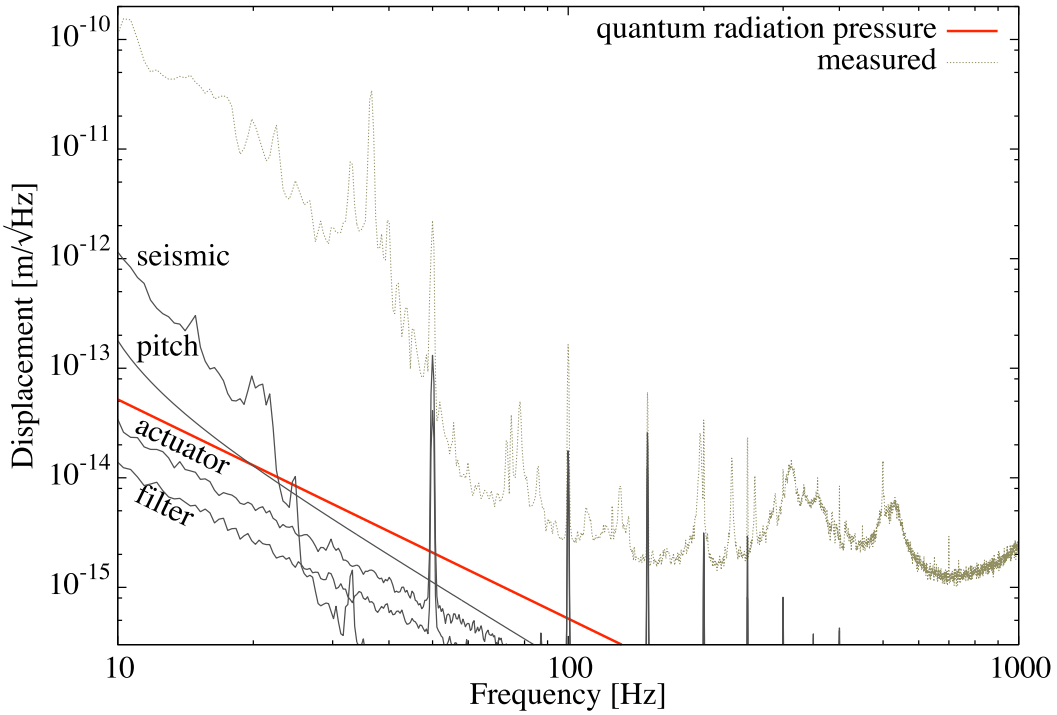

Figure 7.2: Displacement spectra of the dumbbell cavities.

7.1.2 Dumbbell with curved mg-scale mirrors

In this section, another future plan is described. A curved mg-scale mirror can be produced now. The diameter is 3 mm, the thickness is 0.5 mm, the curvature is 100 mm, and the mass is 8 mg. The triangular cavity is not necessary anymore because a linear cavity is stable with mirrors whose g-factors are negative, that is to say, the Sidles–Sigg instability is avoided. Therefore, a dumbbell consisting of two curved mirrors at the edges and a thin fiber between them can be used as torsion pendulum cavities.

In the future experiment, coil springs is used for improved vertical vibration isolation of the platform. The coil spring realizes the vertical resonant frequency of a few Hz. The additional noises at the resonant frequency of the eigen modes can be the issue, but they are typically over 100 Hz The fiber between two curved mirrors is assumed to be made of silica whose diameter is 0.3 mm and length is 20 mm. The total mass is about 20 mg, which is three times larger than the previous future test mass. The radiation pressure fluc-

tuation is 1/3 times, but we can reduce the electric noises also by 1/3 with the mass of the controlled mirrors triple. The interval between the suspension point and the position of the center of mass is 0.15 mm, namely 1/5, so the resonant frequency of the pitch mode decreases to 8.1 Hz and the thermal noise is suppressed.

In Fig. 7.2, the displacement spectra of this plan are shown. The frequency region where the signal to noise ratio is over 1 expands down to the 30 Hz due to the improved vertical seismic noise and the pitch thermal noise. In addition, all mirrors for the cavities are not fixed but suspended, and hence the vibration noise from the platform seems to be dramatically decreased. In the case of the two linear cavities, we can construct a Fabry–Perot Michelson interferometer. Therefore, the common mode rejection ratio can be enhanced.

7.1.3 Application

After observation of the quantum radiation pressure fluctuation with the dumbbell cavities, there are mainly two directions to make use of the device.

For reduction of quantum noise

When we prepare the Fabry–Perot Michelson interferometer whose sensitivity is limited by quantum radiation pressure fluctuation, the ponderomotive squeezing and the homodyne detection can be demonstrated. As shown in Fig. 2.14, the displacement spectrum of the radiation pressure noise has a dip corresponding to each homodyne angle. A small homodyne angle is required to reduce the radiation pressure noise around the frequency region much lower than the SQL frequency. In our experiment the SQL frequency is above kHz, so that is the case. By demonstrating the reduction below 100 Hz, we can confirm the method for future gravitational wave detectors whose sensitivity is limited by the radiation pressure noise.

For test of macroscopic quantum mechanics

The dumbbell cavities are useful in terms of the optomechanical device. We can reach the SQL with those including a silica suspension fiber (the diameter

of 10 μm, the Q-value of 10^5) and a silica connecting fiber (the diameter of 0.2 mm, the Q-value of 10^7) at 300 Hz. They are current feasible parameters. The ground state cooling can be realized by adjusting the resonant frequency of the rotational mode at the SQL frequency with the feedback cooling. We can make use of the cooled test mass for test of macroscopic quantum mechanics proposed by Balushi *et al* [107]. This is an expanded experiment proposed by Marshall *et al.* [24] with cooled torsion pendulum cavities. Measurement of the interferometric visibility reveals the existence of gravitational effects in quantum regimes.

7.2 conclusion

Quantum radiation pressure fluctuation play two important roles. One is in gravitational wave detectors. The detectors have ultra high sensitivity so as to detect gravitational waves. One of the most fundamental noises for the detection is the radiation pressure noise. It originates from the quantum fluctuation of the vacuum field coupling with the laser light. The noise will limit the sensitivity of future detectors around 10-100 Hz which is an important frequency band for observation of gravitational waves. Therefore, it is important to measure it directly and demonstrate its reduction on table-top experiments ahead of the actual detectors. However, it has not been observed yet with suspended mirrors like gravitational wave detectors around the detector band of 10-100 Hz.

The other role is in optomechanics. One of the largest problems about quantum mechanics is how massive it can scale and how to combine it with general relativity. The experimental realization of macroscopic quantum states across various mass scales has the potential to shed light on these questions. Even though mechanical oscillators at the nano- and micro-scale has been developed enough to be cooled to the quantum ground state and entangled, quantum behavior of those heavier than a milligram is hidden due to classical noises such as the thermal noise. It is important to develop macroscopic oscillators and realize ground state cooling. Observing quantum radiation pressure fluctuation is one of the necessary condition for that.

Thus, we have developed a mg-scale torsion pendulum as a bar-shaped

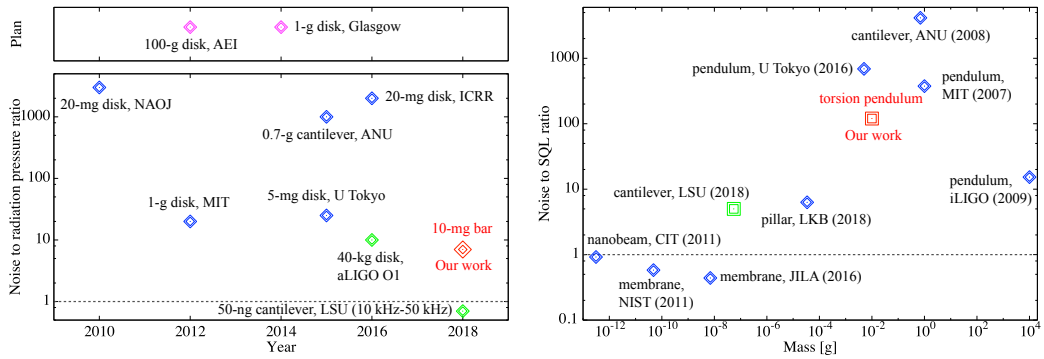

Figure 7.3: Comparison of our result with previous works.

mirror. The mirror is used as a common mirror of two triangular cavities at both edges. The rotational mode is measured by subtracting the signal from the cavities and getting the differential displacement spectrum. This setup has advantages of low suspension thermal noise due to the low resonant frequency of the yaw mode, the light effective mass, and the common mode rejection.

We succeed in locking the cavities simultaneously and achieve stable operation with a stiff optical spring. The sensitivity of the differential displacement spectrum reaches around $3 \times 10^{-15}\,\mathrm{m}/\sqrt{\mathrm{Hz}}$ at 100 Hz. The signal to noise ratio of the quantum radiation pressure fluctuation is estimated to be 0.14 ± 0.03 around 60-100 Hz. This is the highest ratio ever measured around the detector frequency band, especially radiation pressure noise regimes, with oscillators heavier than a milligram as shown in Fig. 7.3. The vertical seismic noise and the thermal noise of the input mirror holders limits the sensitivities below 50 Hz and over 150 Hz, respectively. There are unknown noises around 50-150 Hz, which are likely vibration noise and scattering noise. By reducing the noise which limits the current sensitivity and enhancing the signal with the higher finesse cavities, we can increase the signal to noise ratio to over 1. That benchmark would enable us to demonstrate the reduction method of radiation pressure noise with the homodyne detection and would be an important milestone in cooling the rotational mode of the bar to its quantum ground state.

Appendix A

Non-equilibrium thermal noise

In this appendix we show a direct approach for the fluctuation dissipation theorem under non-equilibrium steady-state conditions. This work is reported by Komori *et al* [108].

A.1 Concept and theory

In KAGRA and future gravitational wave detectors, the test masses and the main suspensions are cooled in order to reduce the suspension and mirror thermal noises. The mirrors absorb the heat energy from the huge intra-cavity power of main arms. The heat goes through the suspension fibers to the upper stages connected with heat links of the cryogenic system. The suspension fibers have temperature distribution. The fluctuation dissipation theorem predicts the precise thermal noise corresponding to the energy loss, but it is only valid for the equilibrium states. Therefore, the theorem cannot be directly applied to the system with non-uniform temperature. Here we show the non-equilibrium thermal noise under steady state conditions. This research can be used to estimate suspension thermal noises of cryogenic gravitational wave detectors and other mechanical oscillators with temperature depending on the position.

It is assumed that the system is divided to numerous tiny parts and they have constant temperature each other in the equilibrium. According to the Levin's approach [49], the single-sided displacement spectrum of the thermal

noise should be written as

$$S_{\mathrm{x}} = \frac{8k_B}{\omega^2} \int d^3r \frac{w_{\mathrm{diss}}(\vec{r}, f)}{F_0^2} T(\vec{r}), \tag{A.1}$$

where $T(\vec{r})$ is the stationary temperature profile, $w_{\mathrm{diss}}(\vec{r}, f)$ is the power dissipation density related to driving the system with the external force, F_0 is an arbitrary normalization of the drive amplitude. This equation can be rewritten with the loss angle $\phi(\vec{r}, f)$ and maximal elastic energy density $u_{\mathrm{max}}(\vec{r}, f)$ via $w_{\mathrm{diss}}(\vec{r}, f) = \omega u_{\mathrm{max}}(\vec{r}, f)\phi(\vec{r}, f)$,

$$S_{\mathrm{x}} = \frac{8k_B}{\omega} \int d^3r \frac{u_{\mathrm{max}}(\vec{r}, f)}{F_0^2} \phi(\vec{r}, f) T(\vec{r}). \tag{A.2}$$

It means that the contribution to the thermal noise of the whole system is large at the points where the stored elastic energy is high at the modal deformation.

On the other hand, the spectrum can be described by not continuous but discrete model with a finite number of degrees of freedom. The impedance matrix of the whole system $\mathbf{Z}$, relating the velocity vector $\mathbf{v}$ and force vector $\mathbf{F}$ via

$$\mathbf{Z}\mathbf{v} = \mathbf{F}, \tag{A.3}$$

can be split up to individual pieces $\mathbf{Z}_l$. The temperature of the l-th part is T_l. Then the force spectrum matrix is given by

$$S_{\mathbf{F}} = 2k_B \sum_l T_l \left(\mathbf{Z}_l + \mathbf{Z}_l^\dagger \right), \tag{A.4}$$

and the displacement spectrum matrix is

$$S_{\mathbf{x}}(f) = \frac{2k_B}{\omega^2} \sum_l T_l \mathbf{Z}^{-1} \left(\mathbf{Z}_l + \mathbf{Z}_l^\dagger \right) \mathbf{Z}^{-1\dagger}. \tag{A.5}$$

When all temperatures T_l are the same value, the sum in Eq. (A.5) reduces to $T(\mathbf{Z}^{-1} + \mathbf{Z}^{-1\dagger})$. This is equivalent to the equilibrium form of the fluctuation dissipation theorem.

A.2 Application

In this section we apply the above theorem to the actual mechanics such as a simple spring, a suspension fiber, and the KAGRA suspension.

A.2.1 Simple spring

First, the thermal noise of a simple spring is discussed with a non-uniform temperature profile attached to a test particle. The spring is divided to n pieces and each piece except for the test particle has the small mass of m_l, $l = 1, ..., n-1$. We label the total spring constant K and the test particle mass $m_n = M(\gg m_l)$. The displacement, spring constant, and temperature are defined as $x_l, \bar{k}_l$, and T_l at every point $l = 1, ..., n$. The spring constant is a complex value of $\bar{k}_l = k_l(1 + i\phi_l)$, where ϕ_l is the loss angle.

The total potential energy of the system V_{total} is described as

$$V_{\text{total}} = \frac{1}{2}\sum_l k_l(x_l - x_{l-1})^2, \tag{A.6}$$

where $x_0 = 0$. The equation of motion of each piece is given by

$$-m_l\omega^2 x_l = -\frac{\partial V_{\text{total}}}{\partial x_l} + F_l, \tag{A.7}$$

where F_l is the external force added to m_l. Then, we get

$$\begin{cases} -m_1\omega^2 x_1 + \bar{k}_1 x_1 + \bar{k}_2(x_1 - x_2) & = F_1 \\ -m_l\omega^2 x_l + \bar{k}_l(x_l - x_{l-1}) - \bar{k}_{l+1}(x_{l+1} - x_l) & = F_l \\ -M\omega^2 x_n + \bar{k}_n(x_n - x_{n-1}) & = F_n, \end{cases} \tag{A.8}$$

where we have written down the cases $l = 1$ and $l = n$ explicitly, and take $l = 2, ..., n-1$ for the middle equation. Here we set the small mass of the spring m to be zero. It means neglecting the internal degrees of freedom of

the spring. The impedance of the system is then

$$i\omega\mathbf{Z} = \begin{pmatrix} \bar{k}_1+\bar{k}_2 & -\bar{k}_2 & & & \\ -\bar{k}_2 & \bar{k}_2+\bar{k}_3 & -\bar{k}_3 & & \\ & -\bar{k}_3 & \bar{k}_3+\bar{k}_4 & \ddots & \\ & & \ddots & \ddots & -\bar{k}_n \\ & & & -\bar{k}_n & \bar{k}_n - M\omega^2 \end{pmatrix}, \tag{A.9}$$

where a blank implies that the matrix element is zero. Since each individual spring element l has a unique temperature T_l, this equation not only describes the full impedance matrix $\mathbf{Z}$, but also splits it up into a sum of individual pieces.

Assuming that the spring constant and the loss angle of all pieces are the same, $k_l = k, \phi_l = \phi$, the force spectrum matrix can be calculated using Eq. (A.4) as

$$S_{\mathbf{F}} = \frac{4k_B k\phi}{\omega} \begin{pmatrix} T_1+T_2 & -T_2 & & & \\ -T_2 & T_2+T_3 & -T_3 & & \\ & -T_3 & T_3+T_4 & \ddots & \\ & & \ddots & \ddots & -T_n \\ & & & -T_n & T_n \end{pmatrix}. \tag{A.10}$$

Describing the inverse of the impedance matrix in terms of row vectors $\boldsymbol{\zeta}_l^T$ as $\mathbf{Z}^{-1} = (\boldsymbol{\zeta}_1^T;\ \boldsymbol{\zeta}_2^T;\ \boldsymbol{\zeta}_3^T;\ \cdots\ ;\boldsymbol{\zeta}_n^T)$, the displacement spectrum of the last (n-th) piece, *i.e.* the test particle, is given by

$$S_{nn} = \frac{2k_B}{\omega^2}\boldsymbol{\zeta}_n^T \sum_l T_l \left(\mathbf{Z}_l + \mathbf{Z}_l^\dagger\right) \boldsymbol{\zeta}_n^*, \tag{A.11}$$

where the last (n-th) row vector is

$$\boldsymbol{\zeta}_n^T = \frac{i\omega}{k(1+i\phi) - nM\omega^2} \begin{pmatrix} 1 & 2 & 3 & \cdots & n \end{pmatrix}. \tag{A.12}$$

Noting that $k = nK$, the displacement spectrum can be calculated as

$$S_{nn} = \frac{4k_B}{\omega n} \sum_l T_l \frac{K\phi}{(K - M\omega^2)^2 + K^2\phi^2}. \tag{A.13}$$

This result means that the average temperature of the whole system contributes to the displacement of thermal noise. Since the dissipation in this example is uniform across the spring, the result is expected based on Eq. A.1.

A.2.2 Suspension fiber

Next, the thermal noise of a suspension fiber is calculated with temperature gradient. As with the case of a simple spring, the suspension fiber is divided to n pieces. Each $n-1$ piece and the n-th mass has the mass of m and M. The angle of l-th piece against vertical direction is defined by $\theta_l \equiv (x_l - x_{l-1})/\Delta z$, where x_l is the displacement of the l-th fiber along horizontal axis and Δz is the length of the l-th fiber. Total potential energy of that case can be described as

$$V_{\text{total}} = \sum_{l=1}^{n+1} \frac{m_l g \Delta z}{2} \sum_{k=1}^{l} \theta_l^2 + \sum_{l=1}^{n+1} \frac{\bar{E}_l I}{2\Delta z} (\theta_l - \theta_{l-1})^2, \tag{A.14}$$

where $\bar{E}_l \equiv E_l(1+i\phi_l)$ is the complex Young's modulus of the fiber, $I = \int x^2 dA$ is the area moment of inertia in the direction of the horizontal axis, and g represents gravitational acceleration. The first term is derived from the gravity potential of each piece and the second term is derived from the elastic energy of each fiber. We set the boundary condition of $\theta_0 = \theta_{n+1} = 0,\ \theta_1 = x_1/\Delta z$. That is, the upper clamp point is fixed, and the fiber is completely vertical at the upper and lower clamp points. While other boundary conditions are possible for a single fibers, this choice is required for the case of four-fiber suspensions as in KAGRA.

The total impedance of the whole system is calculated from the equations of motion as in the case of a simple spring. It is again assumed that the Young's modulus of the fiber E_l, and in particular its loss angle ϕ_l, are independent of the position along the fiber. Using our boundary conditions, the equations of

motion on the 1st, 2nd, a generic i-th, $(n-1)$-th, and n-th piece are given by

$$\begin{cases} -m\omega^2 x_1 + \frac{Mg}{\Delta z}(2x_1 - x_2) + \frac{E(1+i\phi)I}{\Delta z^3}(6x_1 - 4x_2 + x_3) & = F_1 \\ -m\omega^2 x_2 + \frac{Mg}{\Delta z}(-x_1 + 2x_2 - x_3) & \\ + \frac{E(1+i\phi)I}{\Delta z^3}(-4x_1 + 6x_2 - 4x_3 + x_4) & = F_2 \\ -m\omega^2 x_i + \frac{Mg}{\Delta z}(-x_{i-1} + 2x_i - x_{i+1}) & \\ + \frac{E(1+i\phi)I}{\Delta z^3}(x_{i-2} - 4x_{i-1} + 6x_i + 4x_{i+1} + x_i) & = F_i \\ -m\omega^2 x_{n-1} + \frac{Mg}{\Delta z}(-x_{n-2} + 2x_{n-1} - x_n) & \\ + \frac{E(1+i\phi)I}{\Delta z^3}(x_{n-3} - 4x_{n-2} + 6x_{n-1} - 3x_n) & = F_{n-1} \\ -M\omega^2 x_n + \frac{Mg}{\Delta z}(-x_{n-1} + x_n) + \frac{E(1+i\phi)I}{\Delta z^3}(x_{n-2} - 3x_{n-1} + 2x_n) & = F_n. \end{cases} \tag{A.15}$$

Dividing total impedance into three parts $\mathbf{Z}_{total} = \mathbf{Z}_{free} + \mathbf{Z}_{grav} + \mathbf{Z}_{elas}$, they can be written as

$$i\omega\mathbf{Z}_{free} = \begin{pmatrix} -m\omega^2 & & & & & \\ & -m\omega^2 & & & & \\ & & -m\omega^2 & & & \\ & & & \ddots & & \\ & & & & -M\omega^2 \end{pmatrix}, \tag{A.16}$$

$$i\omega\mathbf{Z}_{grav} \simeq \frac{Mg}{\Delta z}\begin{pmatrix} 2 & -1 & & & & \\ -1 & 2 & -1 & & & \\ & -1 & 2 & \ddots & & \\ & & \ddots & \ddots & -1 & \\ & & & -1 & 1 \end{pmatrix}, \tag{A.17}$$

$$i\omega\mathbf{Z}_{elas} = \frac{E(1+i\phi)I}{\Delta z^3}\begin{pmatrix} 6 & -4 & 1 & & \\ -4 & 6 & -4 & \ddots & \\ 1 & -4 & 6 & \ddots & 1 \\ & \ddots & \ddots & \ddots & -3 \\ & & 1 & -3 & 2 \end{pmatrix}. \tag{A.18}$$

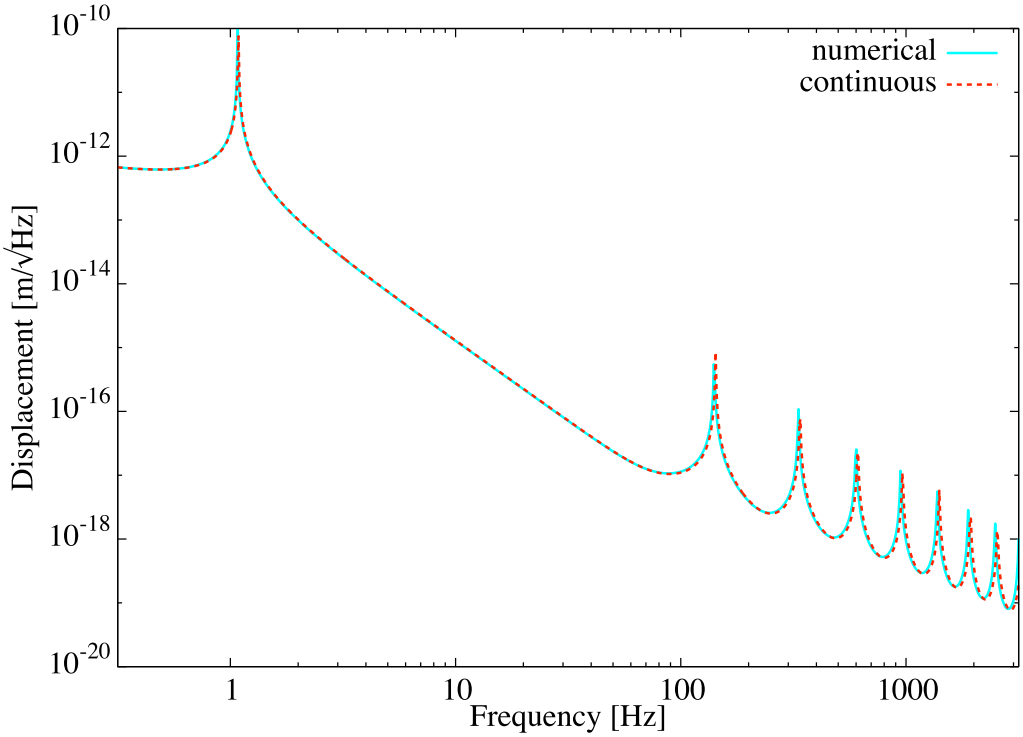

Figure A.1: Displacement spectra of thermal noise from discrete numerical calculation and continuous analytical calculation. The solid cyan and dotted red lines show the numerical and analytical calculation of the suspension thermal noise of a fiber, respectively. We set $M = 1\,\mathrm{kg}$, the length of the fiber $L = 30\,\mathrm{cm}$, the radius of the fiber $r = 0.5\,\mathrm{mm}$, $\phi = 1 \times 10^{-2}$, and $T = 300\,\mathrm{K}$. The material of the fiber is assumed to be sapphire. In the numerical calculation the fiber is divided to 100 pieces.

Here, we do not consider m in $\mathbf{Z}_{free}$ to be zero in order to recover the violin modes of the fiber. It should be noted that we could choose the loss angles ϕ_l of all fiber pieces not to be the same. In the case Eq. (A.18) becomes a sum of matrices over individual segments l.

The thermal noise of a suspension fiber numerically can be calculated with this total impedance. First, the validity of the calculation with the simple situation is demonstrated. Assuming that the temperature is constant, we compare the displacement spectra of thermal noise from discrete numerical calculation of Eq.(A.5) and continuous analytical calculation. The result is shown in Fig. A.1. The floor level of the noise, the resonant frequency of the

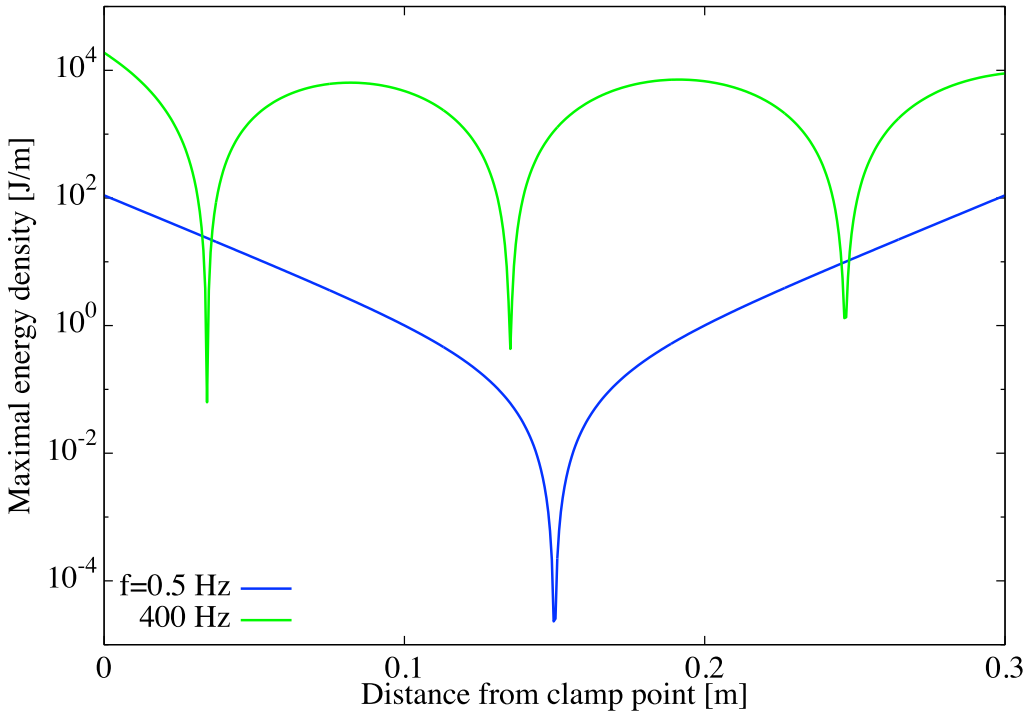

Figure A.2: Elastic energy distribution along the suspension fiber for two frequencies, 0.5 Hz (the blue line) and 400 Hz (the green line). The distributions are calculated using the analytical model, but agree with our numerical model.

pendulum mode and violin modes are different by less than 1%, around 1% and 2%, respectively. The values are reasonable because the number of divided pieces is $n = 100$ and the precision should be on the order of $1/n$. The first peak around 1 Hz is the pendulum mode, while the peaks at 140 Hz and higher harmonics are the violin modes of the fiber.

Next we focus on non-uniform temperature distributions. To get an intuitive understanding of the physics involved, we start with plotting the elastic energy distribution in Fig. A.2 for two examples:

- A frequency below the pendulum mode frequency. The fiber is mostly bending near the clamp point and the test mass attachment point, while the center of the fiber is not deformed.

- A frequency between violin modes. The dips correspond to nodes of the induced motion, where the fiber is not deformed. The traces are

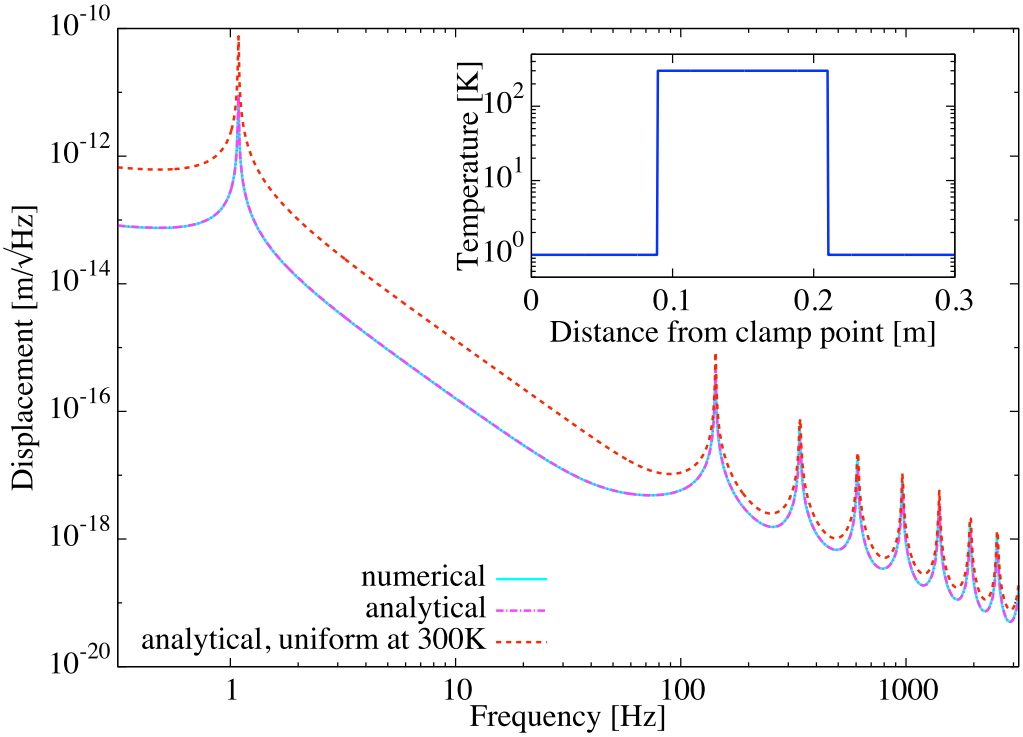

Figure A.3: Numerical and analytical calculation of the suspension thermal noise with a non-uniform temperature distribution. The cyan solid and the magenta dotted lines show the results of the numerical and analytical calculation. For reference, the red dotted line shows the same noise as in Fig. A.1, *i.e.* for a uniform temperature everywhere along the fiber. The parameters are all the same as for the previous simulation, except for the number of fiber sections, which is set to $n = 500$.

calculated using the analytical model, which describes the elastic energy distribution along the position of the fiber, but agree with our discrete model.

The two traces illustrate that different frequencies have the energy losses that dominates at different locations along the fiber, in accordance with Eq. (A.2).

In order to demonstrate the effect of non-uniform temperature distributions, we start with an extreme, although unphysical example. We choose the extreme temperature distribution shown in the inset of Fig. A.3. An elevated temperature (300 K) for only the middle section of the fiber is assumed, as illustrated in the inset. The main part of the figure shows the thermal noise for

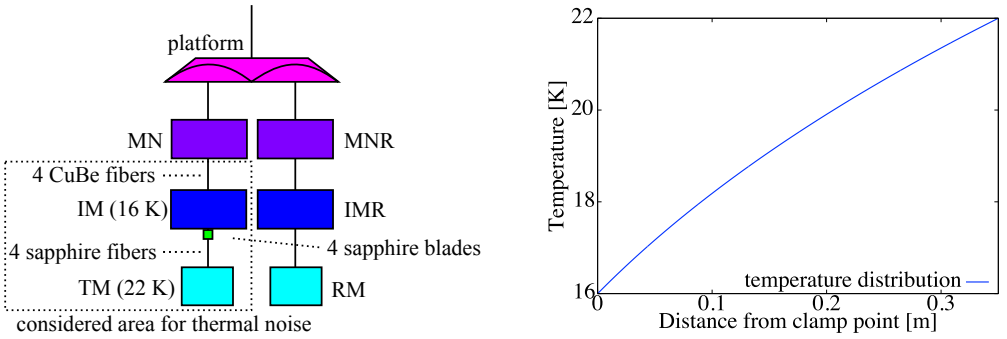

Figure A.4: Left: Schematic picture of the KAGRA cryopayload. Suspension thermal noise on KAGRA derives from the surrounded area by dotted lines. Right: Temperature distribution of the KAGRA sapphire fibers suspending the test mass. The boundary condition is $T(z = 0) = 16\,\mathrm{K}$, and $T(z = 0.35) = 22\,\mathrm{K}$.

this temperature distribution, calculated using our numerical model, as well using the analytical model. For reference the figure also represents the thermal noise for a uniform temperature of 300 K along the fiber. This is the same trace as in Fig. A.1. Compared to this red line, the noise level at low frequencies is improved significantly because the energy loss of the pendulum mode comes from the large distortion around the clamp point and attachment point, where the temperature is much lower than that at the center. Being different from low frequencies, the noise of violin modes does not change largely because some of the antinodes of the energy distribution profile lie in the 300 K region. Finally, the blue and green traces agree within the numerical uncertainties, validating our discrete model and Eq. (A.1).

A.2.3 KAGRA suspension

Finally, the theorem is applied to the actual KAGRA suspension thermal noise. The main test masses of KAGRA are suspended by an eight-stage pendulum called Type-A system. The last four-stage payload of the Type-A system is cooled down to cryogenic temperature and is called a cryopayload. Here we calculate the thermal noise of the KAGRA cryopayload for the input test mass (ITM). The brownian thermal noise is considered since it is dominant as compared with the thermo-elastic noise.

In Fig. A.4, the schematic picture of the KAGRA cryopayload is shown at the left side. The platform is suspended from upper room temperature stages. The marionette is suspended from the platform with 1 maraging steel fiber. The intermediate mass (IM, 20.8 kg) is suspended from the marionette with 4 copper beryllium (CuBe) fibers (26.1 cm long, 0.6 mm diameter). Finally, the sapphire test mass (TM, 22.7 kg) is suspended from the 4 sapphire blades (0.1 kg) attached to the intermediate mass with 4 sapphire fibers (35 cm long, 1.6 mm diameter).

Aluminum heat links are attached to the marionette, and the marionette is cooled down to 15 K. Heat absorption of the laser beam and the thermal conductivity of the fibers determine the test mass temperature. Estimated temperature profile along the sapphire fiber is plotted at the right side in Fig. A.4. Here we assumed temperature of the IM and the TM to be 16 K and 22 K, respectively; the incident beam power from the back surface of the input test mass to be 674 W; the mirror substrate absorption to be 50 ppm/cm; and the coating absorption to be 0.5 ppm [9]. This results in a nominal power loading of 0.724 W for the input test mass. By solving a differential equation about the temperature function of the cramp point, the temperature distribution can be derived. We used the measured thermal conductivity of the sapphire fiber of $\kappa(T) = 7.98 \times T^{2.2}$ W/K/m [109]. The detail of these calculations is written in Appendix B.

We discuss horizontal suspension thermal noise including the system below the CuBe fibers. It is enough to consider only the pendulum mode at the second pendulum consisting of the CuBe fibers and the IM. This is because the displacement thermal noise derived from the second pendulum has dependence of $f^{-4.5}$ above resonant frequency of the differential pendulum mode (1.9 Hz), which results in the violin modes of CuBe fibers getting negligible. Therefore, 4 CuBe fibers can be regarded as effective one fiber, whose tension is 1/4 but

the spring constant is 4 times larger. The horizontal potential is given by

$$V_{\rm hor} = \frac{1}{2}k_{\rm IM,h}x_{\rm IM}^2 + \sum_{\mu=a,b,c,d}\left[\frac{1}{2}k_{\rm bl,h,\mu}(x_{\rm bl,\mu}-x_{\rm IM})^2 + \sum_{l=1}^{n+1}\frac{m_l g\Delta z}{2}\sum_{k=1}^{l}\theta_{l,\mu}^2 + \sum_{l=1}^{n+1}\frac{\bar{E}_{l,\mu}I}{2\Delta z}(\theta_{l,\mu}-\theta_{l-1,\mu})^2\right], \tag{A.19}$$

where $k_{\rm IM,h}, k_{\rm bl,h,\mu}$ are the horizontal spring constant of the IM and blade springs and $x_{\rm IM}, x_{\rm bl,\mu}$ are the displacements. The labeling of a, b, c, and d means 4 blade springs and 4 sapphire fibers. The boundary conditions are $\theta_{0,\mu} = \theta_{n+1,\mu} = 0$ and $\theta_{1,\mu} = (x_{1,\mu} - x_{\rm bl,\mu})/\Delta z$. We can get full horizontal thermal noise by doing the same numerical calculation with this potential.

Similarly, we consider the vertical thermal noise below CuBe fibers. A spring constant of the vertical bounce mode can be written as $k_{\rm v} = ES/L$, where E is the Young's modulus, S is the surface area, and L is the length of the fiber. Thus, 4 fibers can be regarded as one fiber with 4 times the surface area. The vertical potential is written as

$$V_{\rm ver} = \frac{1}{2}k_{\rm IM,v}x_{\rm IM}^2 + \frac{1}{2}k_{\rm bl,v}(x_{\rm bl}-x_{\rm IM})^2 + \frac{1}{2}\sum_{l=1}^{n}\frac{\bar{E}_l S}{\Delta z}(x_l - x_{l-1})^2, \tag{A.20}$$

where $k_{\rm IM,h}, k_{\rm bl,v}$ is the vertical spring constant of the CuBe fibers and blade springs and $x_0 = x_{\rm bl}$.

These two suspension thermal noises and their sum in strain sensitivity are shown in Fig. A.5. Here horizontal and vertical resonant frequencies of the blade spring are assumed to be 2 kHz and 14.5 Hz with the suspended test mass, respectively. First two peaks come from the common and differential pendulum modes. The peak around 30 Hz is due to the resonance of CuBe fiber bounce. The resonant frequency of the first violin mode is around 180 Hz. In this figure the full numerical result is also compared to a simplified suspension thermal noise calculation which uses the average temperature of the IM and TM. The noise level between the two only differs by around 2% in the frequency range of about 10 Hz to 50 Hz, where suspension thermal noise contributes the most to the total noise. This result can be intuitively understood because the elastic energy is symmetric and the upper and lower edge of the fibers provide the

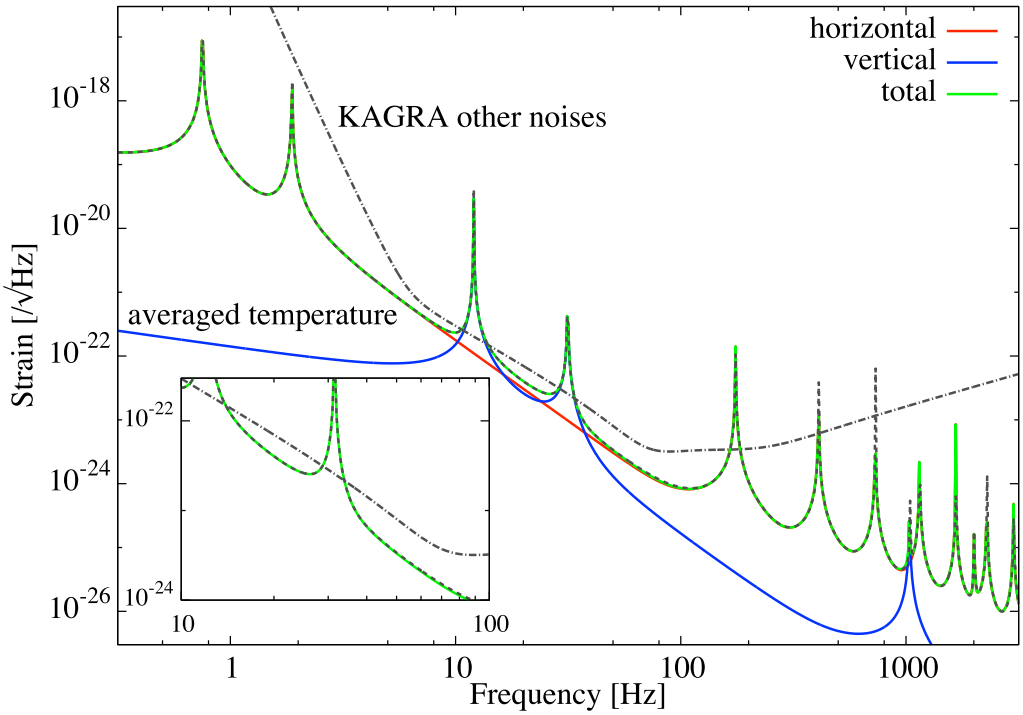

Figure A.5: Total suspension thermal noise of KAGRA in strain considering the temperature distribution. The red and blue lines show the horizontal and vertical thermal noise, and the green line represents the sum of them. The suspension thermal noise using an averaged temperature of the IM and TM, and the level of other expected noise sources in KAGRA are expressed as the black dotted lines.

largest contributions. Thus, we conclude that it is enough to average the IM and TM temperature and apply the equilibrium formulation of the fluctuation-dissipation theorem for the practical purpose of predicting KAGRA and future detectors' suspension thermal noises.

It is assumed that the loss angle and the Young's modulus of fibers are uniform for simplicity in this section. However, in fact, the loss angle can have frequency dependence and both depend on the temperature. Even in this case, we can apply our theorem with each value of them at the corresponding point along the fiber.

A.3 Summary of this chapter

We expand the application of the fluctuation dissipation theorem for mechanical systems to non-equilibrium steady-state conditions where the temperature is only defined locally. In order to calculate the thermal noise, the correct weight for averaging the temperature field is given by the dissipation density of the mechanical system. This result is applied to a simple spring and a fiber suspension for illustration purposes, and finally thermal noise of the KAGRA gravitational-wave interferometer suspension is derived with the actual temperature distribution. We conclude that it is a good approximation for the estimation of the accurate suspension thermal noise of KAGRA to average temperatures at the upper and lower edges of the fibers and use the equilibrium formulation.

Appendix B

KAGRA sensitivity and the upgrade plan

In this appendix, the best estimated sensitivity of KAGRA and the future plan are shown. We reconsider calculation for the design sensitivity of KAGRA. That is modified by the new estimation based on the Appendix A about the non-equilibrium suspension thermal noise. The other parts are also cleaned up and the best estimated sensitivity of KAGRA is introduced. Moreover, we consider some possibilities to upgrade the KAGRA facility and realize higher sensitivity in the near future.

B.1 Current design sensitivity

In this section we introduce the current design sensitivity of KAGRA. The sensitivities on three configurations are shown at first, followed by describing relation of the most important parameters in KAGRA, namely, laser power and mirror temperature. After that we summarize used parameters.

B.1.1 Sensitivities on three configurations

In Fig. B.1, we show the current best estimated sensitivities of KAGRA on three different configurations such as broadband resonant sideband extraction (BRSE) without the homodyne detection, BRSE with the homodyne detection,

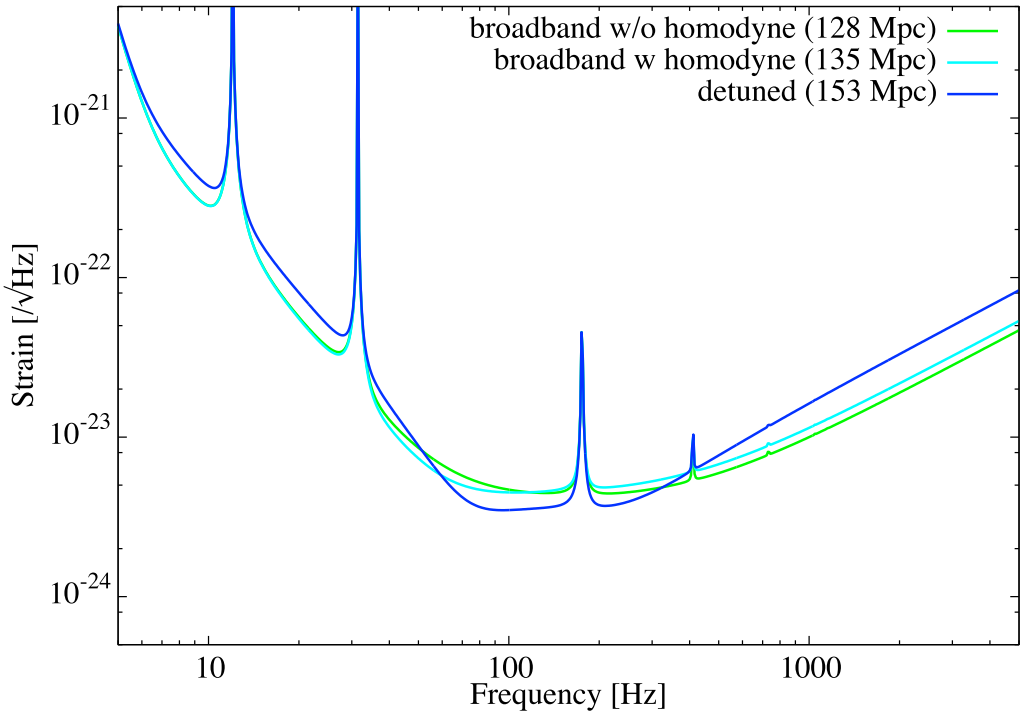

Figure B.1: Current best estimated sensitivities of KAGRA on three different configurations. The green, cyan, and blue lines show the sensitivities on BRSE without homodyne detection, BRSE with homodyne detection, and DRSE, respectively.

and detuned resonant sideband extraction (DRSE). Here how to decide these sensitivities is discussed.

The laser power and the mirror temperature are in one-to-one correspondence relation with the mirror absorption, which is shown in the next subsection. First, the sensitivity of DRSE configuration is optimized in terms of an inspiral range of a binary neutron star merger by changing the homodyne and detune angle, and the mirror temperature. The maximum range is 153 Mpc, and at that sensitivity the mirror temperature is 22 K, and hence corresponding laser power at BS is calculated to be 674 W to keep the temperature. Next, the power on BRSE without the homodyne detection is determined. In that configuration, the best sensitivity is 131 Mpc at the BS power of 1.25 kW and the temperature of 25 K. However, the power over 1 kW is too high and the range of 128 Mpc can be realized even at 674 W and 22 K. Therefore, we decide

to fix the power and temperature. The sensitivity of BRSE with the homodyne detection configuration is optimized by the same power and temperature with varying only homodyne angle. The best inspiral range is 135 Mpc.

B.1.2 Relation between laser power and mirror temperature

The relation between the laser power and the mirror temperature is derived as follows. Heat flow of fibers in the steady state is the same as the energy absorbed by a suspended mass. Therefore, we get [9]

$$K_{\rm abs} = N_{\rm f} \int_{T_{\rm u}}^{T_{\rm l}} \frac{S_{\rm f}\kappa(T)}{l_{\rm f}} dT, \tag{B.1}$$

where $K_{\rm abs}$ is the absorbed energy, $N_{\rm f}$ is the number of fibers, $T_{\rm u}$ ($T_{\rm l}$) is the temperature of an upper (lower) end, $S_{\rm f}$ is the area, $l_{\rm f}$ is the length, and $\kappa(T)$ is the thermal conductivity of the fiber. The marionette of the suspension system is connected to the platform by a thick heat link and the CuBe fibers have the high thermal conductivity. Thus, the temperature of the IM, the CuBe fibers and the marionette can be cooled down to $T_{\rm u} = 16\,{\rm K}$. Here we assume that the test mass temperature is $T_{\rm l} = 22\,{\rm K}$. $\kappa(T)$ is measured to be [109],

$$\kappa(T) = 5.8 \times 10^3 \left(\frac{d_{\rm f}}{1.6\,{\rm mm}}\right)\left(\frac{T}{20\,{\rm K}}\right)^{2.2}, \tag{B.2}$$

where $d_{\rm f}$ is the diameter of the fiber. Substituting $N_{\rm f} = 4$, $l_{\rm f} = 0.35\,{\rm m}$, and $S_{\rm f} = \pi(1.6 \times 10^{-3}/2)^2\,{\rm m}^2$, the total heat flow is calculated as $K_{\rm abs} = 0.724\,{\rm W}$.

The absorbed energy can be divided to that from the sapphire substrate, coating, and radiation from outside as

$$K_{\rm abs} = 2\beta_{\rm sub} t_{\rm m} P_{\rm mich} + \gamma_{\rm coa} P_{\rm circ} + K_{\rm rad}, \tag{B.3}$$

where $\beta_{\rm sub}$ is the absorption rate of the substrate, $t_{\rm m}$ is the mirror thickness, $P_{\rm mich}$ is the power between the BS and ITM, $\gamma_{\rm coa}$ is the absorption of the coating, $P_{\rm circ}$ is the intra-cavity power of the main arm, and $K_{\rm rad}$ is the radiation energy from outside. The mirror thickness is designed to be $t_{\rm m} = 15\,{\rm cm}$. The

Property	Value
Configuration	VRSE
Baseline length	3 km
Wavelength	1064 nm
Laser power at BS	674 W
Power transmission of ITM	0.004 [10]
Amplitude reflectivity of SRM	0.92 [10]
Power transmission of PRM	0.1
Round trip loss of arm	100 ppm
Power loss at SRM	0.002
Power loss at PD	0.1
Detuning phase	86.5°
Homodyne Phase (broadband)	119.1°
Homodyne Phase (detuned)	135.1°

Table B.1: Interferometer parameters.

loss parameters of $\beta_{\rm sub} = 50\,{\rm ppm/cm}$ and $\gamma_{\rm coa} = 0.5\,{\rm ppm}$ are the requirement. Transmittance of the ITM is designed to be $T_{\rm ITM} = 0.004$, so the intra-cavity power is $P_{\rm circ} = 4P_{\rm mich}/T_{\rm ITM} = 10^3 P_{\rm mich}$. Radiation from an opened window for the main beam is dominant in that from outside. That is estimated to be $K_{\rm rad} = 50\,{\rm mW}$ [110]. With these parameters the laser power between the BS and ITM can be increased to be $P_{\rm mich} = 337\,{\rm W}$ in order to keep the mirror temperature of 22 K. Therefore the laser power at the BS is twice than that, $P_{\rm BS} = 674\,{\rm W}$. As described above, the laser power is determined by the mirror temperature. We optimize the design sensitivity of DRSE configuration based on this relation.

B.1.3 Parameters of KAGRA

Here we summarize the KAGRA parameters in tables below. First, the parameters related to the interferometer are represented in Table B.1. VRSE means variable resonant sideband extraction configuration. Compared with LIGO and Virgo, the transmission of the input test mass is lower, in other words the finesse of the main arm is higher. In the case of KAGRA, the laser power inside the substrate of the ITM cannot be increased very high because

Property	Value
Material	Sapphire
Radius	11 cm
Thickness	15 cm
Mass	22.8 kg
Temperature	22 K
Loss angle	1.0×10^{-8} [111]
Absorption	50 ppm/cm

Table B.2: Mirror parameters.

Property	Value
Material	silica/tantala
Numbers of coating layers	22/40 (ITM/ETM)
Loss angle of silica	3.0×10^{-4} [9, 112]
Loss angle of tantala	5.0×10^{-4} [9, 112]
Beam Radius	3.5 cm [10]
Absorption	0.5 ppm

Table B.3: Coating parameters.

we have to keep the cryogenic temperature of the ITM. Instead of that, the finesse of the main cavity is increased and realize the low shot noise level. The power recycling gain is set to be 10. The loss parameters are decided by the requirement.

Next, we show the mirror parameters in Table B.2. The material is sapphire, which is the unique point of KAGRA. Sapphire has the small loss angle and low absorption at the wave length of 1064 nm. The mirror size is lower and the mass is lighter than that of the mirrors of LIGO and Virgo (35 cm diameter, 20 cm thickness, 40 kg mass). It is because making larger sapphire substrate is technically difficult. The development for heavier sapphire is on going.

Moreover, the coating parameters are described in Table B.3. The coating thermal noise of KAGRA is better than that of the other detectors because of the cryogenic temperature. However, the loss angle of the silica-tantala coating is a little bit worse at the cryogenic temperature than that at the room temperature. Also, we cannot expand the beam radius on the test mass

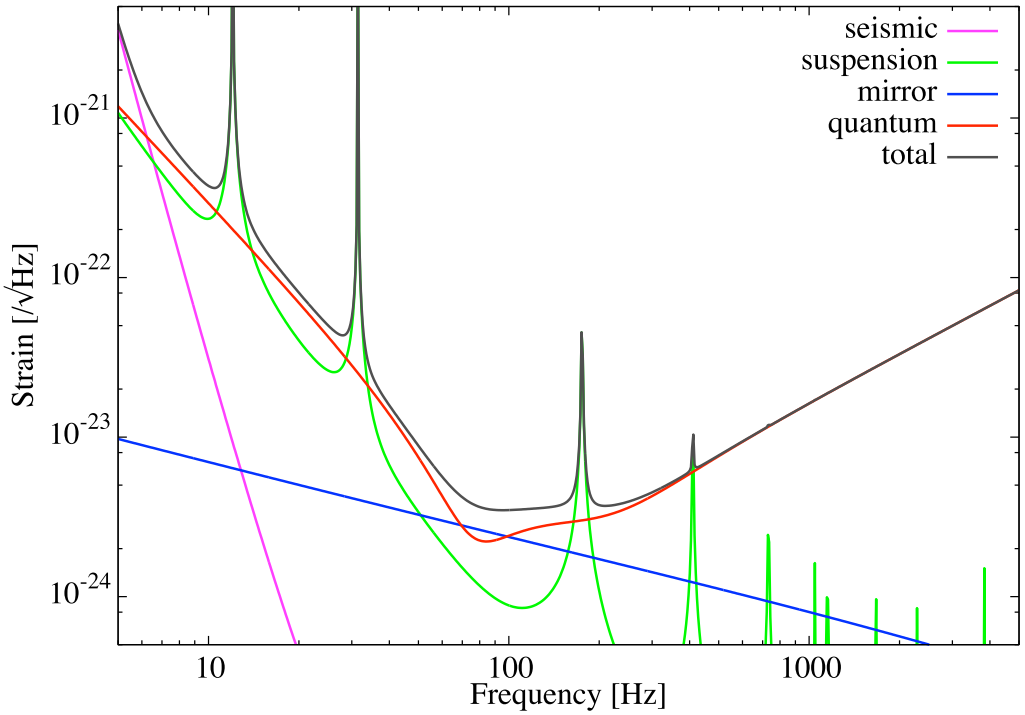

Figure B.2: DRSE sensitivity of KAGRA. The magenta, green, blue, and red lines show the displacement spectrum due to the seismic, suspension thermal, mirror thermal, and quantum noises. The total noise is given by the black line.

due to the small substrate. Thus, the coating thermal noise is not better by a ratio of the mirror temperature compared with LIGO and Virgo (300 K).

Finally, the suspension parameters are shown in Table B.4. The sapphire fibers need to be thick enough to extract the heat from the test mass. The thickness causes the high resonant frequency of the bounce mode which lies in the observation band, and requires the blade springs to decrease the resonant frequency. Suspension thermal noise also should be better owing to the low temperature, but actually it is not the case. The thickness of the fiber contributes to the small dilution factor of the suspension Q-value, and the light mass of the substrate leads to the high suspension thermal noise.

With these parameters we estimate the design sensitivity. In Fig. B.2, we show the sensitivity of DRSE configuration including the contribution of the fundamental noises. These are calculated by the theoretical equations

Property	Value
IM suspension	
Material	CuBe
Number	4
Length	26.1 cm
Diameter	0.6 mm
Loss angle	5×10^{-6}
IM mass	20.5 kg
Temperature	16 K
Blade spring	
Material	Sapphire
Number	4
Horizontal res. freq.	2 kHz
Vertical res. freq.	14.5 Hz (with TM)
Loss angle	7×10^{-7}
Mass	55 g
Temperature	16 K
TM suspension	
Material	Sapphire
Number	4
Length	35 cm
Diameter	1.6 mm
Loss angle	2×10^{-7}
Temperature	19 K (averaged)
Vertical-Horizontal Coupling	1/200

Table B.4: Suspension parameters.

described in Sec. 2.2. The seismic noise includes the gravity gradient noise. The quantum noise is dominant over almost all frequency ranges. The mirror thermal noise is comparable with the quantum noise at the most sensitive band around 100 Hz. The peaks around 12 Hz and 31 Hz come from the resonant frequency of the blade spring and the CuBe bounce mode. The violin modes of the sapphire fiber appear as the peaks above 100 Hz.

B.2 Upgrade plan: KAGRA+

In this section we describe the future upgrade plan of KAGRA, which is called KAGRA+. The second-generation detectors succeed in opening the gravitational wave astronomy, and the plans of the third-generation detectors such as Einstein telescope and Cosmic Explorer are proceeding. Also, LIGO and Virgo are planning their near future upgrades of the current facilities like A+ [113], Voyager, and AdV+ as a step toward the third generation. Many ultimate techniques will be used in the third generation, so it is important to construct these near future detectors and confirm their validity. Moreover, the detectors themselves which have the larger inspiral range by a few can contribute to more detections by around one order of magnitude.

In order to test the ultimate techniques and take part in the near future detector network, KAGRA is required to have a plan of the upgrade. Currently, this plan is called KAGRA+. Here we discuss some candidates of the upgrade focusing on the high frequency, low frequency, and broadband improvement, followed by the further future plan of KAGRA++. Each sensitivity is optimized by a particle swarm optimization method [114].

B.2.1 High frequency

In Fig. B.3, the upgraded sensitivity especially at the high frequency is shown. This version is called KAGRA high frequency (HF). The optimized parameter is localization of a binary neutron star merger, which is $0.114\,\mathrm{deg}^2$, where it is assumed that the LIGO and Virgo are operating with their design sensitivities. The important parameters are the input power of 340 W, the mirror temperature of 30 K, the suspension fiber diameter of 2.4 mm and length of 20 cm,

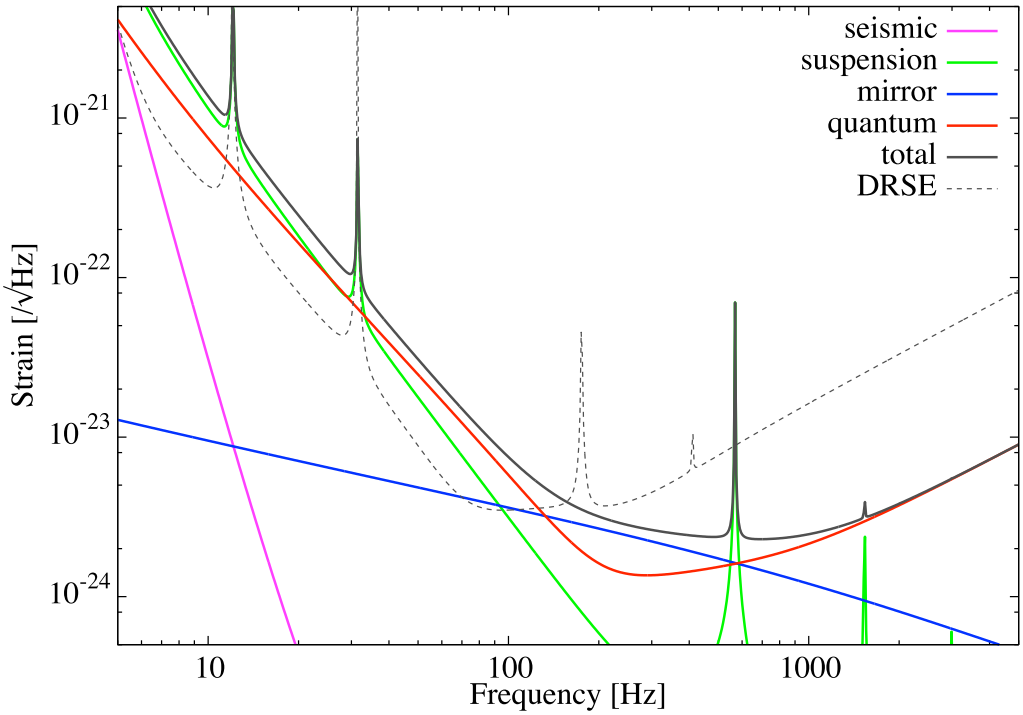

Figure B.3: Strain sensitivity of KAGRA HF. The solid lines show the same noise as the previous figure. The black dotted line means the DRSE total sensitivity.

and the frequency independent squeezing factor of 4 dB at the detection of the squeezed light.

By increasing the laser power dramatically and using the phase squeezing, the shot noise is much lower than that of KAGRA. The suspension thermal noise is worse because the fiber is shorter and thinner owing to the necessity of heat extraction. It is difficult to realize such a huge power with avoiding the angular instability, parametric instability, and the other additional noises. Preparation of the stable high power laser source is also the issue.

Even though the binary neutron star range of 123 Mpc is not so high, digging the high frequency regime can reveal the equation of state of neutron stars, and test of general relativity further with harmonics of ringdown at binary black hole mergers. The HF sensitivity in kHz range is higher than that of A+ and AdV+, so we can get the strictest constraint on the equation

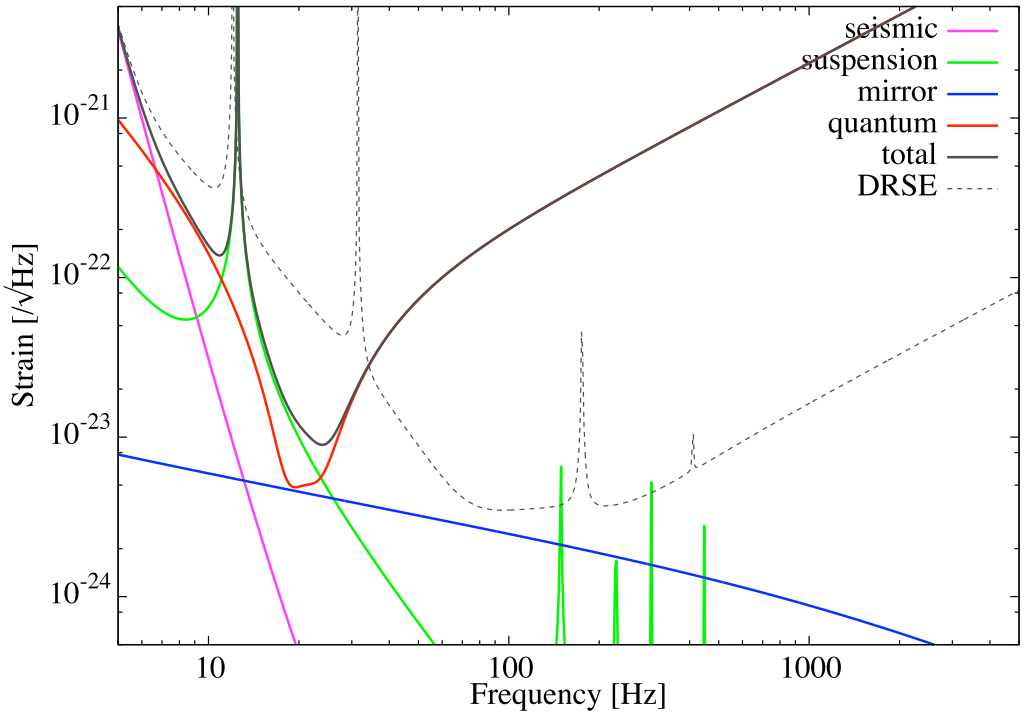

Figure B.4: Strain sensitivity of KAGRA LF.

of state and modified general relativity.

B.2.2 Low frequency

In Fig. B.4, we show the sensitivity improved at the low frequency region. This is the sensitivity of KAGRA low frequency (LF). The optimized parameter is a binary black hole range which has an intermediate mass of 100 $M_\odot$, which reaches 4.3 Gpc. The key parameters are the input power of 1.7 W, the mirror mass of 100 kg, the fiber diameter of 1 mm, and length of 200 cm, and the large detuning phase of 61°.

The suspension thermal noise and radiation pressure noise are much lower because of the long and thin wire resulting in the large dilution factor, and the tiny laser power. Also, the large detuning contributes to improving the most sensitive band. There are many technical problems such as making the heavy sapphire substrate of 100 kg, constructing the long suspension system

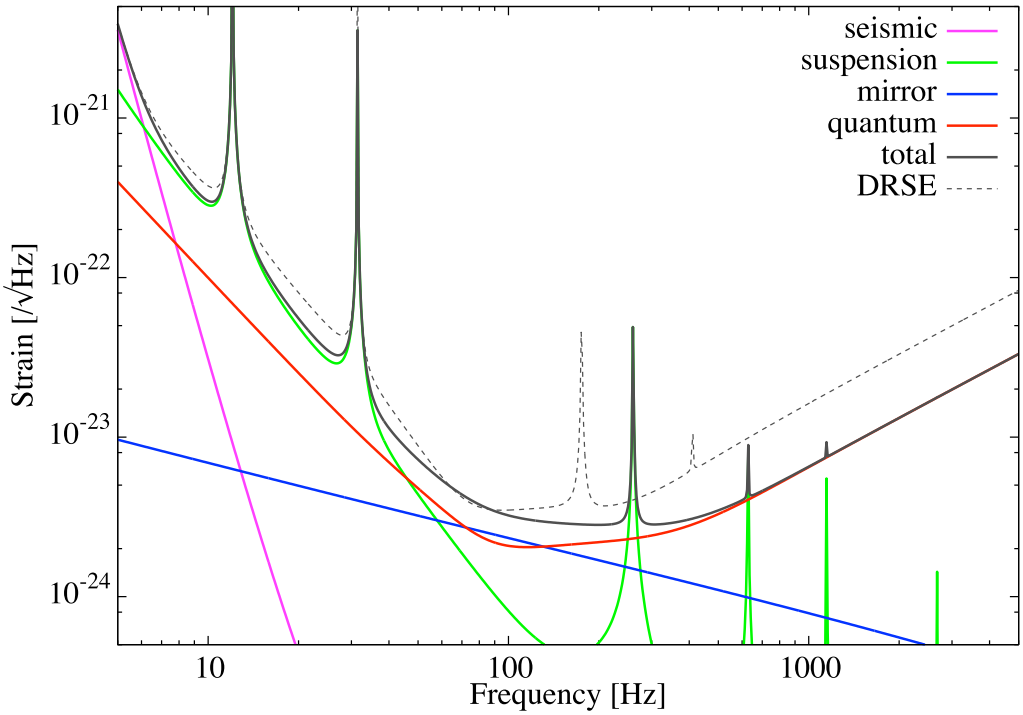

Figure B.5: Strain sensitivity of KAGRA broadband.

in current limited space, and the locking scheme to keep the large detuning phase. Moreover, it is typically difficult to reduce many technical noises around several 10 Hz.

The target of this upgrade is the first observation of the intermediate mass black hole. Confirmation of the existence gives huge impact to astronomy associated with star and galaxy formation. The possibility of the detection is higher than those of upgraded LIGO and Virgo by a factor of 3. In addition, the higher sensitivity at the low frequency helps us to detect the gravitational wave signals earlier. This results in sending the earlier alert to electro-magnetic wave observatories, and even to the other gravitational wave detectors.

B.2.3 Broadband

We describe the sensitivity improved over broad frequency ranges in Fig. B.5. This version is called KAGRA broadband. The sensitivity is optimized by

Property	HF	LF	broadband
Input power [W]	340	1.7	73
Mirror temperature [K]	30	23	22
Mirror mass [kg]	23	100	23
Fiber diameter [mm]	2.4	1	1.6
Fiber length [cm]	20	200	27
Detuning phase [degree]	89.9	60.7	89.6
Squeezing	10 dB w/o FC	N.A.	10 dB w FC
BNS range [Mpc]	123	177	181
BBH30 range [Gpc]	315	2285	1177
BBH100 range [Gpc]	117	4327	470
BNS Localization [deg^2]	0.114	0.479	0.135

Table B.5: Parameters for the near futue upgrade plans.

the binary neutron star range, which improves up to 181 Mpc The notable parameters are the input power of 73 W, the fiber diameter of 1.6 mm and length of 27 cm, and the squeezing of 10 dB with a 100-m filter cavity.

The frequency dependent squeezing reduces the quantum noise broadly. Especially, a little bit higher power and the phase squeezing suppresses the shot noise floor. The filter cavity technic is already on the stage of being developed for the second-generation detectors. It is necessary to discuss how to secure a space for the 100-m filter cavity in the KAGRA tunnel.

This broadband configuration has the biggest inspiral range of the other two upgrade plans, although it is smaller than those of A+ and AdV+. The certain improvement of the binary range with the feasible technic results in the reliable contribution to the detector network signal to noise ratio and the localization. Also, it helps taking more statistics of binary merger population.

B.2.4 KAGRA++

As a further future plan, the KAGRA++ is considered. Combining the key point on each configuration such as the input power of 320 W, the mirror mass of 100 kg, and the 10 dB squeezing with the filter cavity, we can reach the binary neutron star range of 355 Mpc which is higher than that of A+ and AdV+. The sensitivity is shown in Fig. B.6. Main parameters of the upgrade

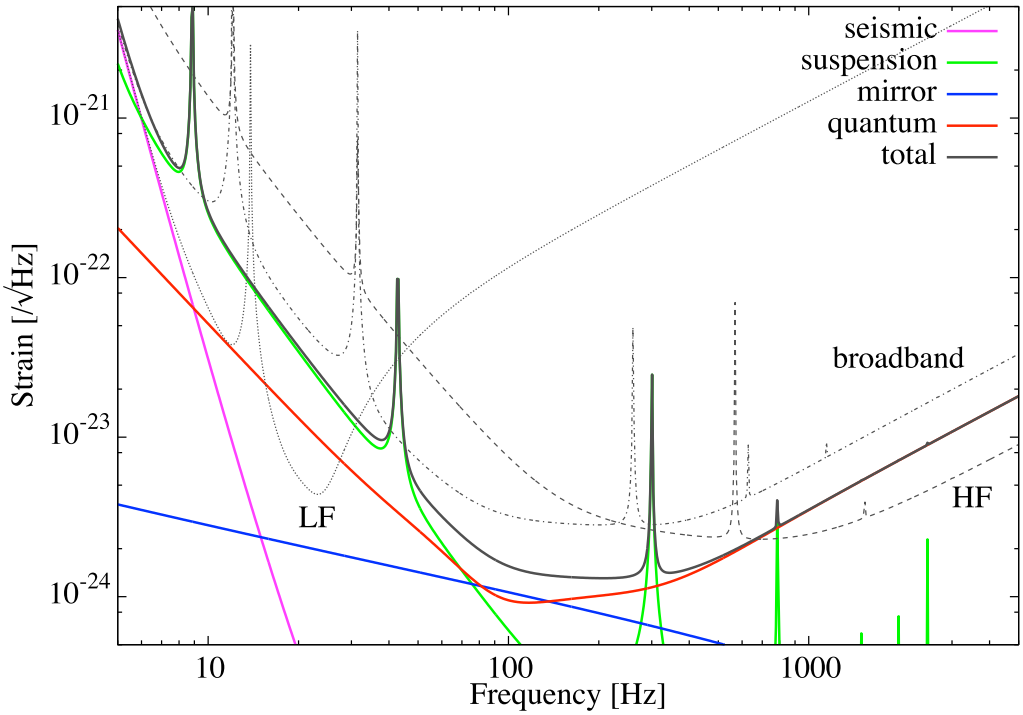

Figure B.6: Strain sensitivity of KAGRA++. The KAGRA+ sensitivities are also described as the dotted lines for the comparison.

Property	KAGRA	++
Input power [W]	67	320
Mirror temperature [K]	22	20
Mirror mass [kg]	23	100
Fiber diameter [mm]	1.6	3.6
Fiber length [cm]	35	34
Detuning phase [degree]	86.5	89.4
Squeezing	N.A.	10 dB w FC
BNS range [Mpc]	153	355
BBH30 range [Gpc]	1095	1956
BBH100 range [Gpc]	353	785
Localization [deg^2]	0.183	0.100

Table B.6: Parameters for KAGRA and the further upgrade plan.

plans are listed in Table B.5, and those of the KAGRA and the further future plan are in Table B.6.

B.3 Summary of this chapter

KAGRA parameters and the designed sensitivities are described. We also introduce the future upgrade plan of KAGRA which focuses on the high frequency, frequency dependent squeezing, and low frequency. In addition, there is a further future plan of KAGRA++ reaching the doubled inspiral range of the designed original KAGRA.

Bibliography

[1] A. Einstein, Sitzungsber. K. Preuss. Akad. Wiss. **1**, 688 (1916).

Näherungsweise Integration der Feldgleichungen der Gravitation

[2] A. Einstein, Sitzungsber. K. Preuss. Akad. Wiss. **1**, 154 (1918).

Über Gravitationswellen

[3] B. P. Abbott *et al.* (LIGO Scientific Collaboration and Virgo Collaboration) Phys. Rev. Lett. **116**, 061102 (2016).

Observation of Gravitational Waves from a Binary Black Hole Merger

[4] B. P. Abbott *et al.* (LIGO Scientific Collaboration and Virgo Collaboration) Phys. Rev. Lett. **119**, 141101 (2017).

GW170814: A Three-Detector Observation of Gravitational Waves from a Binary Black Hole Coalescence

[5] B. P. Abbott *et al.* (LIGO Scientific Collaboration and Virgo Collaboration) Phys. Rev. Lett. **119**, 161101 (2017).

GW170817: Observation of Gravitational Waves from a Binary Neutron Star Inspiral

[6] B. P. Abbott *et al.* Astrophys. J. Lett. **848**, L13 (2017)

Gravitational Waves and Gamma-Rays from a Binary Neutron Star Merger: GW170817 and GRB 170817A

[7] B. P. Abbott *et al.* Astrophys. J. Lett. **848**, L12 (2017)

Multi-messenger Observations of a Binary Neutron Star Merger

[8] B. P. Abbott *et al.* (LIGO Scientific Collaboration and Virgo Collaboration) arxiv:1811.12907 (2018)

GWTC-1: A Gravitational-Wave Transient Catalog of Compact Binary Mergers Observed by LIGO and Virgo during the First and Second Observing Runs

[9] K. Somiya *et al.* (KAGRA Collaboration) Classical Quantum Gravity **29**, 124007 (2012)

Detector configuration of KAGRA-the Japanese cryogenic gravitational-wave detector

[10] Y. Aso *et al.* (KAGRA Collaboration) Phys. Rev. D **88**, 043007 (2013).

Interferometer design of the KAGRA gravitational wave detector

[11] S. Hild *et al.* Classical Quantum Gravity **28**, 094013 (2011)

Sensitivity studies for third-generation gravitational wave observatories

[12] B. P. Abbott *et al.* (LIGO Scientific Collaboration) Classical Quantum Gravity **34**, 044001 (2017)

Exploring the sensitivity of next generation gravitational wave detectors

[13] S. M. Koushiappas & A. Loeb, Phys. Rev. Lett. **119**, 221104 (2018).

Maximum Redshift of Gravitational Wave Merger Events

[14] J. Aasi *et al.* (LIGO Scientific Collaboration) Classical Quantum Gravity **32**, 074001 (2015)

Advanced LIGO

[15] F. Acernese *et al.* (Virgo Collaboration) Classical Quantum Gravity **32**, 024001 (2015)

Advanced Virgo: a second-generation interferometric gravitational wave detector

[16] S. Sakata, O. Miyakawa, A. Nishizawa, H. Ishizaki, & S. Kawamura, Phys. Rev. D **81**, 064023 (2010).

Measurement of angular antispring effect in optical cavity by radiation pressure

[17] T. Westphal *et al.* Appl. Phys. B **3**, 551 (2012)

Design of the 10 m AEI prototype facility for interferometry studies

[18] A. R. Neben, T. P. Bodiya, C. Wipf, E. Oelker, T. Corbitt, & N. Mavalvala, New J. Phys. **14**, 115008 (2012).

Structural thermal noise in gram-scale mirror oscillators

[19] C. Gräf *et al.* Classical Quantum Gravity **31**, 215009 (2014)

Design of a speed meter interferometer proof-of-principle experiment

[20] N. Matsumoto, K. Komori, Y. Michimura, G. Hayase, Y. Aso, & K. Tsubono, Phys. Rev. A **92**, 033825 (2015).

5-mg suspended mirror driven by measurement-induced backaction

[21] T. T-H. Nguyen, C. M. Mow-Lowry, B. J. J. Slagmolen, J. Miller, A. J. Mullavey, S. Goßler, P. A. Altin, D. A. Shaddock, & D. E. McClelland, Phys. Rev. D **92**, 112004 (2015).

Frequency dependence of thermal noise in gram-scale cantilever flexures

[22] M. Aspelmeyer, T. J. Kippenberg, & F. Marquardt, Rev. Mod. Phys. **86**, 1391 (2014).

Cavity optomechanics

[23] C. Genes, D. Vitali, P. Tombesi, S. Gigan, & M. Aspelmeyer, Phys. Rev. A **77**, 033804 (2008).

Ground-state cooling of a micromechanical oscillator: Comparing cold damping and cavity-assisted cooling schemes

[24] W. Marshall, C. Simon, R. Penrose, & D. Bouwmeester, Phys. Rev. Lett. **91**, 130401 (2003).

Towards Quantum Superpositions of a Mirror

[25] A. H. Safavi-Naeini, J. T. Hill, T. P. M. Alegre, A. Krause, & O. Painter, Phys. Rev. Lett. **108**, 033602 (2012).

Observation of Quantum Motion of a Nanomechanical Resonator

[26] T. P. Purdy, R. W. Peterson, & C. A. Regal Science **339**, 801-804 (2013).

Observation of Radiation Pressure Shot Noise on a Macroscopic Object

[27] J. D. Teufel, F. Lecocq, & R. W. Simmonds, Phys. Rev. Lett. **116**, 013602 (2016).

Overwhelming Thermomechanical Motion with Microwave Radiation Pressure Shot Noise

[28] J. D. Teufel, T. Donner, Dale Li, J. W. Harlow, M. S. Allman, K. Cicak, A. J. Sirois, J. D. Whittaker, K. W. Lehnert & R. W. Simmonds, Nature (London) **475**, 359-363 (2011).

Sideband cooling of micromechanical motion to the quantum ground state

[29] J. Chan, T. P. Mayer Alegre, A. H. Safavi-Naeini, J. T. Hill, A. Krause, S. Groeblacher, M. Aspelmeyer & O. Painter, Nature (London) **478**, 89-92 (2011).

Laser cooling of a nanomechanical oscillator into its quantum ground state

[30] R. W. Peterson, T. P. Purdy, N. S. Kampel, R. W. Andrews, P.-L. Yu, K. W. Lehnert, & C. A. Regal, Phys. Rev. Lett. **116**, 063601 (2016).

Laser Cooling of a Micromechanical Membrane to the Quantum Backaction Limit

[31] T. A. Palomaki, J. D. Teufel, R. W. Simmonds, & K. W. Lehnert, Science **342**, 710-713 (2013).

Entangling Mechanical Motion with Microwave Fields

[32] R. Riedinger, A. Wallucks, I. Marinković, C. Löschnauer, M. Aspelmeyer, S. Hong, & S. Gröblacher, Nature (London) **556**, 473-477 (2018).

Remote quantum entanglement between two micromechanical oscillators

[33] C. F. Ockeloen-Korppi, E. Damskägg, J.-M. Pirkkalainen, M. Asjad, A. A. Clerk, F. Massel, M. J. Woolley, & M. A. Sillanpää, Nature (London) **556**, 478-482 (2018).

Stabilized entanglement of massive mechanical oscillators

[34] J. Weber, Phys. Rev. Lett. **117**, 306 (1960).

Detection and Generation of Gravitational Waves

[35] M. E. Gertsenshtein & V. I. Pustovoit, Sov. Phys. JETP **16**, 433 (1962).

On the detection of low frequency gravitational waves

[36] G. E. Moss, L. R. Miller, & R. L. Forward, Appl. Opt. **10**, 2495 (1971).

Photon-Noise-Limited Laser Transducer for Gravitational Antenna

[37] J. H. Taylor & J. M. Weisberg, Astrophys. J. **253**, 908 (1982).

A new test of general relativity - Gravitational radiation and the binary pulsar PSR 1913+16

[38] R. A. Hulse & J. H. Taylor, Astrophys. J. **195**, L51 (1975).

Discovery of a pulsar in a binary system

[39] M. Maggiore, Oxford University Press (2007).

Gravitational Waves Volume 1: Theory and Experiments

[40] J. Creighton & W. Anderson, Wiley Series on Cosmology (2011).

Gravitational-Wave Physics and Astronomy: An Introduction to Theory, Experiment and Data Analysis.

[41] N. Seto, S. Kawamura, & T. Nakamura, Phys. Rev. Lett. **87**, 221103 (2001).

Possibility of Direct Measurement of the Acceleration of the Universe Using 0.1 Hz Band Laser Interferometer Gravitational Wave Antenna in Space

[42] S. Kawamura *et al.* Classical Quantum Gravity **28**, 094011 (2011)

The Japanese space gravitational wave antenna: DECIGO

[43] T. Nakamura *et al.* Prog. Theor. Exp. Phys. **2016**, 093E01 (2016)

Pre-DECIGO can get the smoking gun to decide the astrophysical or cosmological origin of GW150914-like binary black holes

[44] M. Ando, K. Ishidoshiro, K. Yamamoto, K. Yagi, W. Kokuyama, K. Tsubono, & A. Takamori, Phys. Rev. Lett. **105**, 161101 (2010).

Torsion-Bar Antenna for Low-Frequency Gravitational-Wave Observations

[45] H. B. Callen & T. A. Welton, Phys. Rev. **83**, 34 (1951).

Irreversibility and Generalized Noise

[46] R. F. Greene & H. B. Callen, Phys. Rev. **83**, 1231 (1951).

On the Formalism of Thermodynamic Fluctuation Theory

[47] R. Kubo, Rep. Prog. Phys. **29**, 255 (1966).

The fluctuation-dissipation theorem

[48] P. R. Saulson, Phys. Rev. D **42**, 2437 (1990).

Thermal noise in mechanical experiments

[49] Y. Levin, Phys. Rev. D **57**, 659 (1998).

Internal thermal noise in the LIGO test masses: A direct approach

[50] F. Bondu, P. Hello, & J. Y. Vinet, Phys. Lett. A **246**, 227-236 (1998).

Thermal noise in mirrors of interferometric gravitational wave antennas

[51] G. M. Harry *et al.* Classical Quantum Gravity **19**, 897 (2002)

Thermal noise in interferometric gravitational wave detectors due to dielectric optical coatings

[52] M. Cerdonio, L. Conti, A. Heidmann, & M. Pinard, Phys. Rev. D **63**, 082003 (2001).

Thermoelastic effects at low temperatures and quantum limits in displacement measurements

[53] K. Somiya, K. Kokeyama, & R. Nawrodt, Phys. Rev. D **82**, 127101 (2010).

Remarks on thermoelastic effects at low temperatures and quantum limits in displacement measurements

[54] J. A. Sidles & D. Sigg, Phys. Lett. A **354**, 167-172 (2006).

Optical torques in suspended Fabry-Perot interferometers

[55] D. F. Walls & G. J. Milburn, Springer-Verlag Berlin Heidelberg, 127-133 (2008).

Quantum Optics

[56] C. M. Caves, Phys. Rev. D **23**, 1693 (1981).

Quantum-mechanical noise in an interferometer

[57] H. J. Kimble, Y. Levin, A. B. Matsko, K. S. Thorne, & S. P. Vyatchanin, Phys. Rev. D **65**, 022002 (2001).

Conversion of conventional gravitational-wave interferometers into quantum nondemolition interferometers by modifying their input and/or output optics

[58] K. McKenzie, N. Grosse, W. P. Bowen, S. E. Whitcomb, M. B. Gray, D. E. McClelland, & P. K. Lam, Phys. Rev. Lett. **93**, 161105 (2004).

Squeezing in the Audio Gravitational-Wave Detection Band

[59] A. Buonanno & Y. Chen, Phys. Rev. D **64**, 042006 (2001).

Quantum noise in second generation, signal-recycled laser interferometric gravitational-wave detectors

[60] R. E. Slusher, L. W. Hollberg, B. Yurke, J. C. Mertz, & J. F. Valley, Phys. Rev. Lett. **55**, 2409 (1985).

Observation of Squeezed States Generated by Four-Wave Mixing in an Optical Cavity

[61] H. Vahlbruch, M. Mehmet, K. Danzmann, & R. Schnabel, Phys. Rev. Lett. **117**, 110801 (2016).

Detection of 15 dB Squeezed States of Light and their Application for the Absolute Calibration of Photoelectric Quantum Efficiency

[62] K. McKenzie, M. B. Gray, S. Goßler, P. K. Lam, & D. E McClelland. Classical Quantum Gravity **23**, S245 (2006)

Squeezed state generation for interferometric gravitational-wave detection

[63] M. S. Stefszky *et al.* Classical Quantum Gravity **29**, 145015 (2012)

Balanced homodyne detection of optical quantum states at audio-band frequencies and below

[64] E. Oelker, T. Isogai, J. Miller, M. Tse, L. Barsotti, N. Mavalvala, & M. Evans, Phys. Rev. Lett. **116**, 041102 (2016).

Audio-Band Frequency-Dependent Squeezing for Gravitational-Wave Detectors

[65] K. Goda *et al.* Nature Phys. **4**, 472-476 (2008).

A quantum-enhanced prototype gravitational-wave detector

[66] J. Abadie *et al.* (LIGO Scientific Collaboration) Nature Phys. **7**, 962-965 (2011).

A gravitational wave observatory operating beyond the quantum shot-noise limit

[67] J. Aasi *et al.* (LIGO Scientific Collaboration) Nature Photonics **7**, 613-619 (2013).

Enhanced sensitivity of the LIGO gravitational wave detector by using squeezed states of light

[68] K. Nagano, Y. Enomoto, M. Nakano, A. Furusawa, & S. Kawamura, Phys. Lett. A **380**, 983-988 (2016).

New method to measure the angular antispring effect in a Fabry-Perot cavity with remote excitation using radiation pressure

[69] Y. Enomoto, K. Nagano, M. Nakano, A. Furusawa, & S. Kawamura, Classical Quantum Gravity **33**, 145002 (2016)

Observation of reduction of radiation-pressure-induced rotational anti-spring effect on a 23 mg mirror in a Fabry-Perot cavity

[70] D. V. Martynov *et al.* Phys. Rev. D **93**, 112004 (2016).

Sensitivity of the Advanced LIGO detectors at the beginning of gravitational wave astronomy

[71] J. Cripe *et al.* arxiv:1802.10069 (2018).

Observation of a room-temperature oscillator' s motion dominated by quantum fluctuations over a broad audio-frequency band

[72] E. Schrödinger, Naturwissenschaften **23**, 807-812 (1935).

Die gegenwärtige situation in der quantenmechanik

[73] A. Bassi, A. Großardt, & H. Ulbricht, Classical Quantum Gravity **34**, 193002 (2017)

Gravitational decoherence

[74] L. Diósi, Phys. Lett. A **105**, 199-202 (1984).

Gravitation and quantum-mechanical localization of macro-objects

[75] R. Penrose, Gen. Relativ. Gravit. **28**, 581-600 (1996)

On Gravity's role in Quantum State Reduction

[76] G. C. Ghirardi, A. Rimini, & T. Weber, Phys. Rev. D **34**, 470 (1986).

Unified dynamics for microscopic and macroscopic systems

[77] L. Diósi, Phys. Rev. Lett. **114**, 050403 (2015).

Testing Spontaneous Wave-Function Collapse Models on Classical Mechanical Oscillators

[78] S. L. Adler, J. Phys. A: Math. Theor. **40** 2935 (2007).

Lower and upper bounds on CSL parameters from latent image formation and IGM heating

[79] S. L. Adler, J. Phys. A: Math. Theor. **40** 2935 (2007).

Lower and upper bounds on CSL parameters from latent image formation and IGM heating

[80] C. Curceanu, B. C. Hiesmayr, & K. Piscicchia, J. Adv. Phys. **4** 263-266 (2015).

X-rays Help to Unfuzzy the Concept of Measurement

[81] M. Bilardello, S. Donadi, A. Vinante, & A. Bassi, Physica A **462** 764-782 (2016).

Bounds on collapse models from cold-atom experiments

[82] M. Carlesso, A. Bassi, P. Falferi, & A. Vinante, Phys. Rev. D **94**, 124036 (2016).

Experimental bounds on collapse models from gravitational wave detectors

[83] A. Vinante, R. Mezzena, P. Falferi, M. Carlesso, & A. Bassi, Phys. Rev. Lett. **119**, 110401 (2017).

Improved Noninterferometric Test of Collapse Models Using Ultracold Cantilevers

[84] H. Müller-Ebhardt, H. Rehbein, R. Shnabel, K. Danzmann, & Y. Chen, Phys. Rev. Lett. **100**, 013601 (2008).

Entanglement of Macroscopic Test Masses and the Standard Quantum Limit in Laser Interferometry

[85] U. B. Hoff, J. Kollath-Bönig, J. S. Neergaard-Nielsen, & U. L. Andersen, Phys. Rev. Lett. **117**, 143601 (2016).

Measurement-Induced Macroscopic Superposition States in Cavity Optomechanics

[86] F. Y. Khalili, H. Miao, H. Yang, A. H. Safavi-Naeini, O. Painter, & Y. Chen, Phys. Rev. A **86**, 033840 (2012).

Quantum back-action in measurements of zero-point mechanical oscillations

[87] B. S. Sheard, M. B. Gray, C. M. Mow-Lowry, D. E. McClelland, & S. E. Whitcomb, Phys. Rev. A **69**, 051801 (2004).

Observation and characterization of an optical spring

[88] Y. Chen, J. Phys. B: At. Mol. Opt. Phys. **46**, 104001 (2013).

Macroscopic quantum mechanics: theory and experimental concepts of optomechanics

[89] M. Aspelmeyer, T. J. Kippenberg, & F. Marquardt, Springer-Verlag Berlin Heidelberg, 1-3 (2014).

Cavity optomechanics Nano- and Micromechanical Resonators Interacting with Light

[90] J. Jahng, M. Lee, C. Stambaugh, W. Bak, & W. Jhe, Phys. Rev. A **84**, 022318 (2011).

Active feedback cooling of massive electromechanical quartz resonators

[91] D. J. Wilson, V. Sudhir, N. Piro, R. Schilling, A. Ghadimi, & T. J. Kippenberg, Nature (London) **524**, 325-329 (2015).

Measurement-based control of a mechanical oscillator at its thermal decoherence rate

[92] A. H. Safavi-Naeini, S. Gröblacher, J. T. Hill, J. Chan, M. Aspelmeyer, & O. Painter, Nature (London) **500**, 185-189 (2013).

Squeezed light from a silicon micromechanical resonator

[93] J. B. Clark, F. Lecocq, R. W. Simmonds, J. Aumentado, & J. D. Teufel, Nature Phys. **12**, 683-687 (2016).

Observation of strong radiation pressure forces from squeezed light on a mechanical oscillator

[94] T. P. Purdy, P.-L. Yu, R. W. Peterson, N. S. Kampel, & C. A. Regal, Phys. Rev. X **3**, 031012 (2013).

Strong Optomechanical Squeezing of Light

[95] N. Matsumoto, K. Komori, S. Ito, Y. Michimura, & Y. Aso, Phys. Rev. A **94**, 033822 (2016).

Direct measurement of optical-trap-induced decoherence

[96] C. M. Mow-Lowry, A. J. Mullavey, S. Goßler, M. B. Gray, & D. E. McClelland, Phys. Rev. Lett. **100**, 010801 (2008).

Cooling of a Gram-Scale Cantilever Flexure to 70 mK with a Servo-Modified Optical Spring

[97] T. Corbitt *et al.* Phys. Rev. Lett. **98**, 150802 (2007).

An All-Optical Trap for a Gram-Scale Mirror

[98] T. Corbitt, C. Wipf, T. Bodiya, D. Ottaway, D. Sigg, N. Smith, S. Whitcomb, & N. Mavalvala, Phys. Rev. Lett. **99**, 160801 (2007).

Optical Dilution and Feedback Cooling of a Gram-Scale Oscillator to 6.9 mK

[99] B. P. Abbott *et al*, New J. Phys. **11**, 073032 (2009).

Observation of a kilogram-scale oscillator near its quantum ground state

[100] N. Matsumoto, Y. Michimura, Y. Aso, & K. Tsubono, Opt. Express **22**, 12915 (2014).

Optically trapped mirror for reaching the standard quantum limit

[101] G. I. González & P. R. Saulson, J. Acoust. Soc. Am. **96**, 207 (1994).

Brownian motion of a mass suspended by an anelastic wire

[102] M. K. Bantel & R. D. Newman, J. Alloy. Comp. **310**, 233-242 (2000).

High precision measurement of torsion fiber internal friction at cryogenic temperatures

[103] T. Shimoda, N. Aritomi, A. Shoda, Y. Michimura, & M. Ando, Phys. Rev. D **97**, 104003 (2018).

Seismic cross-coupling noise in torsion pendulums

[104] R. W. P. Drever, J. L. Hall, F. V. Kowalski, J. Hough, G. M. Ford, A. J. Munley, & H. Ward, Appl. Phys. B **31**, 97-105 (1983).

Laser phase and frequency stabilization using an optical resonator

[105] P. Kwee, B. Willke, & K. Danzmann, Opt. Lett. **34**, 2912-2914 (2009).

Shot-noise-limited laser power stabilization with a high-power photodiode array

[106] F. Antonucci, E. Majorana, P. Puppo, P. Rapagnani, F. Ricci, S. Ricciardi, & A. Schirone, Phys. Lett. A **315**, 409-417 (2003).

Influence of a mirror holder on thermal noise in gravitational wave interferometers

[107] A. A. Balushi, W. Cong, & R. B. Mann, Phys. Rev. A **98**, 043811 (2018).

Optomechanical quantum Cavendish experiment

[108] K. Komori, Y. Enomoto, H. Takeda, Y. Michimura, K. Somiya, M. Ando, and S. W. Ballmer, Phys. Rev. D **97**, 102001 (2018).

Direct approach for the fluctuation-dissipation theorem under nonequilibrium steady-state conditions

[109] A. Khalaidovski, *et al.* Classical Quantum Gravity **31**, 105004 (2014)

Evaluation of heat extraction through sapphire fibers for the GW observatory KAGRA

[110] Y. Sakakibara, *et al.* Class. Quantum Grav. **31**, 224003 (2014).

Progress on the cryogenic system for the KAGRA cryogenic interferometric gravitational wave telescope

[111] T. Uchiyama, *et al.* Phys. Lett. A **261**, 5 (1999).

Mechanical quality factor of a cryogenic sapphire test mass for gravitational wave detectors

[112] E. Hirose, *et al.* Phys. Rev. D **90**, 102004 (2014).

Mechanical loss of a multilayer tantala/silica coating on a sapphire disk at cryogenic temperatures: Toward the KAGRA gravitational wave detector

[113] J. Miller, L. Barsotti, S. Vitale, P. Fritschel, M. Evans, & D. Sigg, Phys. Rev. D **91**, 062005 (2015).

Prospects for doubling the range of Advanced LIGO

[114] Y. Michimura, K. Komori, A. Nishizawa, H. Takeda, K. Nagano, Y. Enomoto, K. Hayama, K. Somiya, & M. Ando, Phys. Rev. D **97**, 122003 (2018).

Particle swarm optimization of the sensitivity of a cryogenic gravitational wave detector

Acknowledgement

I appreciate numerous supports from various people. Here I introduce a part of them.

First, I would like to thank my supervisor Masaki Ando for his huge supports. Since I entered his laboratory, he watched over my research of the fiber interferometer experiment when I was an under graduated student, the cooling experiment on my master thesis, and this work on my doctoral thesis. He always answered my question clearly, which enabled me to improve my theoretical works and experiments. Also, many experimental setups on my works were purchased by him and I have never felt financial issues. I had much great experience in Ando laboratory, and it is one of my best prides in my life to be his first student.

Next, I cannot thank Yuta Michimura enough. He is assistant professor in our laboratory, and the person I discussed everything with the most times. When I consulted him about from important things such as my experimental motivation to trivial matters, he listened to me and gave various advice every time. He bought me even expensive parts obligingly, so the progress of my experiment was very smooth. I was able to take part in important works of calculation of KAGRA sensitivity thanks to his suggestion. I looked at his activity on various fields and I am convinced that he is one of the best scientists, my role model, and person I should go above.

My excellent colleagues in our laboratory are always exciting me.

Yutaro Enomoto surprised me many times with his great insight, in parti-

cluar on quantum noises. He deepens my understanding with our discussion related to optomechanics, thermal noise, and so on. I thank him for his help of my thesis work with constructing the setup and making high quality circuits.

Koji Nagano has balanced knowledge and experience with high standard in the field of gravitational wave detector. He answered even my tiny questions instantly and discussed with me for long times.

Tomofumi Shimoda gave me much knowledge, especially about suspension and thermal noise. His attentive logical thinking and outstanding experimental technique stimulated me.

Naoki Aritomi has the comprehensive faculty associated with both theory and experiment. His knowledge of filter cavity recalled me the necessity of my more learnings.

Hiroki Takeda is outstanding at theory and analysis of the gravitational wave. Thanks to discussion with him, I can also get the theoretical understanding which I had never touched without him.

Ching Pin Ooi is familiar with Q-values on mechanical experiments. He taught me not only the Q-value but also foreign values in scientific research. He helped me measuring the Q-value of the suspension fiber in my thesis experiment.

Takuya Kawasaki has keen thought, particularly on quantum mechanics and measurement theory. Also, I would like to learn his balancing of experiments in the laboratory and theoretical works at home.

Satoru Takano combines ability and enthusiasm to his experiment, which encouraged me many times. We discussed various things in our laboratory until late at night frequently.

Naoki Kita absorbs knowledge new knowledge and experimental sense fast. I learned important capacity for researchers anytime of the adaptability from him.

Yuki Miyazaki's activities in our laboratory and in KAGRA are surprising and driving me. He also helped me constructing the setup and doing frequency stabilization in my thesis work.

Moreover, I would like to appreciate people out of Ando laboratory.

Kimio Tsubono was my supervisor at the physics seminar when I was an under graduated student. He taught me much attraction of the gravitational wave and that lecture was definitely a beginning of my research life in the field. I gratefully thank him for leading me to this fantastic world.

Seiji Kawamura is also the person who took me into the field of gravitational wave. He was a supervisor at the spring school in ICRR just before I entered Ando laboratory. I was able to work in the gravitational wave group in the school thanks to his recommendation. He always encouraged me to do my experiments after the school.

Stefan W. Ballmer gave me a chance of writing the non-equilibrium thermal noise paper. His suggestion of writing the paper just after short discussion of KAGRA suspension thermal noise resulted in progressing my understanding of thermal noises and accumulating experience of writing and publishing the paper.

Matthew J. Evans was my supervisor at my stay in MIT for two months. I was surprised to look at his energetic activities on both theories and experiments. I appreciate his approval of my stay in MIT at that time and for the following two years as a postdoc with the JSPS fellowships.

Lee McCuller kindly took care of my working on the experiment related to the filter cavity in MIT. With his super grate support, I was able to do experiments without any troubles and learn many things about optics and quantum noise.

Kentaro Somiya attracted me with his clear understanding and description on quantum and thermal noises. The works for KAGRA design sensitivity and KAGRA+ are progressing with his great help. I always enjoyed discussion with him.

Nobuyuki Matsumoto gave me the research theme of optomechanics and trained me from my under graduated student era. He was always an adviser after leaving here. I learned much simple qualitative understanding from him.

I would like to thank previous members of our laboratory: Yoichi Aso, Ayaka Shoda, Kazunori Shibata, Takafumi Ushiba, Yuya Kuwahara, Yuzuru Sakai, Shotaro Wada, Jake Guscott, Meng Luo, Donatella Fiorucci, and Teng

Zhang.

Shigemi Otsuka, Yoshikatsu Nanjo, and Togo Shimozawa made huge amount of mechanical parts for my experiment in the mechanical shop. Their rapid works were also the great help.

Mayuko Niwata and Ami Ito were current and previous office staff for our laboratory. Thanks to their help, I was able to concentrate my research.

Shoji Asai, Takao Nakagawa, Yasunobu Nakamura, Izumi Tsutsui, and Junji Yumoto were reviewers of this thesis. I believe their comments improve the thesis so much.

This work was financially supported by JSPS KAKENHI Grant No. 16J01010. I also recieved financial support and great experience in MIT from ALPS (Advanced Leading Graduate Course for Photon Science) program at the University of Tokyo.

Finally, I appreciate all supports of my father, mother, sister, aunt, uncle, grandfather, and grandmother who went to heaven this year. I would like to dedicate my thesis to them as one of compilations of my life.